Doctoral theses at NTNU, 2020:142

Øyvind Waage Hanssen-Bauer

Near-field response of an axisymmetric jet to transverse acoustic forcing

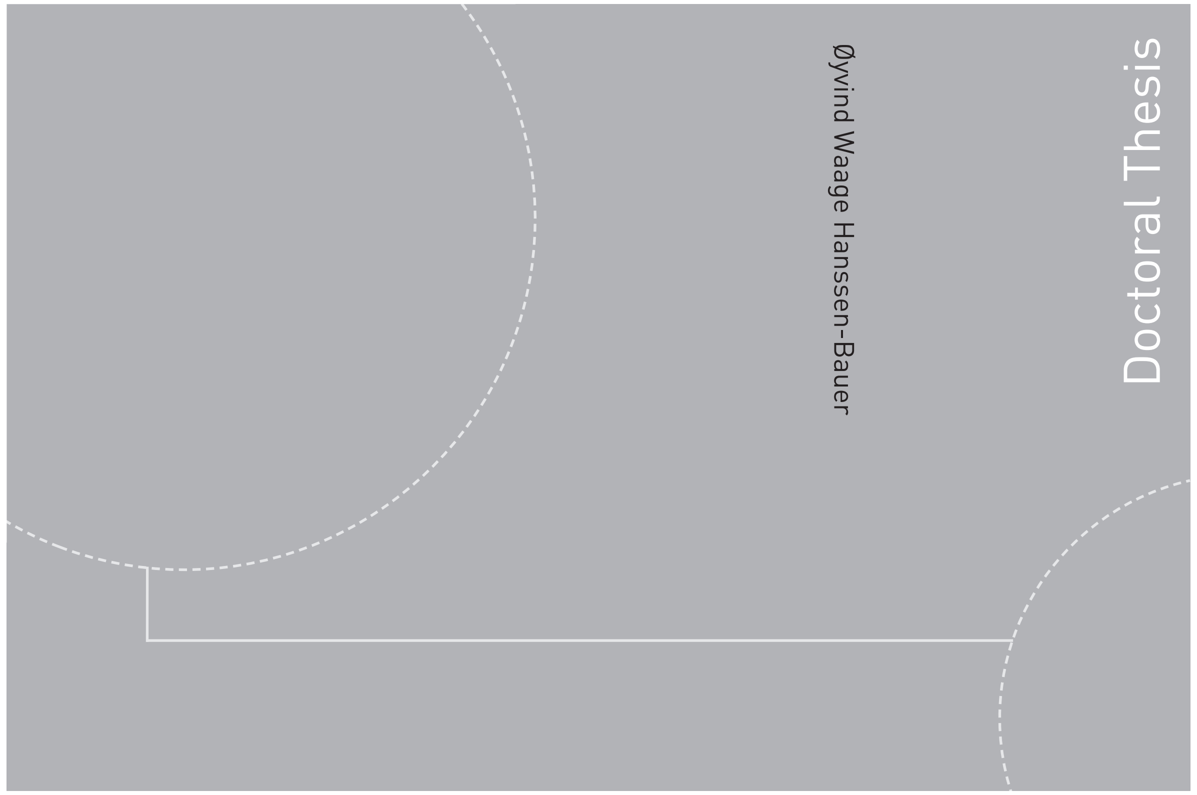

Doctoral theses at NTNU, 2020:142

NTNU
Norwegian University of
Science and Technology
Faculty of Engineering
Department of Energy and Process Engineering

NTNU

ISBN 978-82-326-4632-6 (printed version)
ISBN 978-82-326-4631-9 (electronic version)
ISSN 1503-8181

NTNU
Norwegian University of
Science and Technology

NTNU
Norwegian University of
Science and Technology

Øyvind Waage Hanssen-Bauer

Near-field response of an axisymmetric jet to transverse acoustic forcing

Thesis for the degree of Philosophiae Doctor

Trondheim, December 2019

Norwegian University of Science and Technology
Faculty of Engineering
Department of Energy and Process Engineering

NTNU
Norwegian University of
Science and Technology

NTNU
Norwegian University of Science and Technology

Thesis for the degree of Philosophiae Doctor

Faculty of Engineering
Department of Energy and Process Engineering

ISBN 978-82-326-4632-6 (printed version)
ISBN 978-82-326-4631-9 (electronic version)
ISSN 1503-8181

Doctoral theses at NTNU, 2020:142

Printed by Skipnes Kommunikasjon as

Abstract

The overall aim of this thesis was to investigate a transversely forced, round air-jet, with focus on the coherent vortex structures formed in the near-field of the jet. Increased knowledge about the interaction between the acoustic field and the simple, round jet is relevant for industrial flow scenarios such as thermo-acoustic oscillations in gas turbine combustors. A series of experiments were conducted placing the jet at different positions in a standing-wave pressure field while performing stereoscopic particle image velocimetry.

It is known from previous studies that at the pressure anti-node position, where only axial velocity fluctuations are present, the shear-layer of the jet rolls up into axisymmetric vortex rings. At the pressure node position on the other hand, where only transverse velocity fluctuations are present, the shear-layer rolls up into vortex structures that are in anti-phase on either side of the jet centerline in the direction of the pressure wave.

The results in this thesis suggest that it is the velocity fluctuations at the nozzle exit, either axial, transverse or a combination of both, that drive the formation of the vortex structures in the jet. These structures start to form when the velocity at the nozzle exit turns positive in the cycle; either out of the nozzle in axial direction, or away from the jet centerline for the transverse direction. Vortices formed by transverse fluctuations are found to pinch off one half of the forcing period later, when the jet turns away from the vortex. For positions close to the pressure anti-node, the presence of moderate amplitudes of transverse velocity fluctuations causes the vortex rings to tilt. For the positions between the pressure anti-node and the pressure node where both

velocity fluctuations are present with comparable amplitudes, the jet forms complex vortex structures that can be fundamentally different on either side of the jet. Here the phase between the velocity fluctuations seems to play an important role; either *one* vortex is formed in the shear-layer if the axial and transverse fluctuations are approximately in phase, or the velocity fluctuations form separate structures at different times in the cycle if the phase difference is sufficiently large.

Preface

This thesis is submitted to the Faculty of Engineering at the Norwegian University of Science and Technology (NTNU) for evaluation for the degree of Philosophiae Doctor (PhD). The work has been carried out in the Thermo Fluids group at the Department of Energy and Process Engineering (EPT). The project was supervised by Professor James Richard Dawson and co-supervised by Professor Lars Roar Sætran.

Øyvind Waage Hanssen-Bauer
December 2019

Acknowledgements

First of all I would like to thank my supervisor James for your support during this PhD, this thesis would not be possible without your effort. It has been inspiring to follow how you from scratch have built up a research group of highly competent people. Thank you also to my skiing-supervisor Lars for all the long conversations about the important things in life. Despite that the topic of this work ended up being on the side of your field of expertise, you have nevertheless been helpful and always supportive.

I would also express my gratitude to Nick for all the discussions we have had over the years. You have been crucial for my understanding of many of the fundamental aspects of this work.

A special thanks goes to Dhiren for your help with designing and conducting the experiments during your stay at NTNU.

Thank you to the staff at EPT for your support, and a special thanks to Arnt-Egil, Henning and Aslak for helping out in the lab, and to Debbie and Ingrid in the fluids group's office.

I also wish to thank you Truls for interesting discussions about acoustics, a topic I had limited knowledge about and that turned out to be a larger and more challenging part of this work that expected.

A big thank you goes to all of my fellow colleagues and friends at EPT over the years: Jan, Lars Morten, Pål Egil, Franz, Anna, Andreas, Ben, Simen, Heiner, Ehsan, Marin, Jørgen, Eskil, Vipin, Håkon, Abhijit, Marek, Thomas, Philip, Eirik, Leon, Melissa and Marcel. Thank you all for the lunches, dinners, department trips, and cabin trips as well as skiing, running and climbing activities.

Thank you to my new colleagues in the wind group at IFE, and especially to Roy. Without your support, understanding and patience during the last year, I would not have been able to come this far.

Finally, I would like to thank my family for your patience, understanding and endless support, thank you for listening and advising, making me dinner, arranging and fixing, and giving me time to focus on this work.

Table of contents

List of figures

List of tables

Nomenclature

Roman Symbols

$\mathbf{A}$	The velocity gradient tensor, $\nabla \mathbf{u}$
A_1, A_2, A_3	Cross-sectional area of pipe with area change
A	Amplitude of sinusoidal forcing
A_a	Initial amplitude of acoustic contribution of transverse velocity
A_n	Cross-sectional area of the neck of an Helmholtz resonator
A_v	Initial amplitude of vortex induced contribution of transverse velocity
C	Boundary of integral surface S
$\hat{C}_{m_h}$	Amplitude of hydrodynamic mode m_h
c	Speed of sound
D	Nozzle exit diameter
D_p	Pipe inner diameter
E_a	Voltage acquired during hot-wire measurements
E_{offset}	Voltage offset, used in hot-wire measurements
E_w	Voltage over hot-wire
e_{ac}	Potential energy density gradient

f	Frequency
f_a	Frequency of axisymmetric forcing
f_h	Frequency of helical forcing
f_R	Recording frequency
f_0	Preferred-mode frequency of the jet
G	Gain, used in hot-wire measurements
I	Sound intensity/energy flux density
I_1, I_2	Pixel intensity in frame 1 and 2 in a PIV image pair
i	The imaginary unit, $\mathrm{i}^2 = -1$
k	Wave number
k_1, k_2	Wave number for downstream and upstream wave
L_n	Neck length of Helmholtz resonator
L_P	Piston stroke length
L_x, L_y, L_z	Streamwise, transverse and spanwise dimensions of jet enclosure
l, m, n	Acoustic modes in x, y and z direction
$\dot{M}$	Momentum flow rate
m_h	Hydrodynamic azimuthal mode number
p	Pressure
p_i	Pressure of incident wave
$\mathbf{Q}$	The antisymmetric part of $\mathbf{A}$, $\frac{1}{2}(A - A^T)$
$\dot{q}$	Unsteady heat release rate per unit volume
R	Pressure ratio of reflected and incident wave
$R_{I_1 I_2}$	PIV cross-correlation of pixel intensities between frame 1 and 2

R_w	Electrical hot-wire resistance
Re_D	Reynolds number based on the nozzle exit diameter, $\frac{U_e D}{\nu}$
$r_{1/2}$	Jet half width, defined by $\bar{u}_x(x, r_{1/2}(x)) = \frac{1}{2}\bar{u}_x(x, r = 0)$
$\mathbf{S}$	The symmetric part of $\mathbf{A}$, $\frac{1}{2}(A + A^T)$
S	Integral surface bounded by line C
St_D	Strouhal number based on nozzle diameter, $\frac{fD}{U_e}$
T	Period, $1/f$
T_a	Fluid temperature acquired during hot-wire measurements
T_0	Fluid temperature measured prior to hot-wire calibration
t	Temporal variable
t_l	PIV laser delay time
$t_{\tilde{u}0}$	Time in forcing cycle when $\tilde{u}$ at the centerline of the jet exit changes sign from negative to positive ($\tilde{u}(x = 0, r = 0) = 0$, $\partial\tilde{u}(x = 0, r = 0)/\partial t > 0$)
$t_{\tilde{v}0+}$	Time in forcing cycle when $\tilde{v}$ at the centerline of the jet exit changes sign from negative to positive ($\tilde{v}(x = 0, r = 0) = 0$, $\partial\tilde{v}(x = 0, r = 0)/\partial t > 0$)
$t_{\tilde{v}0-}$	Time in forcing cycle when $\tilde{v}$ at the centerline of the jet exit changes sign from positive to negative ($\tilde{v}(x = 0, r = 0) = 0$, $\partial\tilde{v}(x = 0, r = 0)/\partial t < 0$)
δt	PIV particle-image separation time
U	Mean velocity in x direction
U_c	Time averaged velocity at centerline of the nozzle exit
U_e	Mean velocity at nozzle exit
$\mathbf{u}$	Velocity vector
u, v, w	Velocity components in x, y and z directions
u_p	Piston velocity

$u_{v,c}$	Axial vortex convection velocity
u_x, u_r, u_θ	Velocity components in the axial, radial and azimuthal direction
V	Volume
v_a	Acoustic contribution of transverse velocity
v_v	Vortex induced contribution of transverse velocity
w	Energy density
w_{kin}	Kinetic energy density
w_{pot}	Potential energy density
x, r, θ	Axial, radial and azimuthal coordinates in a cylindrical coordinate system
x_c, r_c	Vortex centroid coordinates
x_0	Virtual origin of a self-similar jet
$\Delta x, \Delta y$	PIV vector spacing in x and y direction
y, z	Transverse and spanwise coordinates in Cartesian, right-handed coordinate system
Z	Acoustic impedance
Z_0	Acoustic characteristic impedance

Greek Symbols

α	Decay rate of vortex induced velocity
Γ	Circulation
δ	Acoustic end correction of an geometry with an open end
$\theta_\mathbf{s}$	Spreading angle of a self-similar jet
λ	Acoustic wavelength, c/f
λ_2	Second eigenvalue (sorted by value) of the symmetric tensor $\mathbf{S}^2 + \mathbf{Q}^2$

ν	Kinematic viscosity
ρ	Air density
$\varphi_{\mathbf{v_a},\mathbf{v_v}}$	Phase angle between the acoustic and vortex induced velocity fluctuations
ϕ	Phase angle in forcing cycle
$\Delta\phi$	Phase angle between vortex structures on the left and right side of the jet
Φ	Velocity potential
ψ	Stream function
ω	Angular frequency, $2\pi f$
$\vec{\omega}$	Vorticity vector
ω_0	Angular resonance frequency

Superscripts

$(\ )^*$	Normalized quantities
$\hat{(\ )}$	Fourier transformed variable
$\bar{(\ )}$	Temporal average
$\langle\ \rangle$	Axial average
$\tilde{(\ )}$	Phase average
$(\ )'$	Perturbation/fluctuating component

Subscripts

$(\ )_{\mathrm{RMS}}$	Root-Mean-Square quantities
$(\ )_x$, $(\ )_r$, $(\ )_\theta$	Components in the axial, radial and azimuthal direction

Acronyms / Abbreviations

DNS	Direct numerical simulation

Nomenclature

FFT	Fast Fourier Transform
LES	Large eddy simulation
LCS	Lagrangian Coherent Structures
PIV	Particle Image Velocimetry
RMS	Root Mean Square
SPIV	Stereoscopic PIV
SR	Spin ratio

Chapter 1

Theoretical background and previous work

1.1 Introduction

The topic of this thesis is an investigation of a transversely forced jet, where pressure waves act perpendicular to the jet's mean flow, and in particular modification of the base flow and the coherent structures formed in the near-field of the jet. There is a great amount of literature on longitudinally forced jets, where the pressure waves are parallel to the jet flow, and the jet response is known for a wide range of forcing configurations. Recently there has been an increasing research activity also on transverse forcing, driven by the gas turbine community and challenges related to thermo-acoustic oscillations. Most of these studies tend to mimic modern industry designs, with complex flow and geometries. The jet used in the experiments in this study was as simple as possible; the flow was incompressible with a uniform inlet velocity without swirl, combustion or heat transfer.

This chapter presents the theory and literature related to transverse acoustic forcing of jets. The research combines fluid mechanics and acoustics, both important to understand the phenomena observed in this study. In section

1.2 the theory of the classical self-preserving, axisymmetric jet is presented, including instability theory. Also pulsed jets, a result of periodic, axisymmetric forcing of jets are covered, together with vortex rings, which is an important type of vortex structures that commonly appear in pulsed jets. In section 1.3, jet manipulation and asymmetric forcing is presented, with focus on what impact it has on the coherent structures in the jet flow. Section 1.4 covers transverse acoustic instabilities mostly associated with gas turbine combustion flows which motivates the thesis topic. Section 1.5 summarizes state-of-the-art and knowledge gaps, while section 1.6 presents the objectives of this study.

1.2 Axisymmetric jets

A jet is a canonical flow where fluid of a constant velocity enters an ambient fluid through an orifice or a nozzle, creating a shear-layer between the jet fluid and its surroundings. The experiments in this study consider an incompressible, axisymmetric air jet discharging into a very long rectangular box. The box width ensures the jet is "free" in the near-field and developing regions, but not in the far field.

The jet flow can be described in cylindrical coordinates x, r, θ by the turbulent boundary layer approximation of the mean continuity and momentum equations for axisymmetric, stationary non-swirling flows (Pope, 2001):

$$\frac{\partial \bar{u}_x}{\partial x} + \frac{1}{r}\frac{\partial (r\bar{u}_r)}{\partial r} = 0, \tag{1.1}$$

$$\bar{u}_x \frac{\partial \bar{u}_x}{\partial x} + \bar{u}_r \frac{\partial \bar{u}_x}{\partial r} = \frac{\nu}{r}\frac{\partial}{\partial r}\left(r\frac{\partial \bar{u}_x}{\partial r} - \frac{1}{r}\frac{\partial}{\partial r}\left(\overline{r u'_x u'_r}\right)\right). \tag{1.2}$$

Here $\bar{u}_x$, $\bar{u}_r$ and $\bar{u}_\theta$ are the time averaged velocity components describing the flow field, x is the symmetry axis of the jet, i.e. x is the dominant flow direction and ν is the kinematic viscosity of the fluid, which for air is $\nu = 1.5 \cdot 10^{-5}$ m^2/s. It is assumed that all gradients except in the r direction can be neglected and that the flow is quiescent or uniform as $r \to \infty$.

The steady, incompressible jet can be characterized by a single, non-dimensional group, the Reynolds number. This is defined as

$$Re_D = \frac{U_e D}{\nu}. \tag{1.3}$$

Here, U_e is the mean velocity at the exit plane and D is the exit diameter of the nozzle.

Downstream of the nozzle exit the jet keeps an almost constant speed before it slows down as a consequence of entrainment of the slower ambient fluid into the jet. For a jet with a so-called top-hat profile, where the velocity of the nozzle exit cross-section is uniform, the potential core can be approximately defined as the part of the jet having a time averaged velocity larger than a certain threshold. In this study 95 % of U_e is used as threshold:

$$\bar{u}_{x,\text{potential core}} > 0.95 \cdot U_e. \tag{1.4}$$

The potential core length is defined as the distance from the nozzle exit along the centerline to where the potential core stops.

Downstream of the potential core, the time averaged velocity profile develops to a nearly Gaussian shape, and the jet becomes self-similar (Pope, 2001). This means that the time averaged axial velocity profiles for different axial positions collapse when the velocity and radial component are normalized by the local centerline velocity and a measure of the local jet width, respectively. Figure 1.1a shows the axial variation for the dimensional profile of a round jet, and figure 1.1b shows how the profiles collapse when they are normalized. The radial component is here normalized by the jet half width, $r_{1/2}$, defined by $\bar{u}_x(x, r_{1/2}(x)) = \frac{1}{2}\bar{u}_x(x, r = 0)$. Even though the volume flow of the jet increases downstream due to entrainment, the momentum of the jet's cross-section must be conserved if there are no external forces acting on it. By neglecting viscosity, equation (1.1) and (1.2) can be combined to obtain the conservative momentum equation:

$$\frac{\partial}{\partial x}(r\bar{u}_x^2) + \frac{\partial}{\partial r}\left(r\bar{u}_x\bar{u}_r + r\overline{u'_x u'_r}\right) = 0. \tag{1.5}$$

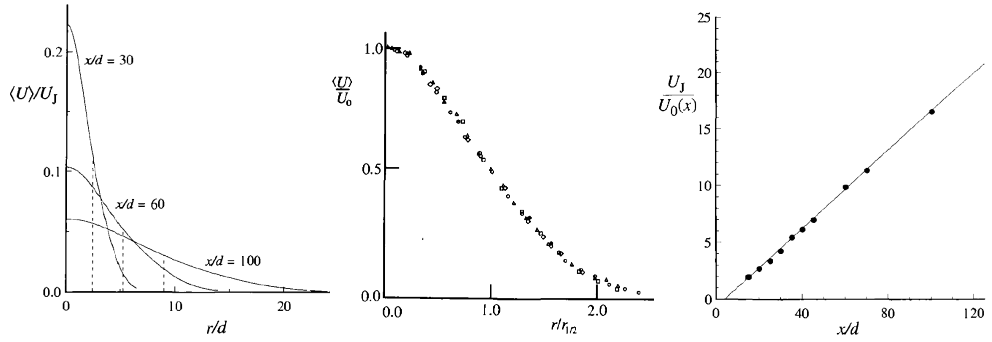

(a) (b) (c)

Figure 1.1: Time averaged axial velocity profiles for different axial positions of a round jet in (a) dimensional and (b) non-dimensional form. (c) shows the jet centerline velocity at the exit divided by the axially varying centerline velocity against axial position. Adapted from Pope (2001).

By integrating with respect to r, the following is obtained:

$$\frac{\mathrm{d}}{\mathrm{d}x}\int_0^\infty r\bar{u}_x^2\mathrm{d}r = -\left[r\bar{u}_x\bar{u}_r + r\overline{u_x'u_r'}\right]_0^\infty = 0. \tag{1.6}$$

By comparing this with the expression for momentum flow rate,

$$\dot{M}(x) \equiv \int_0^\infty 2\pi r\rho\bar{u}_x^2\mathrm{d}r = 2\pi\rho\int_0^\infty r\bar{u}_x^2\mathrm{d}r, \tag{1.7}$$

where ρ is the density of the fluid, it is clear that the jet's momentum is conserved. From this it can be shown that the centerline velocity decreases inversely with x in the self-similar region, as also the experimental data in figure 1.1c shows. The centerline velocity, $U_c(x)$, can therefore be expressed as

$$\frac{U_c(x)}{U_e} = \frac{B}{(x-x_0)/D}, \tag{1.8}$$

where x_0 is the virtual origin obtained by extrapolating the measurements in figure 1.1c to the horizontal axis, and B is a constant. Further, the jet spreads linearly so a constant spreading angle θ_S can be expressed as:

$$r_{1/2}(x) = \theta_S(x-x_0). \tag{1.9}$$

Self-similarity occurs for $x/D > 20$ for the mean velocity profile, while the fluctuating components develop slower, and is not completely self-similar before $x/D > 50$ for the axial and $x/D > 70$ for the radial components (White, 2006). Also Reynolds stresses and dissipation are shown to be self-similar (Pope, 2001). All these self-similar quantities of the jet are independent of Re_D, so that different axisymmetric jet flows with same inlet conditions, all collapse in the self-similar region.

1.2.1 Jet instabilities

In this study the focus is on the near-field of the jet, defined as the first diameters downstream of the nozzle. In this region the jet develops from the initial top-hat velocity profile towards the self-similar Gaussian shape, and here the shear-layer of the jet plays an important role. By performing a stability analysis, it can be shown that this shear-layer is unconditionally unstable (see appendix A). This means that if an oscillation appears in the shear-layer, the amplitude will grow with time (White, 2006). The instabilities are not self-excited, but are dependent on an external disturbance source. The jet is therefore said to be globally stable, but convectively unstable (Schmid & Henningson, 2012). The instabilities in the shear-layer of a round jet is a type of Kelvin–Helmholtz instability, named after Lord Kelvin (Thomson, 1871) and von Helmholtz (1868).

Batchelor & Gill (1962) investigated the temporal stability of an axisymmetric jet. They found that in the limit of short instability waves in the shear-layer of the jet, the phase velocity was going towards half of the jet velocity, which is the average of the jet and the ambient velocity. They also found that the growth rate of the instability increased progressively with Strouhal number, a non-dimensional frequency defined as

$$St_D = \frac{fD}{U_e}, \tag{1.10}$$

where f is the frequency of the instability waves.

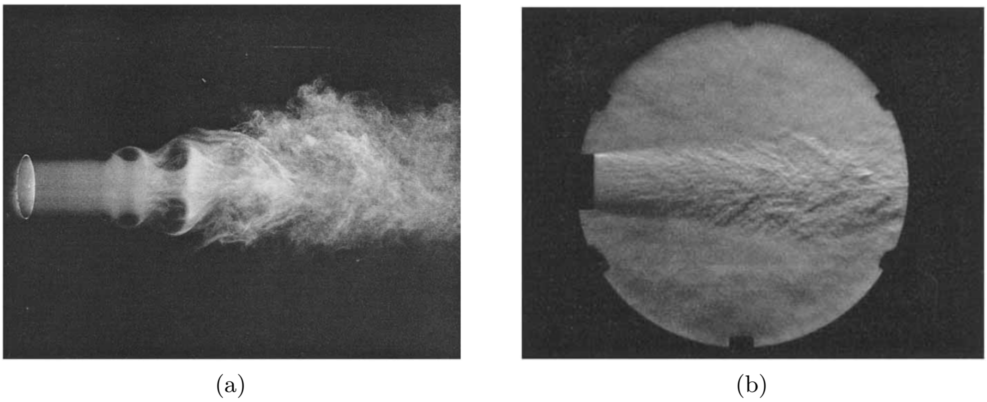

(a) (b)

Figure 1.2: (a) Spark photograph of a fog jet with $Re_D = 1.05 \cdot 10^4$ and (b) Schlieren photograph of a jet with $Re_D = 1.06 \cdot 10^5$, seeded with CO. Adapted from Crow & Champagne (1971).

Crow & Champagne (1971) investigated axisymmetric jets experimentally, and found that instabilities were present in the near-field of unforced, turbulent jets. The instabilities consisted of axisymmetric, coherent vortical structures they referred to as a *train of axisymmetric puffs*. These are visualized in the spark and Schlieren photographs in figure 1.2. In the experiments the formation of the puffs was found to be non-periodic, but they formed on average at a frequency corresponding to $St_D \approx 0.30$. The authors also showed that the frequency of the puffs could be locked by weak forcing from a sinusoidal signal produced by a loudspeaker placed upstream of the nozzle exit. An example of the forced jet flow is shown in figure 1.3. The forcing amplitude was measured as longitudinal oscillations of the flow at the nozzle exit, and was typically $u'_{\mathrm{RMS}}/U_e = 2$ %, where u'_{RMS} is the root-mean-square sinusoidal fluctuation of the axial velocity component. For the weakly forced jets, an optimal Strouhal number of $St_D = 0.3$ was found. Forcing at this frequency gave the highest amplitude of the velocity fluctuations at the end of the potential core, $x/D \approx 4$, for a given forcing amplitude. This was not in accordance with the temporal stability analysis by Batchelor & Gill, who predicted that the amplitude should increase with increasing Strouhal number. Crow & Champagne suggested that the saturation of the instability amplitude is a non-linear phenomenon, and that "The mode having a Strouhal number of 0.30 is preferred in the sense

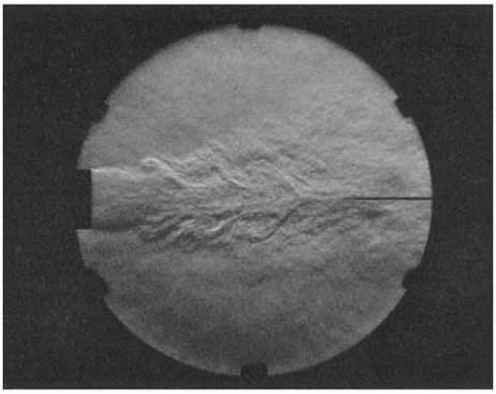

Figure 1.3: Schlieren photograph of a jet with $Re_D = 1.06 \cdot 10^5$ seeded with CO, under influence of 2 % forcing at $St_D = 0.60$. Adapted from Crow & Champagne (1971).

that it can attain the highest possible amplitude under the combined effects of linear amplification and non-linear saturation". Later, studies have shown that the *preferred mode* of an axisymmetric jet lies in the range $St_D = 0.24 - 0.64$ (Gutmark & Ho, 1983). The corresponding preferred-mode frequency is termed f_0.

Crow & Champagne developed a spatial linear stability theory believing that this would better fit the experiments than the temporal theory by Batchelor & Gill. However, this was far off the experimental data of the phase velocity of the instability waves for different wavelengths, while the temporal theory matched the measurements quite well. Also for predicting the amplification rate the temporal instability theory was closest, but here the deviation was larger with the prediction 47 % higher for $St_D = 0.30$. Michalke (1971) later showed that the reason for the divergence between the spatial theory and the experimental data was the assumption of an infinitesimally thin shear-layer of the jet. By taking into account a finite shear-layer thickness, Michalke's spatial instability theory matched the data by Crow & Champagne. Raman *et al.* (1994) showed that for low-amplitude axisymmetric forcing of a round turbulent jet, linear stability theory was only able to predict the development of the fundamental jet instability very close to the nozzle exit, while an energy

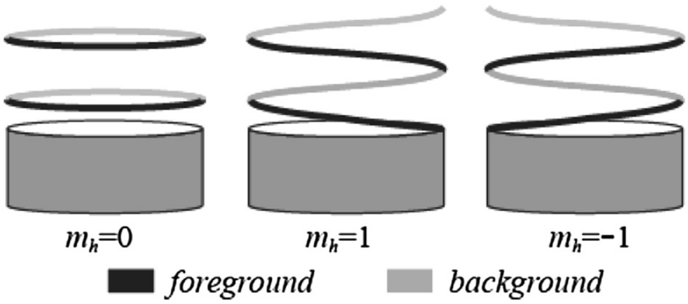

Figure 1.4: Illustration of hydrodynamic azimuthal modes in a round jet. Adapted from O'Connor *et al.* (2015).

integral theory developed by Mankbadi & Liu (1981) was matching quite well in the whole measurement domain, up to $x/D = 6$.

By Fourier series expansion in the azimuthal direction the disturbances in the shear-layer of the jet can be decomposed into the following hydrodynamic instability modes:

$$\hat{u}'(x, r, \theta, f) = \sum_{m_h=-\infty}^{\infty} c_{m_h}(x, r, f) e^{\mathrm{i} m_h \theta} \tag{1.11}$$

where the Fourier coefficients are given by

$$c_{m_h}(x, r, f) = \frac{1}{2\pi} \int_0^{2\pi} e^{\mathrm{i} m_h \theta} \hat{u}'(x, r, \theta, f) d\theta \tag{1.12}$$

and m_h is the hydrodynamic azimuthal mode number. $m_h = 0$ is the axisymmetric mode, while $m_h \neq 0$ are helical modes. The sign denotes the direction of the helical disturbance, and its absolute value denotes the spatial frequency. Figure 1.4 illustrates the three modes $m_h = 0$, 1 and -1. According to the stability analysis by Michalke & Hermann (1982), both the axisymmetric and helical modes exist in round jets. $m_h = 0$ and $m_h \pm 1$ are the modes with the largest growth rates near the exit of a non-swirling jet, and these modes have comparable maximum growth rates for a jet with a top-hat profile. However, experiments by e.g. Crow & Champagne (1971), figure 1.2, show that it is the axial $m_h = 0$ mode that is visible in the near-field of the jet. Measurements by Raman *et al.* (1994) showed that the axisymmetric mode dominated in the near-field of an unforced jet, while after the potential core ($x/D \approx 6$), the helical modes $m_h = \pm 1$ dominated and $m_h = 0$ disappeared. The higher order modes, $|m_h| > 1$, were found to be significantly smaller for all axial positions measured, up to $x/D = 8$.

For a forced jet, the shear-layer rolls up into vortex structures for a certain finite level of disturbance amplitude (Brown & Roshko, 1974). For an axisymmetric jet forced in a similar way as by Crow & Champagne (1971), the $m_h = 0$ mode of the jet will be excited and locked to the forcing frequency. By increasing the forcing, the vortical structures in the shear-layer grow and can eventually form into vortex rings. These flow structures are of great importance in the field of forced jets, and will be presented in the next section.

1.2.2 Vortex rings

Vortex rings are fundamental fluid structures important in jet dynamics. An extensive amount of literature deal with vortex rings and their formation, and reviews of this subject can be found in Shariff & Leonard (1992) and Lim & Nickels (1995). To study vortex rings in isolation and experimentally, starting jets are often used. Then the fluid is pushed impulsively through a nozzle or orifice, and the shear-layer of the jet rolls up to a vortex ring. Lim & Nickels (1995) defines the vortex ring as a bounded region of vorticity in a fluid where the vortex lines form closed loops. The vortex ring gets this vorticity from the vorticity flux provided by the jet shear-layer (Didden, 1979).

Vortex rings can be described mathematically by the vorticity equation:

$$\frac{D\vec{\omega}}{Dt} = \vec{\omega}\nabla\mathbf{u} + \nu\nabla^2\vec{\omega}. \tag{1.13}$$

Here

$$\frac{D\vec{\omega}}{Dt} = \frac{d\vec{\omega}}{dt} + \mathbf{u}\nabla\vec{\omega} \tag{1.14}$$

is the substantial derivative, $\mathbf{u} = (u_x, u_r, u_\theta)$ is the velocity vector and

$$\vec{\omega} = (\omega_x, \omega_r, \omega_\theta) = \nabla \times \mathbf{u} \tag{1.15}$$

is the vorticity vector. By assuming the vortex ring is axisymmetric, inviscid and without swirl ($u_\theta = 0$), the equation simplifies to

$$\frac{D(\omega_\theta/r)}{Dt} = 0. \tag{1.16}$$

In this case, only the azimuthal vorticity component is non-zero. For an inviscid vortex ring with or without a convective velocity, the shape remains constant in time. In a frame-of-reference following the vortex ring we have a steady-state solution, and equation (1.16) reduces to

$$\mathbf{u}\nabla(\omega_\theta/r) = 0. \tag{1.17}$$

The solution of this equation is on the form

$$\frac{\omega_\theta}{r} = F(\psi), \tag{1.18}$$

where $\psi(x, r)$ is the stream function defined as

$$u_x = \frac{1}{r}\frac{\partial \psi}{\partial r} \qquad u_r = -\frac{1}{r}\frac{\partial \psi}{\partial x}, \tag{1.19}$$

and F is some arbitrary function. The azimuthal vorticity can be expressed by the stream function:

$$\omega_\theta = \frac{\partial u_r}{\partial x} - \frac{\partial u_x}{\partial r} = -\frac{1}{r}\left(\frac{\partial^2 \psi}{\partial x^2} + \frac{\partial^2 \psi}{\partial r^2} - \frac{1}{r}\frac{\partial \psi}{\partial r}\right). \tag{1.20}$$

Inserting this into equation (1.18) we get

$$\left(\frac{\partial^2 \psi}{\partial x^2} + \frac{\partial^2 \psi}{\partial r^2} - \frac{1}{r}\frac{\partial \psi}{\partial r}\right) = -r^2 F(\psi). \tag{1.21}$$

A famous solution of this equation is the Hill's spherical vortex (Hill, 1894), where the vorticity is bounded by a sphere of radius a and the center is at the

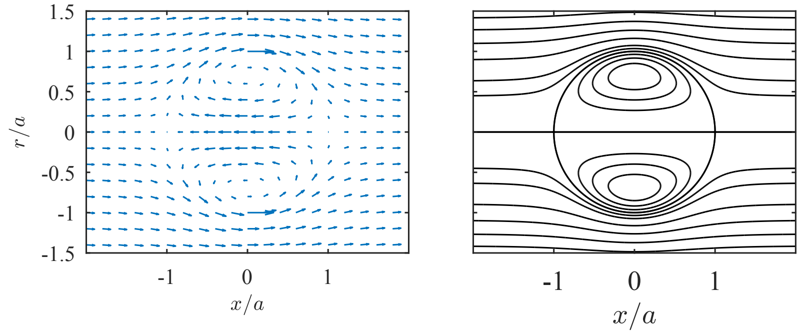

Figure 1.5: Velocity field (left) and stream lines (right) of a Hill's vortex.

origin:

$$\psi = \begin{cases} -\frac{3}{4}\frac{Ur^2}{a^2}\left(a^2 - x^2 - r^2\right), & x^2 + r^2 \leq a^2. \\ \frac{1}{2}Ur^2\left(1 - \frac{a^3}{(x^2+r^2)^{3/2}}\right), & x^2 + r^2 > a^2. \end{cases} \tag{1.22}$$

Here U is the velocity of a uniform axial flow. The velocity field and streamlines of Hill's vortex are shown in figure 1.5. Hill's solution of equation (1.21) can be extended by a parameter representing the mean core radius of the vortex ring, resulting in a family of vortex rings known as the Norbury-Frankel family (Fraenkel, 1972; Norbury, 1972).

For an inviscid vortex ring, the circulation is an invariant. The circulation is defined as the line integral of velocity along a closed circuit C:

$$\Gamma = \oint_C \mathbf{u} \cdot \mathbf{dl} = \int_S \vec{\omega} \cdot \mathbf{dS}. \tag{1.23}$$

Here, S is the surface bounded by C. To find the circulation of an axisymmetric vortex ring, the circuit C can be chosen to be in a plane defined by $\theta =$ constant and to encircle the vorticity through the origin and to one side of the axis of symmetry in that plane. The circuit C needs to move with the vortex ring. Circulation is only an invariant in the inviscid case. For the viscous vortex ring, the vorticity will diffuse in time and the circulation of the vortex ring then decreases.

An analytical model for vortex ring formation is the slug model (Didden, 1979). This model predicts the circulation of a vortex ring produced when a cylindrical slug of fluid is pushed through the nozzle by a piston. The model gives the following expression for the vorticity flux:

$$\frac{d\Gamma_{\text{slug}}}{dt} = \int \omega_\theta u_x dr = \int \left(\frac{\partial u_r}{\partial x} - \frac{\partial u_x}{\partial r}\right) u_x dr \approx \int \left(-\frac{\partial u_x}{\partial r}\right) u_x dr \approx \frac{1}{2}u_p^2(t). \tag{1.24}$$

Here, the boundary layer assumptions are invoked, and it is assumed that the velocity external to the boundary layer at the inside of the nozzle at the exit plane equals the piston velocity, u_p. If u_p is known, the circulation as a function of time can be found by integration:

$$\Gamma_{\text{slug}} \approx \int_0^t \frac{1}{2}u_p^2(\tau)d\tau. \tag{1.25}$$

From the slug model an estimate of the axial convection velocity of the vortex ring can be obtained (Mohseni & Gharib, 1998):

$$u_{v,c} = \frac{1}{2}\bar{u}_p(t). \tag{1.26}$$

Here $\bar{u}_p(t) = \frac{1}{t}\int_0^t u_p(\tau)d\tau$ is the running average of the piston velocity. In practice, the vortex ring velocity has shown to be higher than this estimate.

For a jet acoustically forced by a sinusoidal signal, we can approximate the "piston velocity" to be

$$u_p = U_e(1 + A\sin(\omega t)) \tag{1.27}$$

where $A = (\sqrt{2}/2)u'_{\text{RMS}}/U_e$ is the normalized amplitude of the axial velocity fluctuations in the jet due to the acoustic forcing, and $\omega = 2\pi f$ is the angular frequency of the forcing (not to be confused with the vorticity vector $\vec{\omega}$). By inserting this into equation (1.24) and integrating, we get the following expression for the vortex ring circulation:

$$\begin{aligned}\Gamma_{\text{slug}} \approx & \int_0^t \frac{1}{2}u_p^2(\tau)d\tau = \frac{1}{2}U_e^2\int_0^t (1 + A\sin(\omega\tau))^2 d\tau \\ =& \frac{1}{2}U_e\left(\left(1+\frac{A^2}{2}\right)t - \frac{2A}{\omega}(1-\cos(\omega t)) - \frac{A^2}{4\omega}\sin(4\pi f t)\right).\end{aligned} \tag{1.28}$$

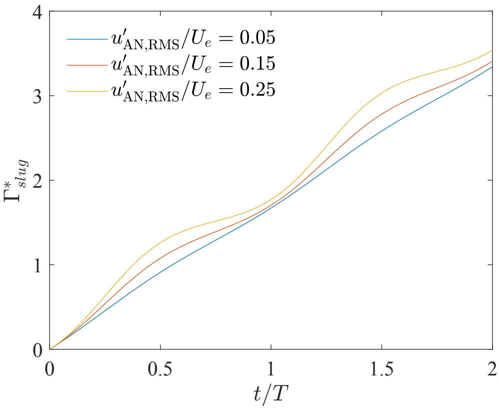

Figure 1.6: Nondimensional circulation Γ^* versus time according to the slug model in equation (1.30) for a jet with Strouhal number $St = 0.3$.

This equation can be written in nondimensional form by dividing with U_eD, and using the nondimensional versions of circulation ($\Gamma^* = \Gamma/(U_eD)$), time ($t^* = t/T = \omega t/(2\pi)$) and frequency ($St = \frac{\omega D}{2\pi U_e}$):

$$\Gamma^*_{\text{slug}} \approx \frac{1}{2 \cdot \text{St}} \left(\left(1 + \frac{A^2}{2}\right) t^* - \frac{A}{\pi} \left(1 - \cos(2\pi t^*) - \frac{A}{8} \sin(4\pi t^*)\right) \right). \tag{1.29}$$

In the experiments in this study, the axial fluctuations never exceed $A \approx 0.35$, causing the amplitude of the high-frequent term $\frac{A}{8} \sin(4\pi t^*)$ never to exceed 5% of the term $\cos(2\pi t^*)$. The circulation can therefore be approximated to:

$$\Gamma^*_{\text{slug}} \approx \frac{1}{2 \cdot \text{St}} \left(\left(1 + \frac{A^2}{2}\right) t^* - \frac{A}{\pi} \left(1 - \cos(2\pi t^*)\right) \right). \tag{1.30}$$

This equation is shown in figure 1.6 for the three different forcing amplitudes $A \approx (\sqrt{2}/2) u'_{\text{AN,RMS}}/U_e$ that are most frequently used in this study.

1.2.3 Optimal vortex rings

Gharib *et al.* (1998) found a universal time scale for vortex ring formation. Their study showed that for a starting jet there is a limiting value of the stroke

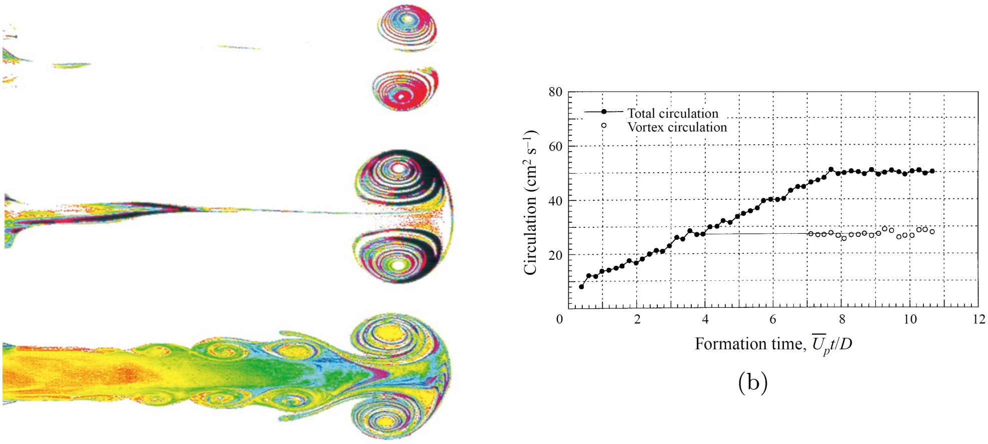

(b)

(a)

Figure 1.7: (a) Flow-visualization of vortex rings for increasing maximum stroke ratios; $L_P/D = 2$ (upper jet), $L_P/D = 3.8$ (middle jet) and $L_P/D = 8$ (lower jet). (b) Total and vortex circulation for $L_P/D = 8$. Adapted from Gharib *et al.* (1998).

ratio, defined as

$$L_P/D = \bar{u}_p(t)t/D, \tag{1.31}$$

where the vortex ring reaches a maximum possible circulation. Here, L_P is the piston stroke or length of ejected fluid. As shown in figure 1.7a, the size of the vortex ring increases from the upper ring ($L_P/D = 2$) to the middle ring ($L_P/D = 3.8$), while the growth does not continue as the stroke length is increased further for the lower ring ($L_P/D = 8$). The lower vortex ring is however followed by a tail of fluid with vorticity that does not enter the ring, whereas this tail is not apparent for the other cases. By measuring the total circulation of the starting jet together with the circulation of the vortex ring as a function of time, as seen in figure 1.7b, Gharib *et al.* showed that the circulation level of the ring corresponds to the circulation produced by the piston at $(L_P/D) \approx 4$, as long as the maximum stroke length of the piston is $(L_P/D) > 4$. Gharib *et al.* called this limit the formation number, and the process where the vorticity from the jet is no longer able to entrain the ring was termed vortex ring pinch-off. If $(L_P/D) < (L_P/D)_{\text{lim}} \approx 4$, all the circulation from the starting jet entrain the vortex ring. For stroke ratios larger than the formation number, the ring pinches off at $(L_P/D)_{\text{lim}} \approx 4$, and the rest of the circulation is seen as a tail of vorticity behind the vortex ring. The authors further showed that the formation number found experimentally matches the theoretically predicted time, where the energy of the Norbury-Fraenkel vortex rings, described in the previous section, exceed the energy of the shear-layer predicted by the slug model. Shusser & Gharib (2000) and Mohseni *et al.* (2001) later proposed that pinch-off is initiated when the axial velocity of the vortex ring exceeds the axial velocity of the trailing jet. It is also shown that the formation number corresponds to an optimal vortex ring in terms of maximum impulse, circulation and volume per piston work (Linden & Turner, 2001).

Lawson & Dawson (2013) found that a trailing pressure maximum forms behind the turbulent vortex ring in a synthetic jet. These maxima were identified by locating where contours of $\partial p/\partial x = 0$ were crossing the jet centerline. The trailing pressure maximum plays an important role in the pinch-off mechanism of the ring as the adverse pressure gradient upstream of this point stops the vorticity flux from the jet to enter the ring structure. A Lagrangian Coherent Structure (LCS) analysis carried out in their study supports this explanation. A repelling LCS is found behind the vortex ring. The fluid is not able to pass this LCS, and therefore it divides the ring from the rest of the shear-layer. It was found that the formation of the trailing pressure maximum and the repelling LCS coincided with the pinch-off time estimated using the circulation method by Gharib *et al.* (1998). Later, Schlueter-Kuck & Dabiri (2016) used a similar method to estimate the pinch-off time of vortex rings, but instead of looking at the pressure at the symmetry line they used the pressure in the shear-layers. Figure 1.8 shows the shear-layer pressure in a $x - t$ diagram. The vortex ring core is identified as a blue diagonal line of low pressure marked as (i), while the trailing pressure maximum follows later in time as a red line of high pressure marked as (ii). After the trailing pressure maximum, a secondary vortex forms. Due to a higher velocity, this vortex catches up and merges with the first vortex. The result of this is that the trailing pressure maximum of the second vortex, marked as (iv), becomes the trailing pressure maximum of the combined vortex as the first pressure maximum disappears. Therefore it is (iv) that is associated with vortex pinch-off, and by following this area of high pressure back to the vertical axis, $x/D = 0$, the pinch-off time is found.

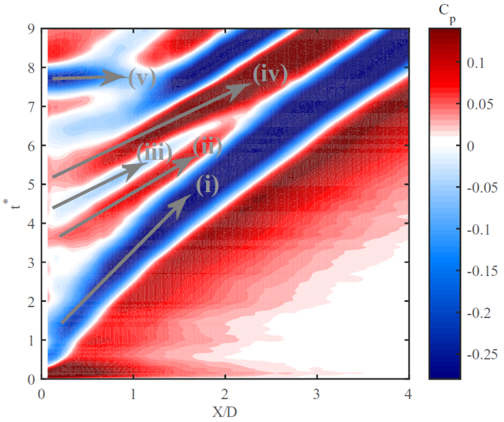

Figure 1.8: Pressure in the shear-layer of a jet under the formation of a vortex ring. Adapted from Schlueter-Kuck & Dabiri (2016).

1.2.4 Pulsed jets

If a jet that initially has a constant exit velocity is longitudinally and periodically forced, e.g. by a pressure wave upstream of the jet nozzle, its exit velocity will turn into a periodic velocity program. For sufficient forcing amplitude, this results in a pulsed jet where the velocity oscillation excites instabilities in the shear-layer and vortical structures are formed. As the amplitude is increased, these structures grow and can eventually form vortex rings. The result is a periodic train of vortex rings convecting downstream in the jet. Külsheimer & Büchner (2002) found that for a swirling jet with a sinusoidal velocity program, the limit amplitude for this transition to happen decreases hyperbolically with the jet's Strouhal number.

Aydemir *et al.* (2012) found that for a pulsed jet with a sinusoidal velocity program equal to equation (1.27), the separation distance between consecutive rings increases with both amplitude and forcing period. Increasing the forcing amplitude also changes the initial roll-up location, causing vortices to form closer to the jet exit. They also found that the same formation number as found by Gharib *et al.* (1998) is valid for pulsed jets, but only when a time scale of one third of the forcing period, $T/3$, is used for calculating the stroke ratio over one forcing period. $t = T/3$ is the time in the forcing cycle when the vortex ring velocity exceeds the velocity of the jet shear-layer, and the *effective* forcing period can therefore be seen as one third of the sinusoidal velocity period. From this Aydemir *et al.* found that for a longitudinal, sinusoidal forcing system, the average piston velocity $\bar{u}_p$ is given by

$$\bar{u}_p = U_e \left(1 + \frac{9A}{4\pi}\right), \tag{1.32}$$

where A is defined in equation (1.27). Asadi *et al.* (2018) performed numerical simulations on a pulsed jet with constant flow of duration $T_s/T = 0.25 - 0.75$ of the forcing period, and no flow between the pulses. They found an empirical relation for the axial center position of the vortex rings generated by the jet:

$$x_v/D = 0.27 \left(\frac{1}{St_D}\right)^{1+1.31Re_D^{-0.2}} \frac{t}{T_s}. \tag{1.33}$$

Here, U_e in St_D and Re_D is the jet exit velocity averaged over the forcing period T.

Pulsed jets have also been investigated in relation to gas turbine combustion. Balachandran *et al.* (2005) showed that for a lean premixed turbulent bluff-body-stabilized flame, upstream longitudinal forcing affected the heat release, which became nonlinear after the inlet velocity amplitudes exceeded a certain limit. It was found that this limit coincided with the appearance of vortex roll-up in the shear-layer.

1.3 Jet manipulation and asymmetric forcing

So far, we have looked at the undisturbed development of jets or jets that are axisymmetrically forced along the flow direction. This results in large-scale axisymmetric structures. In this section we consider the non-axisymmetric response of jets. We present different methods to manipulate the jet or control the development of the jet flow downstream, mostly by applying some kind of radial forcing close to the nozzle exit of the jet. The motivation of this has mainly been to increase the mixing of the jet with the ambient fluid, which can be beneficial in industrial applications (Matta *et al.*, 1996).

By combining longitudinal and helical forcing of a jet, the so-called bifurcating and blooming jets can be achieved (Reynolds *et al.*, 2003). For both cases the longitudinal forcing causes the shear-layer to roll up into vortex rings, but helical forcing breaks the axisymmetry of the jet and offsets the rings relative to each other. An example of a helical forcing system is when the jet nozzle moves in a circular motion in the nozzle exit plane, causing the jet origin to oscillate.

For bifurcating jets, the frequency of the axial forcing needs to be twice the helical forcing frequency, $f_a/f_h = 2$. Then all the rings will be formed at two positions 180° apart in the nozzle orbit, and every second ring will be formed at the same point. For an axisymmetric train of vortex rings, the sum of induced velocity on one ring from the rest is in the direction of the mean flow and causes no rotation or radial motion. For a staggered system of vortex rings, however, the induced velocity rotates the rings. When looking at the symmetry plane of the staggered system of a bifurcating jet flowing upwards, the left and right offset rings will rotate counterclockwise and clockwise, respectively. This again causes the rings to move away from the jet centerline. The result is a jet that splits in two. An example of the bifurcating jet is shown in figure 1.9. The spreading angle in the bifurcation plane increases dramatically compared to the plane normal to the the bifurcation plane, and also compared to an axisymmetric, forced jet. The spreading angle increases with the amplitude of both the axial and helical forcing. Also by increasing St_D, but keeping $f_a/f_h = 2$, the spreading angle increases to a certain point. St_D determines the distance between the vortex rings, and when the vortex rings are getting closer, the induced velocity from the neighboring rings increases, and so does the spreading angle. Parekh *et al.* (1988) reported spreading angles up to 70° for $St_D \approx 0.65$ of the axial forcing. For even higher St_D, however, the rings get entangled because they get too close to each other, and bifurcation does not occur.

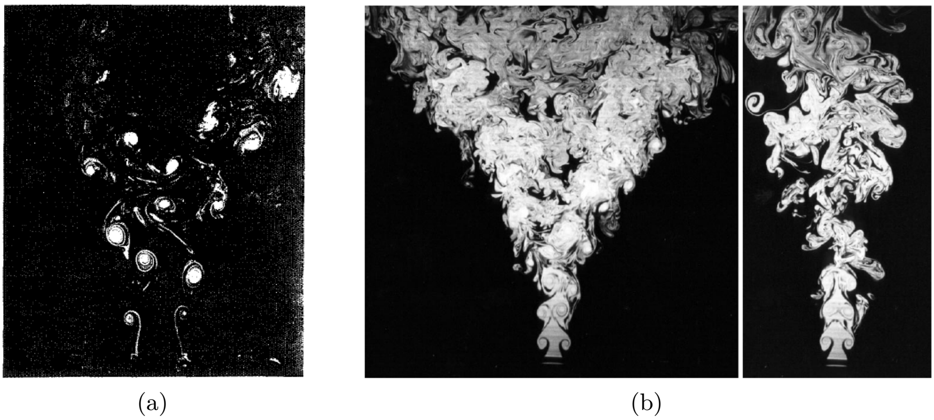

(a) (b)

Figure 1.9: Bifurcating jets: (a) adapted from Parekh *et al.* (1987) and (b) bifurcation plane (left) and normal to the bifurcation plane (right) adapted from Parekh *et al.* (1988).

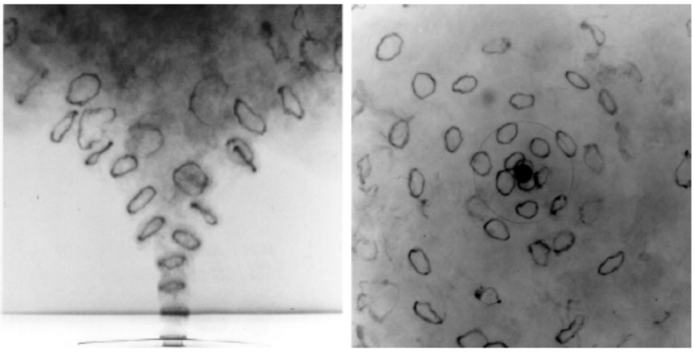

Figure 1.10: Blooming jet from the side (left) and from above (right). Adapted from Reynolds *et al.* (2003).

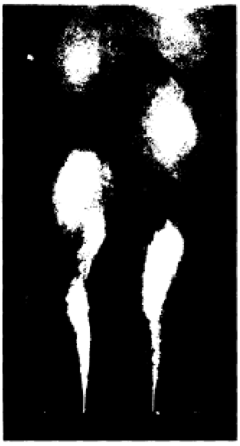

Figure 1.11: Helically forced jet, $Re_D = 100\ 000$, $St_D = 0.27$. Adapted from Parekh *et al.* (1988).

For a blooming jet to form, the axial forcing needs to be a non-integer multiple of the helical forcing frequency (Reynolds *et al.*, 2003). Then the vortex rings form at random points on the nozzle orbit. The mechanisms are otherwise the same as for a bifurcating jet, and the result is a jet where the vortices spread in all directions, as seen in the example in figure 1.10. Also for the blooming jet the spreading angle increases dramatically, but in contrast to the bifurcating jet, this spreading is equal in all directions and the time averaged flow is axisymmetric.

Parekh *et al.* (1988) used an apparatus for combined longitudinal and helical forcing to achieve a bifurcating jet. A system of four external drivers each connected to wave guides focusing the acoustic signal radially at the jet exit and separated azimuthally by 90°, was used for helical forcing. In addition, a speaker used for longitudinal forcing was placed upstream of the nozzle. A sinusoidal signal with the same frequency was sent to all the drivers. For the helical forcing, the phase difference between two neighboring driver signals was 90°, while the amplitude was the same for all of them. By applying only the helical forcing, a system of staggered vortices, as seen in figure 1.11, formed in the near-field of the jet. Parekh *et al.* (1988) suggested that the vortex structures in this jet was tilted rings, alternatively a single vortex line creating a spiral structure. This vortex pattern was not achieved when applying a mechanical, helical forcing system to oscillate the jet nozzle.

Instead of speakers, Yang *et al.* (2016) used two pulsating minijets to manipulate the structure of the main jet. The minijets were pointing radially at the exit of a considerably larger jet, separated by an azimuthal angle of 60°. They found that when the frequency of the unsteady minijets was $f/f_0 = 0.5$, where f_0 is the preferred-mode frequency of the main jet, jet flapping was observed in the symmetry plane defined by the nozzle centerline and the line between the minijets. This caused a large increase in the decay rate of the mean velocity at the jet centerline, and the spreading angle in the symmetry plane. These phenomena are also reported by other researchers; Perumal & Zhou (2018) used the same setup and settings but with only one minijet, while Freund & Moin (2000) conducted DNS on a round jet excited by two anti-phased slot jets on either side of the main jet close to the exit. In the latter study, both $f/f_0 = 0.5$ and $f/f_0 = 1$ resulted in a flapping jet column. The highest decay rate and spreading was found for $f/f_0 = 0.5$. Yang *et al.* (2016) gave a detailed explanation for the flapping. The minijets seem to lock the roll-up of the shear-layer into vortex rings to the preferred-mode frequency, and because $f/f_0 = 0.5$, the pulse from the minijets hit every second ring and pushes them away from the minijet. The result is a train of vortex rings where the axisymmetry is broken in a similar way as for the bifurcating jet. Also here the induced velocity of the other rings rotates each vortex ring to an inclined position. The development of the vortex structures in the jet is showed in the flow visualization and sketch in figure 1.12. The vortices A and B are rotating counterclockwise and clockwise, respectively. This, eventually, causes the lower part of vortex ring B to merge with the lower part of the upstream vortex ring A, and similarly the upper part of vortex ring B merges with the upper part of the downstream vortex ring A. This results in a staggered vortex pattern in the symmetry plane, similar to what Parekh *et al.* (1988) achieved with helical forcing. The induced velocity moves the area where the center of vortex A is upwards and B downwards, and the jet gets a flapping motion.

Kusek *et al.* (1990) used a forcing system consisting of 12 speakers placed around the exit of a round jet to force the jet at the lip of the nozzle with a

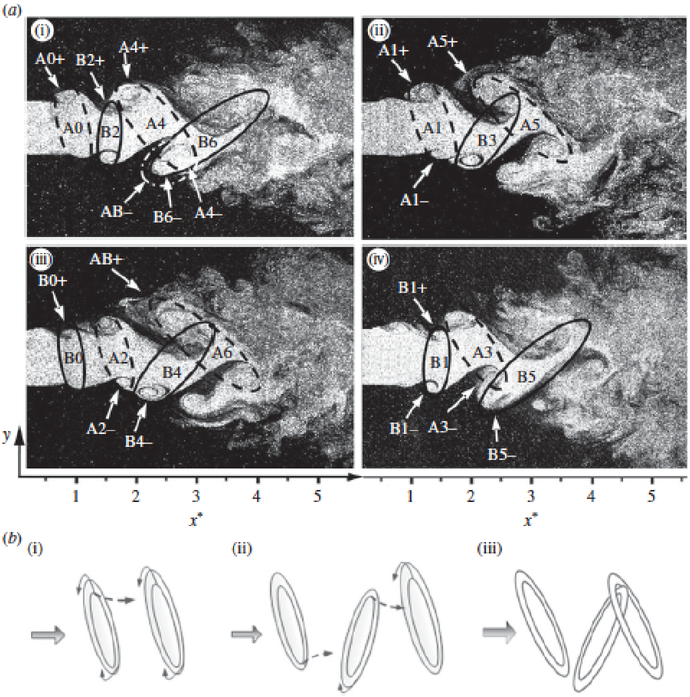

Figure 1.12: (a) Photographs and (b) sketch of vortex structures in a jet manipulated by pulsating minijets. Adapted from Yang *et al.* (2016).

sinusoidal signal. They compared the response of the jet for two different forcing conditions. When the speakers where in phase, axisymmetric vortex structures were formed periodically. For the other forcing condition, the speaker signals formed a standing wave resulting in two amplitude maxima or anti-nodes in anti-phase on opposite sides of the jet, and at these points strong vortex roll-ups were seen. The vortices appeared in anti-phase and formed a staggered vortex system in the jet. Kibens (1980) used a similar forcing system consisting of an acoustic excitation chamber surrounding the nozzle exit. He axisymmetrically forced a round air jet at frequency f_0. This organized the large-scale structures in the shear-layer into a sequence of three successive vortex-pairing stages at fixed streamwise locations, producing the subharmonic frequencies $f_0/2$, $f_0/4$ and $f_0/8$. Corke & Kusek (1993) investigated the frequency response of a jet with $f_0 = 2040$ Hz, subjected to the same helical forcing as introduced by Kusek *et al.* (1990). A weak forcing at $f_h = 1250$ Hz excited a helical mode, but did not interact with the natural instability modes of the jet. However, adding an axisymmetric forcing with frequency $f_a = 2500$ Hz to the helical forcing resulted in an amplification of the subharmonic helical mode $\frac{1}{2}f_h$. Bechert & Pfizenmaier (1975) used a similar setup to show that it was possible to manipulate the strength of the harmonic or the subharmonic by adding a signal of respectively double or half the frequency of the original forcing signal. By changing the phase between the two signals, these frequencies could either be amplified or canceled.

Urbin & Métais (1997) performed a Large Eddy Simulation (LES) of a round jet with a top-hat profile, where periodic perturbations of different types at $St_D = 0.35$ was imposed to the axial velocity at the nozzle. Axisymmetric perturbations resulted in vortex rings, while helical perturbations resulted in helical vortex structures in the near-field of the jet. A third kind of forcing was also applied, where the perturbation amplitude was varying sinusoidally with time. The signal was the same on half of the jet, and in anti-phase compared to the other half. This type of forcing resulted in a periodic response of the jet consisting of vortex structures as seen in figure 1.13. The vortex structures have similarities with the vortex rings formed in axisymmetric forced jets, but with the ring only rolling up in the area with positive perturbation. This results in hairpin like vortices appearing in anti-phase on either side of the

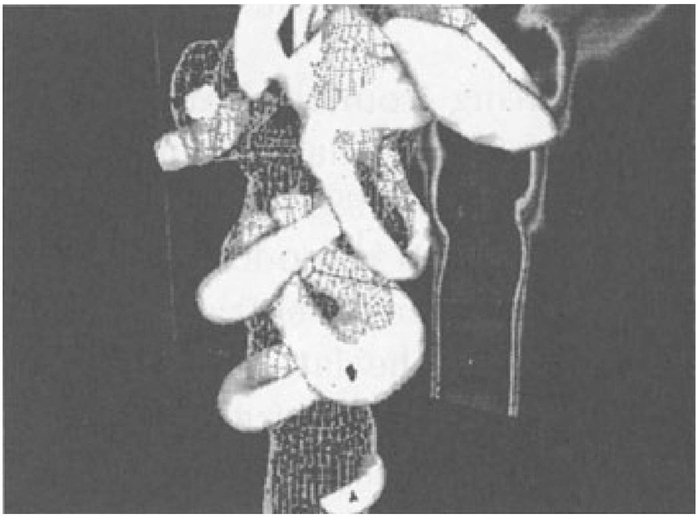

Figure 1.13: Pressure iso-surface of a jet subjected to sinusoidal forcing in anti-phase on either side of the nozzle exit. Adapted from Urbin & Métais (1997).

jet, and twice per forcing period in total. The hairpin vortices are tilted with the legs pointing downstream and partly connecting to the next downstream vortex. The spreading rate of the jet is reported to increase nearly 25 % in the symmetry plane compared to the unforced jet, while normal to the symmetry plane no significant change in the spreading rate was found. Danaila & Boersma (2000) obtained a jet with the same type of vortex structures when performing a Direct Numerical Simulation (DNS) on a jet subjected to a similar perturbation. However, the Strouhal number was $St_D = 0.55$, and the axial perturbation velocity at the nozzle exit, u', was a sum of counter-rotating helical modes, $u' \sim r(\sin(2\pi ft - \theta) + \sin(2\pi ft\theta))$, resulting in a standing wave. Danaila & Boersma called this a flapping mode due to the response of the jet. The simulation also showed that the jet was bifurcating as it was splitting into two branches with the vortex structures forming on the same side included in the same branch. Interestingly, when performing a simulation with a forcing more similar to that Parekh *et al.* (1988) was using, consisting of the flapping mode forcing with $St_D = 0.275$ plus an axial forcing at $St_D = 0.55$, the jet was not found to bifurcate. The mean field was described as Ψ-shaped instead of the Y-shape of a bifurcating jet. Also da Silva & Métais (2002) did LES on a jet applying different types of forcing. Using the forcing method by Urbin & Métais (1997) the jet was found to bifurcate under certain conditions. $St_D = 0.38$ resulted in bifurcation only for low Reynolds numbers, while for $St_D = 0.19$ the bifurcation was present up to $Re_D = 25\ 000$. For the combined axial and helical forcing used by Parekh *et al.* (1988), the jet was bifurcating for all Reynolds numbers investigated, up to $Re_D = 50\ 000$. This type of forcing also resulted in the largest spreading rate.

Several studies have investigated the effect of modifying the shape of the nozzle. Kibens & Wlezien (1985) and Wlezien & Kibens (1986) used nozzles with inclined and stepped trailing edges. For axial forcing, an inclined edge caused the vortex rings to tilt, while for a stepped edge, vortex structures developed independently at each step. Both types of nozzles increased the spreading rate in the symmetry plane compared to standard round nozzles. Longmire & Duong (1996) showed that the stepped nozzles caused the jet to bifurcate, and that the vortex structures consisted of tilted, closed vortex rings. A sawtooth shaped nozzle also resulted in a bifurcating jet with large-scale vortex structures formed as helical loops. Tabs placed inside of the nozzle close to the exit have also been used to modify the large-scale vortex structures of the jet (Bradbury & Khadem, 1975; Reeder & Samimy, 1996; Zaman *et al.*, 1994). Each tab caused a counter-rotating vortex pair to form in the streamwise direction, and by placing two tabs on opposite sides of the nozzle a bifurcating jet was formed. Suzuki *et al.* (2004) performed measurements on a jet where 18 miniature electromagnetic flap actuators where placed with equal distance around the inside of the nozzle close to the exit. By controlling these flaps, the jet could be manipulated in a similar way as the forcing system by Kusek *et al.* (1990) and in the simulations by Urbin & Métais (1997). By controlling the flaps to generate an axisymmetric forcing, the $m_h = 0$ mode of the jet was excited and vortex rings where periodically formed, while helical forcing excited the $m_h = \pm 1$ mode creating continuous helical structures. By controlling the flaps with a square-wave signal that was in anti-phase on half of the nozzle compared to the other half, alternately inclined vortex rings at twice the forcing frequency formed and caused the jet to bifurcate.

Many studies describe vortex rings formed in axially forced and starting jets with oval or elliptic shaped nozzles (Adhikari, 2009; Domenichini, 2011; Hussain & Husain, 1989; O'Farrell & Dabiri, 2014). These rings form initially with similar shape as the nozzle, but while moving downstream the rings deform since the self-induced velocity of a vortex ring is inversely proportional to the local radius of curvature (Arms & Hama, 1965). This causes the parts of the vortex ring in the plane of the minor axis to move slower than the rest of the ring, and therefore the parts of the ring in the plane of the major axis bend inward and toward each other. At this point the ring is shaped similar to the seam of a tennis ball (Hussain & Husain, 1989). Further, the part of the vortex ring that initially had the highest velocity now slows down making the upstream part of the ring move outwards and catch up with the rest of the ring. The result is again a vortex ring with a shape similar to the nozzle, but now the minor and major axes have switched. For high aspect ratio nozzles, even bifurcation has been observed. This can happen if opposite sides of the vortex ring touch and the ring split into two circular rings.

The vortex structures vary around an elliptic vortex ring. Figure 1.14 shows the vortex structures in the major and minor axis plane of a ring formed from a starting jet with and elliptic nozzle, at a time when the ring has the tennis ball seam shape. The vortices in the major axis plane has moved slightly inwards and has a tail of vorticity from the trailing shear-layer. The vortices in the minor axis plane, however, has moved considerably outwards at the same time as the shear-layer has curved around, and are connected on the top of, the slower moving ring. Both Adhikari (2009) and O'Farrell & Dabiri (2014) observed that for sufficiently long stroke ratios, this curved shear-layer separated and formed what from the vorticity field seemed to be an independent vortex structure downstream of the vortex core. However, a LCS analysis by O'Farrell & Dabiri (2014) showed that this structure remained within the LCS ridge defining the downstream boundary of the vortex ring, and therefore suggesting that this vortex and the vortex ring was still *one* connected structure.

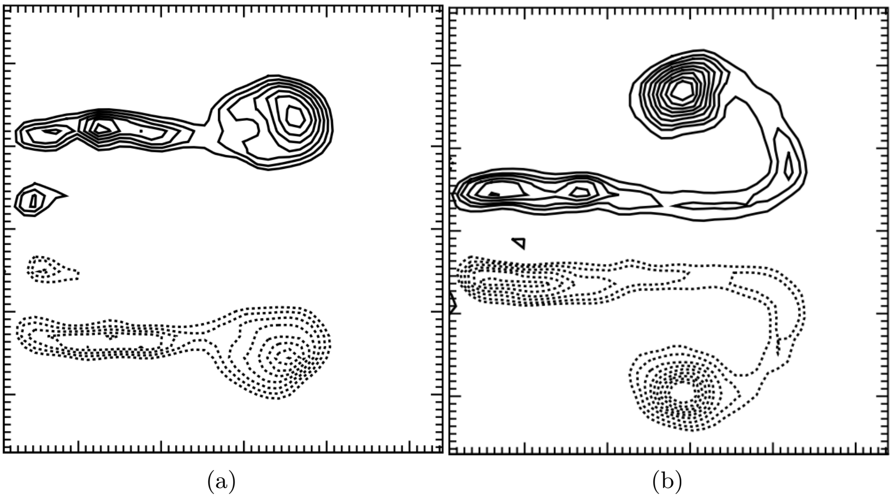
(a) (b)

Figure 1.14: Vorticity field of a jet, going from left to right, from an elliptic nozzle. a) shows the cross-section along the major axis and b) along the minor axis. Adapted from O'Farrell & Dabiri (2014).

1.4 Transverse acoustic instabilities

The response of jets to transverse forcing is fundamentally important to the practical problem of thermo-acoustic instabilities in gas turbine combustion. In annular combustors undergoing thermo-acoustic oscillations, multiple jet flames are stabilized in an azimuthal acoustic field. This is equivalent to a single jet flame subjected to transverse forcing. Simulations have shown that both axial, standing and spinning modes can occur in annular combustion systems (se e.g. Bethke *et al.* (2005); Pankiewitz & Sattelmayer (2002); Wolf *et al.* (2012a,b); Worth & Dawson (2013a,b)). In fact, acoustic measurements have revealed that the acoustic modes are continuously switching between standing waves, and clockwise and counterclockwise traveling waves (Noiray & Schuermans, 2013). In combustion chambers found in modern gas turbines and jet engines, acoustic forcing can appear from self-excited thermo-acoustic instabilities and has the form of pressure waves acting transversely on the fuel jets entering the combustion chamber. For the thermo-acoustic instabilities to be self-excited, net energy must be added to the instabilities by heat:

$$\int_V \int_t p'(\mathbf{x},t)\dot{q}'(\mathbf{x},t)dtdV > 0. \tag{1.34}$$

This is the Rayleigh criterion, and is satisfied if the phase in absolute value between the fluctuations in heat release rate $\dot{q}'(\mathbf{x},t)$ and pressure instabilities $p'(\mathbf{x},t)$ is less than 90°. V is the volume of the system.

Self-excited transverse instabilities are also a well-known problem in rocket engines. Rogers (1956) and Elias (1959) investigated the phenomenon of screech in rectangular combustors. This is characterized by a intense sound with a constant, high frequency that causes the flame zone to shorten, the heat-transfer rate to grow and to highly increase the probability for failure of the combustion chamber. It was shown that the frequencies of these screeches correspond to the modes of transverse oscillation in the burner. The Spark-schlieren photograph in figure 1.15 show that the transverse velocity fluctuations across the combustion chamber form vortices alternately on either side of the fuel inlet. Even though the photograph does not revile the three-dimensional structures of the flow, this pattern has similarities to what was reported in many studies described in section 1.3.

Also can combustors have shown self-excited transverse modes (Schwing *et al.*, 2012; Schwing & Sattelmayer, 2013; Schwing *et al.*, 2011). Schwing *et al.* (2011) investigated fully premixed swirl-stabilized flames and showed that the dominating first mode was rotating. They found that it was the acoustic velocity, and not the pressure, that contributed to the Rayleigh criterion and therefore the self-excited instabilities. The reason for this contribution was that the velocity periodically moved the flame in transverse direction.

The main reason for the interest in transverse, thermo-acoustic instabilities from the gas turbine community is, however, due to the operating limitations this phenomenon introduces to modern, low-emission combustors for both power generation and aeroengines. Self-excited thermo-acoustic instabilities are more likely to appear in lean, premixed combustors because of the absence of a secondary air intake that tend to damp the pressure oscillations (O'Connor *et al.*, 2015). Experiments and simulations has been conducted on several types

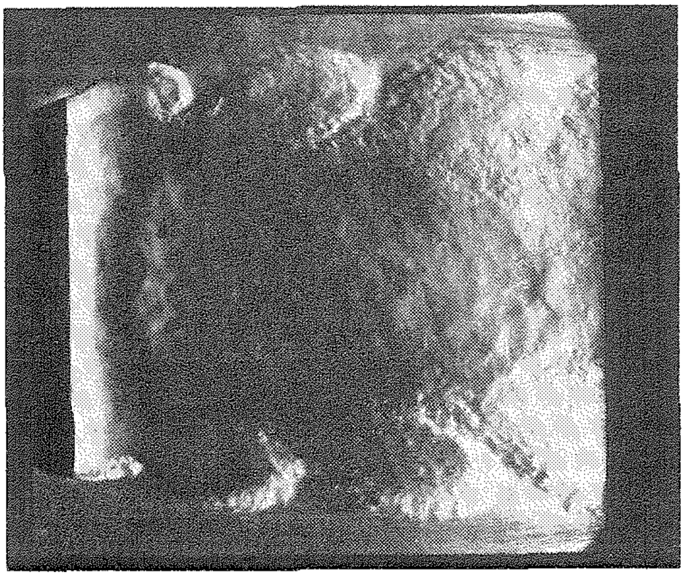

Figure 1.15: Spark-schlieren photograph of screeching combustion in a rectangular combustion chamber. Adapted from Rogers (1956).

of combustors, and an full overview of these studies can be found in the review paper by O'Connor *et al.* (2015). As the instabilities in these combustors are shown to appear as pressure waves transverse to the fuel flow entering the combustion chamber, this phenomenon can be investigated by applying transverse acoustic forcing in a controlled way on relevant flows. Several experimental studies on transverse forcing have been conducted in high aspect ratio, rectangular enclosures surrounding the jet, where speakers have been mounted on tubes on each short-sided wall. The acoustic waves travel in the direction of the largest dimension of the enclosure, and the frequency and phase of the speakers can be adjusted to obtain plane standing waves with varying acoustic modes. This design was first introduced by O'Connor & Lieuwen (2011). O'Connor *et al.* (2013) showed that the flame behavior when standing waves are present is fundamentally similar for an annular combustor as for the unwrapped model. To date, the fundamental response to a round jet at different locations in an acoustic field has yet to be investigated. This is the most general base flow and can reveal the fundamental flow response.

Before the relevant literature of transverse acoustic forcing of jets is presented, an introduction of linear acoustics follows.

1.4.1 Acoustic theory

A one-dimensional sound field in x-direction can be described by the following linearized fundamental equations (Kuttruff, 2007):

$$\frac{\partial p'}{\partial x} = -\rho \frac{\partial u'}{\partial t}, \tag{1.35}$$

$$\rho \frac{\partial u'}{\partial x} = -\frac{1}{c^2} \frac{\partial p}{\partial t}. \tag{1.36}$$

Here, p' is the acoustic pressure, u' is the acoustic velocity in x-direction of the fluid the sound waves are traveling in, ρ is the density of the fluid and c is the speed of sound. By partially differentiating equation (1.35) with respect to x and (1.36) with respect to t, and combine them, we obtain the one-dimensional wave equation:

$$\frac{\partial^2 p'}{\partial x^2} = \frac{1}{c^2} \frac{\partial^2 p'}{\partial t^2}. \tag{1.37}$$

This equation is satisfied by any function of the pressure with existing second derivatives on the form $p' = p'(x \pm ct)$ (Kuttruff, 2007). The general solution is therefore

$$p'(x,t) = g(x - ct) + h(x + ct). \tag{1.38}$$

Here, $g(x-ct)$ represents a sound wave moving with the speed c in the positive x direction and $h(x+ct)$ a sound wave moving with the same speed in the negative x direction. To satisfy equation (1.35) and (1.36), the fluid velocity needs to have a similar distribution as the pressure in equation (1.38); $u' = u'(x \pm ct)$.

With this in mind, the following expression for the acoustic velocity of a sound wave traveling in the positive x direction can be derived from equation (1.35):

$$u' = \frac{1}{\rho c} p'. \tag{1.39}$$

The ratio between the sound pressure and the acoustic velocity is called the characteristic impedance, Z_0:

$$Z_0 = \frac{p'}{u'} = \pm \rho c. \tag{1.40}$$

For a wave traveling in the negative x direction, the ratio equals $\frac{p'}{u'} = -Z_0$.

For the special case where the two waves $g(x,t)$ and $h(x,t)$ in equation (1.38) are sinusoidal with frequency f and amplitudes A and B, respectively, we have:

$$g(x,t) = A e^{\mathrm{i}\frac{2\pi f}{c}(x-ct)}, \tag{1.41}$$

$$h(x,t) = B e^{\mathrm{i}\frac{2\pi f}{c}(x+ct)}. \tag{1.42}$$

By defining the wave number $k = \frac{2\pi f}{c}$ and the angular frequency $\omega = 2\pi f$ we get

$$p'(x,t) = A e^{\mathrm{i}(kx-\omega t)} + B e^{\mathrm{i}(kx+\omega t)}. \tag{1.43}$$

The acoustic velocity is found by dividing equation (1.43) by $\pm Z_0$:

$$u'(x,t) = \frac{A}{\rho c} e^{\mathrm{i}(kx-\omega t)} - \frac{B}{\rho c} e^{\mathrm{i}(kx+\omega t)}. \tag{1.44}$$

By using Eulers formula, $e^{\mathrm{i}x} = \cos x + \mathrm{i} \sin x$, we can find the real part of the pressure:

$$\begin{aligned}\Re\{p'(x,t))\} =&\Re\{Ae^{\mathrm{i}(kx-\omega t)} + Be^{\mathrm{i}(kx+\omega t)}\}\\ =&\Re\{A(\cos(kx)+\mathrm{i}\sin(kx))(\cos(\omega t)-\mathrm{i}\sin(\omega t))\\ &\quad + B(\cos(kx)+\mathrm{i}\sin(kx))(\cos(\omega t)+\mathrm{i}\sin(\omega t))\}\\ =&(A+B)\cos(kx)\cos(\omega t)+(A-B)\sin(kx)\sin(\omega t),\end{aligned} \tag{1.45}$$

and similarly with the velocity:

$$\begin{aligned}\Re\{u'(x,t)\} =&\Re\left\{\frac{A}{\rho c}e^{\mathrm{i}(kx-\omega t)} - \frac{B}{\rho c}e^{\mathrm{i}(kx+\omega t)}\right\}\\ =&\Re\left\{\frac{A}{\rho c}(\cos(kx)+\mathrm{i}\sin(kx))(\cos(\omega t)-\mathrm{i}\sin(\omega t))\right.\\ &\quad\left. - \frac{B}{\rho c}(\cos(kx)+\mathrm{i}\sin(kx))(\cos(\omega t)+\mathrm{i}\sin(\omega t))\right\}\\ =&\frac{A-B}{\rho c}\cos(kx)\cos(\omega t)+\frac{A+B}{\rho c}\sin(kx)\sin(\omega t).\end{aligned} \tag{1.46}$$

From these expressions we see that a standing wave is obtained by setting $A = B$:

$$\begin{aligned}\Re\{p'(x,t)\} &= 2A\cos(kx)\cos(\omega t),\\ \Re\{u'(x,t)\} &= \frac{2A}{\rho c}\sin(kx)\sin(\omega t).\end{aligned} \tag{1.47}$$

From now on, if nothing else is specified, we will refer to the real part of pressure and velocity as just pressure and velocity, as this is what is measured in experiments by e.g. a microphone. In a sinusoidal standing wave, the acoustic velocity is 90° out of phase with the pressure in both space and time. An anti-node is the position in a standing wave where the fluctuations has a maximum, while a node is where there are no fluctuations. A pressure anti-node is therefore a velocity node, and a pressure node is a velocity anti-node. In between these two positions, both pressure and velocity fluctuations are present, but the amplitude of the fluctuations decreases from the anti-node to the node.

The time instant when the pressure waves has a maximum amplitude, the velocity is zero for all x, and the other way around; when the pressure is zero, the velocity has its maximum amplitude.

By setting either $A = 0$ or $B = 0$ in equations (1.45) and (1.46), we get a traveling wave moving in the negative or positive x direction, respectively. This wave differs from the standing wave in that sense that both pressure and velocity fluctuations are present independent of position. A traveling wave has therefore similar properties as the positions between the pressure anti-node and pressure node in a standing wave. The difference, however, is that while the pressure and velocity fluctuations are 90° out of phase in a standing wave, they are in phase for a wave traveling in the positive direction and in anti-phase for a wave traveling in the negative direction.

For the general case where we neither have a purely standing wave or a purely traveling wave, a mixed mode occurs and the spin ratio can be defined using the constants A and B from equation (1.45) and (1.46) (Evesque *et al.*, 2003):

$$SR = \frac{|A| - |B|}{|A| + |B|}. \tag{1.48}$$

The spin ratio has its name from annular combustors, where the traveling wave in the azimuthal direction in an annulus is said to be spinning. The spin ratio varies from $SR = -1$ for a wave traveling in negative direction to $SR = 1$ for a wave traveling in positive direction, and is zero for a standing wave.

A sound wave contains energy. The energy density is the energy content of a sound wave per unit volume, and can be divided into kinetic and potential energy (Kuttruff, 2007):

$$w = w_{kin} + w_{pot} = \rho \frac{u'^2}{2} + \frac{p'^2}{2\rho c^2}. \tag{1.49}$$

By inserting equation (1.39) for u' we see that for a harmonic wave the kinetic energy equals the potential energy. Another important acoustic quantity is the sound intensity or energy flux density, I. This is the energy flow transported

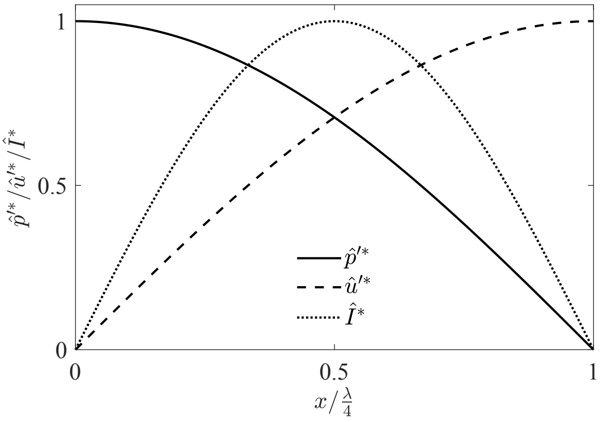

Figure 1.16: Normalized pressure, acoustic velocity and energy flux density in a standing wave.

by the acoustic wave traveling through the fluid, and is given by

$$I(x,t) = p'(x,t)u'(x,t). \tag{1.50}$$

As for the energy density, the kinetic part equals the potential part of the energy flux density for a harmonic wave. Figure 1.16 shows the energy flux density together with the pressure and acoustic velocity for a one-dimensional standing wave with length $\lambda = c/f$. The pressure anti-node is here defined to be positioned at $x = 0$, and the pressure node is therefore at $x = \lambda/4$. The energy flux density is zero at the pressure anti-node and node, and has its maximum at $x/\frac{\lambda}{4} = 0.5$.

In this thesis, acoustics in a rectangular box is of interest since the transverse forcing is conducted by placing the jet in a rectangular enclosure where an acoustic standing wave is established. This occurs when there is resonance. For a closed rectangular box, the resonance frequency or eigenfrequency is given by (Kuttruff, 2007):

$$f = \frac{c}{2}\sqrt{\left(\frac{l}{L_x}\right)^2 + \left(\frac{m}{L_y}\right)^2 + \left(\frac{n}{L_z}\right)^2}. \tag{1.51}$$

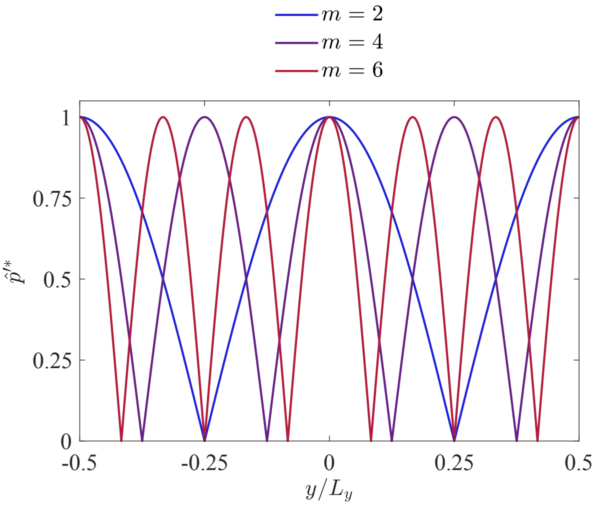

Figure 1.17: Standing waves for even acoustic mode numbers in y direction.

L_x, L_y and L_z are the three box dimensions and l, m and n are non-negative integers. The numbers l, m and n define the acoustic modes of the box and physically they are the number of acoustic nodal planes perpendicular to the axes x, y and z, respectively. The number of wavelengths corresponds to half the mode number in that dimension. For a closed box with pressure waves in the y-direction and constant pressure along x and z, we have $l = n = 0$ and equation (1.51) simplifies to

$$f = \frac{c}{2}\frac{m}{L_y}. \tag{1.52}$$

The walls perpendicular to the pressure waves are acoustic anti-nodes. At even mode numbers, the pressure is identical at the two walls, while at odd mode numbers the pressure at the two walls has opposite signs and are in anti-phase. Figure 1.17 shows the theoretical pressure distribution for the acoustic mode numbers used in the jet enclosure in this study. The enclosure will be described in chapter 3 and is shown in figure 2.2 and 2.3a.

For an open box, with one wall missing, the pressure can be approximated as constant and equal to atmospheric at this plane, and therefore it is a node[a].

---

[a] This is only valid if the characteristic length of the cross-section of the open end is small compared to the length of the box normal to this plane. If not, an end correction like δ in equation (1.55), needs to be applied.

Symmetry gives that this corresponds to having a closed box with twice the length perpendicular to the missing wall plane, or alternatively a mode number equal to 0.5 in this dimension. For a box similar to the one in equation (1.52), but with one wall missing in the x plane, we get:

$$f = \frac{c}{2}\sqrt{\left(\frac{1}{2L_x}\right)^2 + \left(\frac{m}{L_y}\right)^2}. \tag{1.53}$$

Another part of the setup of a transverse forcing facility, where the acoustics play a crucial role, is the nozzle setup. This can for a typical round jet be approximated as a pipe with one open and one close end. For a round pipe with small diameter, the one-dimensional acoustics is described by equation (1.45) and (1.46). By using the same symmetry argument as for equation (1.53), we get the following resonance frequency for a pipe of length L:

$$f = \frac{c}{4L}. \tag{1.54}$$

This means that resonance will occur if the pipe length is a quarter of the length of the acoustic wave. Unless the diameter of the pipe is small compared to L, an end correction needs to be added to L making the effective pipe length $L + \delta$. This is due to the fact that the inertia of the flow makes the acoustic flow continue a distance δ outside the open end of the pipe. For small wave numbers k, the end correction for an unflanged thin-walled open pipe with inner diameter D_p is given by Rienstra & Hirschberg (2017):

$$\delta = 0.61\frac{D_p}{2}. \tag{1.55}$$

So far, we have been considering acoustics where the velocity field only consists of the fluctuating acoustic velocity. In the experiments in this study, however, the acoustics in the jet apparatus is affected by a mean flow. For acoustics in a pipe with mean velocity U, the wave will propagate with a velocity $c \pm U$, and we get the following expressions for the acoustic pressure and velocity:

$$p'(x,t) = Ae^{\mathrm{i}(k_1x-\omega t)} + Be^{\mathrm{i}(k_2x+\omega t)}, \tag{1.56}$$

$$u'(x,t) = \frac{A}{\rho c}e^{\mathrm{i}(k_1x-\omega t)} - \frac{B}{\rho c}e^{\mathrm{i}(k_2x+\omega t)}. \tag{1.57}$$

Here, $k_1 = \frac{2\pi f}{c+U}$ and $k_2 = \frac{2\pi f}{c-U}$.

Normally, the pipe in the nozzle setup has one or more area changes. For a pipe where the cross-sectional area has a discontinuity from A_1 to A_2, the pressure at each side of the area change still needs to be equal, $p_1' = p_2'$ (Kuttruff, 2007). The area change causes part of the wave traveling in the pipe with area A_1 to be reflected, and the total pressure here is the sum of the incident wave p_i' and the reflected wave Rp_i': $p_1' = p_i' + Rp_i$. If the pipe has an open end, represented by another area change from A_2 to A_3 where $A_3 >> A_2$, it can be shown that the impedance from right before the first area change to right after the second area change is given by

$$\frac{Z}{Z_0} = \frac{A_1}{A_2} \cdot \frac{A_2 + iA_3\tan(kL_2)}{iA_2\tan(kL_2) + A_3}, \tag{1.58}$$

where L_2 is the length between the two area changes. By also assuming that this section of the pipe is acoustically compact ($kL_2 << 1$), we get

$$\frac{Z}{Z_0} = ikL_2\frac{A_1}{A_2}. \tag{1.59}$$

The acoustic impedance of the nozzle and the upstream pipe shown in figure 2.1a can be approximated by equation (1.59), by setting A_1 to the area of the 35 mm pipe, A_2 to the exit area of the nozzle and L_2 to an estimate of the length of the small-area part of the nozzle.

As the jet apparatus, shown in figure 2.1a, also has a plenum, an alternative approach is to model the nozzle setup as a Helmholtz resonator. A Helmholtz resonator is a pipe shaped as a bottle, with a body and a neck with an open end (Rienstra & Hirschberg, 2017). If the bottle is short compared to the acoustic wavelength, the body of the bottle acts as an acoustic spring while the neck acts as an acoustic mass. The main purpose of a Helmholtz resonator is to damp pressure oscillations, and a pressure fluctuation p' outside the resonator neck from an external source will move the air in the body. For a certain angular frequency ω of the pressure oscillations, the mass-spring system will resonate, and the energy in the pressure wave will effectively dissipate into heat. The resonance frequency of a Helmholtz resonator with a bottle volume V, a neck cross-sectional area A_n and a neck length L_n is given by

$$\omega_0 = \frac{A_n c^2}{(L_n + 2\delta)V}. \tag{1.60}$$

This expression is valid if the cross-sectional area of the bottle is much larger than the area of the neck so that the acoustic velocities in the bottle are small. It is also assumed that the neck is acoustically compact, i.e. $kL_n << 1$, and that there are no friction losses in the resonator. The term 2δ is added to the neck length as end corrections to both sides of the neck. By introducing a mean flow through the Helmholtz resonator resulting in a mean exit velocity U_e, we get the following expression for the amplitude of the velocity fluctuations u' in the resonator neck:

$$\frac{\rho c \hat{u}'}{\hat{p}'} = -\frac{U_e/c + \mathrm{i}\omega_1\omega/\omega_0^2}{1 - (\omega/\omega_0)^2 + \mathrm{i}U_e\omega_1\omega/(c\omega_0^2)}, \tag{1.61}$$

where $\omega_1 = c/(L_n + 2\delta)$, and the hat denotes the Fourier transform of the fluctuating value. It is assumed that the pressure in the jet is equal to p', which is valid for low Mach numbers, $U_e/c << 1$, and low Strouhal numbers, $\omega(A_n/\pi)^{1/2}/U \sim fD_n/U_e << 1$. Also, higher order terms are neglected which is valid for small perturbations, $|\hat{u}'|/U_e << 1$. The amplitude and phase of equation (1.61) is given in figure 1.18 for zero mean flow together with the velocities used in this study. An ideal Helmholtz resonator without mean flow has a discontinuity at $\omega = \omega_0$ as the amplitude goes to infinity and the phase jumps 180°. The mean flow introduces a damping factor even though we have assumed no friction losses, and the phase jump is smeared out. This is due to loss of acoustic kinetic energy because of increased vorticity shedding at the exit of the resonator neck for increasing velocity.

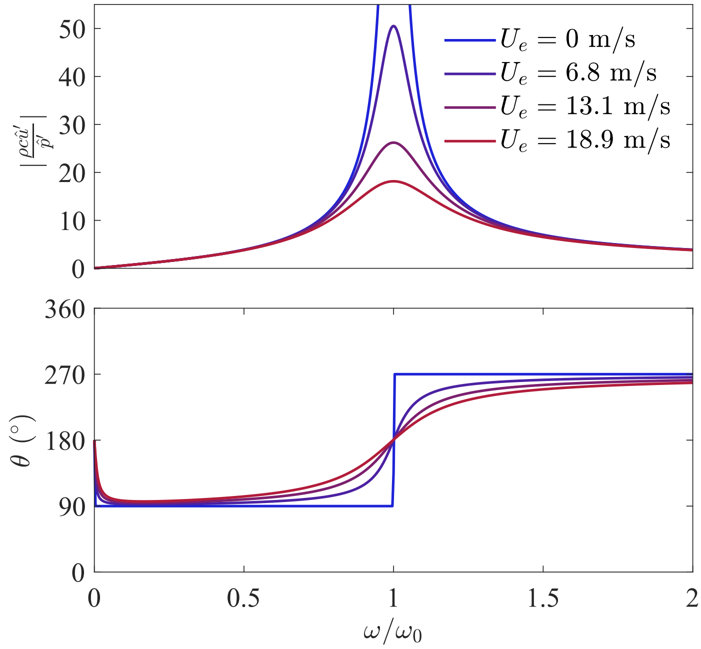

Figure 1.18: Amplitude and phase of the acoustic velocity in the neck of a Helmholtz resonator for different mean flows.

1.4.2 Transverse acoustic forcing of jets

For transverse forcing of a jet, the forcing acts perpendicular to the jet's flow direction. This can be conducted in different ways. For transverse *acoustic* forcing, the perturbation is a sound wave that is either traveling or standing. A traveling wave in y direction can be decomposed into the following sum (O'Connor *et al.*, 2015):

$$e^{\mathrm{i}ky} = \sum_{m_h=-\infty}^{\infty} \hat{C}_{m_h}(kr)e^{\mathrm{i}m_h\theta} = \sum_{m_h=-\infty}^{\infty} \mathrm{i}^{m_h} J_{m_h}(kr)e^{\mathrm{i}m_h\theta}. \tag{1.62}$$

Here J_{m_h} is the Bessel function of the first kind and m_h is the hydrodynamic, azimuthal mode number illustrated in figure 1.4. This shows that a traveling wave can be expressed as an infinite sum of helical disturbances where $\hat{C}_{m_h}(kr)$ denotes the strength of mode m_h. Similar expressions can be derived for symmetric forcing $\frac{1}{2}(e^{\mathrm{i}ky} + e^{-\mathrm{i}ky})$ corresponding to a pressure anti-node in a standing wave, and asymmetric forcing $\frac{1}{2i}(e^{\mathrm{i}ky} + e^{-\mathrm{i}ky})$ corresponding to a pressure node. We are interested in the solution in the region close to the jet. By assuming the nozzle is much smaller than the acoustic wavelength, i.e. $kD \ll 1$, the higher order terms in a Taylor expansion of the Bessel function can be neglected. We then get the following expressions for the modal amplitude strength:

Traveling wave:

$$\hat{C}_{m_h} = \frac{\mathrm{i}^{m_h}(kr)^{m_h}}{2^{m_h} m_h!}. \tag{1.63}$$

Symmetric forcing (pressure anti-node):

$$\hat{C}_{m_h} = \begin{cases} \frac{\mathrm{i}^{m_h}(kr)^{m_h}}{2^{m_h} m_h!}, & m_h = 0, 2... \\ 0, & m_h = 1, 3... \end{cases} \tag{1.64}$$

Asymmetric forcing (pressure node):

$$\hat{C}_{m_h} = \begin{cases} 0, & m_h = 0, 2... \\ \frac{\mathrm{i}^{m_h - 1}(kr)^{m_h}}{2^{m_h} m_h!}, & m_h = 1, 3... \end{cases} \tag{1.65}$$

By inspecting these expressions and remembering that kr is small, it is clear that $\hat{C}_{m_h}$ decreases quickly for increasing m_h for all of the forcing conditions. Also, it shows that symmetric and asymmetric forcing does not excite odd and even modes, respectively, at all. Figure 1.19, adapted from O'Connor *et al.* (2015), compares the forcing amplitudes from equation (1.64) and (1.65) with velocity fluctuation amplitudes from experiments on a swirling annular jet by O'Connor & Lieuwen (2012b) whose mathematical expressions are given in equation (1.11). In general, the forcing strength of the hydrodynamic modes coincides with the jet response of the same modes. The exception is $m_h = 2$ and especially $m_h = -2$ for symmetric forcing, where the jet in the experiments has a higher response than expected. This is probably due to the fact that these modes are close to the preferred mode of the swirling jet used in these experiments (O'Connor *et al.*, 2015).

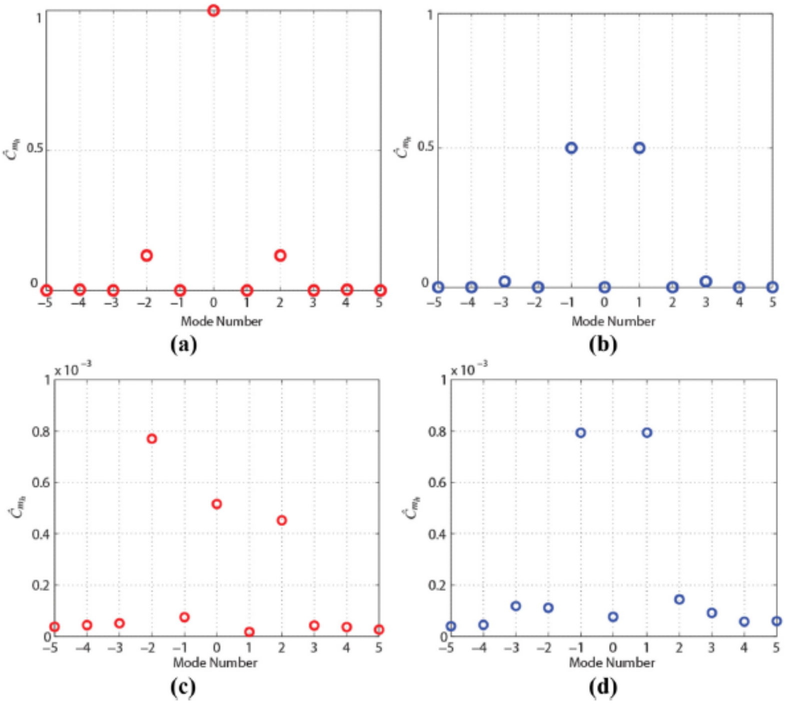

Figure 1.19: Modal amplitudes $\hat{C}_{m_h}$ from (a) equation (1.64) (symmetric forcing) and (b) equation (1.65) (asymmetric forcing) compared to results from transversely forced cold-flow experiments on a swirling jet by O'Connor & Lieuwen (2012b) for 1200 Hz (c) symmetric forcing and (d) asymmetric forcing. Adapted from O'Connor *et al.* (2015).

A limited number of experiments have been conducted on transverse acoustic forcing of round air jets. Matta *et al.* (1996) investigated the effect of a turbulent round air jet entering a rectangular enclosure where two loudspeakers placed on opposite walls created a standing wave perpendicular to the flow with a pressure node at the jet centerline. The jet was found to be flapping back and forth in the direction of the waves, and the vortices were rolling up in the shear-layer on either side of the jet in anti-phase. This vortex shedding was not found in the shear-layers perpendicular to the wave direction, resulting in an elliptic jet shape of the time averaged cross-section in the near-field. Compared to the unforced case, the forcing increased the spreading rate and decreased the potential core length of the jet. This was most effective at $St_D \approx 0.5$. More studies are found on complex jet flows placed in the pressure node. O'Connor *et al.* (2013) reported that an annular nozzle with swirling inflow had similar response as the round jet, with a swaying jet flow and a staggered vortex pattern. From this, O'Connor and Lieuwen suggested that the shear-layer had rolled up into helical structures. These helical structures have also been observed in LES of a similar annular jet with swirl positioned at the pressure node (Huang *et al.*, 2006; Huang & Yang, 2005). For reacting flows this has shown to result in a region of higher heat release, rotating around the jet shear-layer with the forcing frequency, i.e. with the helical disturbance. Also in non-forced swirling flows, the presence of helical structures is documented (Ruith *et al.*, 2003).

A different response is shown for a jet with a pressure anti-node at the centerline, where a periodic and axisymmetric roll-up of the shear-layer has been reported. In experiments on annular jets, both with swirling inflow (O'Connor & Lieuwen, 2011; Saurabh & Paschereit, 2013) and without (Baillot & Lespinasse, 2014), the response of the jets were similar to the longitudinally forced, pulsating jets from chapter 1.2.4, where vortex rings formed because of axisymmetric, streamwise velocity fluctuations at the nozzle exit. Similar velocity fluctuations are also present in the pressure anti-node case despite the fact that this is the position in the transverse pressure wave where there is no acoustic velocity. LES's of self-excited, annular combustors have also reported axial fluctuations of the fuel entering the combustion chamber (Staffelbach *et al.*, 2009; Wolf *et al.*, 2009). This is due to the pressure field inducing velocity oscillations upstream of the nozzle exit and is known as *injector coupling* in the rocket community (Davis &

Chehroudi, 2003; Hutt & Rocker, 1995). It can be explained by the theory in section 1.4.1 by approximating the nozzle setup either as a pipe with changing cross-section area or a Helmholtz resonator. Saurabh & Paschereit (2013) suggested that these axisymmetric, vortical structures convecting downstream drive heat-release oscillations for reacting jets.

Lespinasse *et al.* (2013) considered a rod-stabilized, laminar flame placed in five different positions in the transverse standing wave. The flow response at the pressure anti-node and node were reported to have the same response as the experiments by O'Connor & Lieuwen (2012b). For the other positions between the node and the anti-node, the jet showed asymmetric behavior. The vortices on the side towards the pressure anti-node were visually larger than the vortices on the side towards the node. In addition, the position of the flame centerline was greatly inclined to the side towards the pressure node for the intermediate jet position (figure 1.20). It was suggested that these asymmetries result from the product of the pressure field and the transverse gradient of the pressure field. This product is referred to as the potential energy density gradient, e_{ac}. Since the transverse pressure gradient is proportional to the acoustic velocity, e_{ac} is proportional to the energy flux density I given in equation (1.50). As seen in figure 1.16, this is zero at the pressure anti-node and node, and exhibits a maximum in the middle between these two points. This maximum corresponds to where Lespinasse *et al.*reported the asymmetry of the vortices to be most significant.

Studies have also been conducted on jets subjected to axial forcing simultaneously as transverse forcing at the pressure node in a standing wave. This causes the jet to experience transverse and axial velocity fluctuations at the same time, which is also the case for all the positions in a standing wave except at the pressure node and anti-node. For the combined forcing on an annular flame with swirl, the helical mode associated with the pressure node is present, but the effect of axial forcing is superimposed onto this (Hauser *et al.*, 2010). For a flame subjected to transverse forcing, the flame was found to move periodically in transverse direction, while for axial forcing the flame had a similar movement in the axial direction. For the simultaneous forcing, the flame movement was close to a superposition of the two independent motions, but with amplitudes in

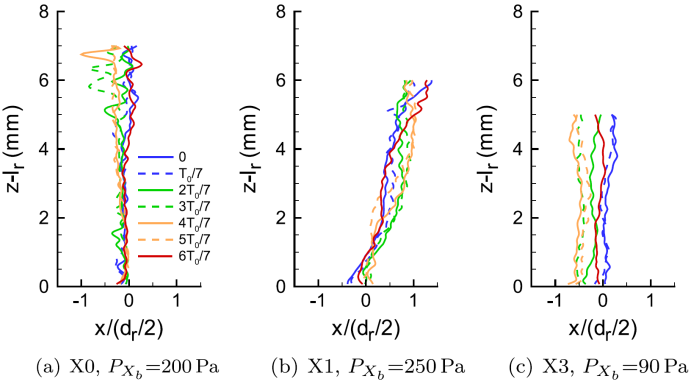

(a) X0, P_{X_b}=200 Pa (b) X1, P_{X_b}=250 Pa (c) X3, P_{X_b}=90 Pa

Figure 1.20: Flame centerline colored by the phase in the forcing cycle. (a) Pressure anti-node, (b) in the middle of the pressure anti-node and node, and (c) pressure node. Adapted from Lespinasse *et al.* (2013).

both directions slightly larger for the combined case. This resulted in a almost circular movement of the flame.

Suzuki *et al.* (2007) investigated a methane jet with and without combustion, both forced by a single loudspeaker sending a traveling wave normal to the jet flow. For some range of Reynolds and Strouhal numbers the jet was found to meander, and sometimes even bifurcate, in the plane defined by the jet and acoustic wave directions. Bifurcation was also shown in a similar setup for both plane and round microjets (Kozlov *et al.*, 2008, 2009, 2011). Saurabh *et al.* (2014) investigated the effect of traveling waves on swirling flames. They reported that the flame response was similar to that of a swirling flame positioned in the pressure anti-node of a standing wave field. In an acoustic simulation of a similar setup, the traveling wave was however reported to give a mixed response between the node and anti-node cases (Blimbaum *et al.*, 2012).

The jet response when subjected to transverse forcing varies due to different mechanisms. The transverse acoustic forcing can affect the jet directly through the transverse velocity fluctuations, but as explained it can also go via longitudinal acoustics causing axial velocity fluctuations at the nozzle exit (O'Connor & Lieuwen, 2012a). Alternatively, both the axial and transverse velocity fluctuations can excite different hydrodynamic instability modes of the jet that form vortical structures in the jet flow. These again induce velocities that affect the flame behavior. The pressure anti-node and pressure node for example, excites symmetric and asymmetric modes, respectively. This in turn results in symmetric and asymmetric flames if combustion is present (O'Connor & Lieuwen, 2012b; Worth & Dawson, 2013b).

The velocity fluctuations in the jet is a combination of velocities from these different mechanisms. The amplitudes of the velocities directly from the acoustic waves, that can be both transverse and axial, are dependent on transverse position and has the longest wavelengths. The velocities induced by the vortices, on the other hand, have shorter wavelengths and are convecting downstream. In the near-field of the jet both of these velocities are present, while further downstream the vortex structures disappear and causes the acoustic velocities to dominate. Also the axial part of the induced velocities decreases in strength as the flow moves downstream and away from the nozzle (O'Connor & Lieuwen, 2012a). For the pressure node case the combination of velocity fluctuations results in an interesting interference pattern in the RMS plots of the near-field of the jet; at some positions there is cancellation of the different velocity fluctuations, while at other positions they are amplified. In the study by O'Connor & Lieuwen (2012a) this pattern is visible in the jet's velocity and vorticity fluctuation fields, for flow both with and without combustion. In figure 1.21 an example of this phenomenon for the transverse velocity component is shown. Also Emerson *et al.* (2013) reported this type of pattern for a similar setup. To show that this pattern is a result of interference between the different velocity fluctuations, O'Connor & Lieuwen (2012a) developed a simple model for the transverse velocity field which showed to match quite well with the experimental data:

$$v_a = A_a e^{-\mathrm{i}(\omega t + \varphi_{v_a,v_v})} \tag{1.66}$$

$$v_v = A_v e^{-\mathrm{i}\omega(t - x/u_{v,c})} e^{-\alpha x}. \tag{1.67}$$

Here, v_a is the acoustic velocity, v_v is the vortex induced velocity, A_a and A_v are the initial amplitudes of each velocity fluctuation, α is the decay rate, $u_{v,c}$ is the axial convection speed of the vortices and φ_{v_a,v_v} is the phase between the velocity fluctuations.

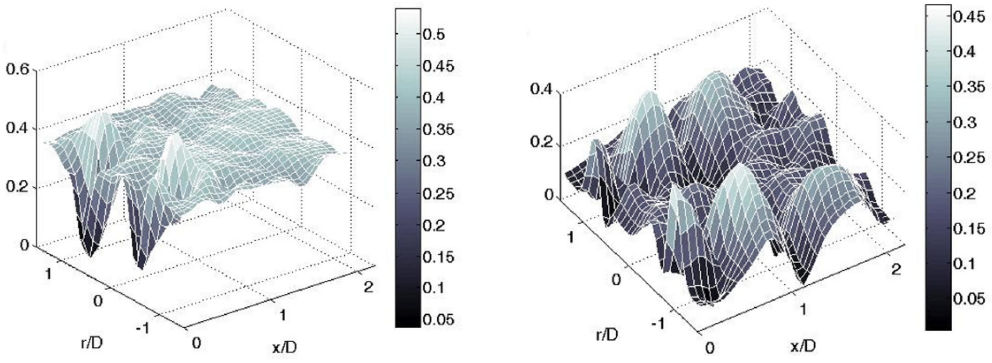

(a) (b)

Figure 1.21: Normalized amplitude of transverse velocity fluctuations at the forcing frequency for (a) nonreacting and (b) reacting flow for an annular jet with exit velocity $U_e = 10$ m/s subjected to a pressure node with forcing frequency 400 Hz. Adapted from O'Connor & Lieuwen (2012a).

A variety of different jet responses can be explained purely by acoustics. Blimbaum *et al.* (2012) studied the acoustic response of an annular nozzle in a rectangular box using a finite element acoustic model. At the pressure anti-node the velocity across the jet centerline was reported to be symmetric, with zero transverse velocity but with axial velocity fluctuations. In the case of the nozzle at the pressure node, the flow exhibited large transverse velocity fluctuations that resulted in a three-dimensional flow response. In this case, pressure fluctuations with 180° phase shift between the opposite sides of the jet centerline were driving axial velocity fluctuations with the same phase shift. These fluctuations were smaller in amplitude compared to the pressure anti-node case. This was explained by the fact that the pressure fluctuations are zero at the nozzle center line, and an acoustically compact nozzle experiences small pressure fluctuations also at the edges. But also if the axial velocity fluctuations at the nozzle outlet are too large to be negligible, they are of opposite directions on each side of the nozzle. For that reason, the fluctuations cancel each other and decay progressively as they propagate upstream in the nozzle. Therefore, the nozzle impedance has no influence on the response in the pressure node case. This is in contrast to all other positions in the standing wave, and also for the traveling wave. For these cases the system is referred to as *pressure-coupled*, and the nozzle response due to the pressure fluctuations are dependent on the nozzle impedance. The pressure and velocity at the nozzle exit are then related by the net translated impedance, Z_{tr}. For a nozzle with an acoustically compact length h, $h \ll \alpha$, and boundary condition Z_0 at the lower end of the nozzle, $x = -h$, Z_{tr} can be derived by dividing equation (1.43) by (1.44) and expressing A and B by Z_0 :

$$\frac{Z_{tr}}{\rho c} = \frac{\hat{p}(x,\omega)}{\hat{u}(x,\omega)} = - \left[\frac{\left(-\frac{Z_0}{\rho c} - 1\right) e^{-\mathrm{i}k(x+h)} + \left(-\frac{Z}{\rho c} + 1\right) e^{\mathrm{i}k(x+h)}}{\left(\frac{Z_0}{\rho c} + 1\right) e^{-\mathrm{i}k(x+h)} + \left(-\frac{Z_0}{\rho c} + 1\right) e^{\mathrm{i}k(x+h)}} \right]. \tag{1.68}$$

For the pressure node case, the pressure at the exit of the nozzle is independent of Z_{tr} and therefore also the nozzle impedance, and is also close to the one-dimensional acoustic solution. For the other cases, the pressure is only close to the one-dimensional solution for the anechoic boundary condition, $Z_{tr}(x = 0) = 1$, but change with Z_{tr} as it gets affected by the presence of the nozzle. For $Z_{tr}(x = 0) = 0.01$, described as pressure release condition, standing pressure waves upstream of the nozzle will try to change the nozzle exit to a pressure node, as it acts as an open end of a pipe as described in section 1.4.1.

1.5 Summary of the literature

Transverse acoustic forcing has been shown to result in different vortex structures in the shear-layer of a jet. The jet's position in the wave is significant here. Even though several aspects of the vortex structures of these jets have been documented, three-dimensional measurements of these jets have not been reported in the literature.

The pressure anti-node has the same effect on the jet as longitudinal forcing, where the shear-layer rolls up into periodic, axisymmetric vortex structures controlled by the forcing frequency. At a certain finite level of forcing amplitude, coherent vortex rings form in the near-field. This axisymmetric response has been observed in many types of jets, from simple, round jets of constant density, to swirling annular jets with combustion.

For a jet positioned at the pressure node, measurements in the plane parallel to the acoustic waves have revealed that the jet undergoes a flapping motion, and the shear-layer rolls up in anti-phase about the jet centerline resulting in a staggered arrangement of vortices. For a jet at a pressure node, the vortex structures are affected by the inlet conditions. For swirling inflow it has been suggested in several studies that the shear-layer rolls up into continuous, helical structures, and this has some support for the specific conditions from three-dimensional LES (Huang *et al.*, 2006; Huang & Yang, 2005). For non-swirling inflow, Matta *et al.* (1996) found that the vortex shedding was only present in the plane parallel, and not normal, to the acoustic waves. This eliminates the possibility for the vortex structures in the jet to be a continuous helix. The description of the jet shape fits however well with what was reported from the simulations by Urbin & Métais (1997) and Danaila & Boersma (2000) of a jet forced by a flapping mode, and the three-dimensional vortex structure of the jet in a pressure node is therefore likely to have a shape similar to what is shown in figure 1.13. This similarity is also expected from the fact that equation (1.65) shows that the pressure node of a transverse wave can be approximated as a sum of the $m_h \pm 1$ modes, which is equivalent to a flapping mode.

Fewer studies have investigated the flow response of traveling waves and of jets positioned in between the pressure anti-node and node of a standing wave. Here, the presence of both pressure fluctuations and pressure gradients result in acoustic velocities in the transverse and axial directions simultaneously, and the response has been reported to be a combination of those of a pressure anti-node and a pressure node (Saurabh *et al.*, 2014). A different behavior at the intermediate position in a standing wave, that has not been seen in either the pressure anti-node or the pressure node case, was reported by Lespinasse *et al.* (2013). Here, the vortex structures on the jet shear-layer towards the pressure anti-node was larger than on the other side, and the jet was leaning towards the pressure node. This resulted in an asymmetric mean flow-field. It was suggested that this was caused by the product of the pressure fluctuations and the pressure gradient fluctuations, that is non-zero in a traveling wave, and everywhere in a standing wave except at the pressure anti-node and pressure node positions.

1.6 Objectives

This chapter has summarized the state-of-the-art in forced jets, vortex formation and active control of jets. It shows there are significant areas that are unexplored, and in particular the large-scale structures of a jet within a transverse acoustic field appears to be unknown. There have been studies that consider the structure of jets and flames in a transverse acoustic field (Lespinasse *et al.*, 2013; O'Connor & Lieuwen, 2012b), but the complex conditions of these studies (i.e. combustion, swirl at inlet, annular jet) limit the understanding of the flow interaction with the acoustic field. Understanding this for a simple, non-reacting flow such as a round jet, offers insight that can be applied to industrial flow scenarios that are significantly more complex such as thermo-acoustic oscillations in gas turbine combustors that in the simplest sense, are an array of jets around an annulus discharged into a transverse acoustic field. In this regard, the single round jet can help elucidate the fundamental flow response observed in more complex configurations. This thesis will investigate the following research questions:

- How are the mean properties of the jet (deflection of the flow, potential core, shear-layers and jet centerline) affected by transverse acoustic forcing?
- What is the nature of the vortex structures in the jet and how they are formed? What is the role of pressure fluctuations, pressure gradient fluctuations and their interaction, in the vortex formation and the asymmetry of the jet?
- How is the pinch-off process for the vortex structures in the near-field affected by jet position? Can the pinch-off time of the vortex structures in a transversely forced jet be determined using the same methods as developed for vortex rings?

Chapter 2

Experimental methods

This chapter describes the experimental setup as well as the measurement and analysis techniques used. In section 2.1 and 2.2 the apparatus, as well as the measurements used to characterize the acoustic field, is described. Velocity measurements were performed, using both constant temperature hot-wire anemometry at the nozzle exit and stereo particle image velocimetry in the transverse-streamwise plane in the near-field of the jet. These techniques are described in section 2.3 and 2.4, respectively. Finally, section 2.5 presents the post-processing methods used to analyze the data.

2.1 Experimental setup

Figure 2.1a shows a sketch of the jet apparatus used in this study. The flow enters horizontally from two 12 mm inner diameter rubber tubes below the 300 mm long plenum chamber with inner diameter of 94 mm. There are two speaker holders, 61 mm long pipes with inner diameter of 25 mm, on opposite sides of the plenum that has been used in previous studies for longitudinal forcing (Aydemir *et al.*, 2012; Lawson & Dawson, 2013). These holders are sealed with rubber gaskets and metal plates from outside and not used is this study, but might have an impact on the acoustic properties of the nozzle setup. At the beginning of the constant area part of the plenum there is a 40 mm long honeycomb section of hexagonal cells with cross-sections of 3 mm, for flow conditioning. Downstream of the plenum chamber, the flow goes through a pipe of length 400 mm with an inner diameter of 35 mm. This pipe has two microphone holders 200 mm apart with 8 mm diameter round holes perpendicular into the side of the pipe which enable to place microphones flush with the inner wall of the pipe. These holes were sealed during measurements with modeling clay to prevent losses, either completely or around the microphones when pressure measurements were performed. At the end of the pipe, the jet nozzle comprised of a 61.5 mm long converging nozzle with a fifth order profile and a knife-edged exit of diameter 10 mm. Figure 2.1b shows a detailed sketch of this nozzle. Previous works (Aydemir *et al.*, 2012; Lawson & Dawson, 2013) demonstrated that the jet exhibits an approximately top-hat velocity profile at the nozzle exit. The air was supplied from a 5.5 bar pressure supply, and a mass flow controller (Alicat MCR-500SLPM-D, $\pm 1.9\% - 3.9\%$ $(89.1 - 32.0$ SLPM) flow uncertainty) was used to control the flow rate.

The jet was discharged into a long rectangular enclosure shown in the sketch of the experimental setup in figure 2.2, and in the photograph in figure 2.3a. The nozzle exit protruded 13 mm above the base. The enclosure was made of 15 mm thick, clear lexan walls for optical access and with two speakers mounted on adjustable side walls to create approximately one-dimensional acoustic standing waves along the enclosure. The speakers were fitted to 35 mm inner diameter resonance tubes. The speaker tube lengths could be altered to deliver significantly higher power compared to without the tubes. The tubes were terminated on the speaker end, and their lengths plus the end-correction in equation (1.55) were matched to the quarter wavelength of the speaker signal according to equation (1.54) to obtain resonance. Tubes with lengths depending on the forcing frequency were therefore used and mounted on the side walls with its center 60 mm above the enclosure base. As shown in figure 2.3b, an extra pair of speakers could be added 125 mm above the first pair to increase the range of obtainable pressure amplitudes in the enclosure when necessary. The enclosure was 590 mm high and 220 mm deep, and had an open top. The speaker side walls were movable to be able to adjust the box length to match the acoustic wavelength, and also adjust the jet position within the standing

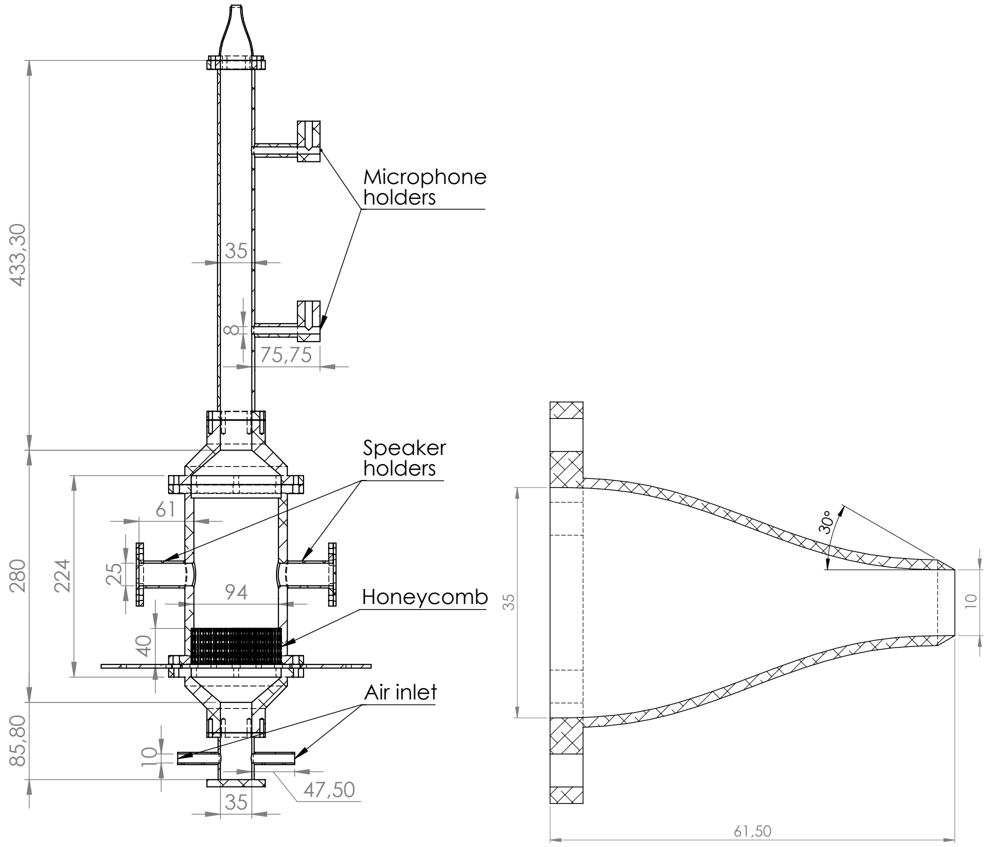

(a) (b)

Figure 2.1: Sketch of (a) nozzle setup and (b) nozzle. Dimensions are given in mm.

wave. For all the measurements in this thesis the distance between the speaker walls was kept constant at 1600 mm. The dimensions in the enclosure will be referred to as streamwise (vertical), transverse (normal to speaker walls and in the direction of the sound waves) and spanwise, which correspond to the coordinates x, y and z, respectively.

To measure the box modes the enclosure had five microphone holders with 7.5 mm diameter round holes, shown in figure 2.4. These were located 60 mm above the base of the enclosure at transverse positions $-600, -400, -200, 0$ and 200 mm relative to the center of the nozzle. The microphones where either placed with the sensor flush with the wall (figure 2.4a), or in the side holes (figure 2.4b) when the microphones were used during PIV measurements to prevent the microphones from being covered by the olive oil seeding.

Monacor KU-516 (75W, 16Ω) horn drivers were used for acoustic forcing. Each of them was driven by a separate channel on a two-channel Skytec PRO1000 power amplifier. An Aim-TTi TGA1244 40 MHz signal generator delivered a sine wave signal with prescribed amplitude and frequency to the amplifier channels. Brüel and Kjær Free-field 1/4 inch microphones (model 4939, frequency range 4 Hz-100 kHz) were used for the pressure measurements. Each pressure sensor and its preamplifier (Brüel and Kjær model 2670, frequency range 15 - 200 000 Hz) were calibrated by the manufacturer and had a sensitivity of $\approx$ 4 mV/Pa (-48dB re 1V/Pa, 95 % confidence level uncertainty of 0.3 dB). The microphone signals were recorded by a National Instruments 24 bit compactDAQ NI-9234 data acquisition unit, while the loudspeaker signals were recorded by a National Instruments 16 bit compactDAQ NI-9215.

By recording the pressure for the same forcing and enclosure settings for the two microphone positions, an amplitude conversion factor of 2.72 (pressure at position shown in figure 2.4a divided by pressure at position shown in figure 2.4b) was obtained. The phase difference between the measurements was below 1°, and was therefore not corrected for.

The response of the speakers was changing over time and did also vary slightly from speaker to speaker. The procedure for changing the forcing amplitude was therefore to place a microphone in the middle of the two speaker walls, and

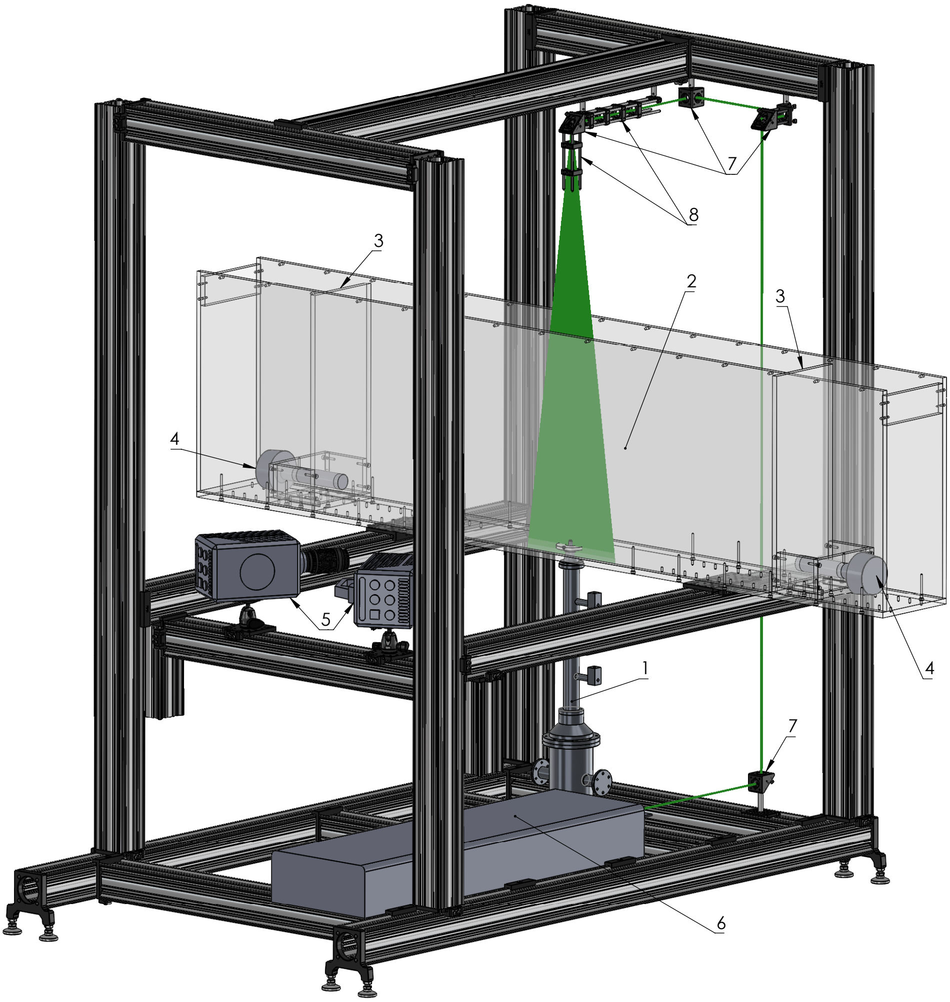

Figure 2.2: Sketch of experimental setup including nozzle setup (1), jet enclosure (2) with adjustable walls (3) and speakers for acoustic forcing (4). The Stereo-PIV equipment is also shown, including cameras (5), laser (6), mirrors for guiding laser beam (7) and sheet forming optics (8). The laser path is shown in green.

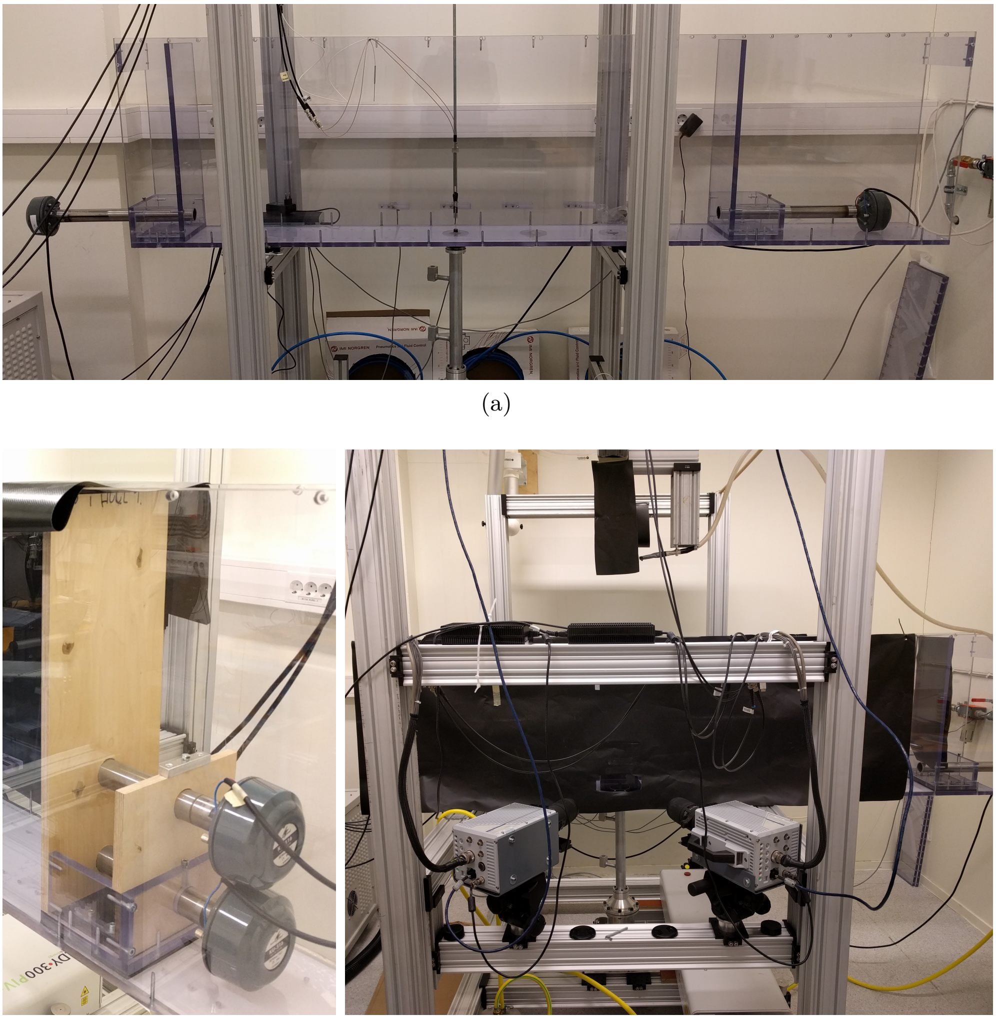

(a)

(b)

(c)

Figure 2.3: Photographs of the experimental setup. (a) The jet enclosure with one speaker on each side and hot-wire placed at the nozzle exit. (b) Setup with two speakers on each side of the enclosure. (c) Stereo-PIV setup.

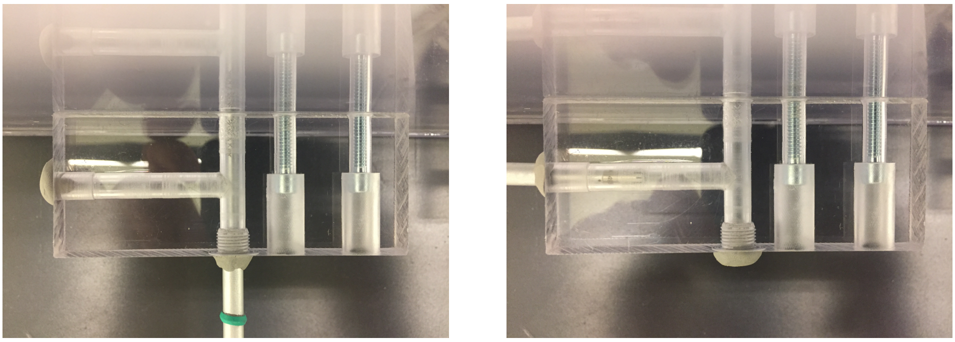

(a) (b)

Figure 2.4: Photographs of microphone holder with (a) microphone at position 1 and (b) microphone at position 2.

then to force from one side at the time while adjusting the input voltage on this speaker so both sides gave the same forcing amplitude and phase, while at the same time the two sides gave the wanted amplitude combined. This needed some iterations, since the two sides combined did not give exactly twice the amplitude as one side at the time.

2.2 Two-microphone technique

In this study we wanted information about the acoustic field in the jet enclosure during the measurements to have control over the forcing conditions of the jet. Also the pressure waves in the jet apparatus were of interest. The pressure was therefore measured at different positions in the jet enclosure and in the pipe upstream of the nozzle using microphones. From these data the two-microphone technique by Seybert & Ross (1977) was used to find an estimate of the acoustic properties in these geometries by assuming one-dimensional, plane-wave propagation and that the complex pressure distribution was on the form of equation (1.43):

$$p'(x,t) = Ae^{\mathrm{i}(k_1 x - \omega t)} + Be^{\mathrm{i}(k_2 x + \omega t)}.$$

The technique requires measured time-series of the pressure from at least two positions, x_1 and x_2, in the tube. The measured values are the real part of the pressure, and can be expressed as

$$\begin{aligned} p_1'(t) &= \Re\{p'(x_1,t)\} = \Re\{Ae^{\mathrm{i}(k_1x_1-\omega t)} + Be^{\mathrm{i}(k_2x_1+\omega t)}\} \\ &= \frac{1}{2}A\left[e^{\mathrm{i}(k_1x_1-\omega t)} + e^{-\mathrm{i}(k_2x_1-\omega t)}\right] + \frac{1}{2}B\left[e^{\mathrm{i}(k_2x_1+\omega t)} + e^{-\mathrm{i}(k_2x_1+\omega t)}\right], \end{aligned} \tag{2.1}$$

$$\begin{aligned} p_2'(t) &= \Re\{p'(x_2,t)\} = \Re\{Ae^{\mathrm{i}(k_1x_2-\omega t)} + Be^{\mathrm{i}(k_2x_2+\omega t)}\} \\ &= \frac{1}{2}A\left[e^{\mathrm{i}(k_1x_2-\omega t)} + e^{-\mathrm{i}(k_2x_2-\omega t)}\right] + \frac{1}{2}B\left[e^{\mathrm{i}(k_2x_2+\omega t)} + e^{-\mathrm{i}(k_2x_2+\omega t)}\right]. \end{aligned} \tag{2.2}$$

The Fourier transforms of $p_1'(t)$ and $p_2'(t)$ at the angular frequency ω are given by

$$\hat{p}_1'(\omega) = \mathcal{F}(p_1'(t)) = \frac{1}{2}\mathrm{conj}(A)e^{-\mathrm{i}k_1x_1} + \frac{1}{2}Be^{\mathrm{i}k_2x_1}, \tag{2.3}$$

$$\hat{p}_2'(\omega) = \mathcal{F}(p_1'(t)) = \frac{1}{2}\mathrm{conj}(A)e^{-\mathrm{i}k_1x_2} + \frac{1}{2}Be^{\mathrm{i}k_2x_2}, \tag{2.4}$$

where conj(A) is the complex conjugate of A. This is a system of two equations with two unknowns, A and B, and has the analytical solution

$$\mathrm{conj}(A) = 2\frac{\hat{p}_1'e^{-\mathrm{i}k_2x_1} - \hat{p}_2'e^{-\mathrm{i}k_2x_2}}{e^{-\mathrm{i}(k_1+k_2)x_1} - e^{-\mathrm{i}(k_1+k_2)x_2}}, \tag{2.5}$$

$$B = 2\frac{\hat{p}_1'e^{\mathrm{i}k_1x_1} - \hat{p}_2'e^{\mathrm{i}k_1x_2}}{e^{\mathrm{i}(k_1+k_2)x_1} - e^{\mathrm{i}(k_1+k_2)x_2}}. \tag{2.6}$$

If the pressure is measured at $n > 2$ positions, we have an overdetermined system of equations of the form

$$\begin{bmatrix} \hat{p}_1'(\omega) \\ \hat{p}_2'(\omega) \\ \vdots \\ \hat{p}_n'(\omega) \end{bmatrix} = \begin{bmatrix} \frac{1}{2}\mathrm{conj}(A) & \frac{1}{2}B \end{bmatrix} \begin{bmatrix} e^{-k_1 x_1} & e^{-k_1 x_2} & \dots & e^{-k_1 x_n} \\ e^{k_1 x_1} & e^{k_1 x_2} & \dots & e^{k_1 x_n} \end{bmatrix}. \tag{2.7}$$

This was solved using the least squares method.

2.3 Constant temperature hot-wire anemometry

To characterize the velocity amplitudes and the mean profiles at the jet exit, velocity measurements were carried out using constant temperature hot-wire anemometry. This is an intrusive velocity measurement technique consisting of an electrically heated wire placed in a flow field, and the heat transfer to the flow is measured. For a constant temperature hot-wire, the heat lost to the flow is balanced by the electric power E_w^2/R_w added to the wire, where E_w is the voltage over the wire and R_w is the electrical resistance in the wire. The resistance of a specific wire is constant when the wire temperature is fixed. King's law suggests a relation between the voltage and the flow velocity u (Anthoine, 2009):

$$E_w^2 = A + Bu^n. \tag{2.8}$$

where A and B are calibration constants and n has typically a value of $n \approx 0.45$. Alternatively, polynomial curve fitting can be used:

$$u = k_{w0} + k_{w1} \cdot E_w + k_{w2} \cdot E_w^2 + k_{w3} \cdot E_w^3 + k_{w4} \cdot E_w^4. \tag{2.9}$$

For the work presented in this thesis the polynomial curve fit was chosen since it is known to be more accurate than King's law, partly because n in equation (2.8) has a weak velocity dependence. To ensure that the measurements are not restricted by the voltage limits of the data acquisition unit, an offset and gain can be applied to the hot-wire signals. A gain will also lower the uncertainty from the unit. When an offset E_{offset} and a gain G is applied, the acquired signal E_a needs to be converted by the following formula (Jørgensen, 2005):

$$E_w = \frac{E_a}{G} - E_{\text{offset}}. \tag{2.10}$$

Varying fluid temperature during measurements will affect the results since the heat convection is dependent on the difference between the wire and fluid temperature. To adjust for this, the fluid temperature was measured together with the hot-wire signal, and a temperature correction on the hot-wire anemometry signal E was performed (Jørgensen, 2005):

$$E_{w,\text{corr}} = \left(\frac{T_w - T_0}{T_w - T_a} \right)^{0.5} E_w. \tag{2.11}$$

Here T_w is the wire temperature, T_0 is the fluid temperature measured prior to calibration, and T_a is the fluid temperature acquired during the measurements.

A Dantec Dynamics StreamLine Pro constant temperature anemometry system was used with a straight, single-wire probe (type 55P11) with a sensor made of platinum-plated tungsten with diameter 5 μm, length 1.25 mm, and frequency response of 400 kHz. The probe was mounted with the wire oriented in the spanwise direction to a 4 mm diameter and 200 mm long probe support centered over the exit of the nozzle in the spanwise direction. This was again mounted to a 10 mm diameter metal rod that was suspended vertically over the nozzle on a traversing system situated approximately 1 meter downstream of the nozzle exit. This enabled the wire to be traversed in the transverse direction. The hot-wire measurements were performed with an offset of 1.297 V and a gain of 4, and the hot-wire and temperature probe signals were recorded with a frequency of 5

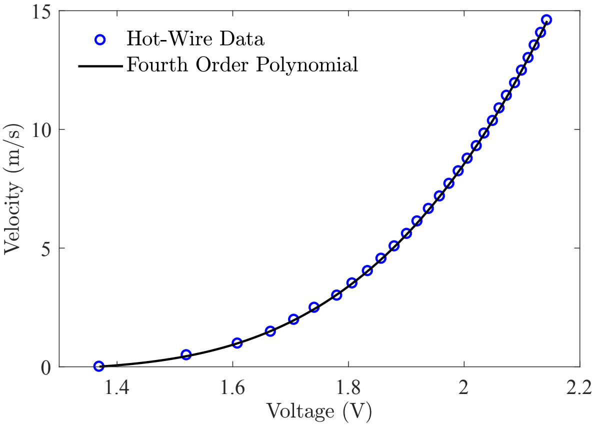

Figure 2.5: Example of hot-wire calibration.

kHz over 10 seconds for every measurement point using a National Instruments 16 bit compactDAQ NI-9215 data acquisition unit.

To calibrate the hot-wire probe, the velocity in the center of the nozzle exit was measured with different mass flow rates set on the mass flow controller. To account for the nozzle not having a perfectly top-hat profile, the mean velocity calculated from the volume flow was multiplied by a correction factor. This correction factor, depending on the volume flow in the nozzle, was found by comparing the volume flow set at the mass flow controller with the volume flow achieved from integrating the velocity profile measured with the hot-wire probe. An example of a calibration curve achieved is shown in figure 2.5.

2.4 Stereo particle image velocimetry

2.4.1 Background

The velocity in the near-field of the jet was measured using the non-intrusive Particle Image Velocimetry (PIV) technique. This method does not measure the fluid velocity directly, but the correlation between displacements of particles added to the fluid that are expected to follow the flow. A sheet or a volume of the seeded flow is illuminated by a light source, and time-series of the Mie scattering of the particles are then captured by one or several cameras. In this study a double-pulsed laser with two heads was used as the light source. By synchronizing the cameras and the laser, the flow is illuminated once per exposure of the camera, and the particle position in two particle images separated by a time δt are correlated to obtain a velocity field. Either double frames or time-series of single frames are used. For the double frame method, the two laser heads are sending pulses with a separation time δt appearing in two consecutive camera exposures. These two particle images are making up one frame pair resulting in one vector field, and the frame pairs are recorded with a frequency f_R that can be chosen with the only restriction $1/f_R > 2\delta t$. When using time-series of single frames, only one of the laser heads are used, and single frames are recorded with frequency f_R. Then frame 1 and 2, 2 and 3 and so on are combined to frame pairs each giving one vector field. With this method the separation time is fixed to $\delta t = 1/f_R$. To the left of figure 2.6, two example particle images that make up a frame pair are illustrated. Each particle image is divided into so-called interrogation windows. Two of the belonging interrogation windows are enlarged in the figure. The idea behind the cross-correlating function is to correlate the pixel intensities in the interrogation window in frame 1 at time t, $I_1(x_i, y_j)$, with that in frame 2 at time $t + \delta t$, $I_2(x_i, y_j)$, using the discrete cross-correlation function (Raffel *et al.*, 2007):

$$R_{I_1 I_2}(dx, dy) = \sum_{i=-K}^{K} \sum_{j=-L}^{L} I_1(x_i, y_j) I_2(x_i + dx, y_j + dy). \tag{2.12}$$

Here, i denotes the pixels in x direction and j in y direction, going from $-K$ to K and $-L$ to L, respectively, in the current interrogation windows. The cross-correlation $R_{I_1 I_2}(dx, dy)$ is the sum of products of the intensity values at time t shifted a distance (dx, dy), and the intensity values at time $t + \delta t$. The result is a measure of how well the two frames match when shifted the distance (dx, dy). This can be done for a range of shifts in x and y direction, and the resulting $R_{I_1 I_2}$ are then plotted in a correlation map, also shown in figure 2.6. If the particles inside the interrogation window have similar velocities they will have moved the same distance in time δt, and a peak for this displacement will appear in the correlation map. The particle velocity is then found by simply dividing the displacement with δt. In practice the correlation map does not

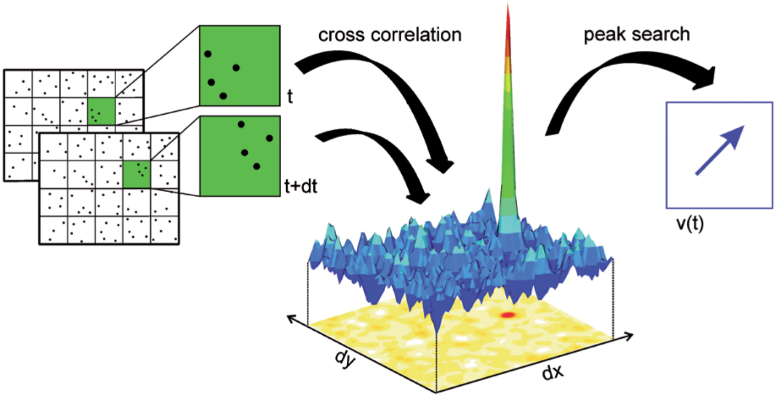

Figure 2.6: Illustration of the principle of cross-correlation. Adapted from LaVision (2017).

necessarily give such a distinct peak as in this example. This can be due to noise, the fact that the particles do not have exactly the same velocity or that there are not enough particles in the interrogation window.

The edges of frame 1 that are not overlapping with frame 2 when shifted, are not taken into account. Therefore, the strength of the correlation peak will decrease with the size of the particle shift since the number of possible particle matches decreases. A much used limit is that the particle shift should not exceed one fourth of the interrogation window side length. A way to get around this limit is to shift the interrogation windows relative to each other with the expected particle displacement. This expected displacement can be achieved from a previous processing pass where a bigger window size satisfying the one fourth rule is used. The final interrogation window size should still be large enough to achieve a sufficient amount of particle matches. When the number of particle matches goes below 4, the accuracy decreases drastically (Raffel *et al.*, 2007). The interrogation windows can also be deformed according to the gradients in the previous pass. The procedure of shifting and deforming the interrogation windows before repeating with a smaller window size can be repeated several times. It is also possible to let the neighboring interrogation windows overlap to achieve a higher vector density without making the windows

]

smaller. This improves the quality of gradients calculated from the velocity field. However, it will not increase the resolution in terms of capturing finer structures, since each vector is calculated over the same area size as if the interrogation windows were not overlapping.

Standard two-dimensional, two-component PIV requires one camera and results in a velocity field including the two velocity components in-plane of the laser sheet. This enable calculating 4 of the 9 components in the three-dimensional velocity gradient tensor. Stereoscopic PIV (SPIV) results in a two-dimensional velocity field in the plane of the laser sheet including all three velocity components. This requires two cameras with different viewing angles not normal to the laser sheet, and the sheet must have a certain thickness. By combining the images from the two cameras from the same time instant it is possible to find the out-of-plane position of the particle in the laser sheet. The difference in the correlation maps from the two cameras are then a result of the out-of-plane motion of the particles. SPIV measurements enable calculating 6 of the 9 components in the three-dimensional velocity gradient tensor, only missing the out-of-plane gradients since only one velocity vector in this direction is achieved.

To know the relation between the displacement of the particles in terms of pixels in the image and physical coordinates, a calibration is required. This is carried out by placing a calibration target, a plate with a known pattern, in focus of the cameras in the same plane as the laser sheet will be. The result of the calibration is a mapping function that converts the displacement from image to object space. In this study a third order polynomial calibration function has been used. For SPIV, two or more calibration images with the calibration plate displaced a known distance in the out-of-plane direction are required. Alternatively, as in this study, a multi-level calibration plate with patterns in different out-of-plate positions can be used (Raffel *et al.*, 2007). The result is a projection coefficient converting the image from the angeled camera into a image as if the camera was pointing normal to the image plane. The process of placing the calibration plate exactly in the plane of the laser sheet is associated with an uncertainty, and a method to correct for this is camera self-calibration (Raffel *et al.*, 2007). Particle images from the different cameras are first dewarped using the projection coefficient from the original calibration. The images taken at the same time, but with different camera angles, are then correlated. Since these images are supposed to be identical, the result is a displacement field due to the misalignment between the calibration plate and the laser sheet. The original calibration function is therefore adjusted to minimize the displacements in this field.

Prior to processing the particle images into vector fields, it is often advantageous to perform image preprocessing. On the PIV measurements presented in this thesis two types of filters are used. A subtracting sliding background filter is a high-pass filter that removes low-frequency variations in the background. A filter kernel size must be specified, and should be larger than the size of the particle images (Raffel *et al.*, 2007). Another preprocessing filter used is the particle intensity normalization filter, also called the min/max filter. By applying this, the contrast in the particle image is normalized while also the spatial variation of the contrast throughout the image is adjusted. Also for this case the filter size should be larger than the size of the particle images.

2.4.2 SPIV measurements

In this study, high-speed SPIV was performed in the transverse-streamwise plane along the centerline of the jet. A sketch of the setup is shown in figure 2.2, and a photograph in figure 2.3c. The measurement plane was illuminated from a position downstream of the jet using a Litron LDY303HE-PIV dual cavity laser, and the beam was formed to an approximately 1 mm thick sheet by first converging it through a set of round lenses, and then expanding it again through a cylinder lens.

The jet flow was seeded with oil droplets generated using a Laskin nozzle submerged into a reservoir of olive oil. The amount of oil particles created by the seeder depends on the volume flow through the Laskin nozzle. To enable the seeding density to be adjusted independently of the total volume flow to the nozzle, the tube coming from the mass flow controller was split through a T-joint. Both of the tubes downstream of the T-joint went through a ball valve before one of the tubes went into the seeder and the other bypassed it. Then the two tubes were recombined before the tube again was split through a T-joint and connected to the two inlets of the jet apparatus shown in figure 2.1a. When running the experiments without conducting PIV measurements, the valve upstream of the seeder was closed and the bypass valve was fully opened. Before each PIV measurement run, the valves where adjusted during a test run until the desired seeding density was achieved. Then the box was seeded by having the jet running with the enclosure covered for a period of 6, 5 and 4 minutes for the jet mean exit velocities $U_e = 6.8$, 13.1 and 18.9 m/s, respectively, that are the three jet velocities investigated in this study. The measurements were taken after the enclosure had been open for 10 seconds. Also measurements with zero mean flow were conducted. Then the enclosure was seeded for 5 minutes using the same mass flow controller and valve settings as for the 13.1 m/s case. Then both valves were closed completely, and a rest time of 30 seconds was used before the recording started.

Two Photron SA1.1 cameras fitted with Scheimpflug adapters and 180 mm lenses with aperature set to f/3.5 were used to capture the Mie scattering from the particles. The cameras were oriented with their lenses approximately ±15° relative to the measurement plane normal, and parallel to the transverse-azimuthal plane. The Scheimpflug adapters make an angle between the camera and the lens to enable the whole camera image to be in focus (Adrian & Westerweel, 2011). The cameras recorded a field of view spanning 4.8D downstream from the nozzle exit and 2.5D in the radial direction centered at the nozzle centerline. These images were recorded with a camera resolution of 1024×512 pixels (streamwise times transverse).

A Lavision two-level calibration plate model 106-10 with 10 mm dot distance, 2.2 mm dot size and 2 mm level separation was used for calibration. The average deviation between the third order polynomial calibration mapping function and the marks were less than 0.15 pixels. Figure 2.7a shows an example of a calibration image used, and figure 2.7b an example of a Mie scattering image.

For the $U_e = 6.8$ m/s, $U_e = 13.1$ m/s and $U_e = 18.9$ m/s cases, a double frame method was used and the paired particle images were separated by $\delta t = 25\mu$s,

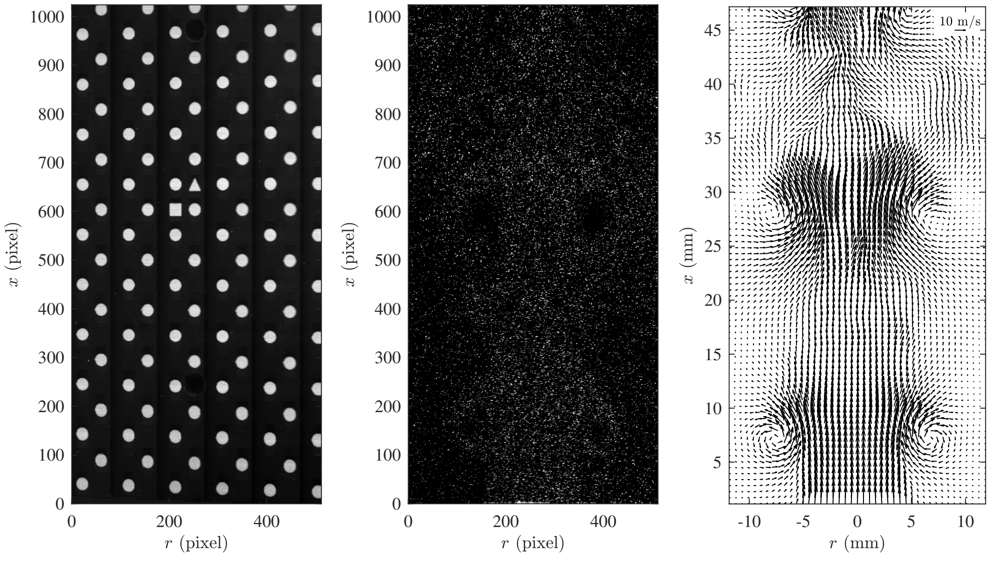

(a)

(b)

(c)

Figure 2.7: Example of (a) calibration image, (b) Mie scattering image and (c) velocity field, for the case $f = 450$ Hz, $U_e = 13.1$ m/s, $u'_{\text{RMS}}/U_e = 0.25$ m/s, $y/\frac{\lambda}{4} = 0$.

18μs and 12μs, respectively. Three different forcing frequencies, $f = 250$ Hz, $f = 450$ Hz and $f = 655$ Hz, were used in the measurements. The image pairs were recorded at a rate of $f_R = 5.0$ kHz, $f_R = 5.4$ kHz and $f_R = 5.24$ kHz for these cases, respectively, which gave 20, 12 and 8 time-steps per forcing cycle. A total of 200 forcing cycles were recorded per experimental run for each jet location. For the zero mean flow cases, a single frame method was used since the particles were moving very slowly and therefore the separation time between the paired images needed to be as large as possible. This gave $\delta t = (1/5400$ Hz$)$ ≈ 185 μs. 240 images were saved, resulting in 120 vector fields and 10 forcing cycles.

Figure 2.8 shows the timing diagram for the simultaneous double frame PIV, pressure measurements and acoustic forcing, where the PIV recording rate is 12 times the sinusoidal speaker signal period. $t_l = 4$ μs is the laser delay time. The system was controlled by a LabVIEW 14.0 (National Instruments Corporation) program developed for the purpose, except for the cameras that were used with Photron FASTCAM Viewer 3.

The particle images were processed in DaVis 8.4.0 (LaVision GmbH). First a self-calibration algorithm, correcting for the misalignment between the laser sheet and the calibration plate, was used. The particle images were then preprocessed using a subtracting sliding background scheme with a 8 pixel filter length and a particle intensity normalization filter with a filter length of 6 pixels. Finally, the velocity vectors were calculated using a multi-pass, stereo cross-correlation scheme. Interrogation windows of decreasing size were used, starting at 64x64 pixels and 75 % overlap and ending at 24x24 pixels and 50 % window overlap with in total four passes. All the passes used a circular Gaussian weighting function. Then the total area evaluated are of twice the width and height, but the Gaussian function is scaled so the sum of all weighted pixels is equivalent to the window size specified (LaVision, 2017). The interrogation window pairs were shifted and deformed based on the previous passes. For the two first passes a standard correlation function was used, while a correlation function normalized by the standard deviation of the second interrogation window was used for the two last passes. The normalization prevents varying background intensities and signal densities from biasing the correlation function (LaVision,

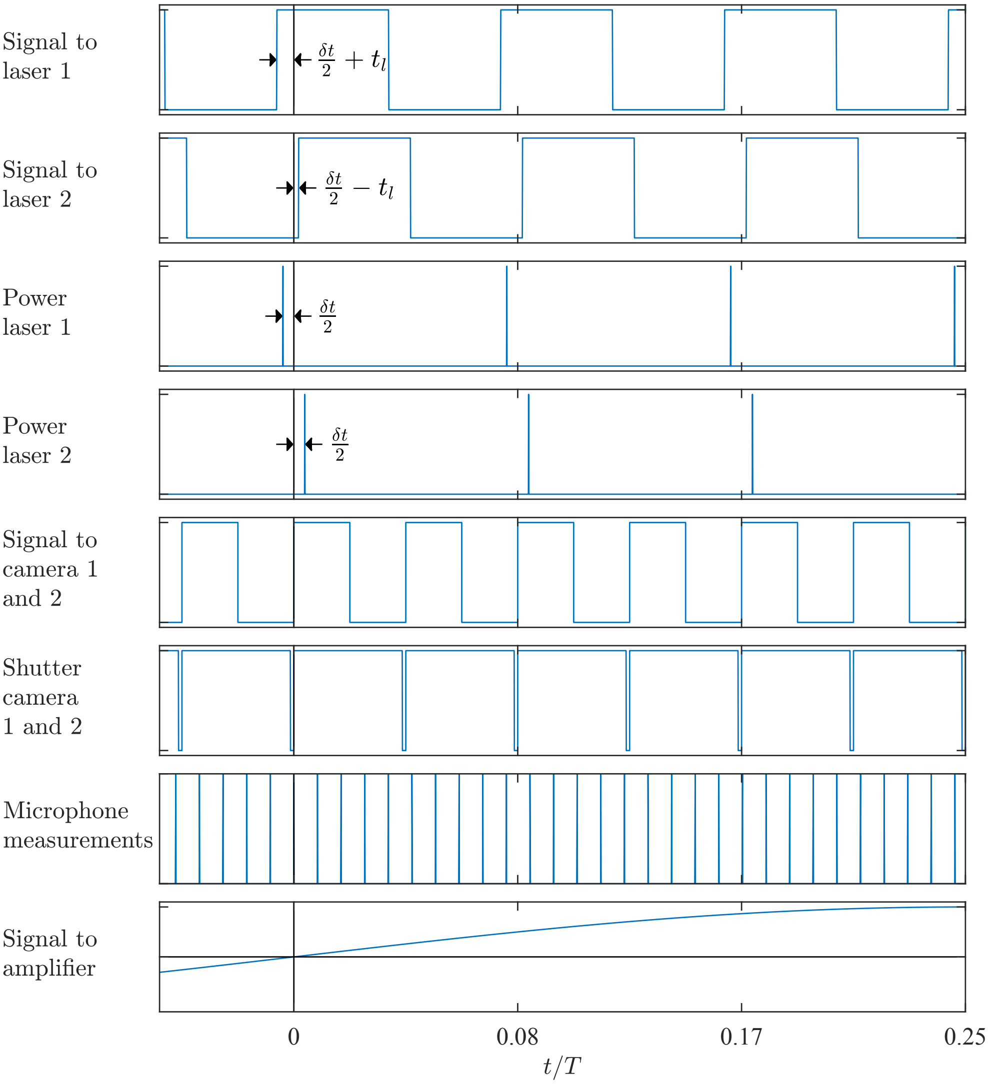

Figure 2.8: Synchronization scheme of two-frame PIV, pressure measurements and acoustic forcing. Only a part of the forcing period is shown for clarity.

2017). The resulting velocity field vector spacing was $\Delta x = \Delta y = 0.028D$. Figure 2.7 (c) shows an example of a velocity field obtained from the PIV measurements with every second vector shown.

2.5 Data post processing methods

2.5.1 Decomposition of flow field

From the time-resolved pressure and velocity data obtained, a variety of other quantities are derived. A transient flow field can be decomposed in different ways. Reynolds decomposition divides a quantity into a mean and a fluctuating part, where the latter per definition average to zero. For the velocity this yields:

$$\mathbf{u}(\mathbf{x},t) = \bar{\mathbf{u}}(\mathbf{x}) + \mathbf{u}'(\mathbf{x},t) \tag{2.13}$$

The Root-Mean-Square (RMS) of the fluctuating part is a measure of the unsteadiness of the flow:

$$\mathbf{u}'_{\mathrm{RMS}}(\mathbf{x}) = \sqrt{\frac{1}{n}\sum_{i=1}^{n}((\mathbf{u}'(\mathbf{x},t))^2)} = \sqrt{\frac{1}{n}\sum_{i=1}^{n}((\mathbf{u}(\mathbf{x},t) - \bar{\mathbf{u}}(\mathbf{x}))^2)} \tag{2.14}$$

The periodic, acoustic forcing introduces a periodic component in the flow field. For the measurements obtained while this forcing was present, the data was decomposed into time averaged, periodic and fluctuating components following the triple decomposition by Hussain & Reynolds (1970):

$$\mathbf{u}(\mathbf{x},t) = \bar{\mathbf{u}}(\mathbf{x}) + \tilde{\mathbf{u}}'(\mathbf{x},t) + \mathbf{u}''(\mathbf{x},t). \tag{2.15}$$

The phase averaged velocity for a given phase angle $\phi = \frac{2\pi t}{T}$ in the periodic signal is defined as $\tilde{\mathbf{u}}(\mathbf{x},\phi) = \bar{\mathbf{u}}(\mathbf{x}) + \tilde{\mathbf{u}}'(\mathbf{x},\phi)$. The turbulent fluctuations, $\mathbf{u}''$, average to zero in the phase averaged fields. This part is small in the near-field of the jet where the measurements are taken, as the jet is not turbulent here. By phase averaging the data, the effect of the forcing is isolated and the development of the flow throughout the forcing period can be investigated.

2.5.2 Vorticity fields and vortex detection

To study the vortex structures of the jet, the vorticity defined in equation (1.15) was calculated. The out-of-plane vorticity component is given by

$$\omega_\theta = \frac{\partial v}{\partial x} - \frac{\partial u}{\partial y}. \tag{2.16}$$

The vorticity fields were normalized by the jet exit velocity and diameter: $\omega_\theta^* = \omega_\theta D/U_e$. Spatial differentiation of the velocity fields was performed using a second order-accurate, least squares scheme:

$$\partial u/\partial x|_i = (2u_{i+2} + u_{i+1} - u_{i-1} - 2u_{i-2})/10\Delta x. \tag{2.17}$$

Here, i is the index of the velocity vector in x direction and Δx the vector separation distance in x direction. This scheme is designed to reduce the random errors or measurement uncertainty, and is therefore suitable for PIV (Raffel *et al.*, 2007).

Identifying a vortex in a flow field can be a complicated task, and no complete method is objectively agreed upon. A common way to detect vortices is the λ_2 criterion developed by Jeong & Hussain (1995). This method determines the existence of a local pressure minimum due to vortical motion, and defines a vortex core as a connected region were two of the eigenvalues of the symmetric tensor $\mathbf{S}^2 + \mathbf{Q}^2$ are negative. $\mathbf{S} = \frac{1}{2}(A + A^T)$ and $\mathbf{Q} = \frac{1}{2}(A - A^T)$ are the symmetric and antisymmetric parts of the velocity gradient tensor $\mathbf{A}$, respectively, which is given by:

$$\mathbf{A} = \nabla \mathbf{u} = \begin{bmatrix} \frac{\partial u}{\partial x} & \frac{\partial u}{\partial y} & \frac{\partial u}{\partial z} \\ \frac{\partial v}{\partial x} & \frac{\partial v}{\partial y} & \frac{\partial v}{\partial z} \\ \frac{\partial w}{\partial x} & \frac{\partial w}{\partial y} & \frac{\partial w}{\partial z} \end{bmatrix}. \tag{2.18}$$

Six of these components are achieved from the PIV measurements, while the out-of-plane velocity gradients are unknown. $\frac{\partial w}{\partial z}$ can however be found from continuity, giving $\frac{\partial w}{\partial z} = -\frac{\partial u}{\partial x} - \frac{\partial v}{\partial y}$. The last two components are approximated to zero as the jet can be assumed to be symmetric around $z = 0$, where the PIV measurements are conducted. The derivatives were found using second order central differences. The binary λ_2 field was calculated and used to track the vortex structures in the jet as they moved downstream. The λ_2 fields from the different time steps were compared, and if the vortex defined by the λ_2 criterion overlapped with a vortex from the previous time step, it was defined to be the same vortex. Any separation or pairing of the vortex structures were also tracked. For the vortices tracked, the centroid coordinates and circulation were calculated. The definition by Saffman (1992) was used to find the vortex centroid coordinates:

$$x_v = \frac{\iint_S 2\pi x r \omega_\theta dr dx}{\iint_S 2\pi r \omega_\theta dr dx}, \qquad r_v = \frac{\iint_S 2\pi x r \omega_\theta dr dx}{\iint_S 2\pi x \omega_\theta dr dx}. \tag{2.19}$$

Here, S is the vortex core surface found by using the λ_2 criterion.

2.5.3 Circulation of jet shear-layer and vortex structures

Both the circulation of the jet shear-layers and the circulation of the vortices were calculated using the last formulation in equation (1.23), i.e. by integrating the vorticity within a surface S bounded by the closed circuit C. The circulation was normalized with jet mean exit velocity and nozzle diameter, $\Gamma^* = \Gamma/(U_e D)$. For the vortex circulation, the circuit C was defined using a contour of constant vorticity. For a starting jet like in the experiments by Gharib *et al.* (1998), the total circulation was found by integrating the vorticity in the whole field of view at the current time step. Then, the vortex circulation was calculated when the vortex ring had separated from the shear-layer, and an iso-contour of rather low vorticity value was used when calculating the vortex ring circulation ($|\omega_\theta^*| = |\omega_\theta \cdot D/U_e| \approx 0.34$ was used for the case shown in figure 1.7b). The method by Gharib *et al.* is not directly applicable in this study. Firstly, since we are not investigating a starting jet, but a jet with periodic forcing, circulation from several forcing cycles are always apparent in the field of view. The total circulation should represent the circulation ejected by the jet from a chosen starting point in the cycle, but by integrating the whole field of view also circulation from previous cycles are included. Secondly, the method often fails to calculate the vortex circulation for the more complicated flow fields investigated in this study. For some cases the vortex structures break down before the circulation has reached a steady value. For other cases iso-contours as high as $|\omega_\theta^*| = 4$ encircles vortex structures from more than one forcing cycle, and a very high threshold is needed to be able to distinguish between these structures. In addition, since the jet is not symmetric for most of the cases in this study the left and right hand side need to be handled separately.

A method to calculate the total circulation and the circulation of the vortex structures was developed, that gave satisfactory results for most of the cases in this study, but not all. The circulation on the left and right hand side were calculated by excluding the positive or negative vorticity, respectively. When calculating the vortex circulation, each individual vortex structure was tracked from a chosen starting point in the cycle, and the circulation was calculated by integrating the vorticity over the area defined by the iso-contour $|\omega_\theta^*| = 1$ encircling all the vortex cores tracked. However, only the vorticity between the two horizontal lines defined to be $D/2$ upstream of the most upstream and $D/2$ downstream of the most downstream vortex core from the current forcing cycle at each time step was taken into account. This was done to prevent vortex structures from previous or later forcing cycles that were connected to the vortices of interest by the $|\omega_\theta^*| = 1$ iso-contours, to be included. The total circulation was calculated by integrating the whole area upstream of the same downstream boundary as used for the vortex circulation.

When plotting the total circulation and the circulation of the vortex structures, the pinch-off time was then set to be the time when the total circulation had reached the maximum value of the vortex circulation.

2.5.4 Pressure fields

To estimate the pinch-off time by following the methods by Lawson & Dawson (2013) and Schlueter-Kuck & Dabiri (2016) as described in section 1.2.3, the pressure gradient field and pressure field, respectively, are needed. From the complete velocity gradient tensor, the pressure gradient in the flow field can be calculated. The incompressible momentum equations give an expression for the pressure gradient:

$$\nabla p = -\rho \left(\frac{D\mathbf{u}}{Dt} - \nu \nabla^2 \mathbf{u} \right). \tag{2.20}$$

The viscous term can generally be neglected (De Kat & Van Oudheusden, 2012). This gives

$$\nabla p \approx \rho \frac{D\mathbf{u}}{Dt}. \tag{2.21}$$

As for the λ_2 criterion calculations described in the previous section, $\frac{\partial u}{\partial z}$ and $\frac{\partial v}{\partial z}$ can be neglected. This results in the following expressions for the in-plane components of the pressure gradient, that can be calculated from the PIV measurements:

$$\begin{aligned} \frac{\partial p}{\partial x} \approx -\frac{Du}{Dt} &= -\left(\frac{\partial u}{\partial t} + u\frac{\partial u}{\partial x} + w\frac{\partial u}{\partial y} + w\frac{\partial u}{\partial z} \right) \\ &\approx -\left(\frac{\partial u}{\partial t} + u\frac{\partial u}{\partial x} + v\frac{\partial u}{\partial y} \right), \end{aligned} \tag{2.22}$$

$$\begin{aligned} \frac{\partial p}{\partial r} \approx -\frac{Dv}{Dt} &= -\left(\frac{\partial v}{\partial t} + u\frac{\partial v}{\partial x} + v\frac{\partial v}{\partial y} + w\frac{\partial v}{\partial z} \right) \\ &\approx -\left(\frac{\partial v}{\partial t} + u\frac{\partial v}{\partial x} + v\frac{\partial v}{\partial y} \right). \end{aligned} \tag{2.23}$$

The derivatives were found by first order differentiation of the phase averaged data in time, and second order least-squares differentiation in space, given in equation (2.17). The pressure gradient field was filtered using a 9 × 9 point averaging filter, and the pressure field calculated by integrating the pressure gradient field from a common reference point to each point in the flow field.

Chapter 3

Characterization of the experimental setup

In this chapter the experimental setup described in the previous chapter is characterized. In section 3.1 the acoustic properties of the enclosure and the jet apparatus is presented. The flow properties of both the unforced and axisymmetrically forced jet is described in section 3.2. In addition, time averaged and RMS flow fields of the jet when subjected to different positions in a standing acoustic wave for varying frequencies and forcing amplitudes are presented, together with the behavior of the jet centerline for these forcing conditions. Finally, a summary of the findings follows in section 3.3.

3.1 Acoustic characterization

A consistent coordinate system is used for presenting the results, where the transverse dimension of the jet enclosure spans from $y = -0.5L_y$ to $y = 0.5L_y$ and the spanwise dimension from $z = -0.5L_z$ to $z = 0.5L_z$, and therefore $y = 0, z = 0$ denotes the middle of the enclosure. We have limited this study to include only even mode numbers for the acoustic forcing in y direction with the result that the plane $y = 0$ is always a pressure anti-node. $x = 0$ is defined to

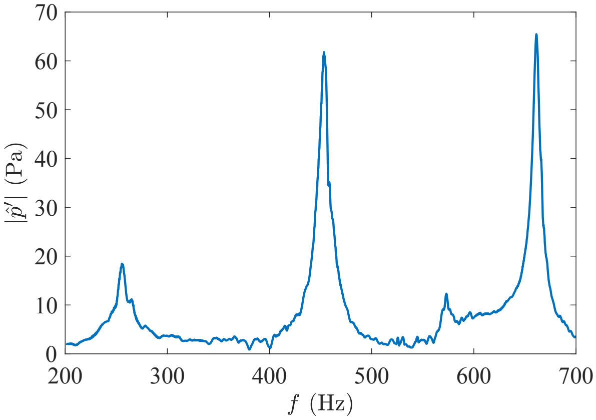

Figure 3.1: Amplitude of pressure fluctuations at $y = 0$ as a function of forcing frequency.

be at the nozzle exit plane, while $r = 0$ is at the nozzle centerline and follows the nozzle.

Figure 3.1 shows the response of the pressure in the enclosure at $y = 0$ when performing a frequency sweep. The sinusoidal speaker signals were varied over a range of frequencies while keeping the amplitude constant, and for each frequency the amplitude of the Fast Fourier Transform (FFT) centered at the speaker signal frequency was calculated. The frequency sweeps were performed with one speaker on each side of the enclosure, and *without* any resonance tubes attached to ensure that the signal where the frequencies were matching with the resonance frequencies of the tubes were not amplified compared to the other signals. In that way the pure response of the enclosure is obtained. The figure shows that the frequency spectrum of the enclosure has three peaks, at $f = 256$ Hz, $f = 453$ Hz and $f = 661$ Hz, corresponding to the 2nd, 4th and 6th transverse mode of the enclosure, respectively.

The two-microphone technique described in section 2.2 was used to investigate the excited modes of the enclosure. After comparing the wave shapes and spin ratios of the frequencies close to the three peaks from the frequency sweep in real-time in LabVIEW, it was decided to carry on doing experiments with the forcing frequencies $f = 250$ Hz, $f = 450$ Hz and $f = 655$ Hz. At these frequencies the amplitude of the pressure node was small relative to the anti-

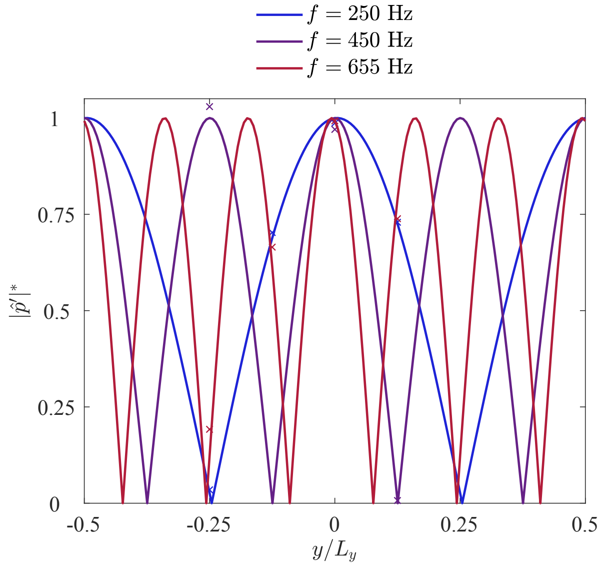

Figure 3.2: Pressure distribution in transverse direction y in the enclosure over its length L_y.

node, and the spin ratio defined in equation (1.48) was close to zero. The pressure distribution for these frequencies are shown in solid lines in figure 3.2 together with the measured pressure from the microphones marked by the symbol ×.

Figure 3.3 shows phase averaged acoustic velocity at the pressure node, and phase averaged acoustic pressure at the anti-node for forcing frequency $f = 450$ Hz, as a function of time. T is the period of the forcing cycle, $T = 1/f$. The acoustic velocity was calculated from the PIV measurements taken when the nozzle was positioned at the pressure node with zero mean flow, by averaging the transverse velocity of the upper half of the field of view. In this area the flow was seen not to be affected by the nozzle. The pressure was measured by a microphone placed in the enclosure wall, at the same x position as the speaker centers. The phase difference between the pressure and the velocity is 80.6°, a deviation of 9.4° or 0.058 ms from the theoretical value of 90° from equation (1.47). This is probably due to a time delay somewhere in the system. The start of the phase averaged forcing cycle, $t/T = 0$, is defined to be when the phase averaged acoustic pressure in the enclosure at the pressure anti-node is zero and

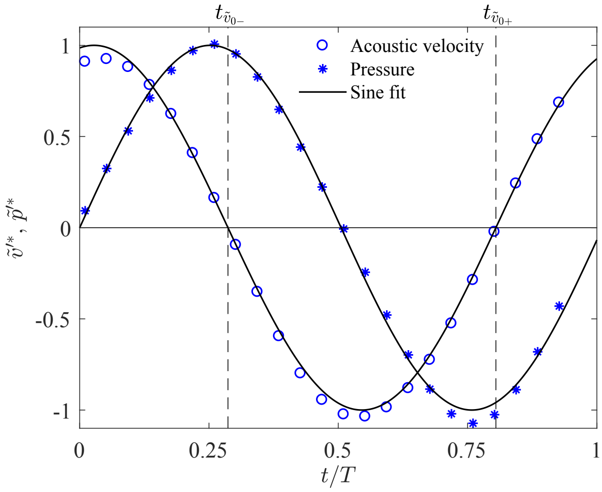

Figure 3.3: Phase averaged acoustic velocity at the pressure node and pressure at the anti-node in the enclosure, for $f = 450$ Hz. The velocity data are from PIV measurements with zero jet mean flow, see table 3.1.

rising, i.e. when $\tilde{p}'(y/\frac{\lambda}{4} = 0, t/T = 0) = 0$ and $\partial\tilde{p}'(y/\frac{\lambda}{4} = 0, t/T = 0)/\partial t > 0$. The dashed, vertical lines mark $t_{\tilde{v}0-}$ and $t_{\tilde{v}0+}$, which is defined to be when the transverse velocity changes direction to the left ($\tilde{v}' = 0$ and $\partial\tilde{v}'/\partial t < 0$) and to the right ($\tilde{v}' = 0$ and $\partial\tilde{v}'/\partial t > 0$), respectively. These definitions will be useful in chapter 4 and 5 when analyzing the jet development throughout the forcing cycle, and will then be measured at the center of the nozzle exit, $x = 0, r = 0$.

The acoustic response of the nozzle setup by longitudinal forcing was characterized by Aydemir *et al.* (2012) by performing a frequency sweep from $f = 0$ to 300 Hz. This showed resonance peaks at around $f = 40$ Hz, $f = 150$ Hz and $f = 260$ Hz. In this study the acoustic response was further characterized by placing the nozzle at $y = 0$, and performing hot-wire measurements at the nozzle exit together with pressure measurements for varying mass flows, forcing frequencies and forcing amplitudes. The pressure was recorded both in the enclosure at $y = 0$, and in the 35 mm diameter pipe upstream of the nozzle at $x = -160$ mm and $x = -360$ mm. The two-microphone technique gave the pressure distribution in the pipe, and from equation (1.56), (1.57) and (1.59), axial velocity fluctuations at the nozzle exit were obtained by approximating the nozzle as an abrupt area change from the 35 mm diameter pipe, to a 10 mm diameter pipe with $L_2 = 30$ mm length. In equation (1.59), 2δ from equation (1.55) was added to L_2 to account for end effects. Figure 3.4 shows that both the amplitude of the velocity fluctuations and its phase relative to the enclosure pressure using this approach is in good agreement with the hot-wire measurements, even though the two-microphone technique over-predicts the amplitudes for the second and third peak. This could be because the method assumes that the length of the converging part of the nozzle is acoustically compact ($kL_2 << 1$), which might not be valid for the highest frequencies. Figure 3.5 plots the amplitude and phase of the velocity fluctuation at the nozzle exit from hot-wire measurements for different nozzle exit velocities U_e. The amplitude is affected strongly by U_e. The largest effect is seen at $f = 250$ Hz, where the relative amplitude $|\hat{u}'|/U_e$ is decreased with a factor 6 and the absolute amplitude $|\hat{u}'|$ is halved from $U_e = 6.8$ to 18.9 m/s. Also the peaks at $f = 450$ Hz and $f = 655$ Hz decrease with higher U_e, but here the absolute fluctuations are increasing slightly with U_e. The frequency of the amplitude peaks coincides with the peaks in figure 3.1, but the relative magnitude between them are changed. The peak at the lowest frequency, $f \approx 256$ Hz, that has the lowest pressure amplitude in figure 3.1, is the largest in the velocity amplitude plot for all U_e. This is most probably due to the resonance frequency of the enclosure at $f = 250$ Hz being close to one of the resonance frequencies of the nozzle setup, $f = 260$ Hz, and therefore a lower pressure fluctuation is needed to create the same velocity fluctuation for this frequency.

U_e has a less pronounced effect on the phase, plotted in the the lower part of figure 3.5. Around $f = 260$ Hz, where the nozzle setup has a resonance frequency, the phase has a transition point for all U_e where it increases rapidly with frequency. Around $f = 260$ Hz, where the nozzle setup has a resonance frequency, the phase increases rapidly with frequency for all U_e, resulting in a phase shift of almost 180° from below to above the resonance frequency. This phase shift is more abrupt for lower U_e. For $f \gtrsim 300$ Hz the phase stays fairly constant at $250° - 280°$ except for two regions of lower phase angle around $f = 500 - 550$ Hz and $f = 620 - 650$ Hz. In the regions of constant phase angle, the value is slightly lower for higher U_e. For the three chosen frequencies $f = 250$ Hz, $f = 450$ Hz and $f = 655$ Hz, the phase angle is $\phi \approx 150°$, 270° and 240°, respectively. This phase is relative to the enclosure pressure, which is

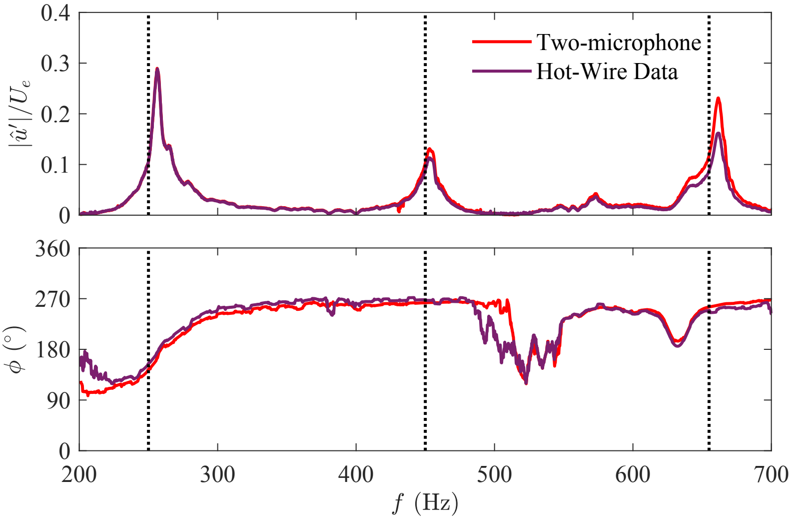

Figure 3.4: Amplitude and phase of velocity fluctuations at nozzle exit as function of forcing frequency for $U_e = 13.1$ m/s, from pressure and hot-wire measurements. The phase of the velocity is given relative to the phase of the enclosure pressure. The frequencies $f = 250$ Hz, $f = 450$ Hz and $f = 655$ Hz are marked in black, dotted lines.

90° out the phase of the transverse acoustic velocity in the enclosure, v'. The phase difference between u' and v' is therefore varying with forcing frequency, but stays approximately constant for different U_e.

The phase plots in figure 3.5 have similarities to the shape of the phase plots for the ideal Helmholtz resonator with mean flow given in figure 1.18. Also the effect of increasing the mean flow is similar to a Helmholtz resonator, with the amplitude of the velocity fluctuations being damped and the phase shift around the resonance frequency being smeared out and less pronounced. By using equation (1.61) with resonance frequency $\omega_0 = 2\pi \cdot 260$ Hz, neck length $l = 3$ cm with end correction 2δ from equation (1.55), and the external pressure fluctuations $\hat{p}'(\omega)$ taken from figure 3.1, we see from figure 3.6 that the nozzle setup can be well modeled as a Helmholtz resonator, even though the magnitude of the velocity fluctuations is under-predicted by the model. Also the phase deviates strongly around $f = 520$ Hz and $f = 630$ Hz. This could be because the nozzle setup has higher order modes outside the range of the frequency

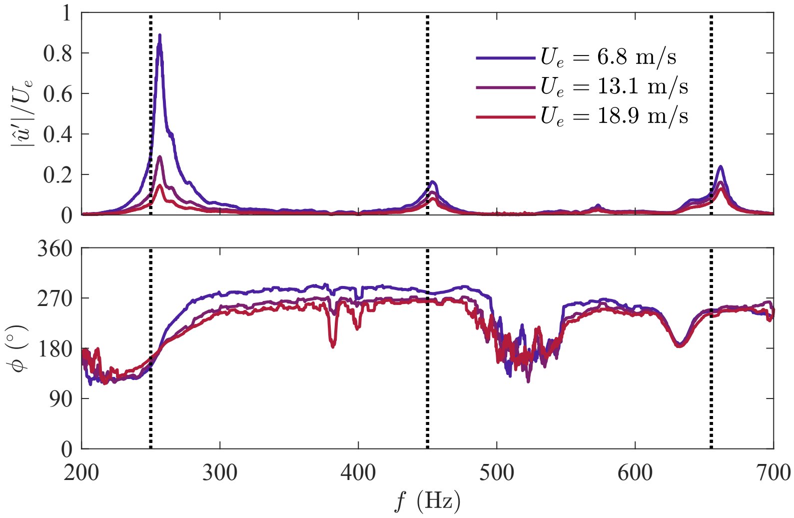

Figure 3.5: Amplitude and phase of velocity fluctuations at nozzle exit as function of forcing frequency for $U_e = 6.8$ m/s, $U_e = 13.1$ m/s and $U_e = 18.9$ m/s, from hot-wire measurements. The phase of the velocity is given relative to the phase of the enclosure pressure. The frequencies $f = 250$ Hz, $f = 450$ Hz and $f = 655$ Hz are marked in black, dotted lines.

sweep conducted by Aydemir *et al.* (2012), restricting the validity of the model when assuming a single resonance frequency at $f = 260$ Hz.

3.2 Flow characterization

Figure 3.7 shows that the forced flow response from hot-wire measurements at the nozzle exit for the jet positioned at $y = 0$, exhibits a nearly linear relationship between the RMS of the fluctuating part of the centerline axial exit velocity and the RMS of the pressure. Figure 3.8 shows the corresponding response of the phase averaged axial exit velocity over the forcing period. The figure shows an approximately sinusoidal behavior for low forcing amplitudes, while for the higher fluctuations the first part of the forcing cycle with high velocity becomes shorter than the part of low velocity. The horizontal axis starts at $t_{\tilde{u}0}$, which is defined to be when the fluctuating part of the phase averaged axial velocity at the jet exit is changing sign from negative to positive

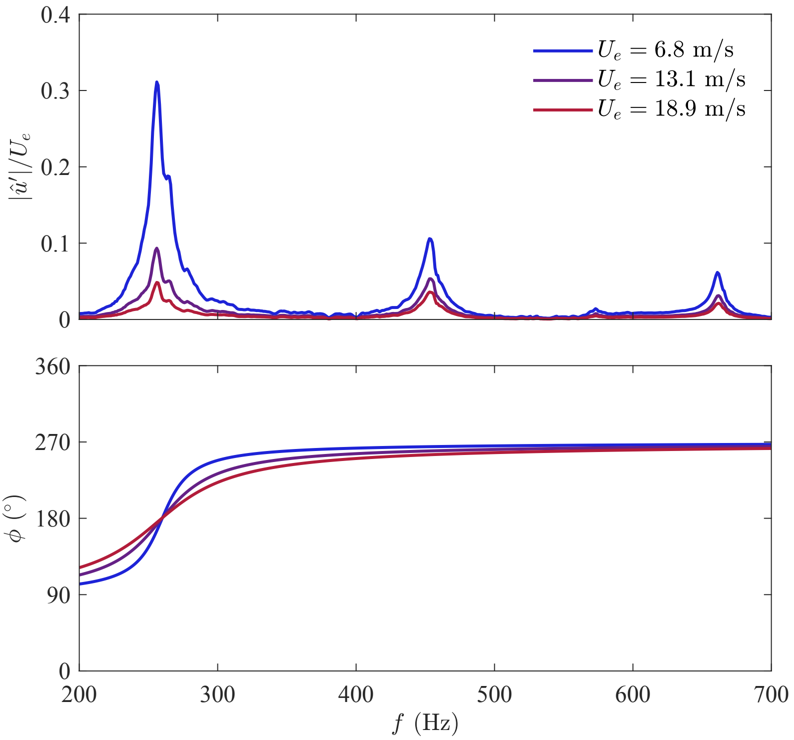

Figure 3.6: Amplitude and phase of velocity fluctuations at the exit of an ideal Helmholtz resonator as a function of forcing frequency, for $U_e = 6.8$ m/s, $U_e = 13.1$ m/s and $U_e = 18.9$ m/s. The phase of the velocity is given relative to the phase of the ambient pressure.

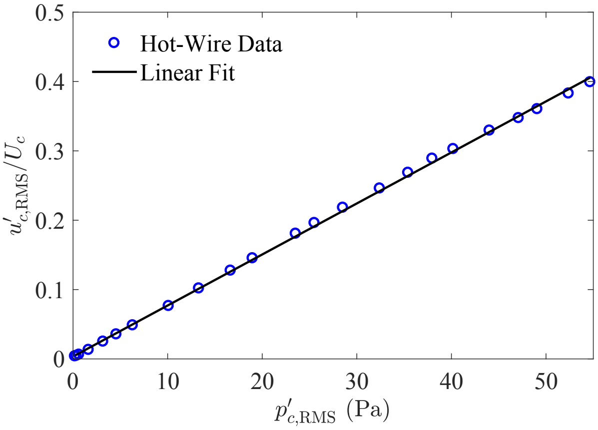

Figure 3.7: Axial velocity RMS as a function of pressure RMS, for $f = 260$ Hz, $U_c = 10$ m/s.

($\tilde{u}'(x = 0, r = 0) = 0$, $\partial\tilde{u}'(x = 0, r = 0)/\partial t > 0$). $t_{\tilde{u}_0}$ depends on the phase of the axial velocity fluctuations relative to the enclosure pressure, and varies therefore with frequency as shown in the lower part of figure 3.5.

Figure 3.9 plots $u'_{c,\mathrm{RMS}}/p'_{\mathrm{RMS}}$ obtained from hot-wire measurements as a function of U_e for $f = 260$ Hz together with the analytical solution for a Helmholtz resonator from equation (1.61). For high velocities, theory and measurements agree quite well, while deviations occur for velocities lower than $U_e \approx 10$ m/s. Here u'_{RMS}/U_e exceeds 40 %, and the assumption in the derivation of equation (1.61) of small perturbations in order to neglect higher order terms is clearly not valid. For the analytical solution we see that $u'_{\mathrm{RMS}} \sim 1/U_e$ for $f = 260$ Hz, and also for $f = 250$ Hz for velocities higher than $U_e \approx 10$ m/s. This is in agreement with equation (1.61) which gives $u'_{c,\mathrm{RMS}}/p'_{\mathrm{RMS}} \approx 1/\rho U_e$ for $\omega \approx \omega_0 = 2\pi \cdot 260$ Hz and $\omega_1/\omega_0 >> U_e/c$. The latter is satisfied in our case since $\omega_1/\omega_0 \approx 36$. $f = 450$ Hz and $f = 655$ Hz, however, are deviating too much from the resonance frequency ω_0. For these frequencies $u'_{c,\mathrm{RMS}}/p'_{\mathrm{RMS}}$ is almost independent of U_e in the velocity range we are investigating in this study.

Table 3.1 shows the experimental conditions for the PIV measurements conducted in this study. For the cases when the jet is moved transversely and subjected to different positions in the acoustic wave, the nozzle position rela-

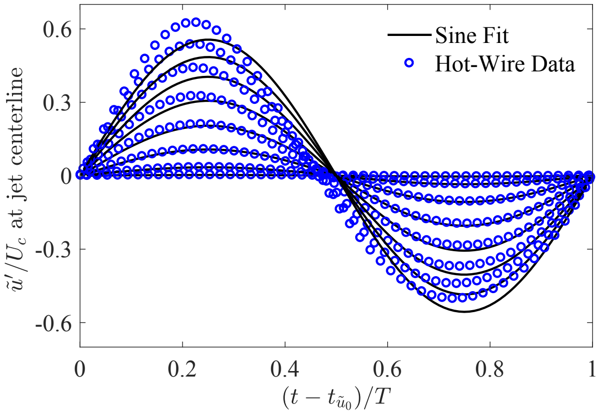

Figure 3.8: Response of the phase averaged axial exit velocity over the forcing period, for $f = 260$ Hz, $U_c = 10$ m/s.

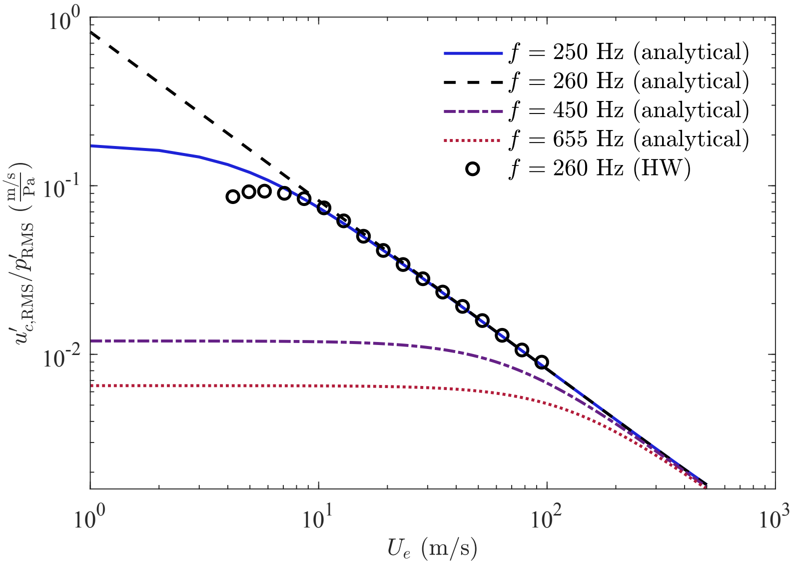

Figure 3.9: $u'_{c,\mathrm{RMS}}/p'_{\mathrm{RMS}}$ as a function of U_e for hot-wire measurements together with the solution for an ideal Helmholtz resonator, equation (1.61).

tive to the acoustic wave is given as its centerline y coordinate normalized by the distance between the pressure anti-node and the the pressure node, $\lambda/4$. The position of the nozzle is therefore given as a number between 0 and 1, where $y = 0$ denotes the pressure anti-node and $y/\frac{\lambda}{4} = 1$ denotes the pressure node. For these cases the Strouhal number were kept approximately constant while varying the forcing frequency. This was done to scale the vortex ring separation distance to be the same for the pressure anti-node position cases. For longitudinally forced, pulsed jets, described in section 1.2.4, the forcing amplitude is normally measured as the axial fluctuations of velocity relative to the mean velocity. In this study it was chosen to use the same measure for the pressure anti-node position, which has many similarities to longitudinal forcing. This is however not a feasible measure of the forcing when the jet is moved towards the pressure node and the axial velocity fluctuations goes towards zero. It was therefore chosen to measure the forcing amplitude as RMS of the axial velocity fluctuations the jet would experience *if* it was positioned in the pressure anti-node of the same standing wave. This is denoted $u'_{\mathrm{AN,RMS}}/U_e$. In practice this was done by calibrating the jet forcing amplitude u'_{RMS}/U_e when positioned at the pressure anti-node against the pressure fluctuations in the enclosure at the same position for the different combinations of jet velocities U_e and forcing frequencies. Then, for the other jet positions, the speaker signal was tuned to set the pressure fluctuations at the anti-node to what, according to the calibration, was needed to obtain the wanted $u'_{\mathrm{AN,RMS}}/U_e$ when the jet was placed at the pressure anti-node.

Figure 3.10 shows that the exit velocity profile for the unforced jet for different velocities approximates a top hat profile, even though the PIV measurements cannot fully resolve the high gradients at the shear-layer of the jet. This is in agreement with previous work on the same nozzle (Aydemir *et al.*, 2012; Lawson & Dawson, 2013). The velocity profiles were integrated over the circular nozzle exit, to obtain the time averaged volume flow of the jet. When comparing this with the volume flow set by the mass flow controller, the deviation was less than 3%.

The mean axial velocity field of the unforced jet is shown in figure 3.11 for different U_e. The boundary of the potential core is plotted in black and is

Table 3.1: List of experimental conditions for the PIV measurements

Case	f (Hz)	U_e (m/s)	Re_D	Jet position $y/\frac{\lambda}{4}$					$u'_{\mathrm{AN,RMS}}/U_e(\%)$	St_D
				0	0.25	0.5	0.75	1		
No forcing	-	6.8	4 533						-	-
	-	13.1	8 733						-	-
	-	18.9	12 600						-	-
No mean flow	450	0	-	×	×	×	×	×	25[a]	-
Anti-node	250	6.8	4 533	×					5, 15, 25	0.3676
	450	13.1	8 733	×					5, 15, 25	0.3435
	655	18.9	12 600	×					5, 15, 25	0.3466
Node	250	6.8	4 533					×	5, 15, 25, 50, 100	0.3676
	250	13.1	8 733					×	5, 15, 25	0.1908
	250	18.9	12 600					×	5, 15, 25	0.1323
	450	6.8	4 533					×	5, 15, 25	0.6618
	450	13.1	8 733					×	5, 15, 25	0.3435
	450	18.9	12 600					×	5, 15, 25	0.2381
	655	6.8	4 533					×	5, 15, 25	0.9632
	655	13.1	8 733					×	5, 15, 25	0.5000
	655	18.9	12 600					×	5, 15, 25	0.3466
Varying position	250	6.8	4 533	×	×	×	×	×	25	0.3676
	450	13.1	8 733	×	×	×	×	×	5, 25	0.3435
	655	18.9	12 600	×	×	×	×	×	25	0.3466

---

[a] In percent of 13.1 m/s

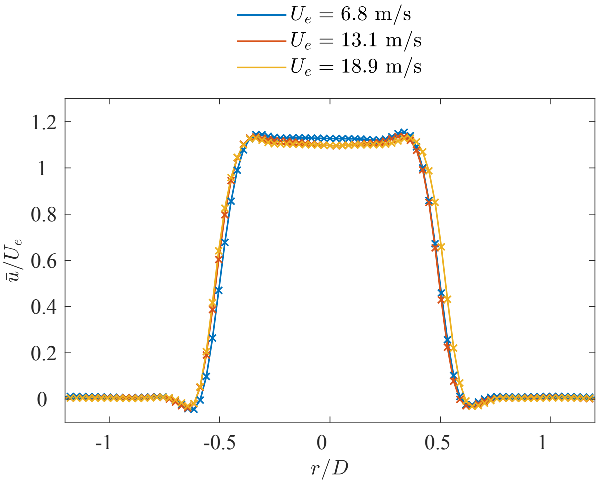

Figure 3.10: Unforced jet exit profiles for different velocities, from PIV measurements.

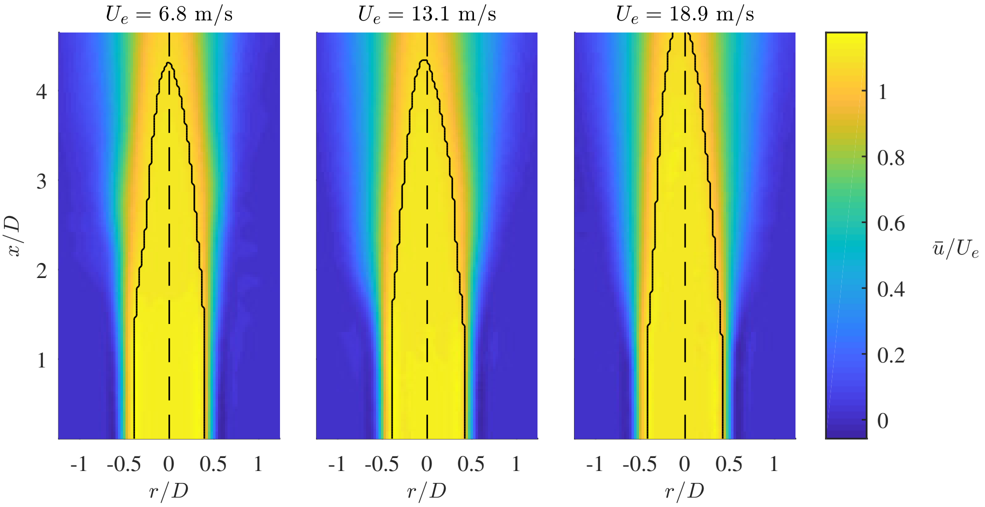

Figure 3.11: Temporal mean of axial velocity component of the unforced jet normalized by the exit velocities U_e, for $U_e = 6.8$ m/s, $U_e = 13.1$ m/s and $U_e = 18.9$ m/s. The potential core boundary is plotted in solid, black lines and $r/D = 0$ is marked with dashed, black lines.

defined as the area where the velocity is greater than 95 % of the centerline exit velocity, U_c. The jet exhibits approximately the same symmetric shape for all U_e, even though the potential core is slightly longer for $U_e = 18.9$ m/s. Figure 3.12 shows the RMS fields of the axial and transverse velocity components of the unforced jet for the same cases, and also these fields are symmetric. For all U_e, both u'_{RMS} and v'_{RMS} stays close to zero for about one diameter downstream of the nozzle exit, but this distance is slightly decreasing for higher velocities. The shear-layers, that further downstream can be identified as areas of high RMS values around $r = \pm 0.5$, become thinner for higher U_e. The effect of Re_D on the potential core length is also seen in these plots by the extended quiescent region along $r = 0$. In addition, the RMS values in the shear-layer relative to U_e decreases slightly with increased velocity.

For the remaining part of this chapter some initial investigation of the jet when subjected to different positions in the standing acoustic wave, from the pressure anti-node at $y/\frac{\lambda}{4} = 0$ to the pressure node at $y/\frac{\lambda}{4} = 1$, is presented. Figure 3.13 shows the mean fields of the axial velocity components of the forced jet. Each column shows different jet positions, while each row shows different forcing frequencies and exit velocities while the Strouhal number is kept constant for all cases. For forcing frequency $f = 250$ Hz, which corresponds to the 2nd transverse mode in the jet enclosure, the velocity field does not change particularly for the different jet positions and the jet stays close to axisymmetric. The potential core boundary plotted in black, however, indicates that the core length increases as the jet moves towards the node. For $f = 450$ Hz and $f = 655$ Hz, the jet position has a larger impact on the velocity field. The jet is axisymmetric at $y/\frac{\lambda}{4} = 0$ and $y/\frac{\lambda}{4} = 1$, but this symmetry is clearly broken at the other positions and is most pronounced at $y/\frac{\lambda}{4} = 0.5$. The asymmetry is shown by the potential core bending towards the pressure anti-node, and further downstream by the bending of the high velocity region of the jet towards the node. For $f = 655$ Hz the potential core length, as for the $f = 250$ Hz case, increases from $y/\frac{\lambda}{4} = 0$ to $y/\frac{\lambda}{4} = 1$, but this is not seen for $f = 450$ Hz. Compared to the unforced jet, the potential core is shorter for all forced jet cases. For all frequencies it is also clear that the shear-layer thickness increases in the near-field as the jet is moved from $y/\frac{\lambda}{4} = 0$ to $y/\frac{\lambda}{4} = 1$, but this is also more pronounced for the higher forcing frequencies.

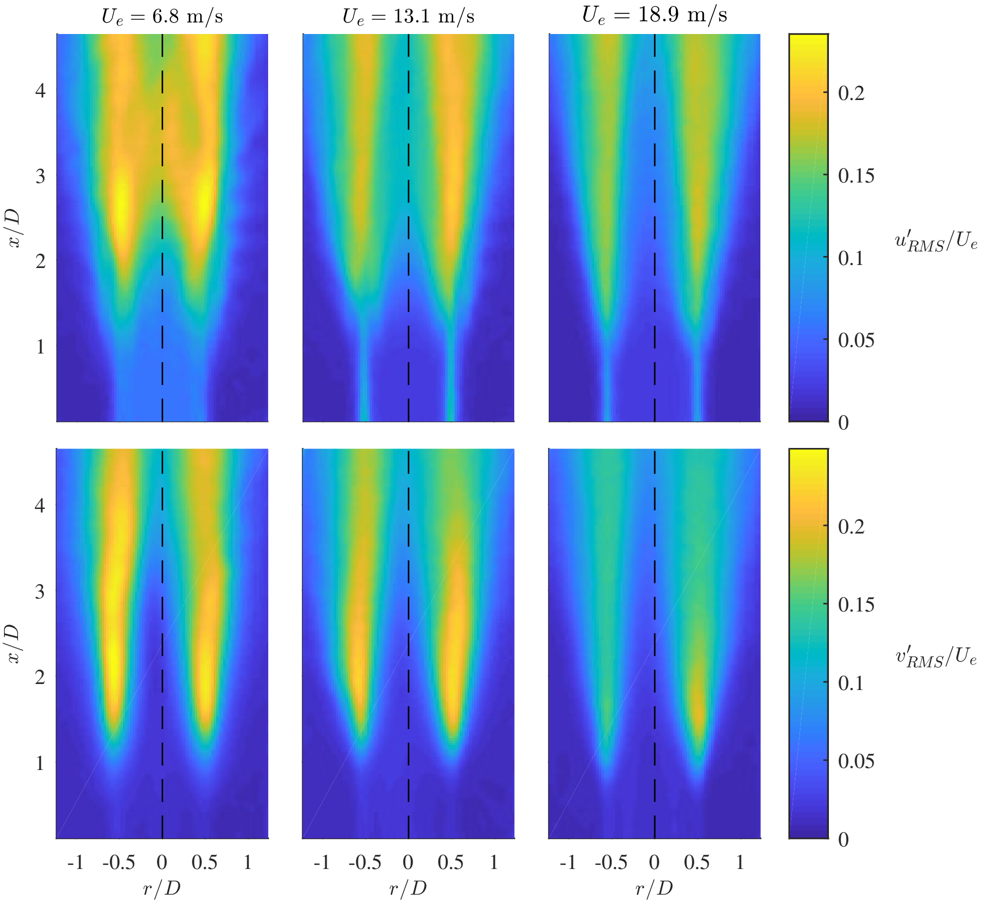

Figure 3.12: RMS of axial and transverse velocity components of the unforced jet normalized by the exit velocities U_e, for $U_e = 6.8$ m/s, $U_e = 13.1$ m/s and $U_e = 18.9$ m/s. $r/D = 0$ is marked with dashed, black lines.

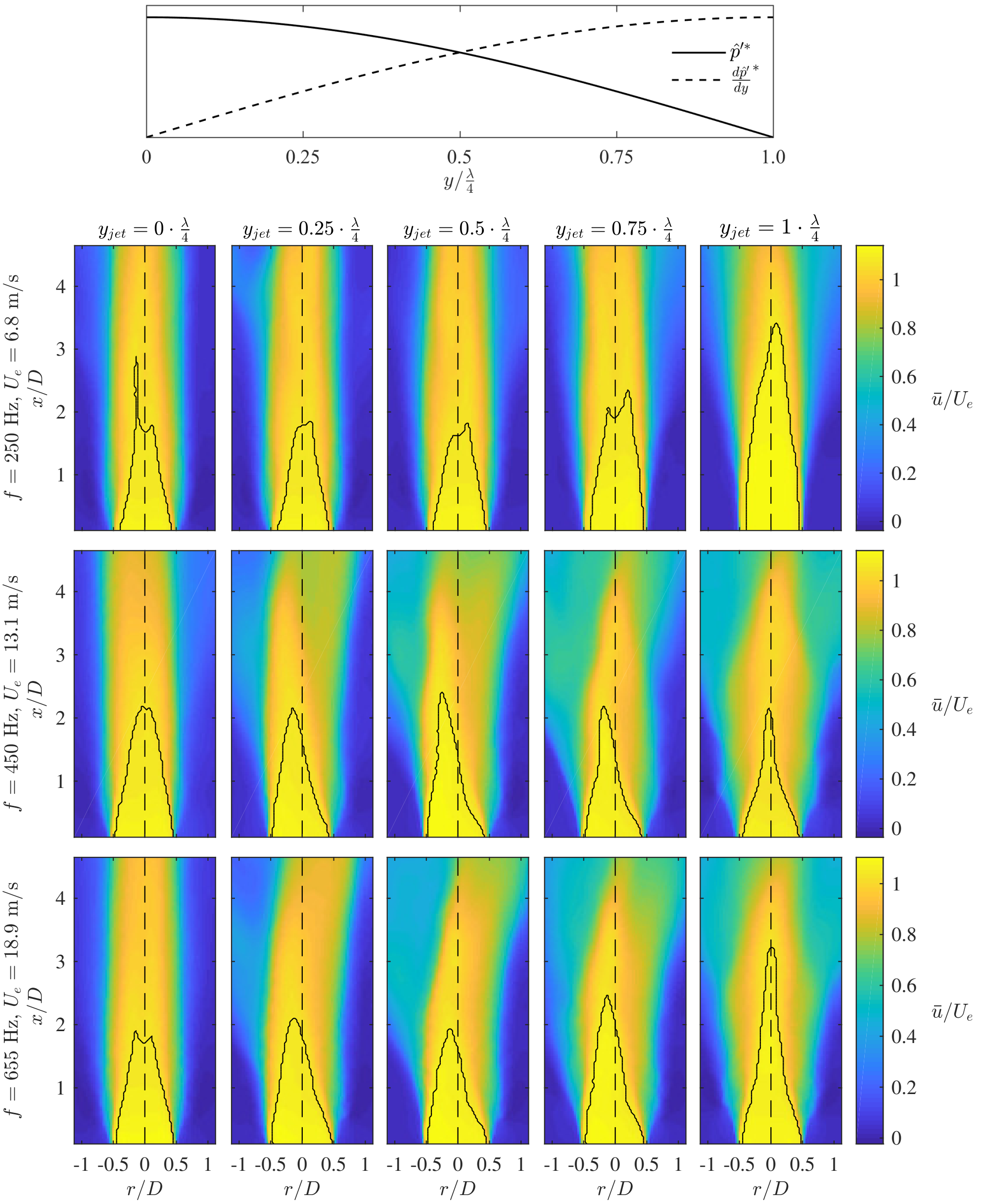

Figure 3.13: Temporal mean of axial velocity component normalized by exit velocity U_e for varying jet positions, forcing frequencies and exit velocities. The potential core boundary is plotted in solid, black lines and $r/D = 0$ is marked with dashed, black lines. Above the velocity fields the theoretical pressure wave in the enclosure is sketched.

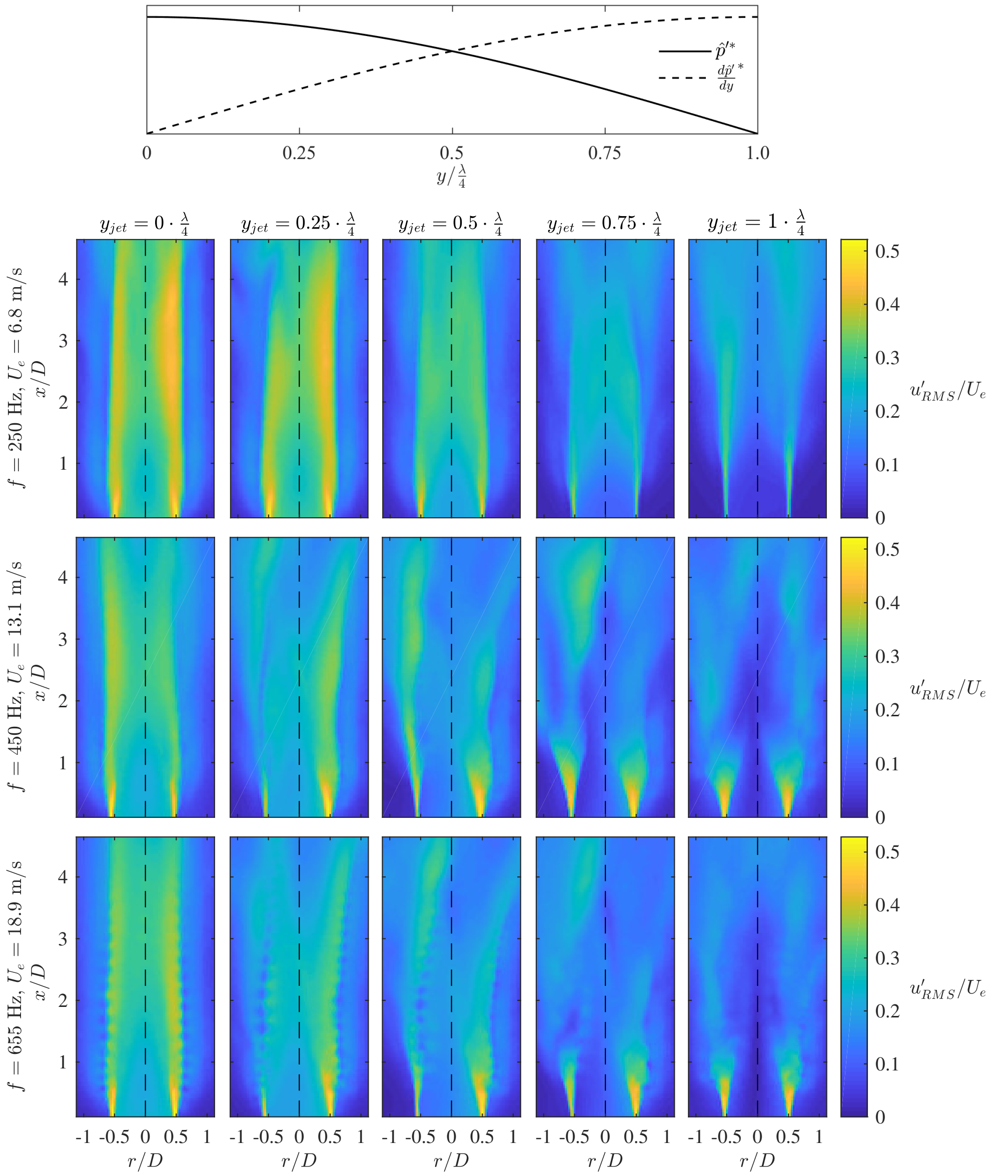

Figure 3.14: RMS of axial velocity component normalized by U_e for varying jet positions, forcing frequencies and exit velocities. Above the RMS fields the theoretical pressure wave in the enclosure is sketched.

Figure 3.14 and 3.15 show RMS fields for the different jet positions[a]. The RMS fields for the jet positioned at $y/\frac{\lambda}{4} = 0$ has a similar shape as the unforced jet, with high RMS magnitudes at the shear-layer. For the forced jet, however, these high magnitude regions appear already at the nozzle exit for the axial component and shortly after the exit for the transverse component, and the magnitude then stays fairly constant in the shear-layers throughout the whole field of view. By moving the jet away from the pressure anti-node for $f = 250$ Hz, the RMS magnitude drops for both components. For the other two forcing frequences, $f = 450$ Hz and $f = 655$ Hz, u'_{RMS} decreases quickly downstream for the positions away from the pressure anti-node, and at $y/\frac{\lambda}{4} = 0.75$ and $y/\frac{\lambda}{4} = 1$ it is close to zero already one diameter downstream of the nozzle exit. For v'_{RMS} the high magnitude regions are still more or less coherent through the whole field of view for $y/\frac{\lambda}{4} = 0.25$, while for $y/\frac{\lambda}{4} = 0.5$, and especially for $y/\frac{\lambda}{4} = 0.75$ and $y/\frac{\lambda}{4} = 1$, the v'_{RMS} field consist of separated spots of high RMS magnitude, with areas of low RMS magnitude in between. A similar pattern was reported by O'Connor & Lieuwen (2012a) for both nonreacting and reacting flow experiments on an annular jet positioned in the pressure node (see figure 1.21). The pattern is a result of interference between the transverse velocity fluctuations directly from the acoustic waves, and velocity fluctuations induced by the vortices. The RMS fields for $f = 450$ Hz and $f = 655$ Hz are asymmetric for the jet positions in between the anti-node and the node, as was also seen for the time averaged velocity fields. At these jet positions the shear-layer seems to bend to the right towards the end of the field of view.

To investigate the velocity fluctuations close to the nozzle exit in detail, profiles of the RMS of the phase averaged velocity for the different jet positions are plotted in figure 3.16. In this regard, the choice of axial position of the RMS profiles is significant. This is shown in figure 3.17, where an example of RMS of axial and transverse fluctuations are plotted against axial position along $r = 0$. While the RMS of axial fluctuations are nearly constant for the first 2-3 diameters downstream of the nozzle exit, the RMS of transverse velocity fluctuations has an oscillating development downstream. The position of the

---

[a] In some of the fields on the lower row ($f = 655$ Hz), ripples of size in the order of $0.1D$ are visible. This is most probably a processing issue due to the low temporal resolution of 8 frames per forcing period for this frequency.

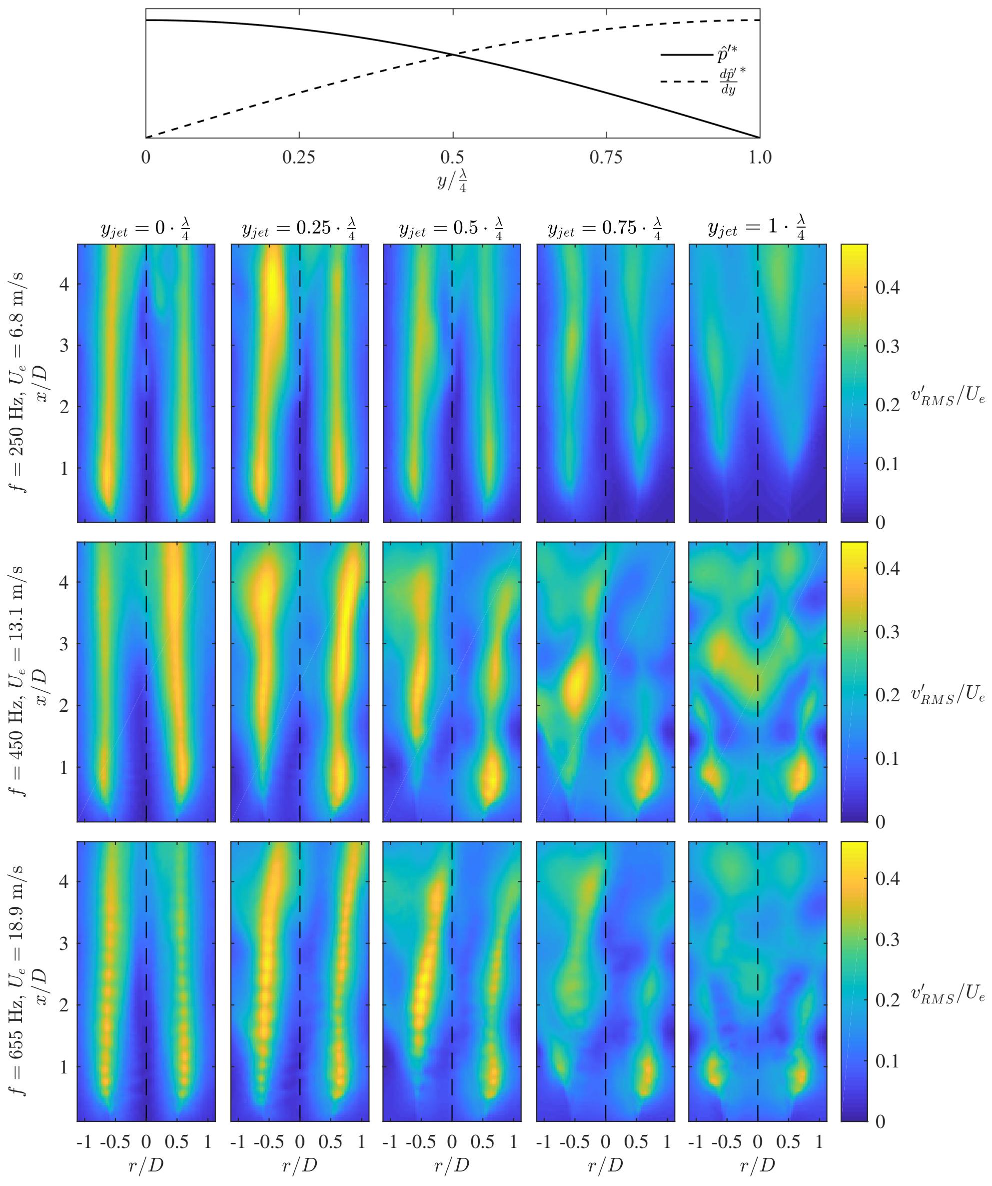

Figure 3.15: RMS of transverse velocity component normalized by U_e for varying jet positions, forcing frequencies and exit velocities. Above the RMS fields the theoretical pressure wave in the enclosure is sketched.

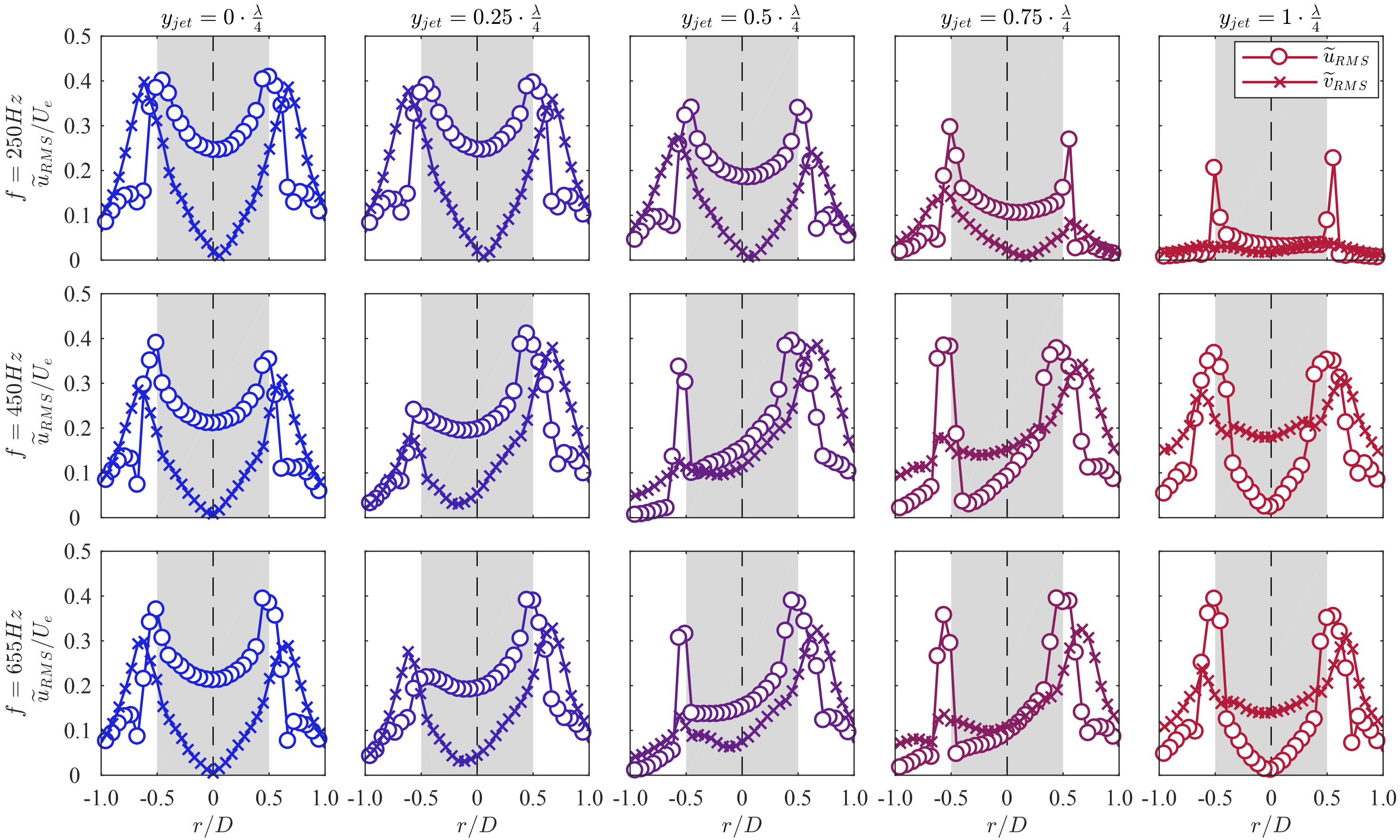

Figure 3.16: RMS profiles for the phase averaged axial and transverse velocity components at $x/D = 0.6$ for $u'_{\mathrm{AN,RMS}}/U_e = 0.25$, for varying jet positions, forcing frequencies and exit velocities.

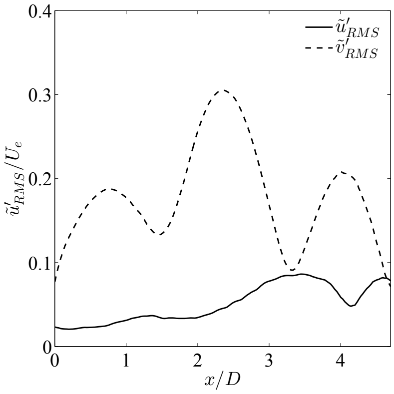

Figure 3.17: RMS of the phase averaged axial and transverse velocity components as a function of axial position at $r = 0$ for $f = 450$ Hz, $U_e = 13.1$ m/s and $y/\frac{\lambda}{4} = 1$.

maxima change with Strouhal number, but not significantly with jet position. For $St \approx 0.3$ the first maximum is located at $x/D \approx 0.6$, and is where the RMS profiles presented here are taken. The RMS profiles in figure 3.16 show axisymmetry for $y/\frac{\lambda}{4} = 0$ and $y/\frac{\lambda}{4} = 1$. All the RMS profiles have a local maximum at the shear-layer and a local minimum close to the centerline of the jet. For the two highest frequencies at the jet positions $y/\frac{\lambda}{4} = 0.25$, $y/\frac{\lambda}{4} = 0.5$ and $y/\frac{\lambda}{4} = 0.75$, the RMS values for both the axial and transverse velocity components are larger on the half of the jet facing the pressure node compared to the half facing the anti-node. For these cases the position of the local minimum is also shifted towards the anti-node. This is in contrast to $f = 250$ Hz, where the differences in RMS values for the two sides are much smaller, and $y/\frac{\lambda}{4} = 0.75$ is the only position where the RMS profiles are clearly asymmetric. For this case the RMS values are slightly larger at the left hand side compared to the right hand side, and the local minimum is shifted slightly towards the node.

There are several similarities between the RMS profiles for $y/\frac{\lambda}{4} = 0$ and $y/\frac{\lambda}{4} = 1$ for the two highest forcing frequencies in figure 3.16. For both of the jet positions the RMS profiles are symmetric, and at the shear-layers the axial and transverse velocity components are of the same order of magnitude. The main difference lays in the value at the nozzle centerline. While $\tilde{v}'_{\mathrm{RMS}}(r/D = 0)$

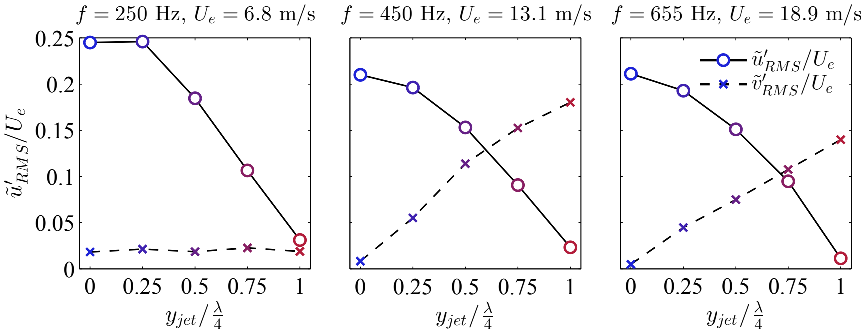

Figure 3.18: Velocity RMS at jet centerline at $x/D = 0.6$ as a function of jet position, for $u'_{\mathrm{AN,RMS}}/U_e = 0.25$.

is approximately zero and $\tilde{u}'_{\mathrm{RMS}}(r/D = 0)$ clearly non-zero at $y/\frac{\lambda}{4} = 0$, the opposite is true at $y/\frac{\lambda}{4} = 1$. In figure 3.18, $\tilde{u}'_{\mathrm{RMS}}$ and $\tilde{v}'_{\mathrm{RMS}}$ at $r/D = 0$ are plotted as function of jet position for the different forcing frequencies. $\tilde{u}'_{\mathrm{RMS}}$ decreases from its maximum at $y/\frac{\lambda}{4} = 0$ towards zero at $y/\frac{\lambda}{4} = 1$. Except for $f = 250$ Hz, $\tilde{v}'_{\mathrm{RMS}}$ behaves the opposite way by going from approximately zero at $y/\frac{\lambda}{4} = 0$ to a maximum at $y/\frac{\lambda}{4} = 1$. This behavior of $\tilde{u}'_{\mathrm{RMS}}$ and $\tilde{v}'_{\mathrm{RMS}}$ is expected as $\tilde{u}'_{\mathrm{RMS}}$ scale linearly with the pressure fluctuations (as shown in figure 3.7), while $\tilde{v}'_{\mathrm{RMS}}$ scale with the acoustic velocity in the enclosure, that again scale with the pressure gradient[b]. For $f = 250$ Hz, however, the value of $\tilde{v}'_{\mathrm{RMS}}$ stays approximately zero at $r/D = 0$ for all jet positions. This can be explained by the acoustic properties of the nozzle setup, which in section 3.1 was shown to be similar to a Helmholtz resonator. The nozzle setup has a resonance frequency at 260 Hz, which is much closer to $f = 250$ Hz than $f = 450$ Hz and $f = 655$ Hz. This also means that the amplitude of the pressure fluctuations in the jet enclosure needed to achieve the same axial velocity fluctuations at the nozzle exit at $y/\frac{\lambda}{4} = 0$ is varying with orders of magnitudes between the forcing frequencies, as seen by comparing figure 3.1 and 3.5. The transverse velocity fluctuations on the other hand is not a property of the nozzle setup, but is directly related to the pressure fluctuation in the enclosure. Since the amplitude of the pressure fluctuations is much smaller in the enclosure for $f = 250$ Hz

---

[b] The acoustic velocity can be seen to scale with the pressure gradient from equation (1.47). For a standing wave with $p'_{\mathrm{RMS}} \sim \cos(ky)$ and $v'_{\mathrm{RMS}} \sim \sin(ky)$, we have $\partial p'_{\mathrm{RMS}}/\partial y \sim \sin(ky)$, and therefore $v'_{\mathrm{RMS}} \sim \partial p'_{\mathrm{RMS}}/\partial y$.

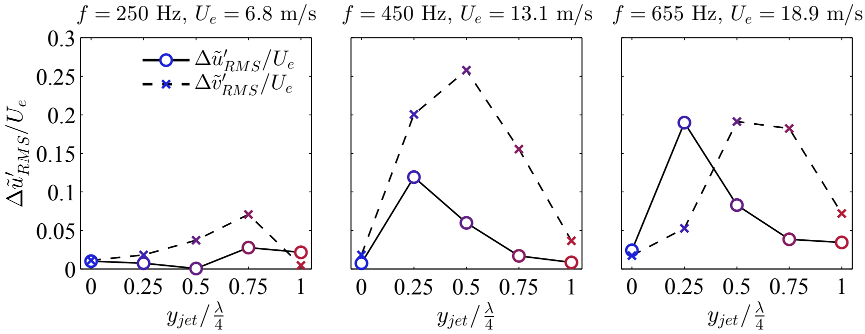

Figure 3.19: Difference in velocity RMS between the left and the right hand side shear-layer at $x/D = 0.6$ as a function of jet position, for $u'_{\text{AN,RMS}}/U_e = 0.25$.

compared to the other frequencies for a given $u'_{\text{AN,RMS}}/U_e$, also the transverse velocity fluctuations are much smaller.

To analyze the asymmetry in the RMS profiles in figure 3.16, the RMS values on the two sides of the jet are compared in figure 3.19 by plotting the absolute value of the difference between the maximum RMS value on each side of $r = 0$. For $f = 250$ Hz the peak in asymmetry is at jet position $y/\frac{\lambda}{4} = 0.75$, and the difference in v'_{RMS} at this position is the only value that exceeds 5 % of the exit velocity U_e. For the two higher frequencies the peak in RMS difference is found at $y/\frac{\lambda}{4} = 0.25$ for u'_{RMS}, and at $y/\frac{\lambda}{4} = 0.5$ for v'_{RMS}. The shapes of $\Delta u'_{\text{RMS}}$ and $\Delta v'_{\text{RMS}}$ are similar for $f = 450$ Hz and $f = 655$ Hz, but while the peak in RMS difference is about twice as high in value for u'_{RMS} compared to v'_{RMS} for $f = 450$ Hz, these peaks have similar values for $f = 655$ Hz.

Lespinasse *et al.* (2013) introduced the flow intensity or the energy flux density as a measure of the asymmetry of the jet. This acoustic quantity is defined in equation (1.50), and the plot in figure 1.16 shows that it is zero at $y/\frac{\lambda}{4} = 0$ and $y/\frac{\lambda}{4} = 1$ and has a maximum at $y/\frac{\lambda}{4} = 0.5$. Since the energy flux density is the product of the pressure fluctuations and the transverse velocity fluctuations, the product $\tilde{u}'_{\text{RMS}} \cdot \tilde{v}'_{\text{RMS}}$ should scale with the energy flux density, since $\tilde{u}'_{\text{RMS}} \sim \tilde{p}'_{\text{RMS}}$. Figure 3.20 shows that for the two highest frequencies, $\tilde{u}'_{\text{RMS}} \cdot \tilde{v}'_{\text{RMS}}$ at $r = 0$ has a similar shape as the energy flux density and that it can be a good measure of the asymmetry of the jet RMS profiles. For $f = 250$

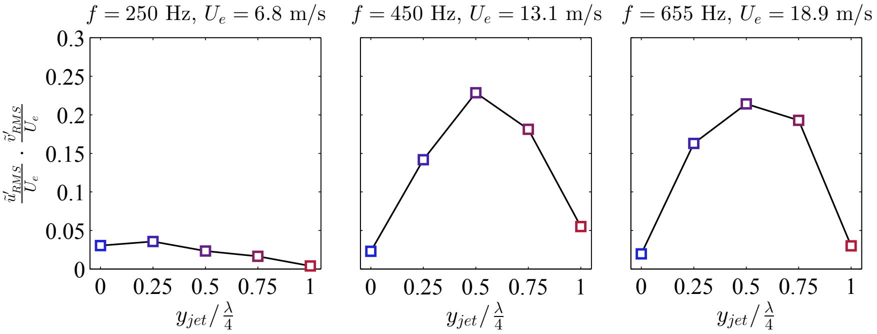

Figure 3.20: $\tilde{u}'_{\mathrm{RMS}} \cdot \tilde{v}'_{\mathrm{RMS}}$ at jet centerline at $x/D = 0.6$ as a function of jet position, for $u'_{\mathrm{AN,RMS}}/U_e = 0.25$.

Hz, however, the shape of $\tilde{u}'_{\mathrm{RMS}} \cdot \tilde{v}'_{\mathrm{RMS}}$ does not agree with the theoretical shape of the energy flux density shown in figure 1.16. Any dependency between the asymmetry of the RMS profiles and $\tilde{u}'_{\mathrm{RMS}} \cdot \tilde{v}'_{\mathrm{RMS}}$ for this frequency is hard to deduce since both are small and does not change particularly with jet position.

Figure 3.21-3.23 shows the jet centerline for different jet positions, forcing frequencies and jet exit velocities. The jet centerline is defined at every axial position as the position in transverse direction where the two-dimensional volume flow is equal on both sides:

$$\int_{-\infty}^{r_c} \tilde{u} dr = \int_{r_c}^{\infty} \tilde{u} dr \tag{3.1}$$

In the figures, the centerline of the phase averaged data is colored by the phase in the forcing cycle. The thick, black line shows the time averaged position of the centerline. For the lowest frequency, independent of jet position, the centerline is barely moving away from $r/D = 0$ over the forcing cycle. For the higher frequencies, however, the centerline has transverse fluctuations of significant amplitude for all jet positions except at $y/\frac{\lambda}{4} = 0$. At $y/\frac{\lambda}{4} = 0.25$, $y/\frac{\lambda}{4} = 0.5$ and $y/\frac{\lambda}{4} = 0.75$, the jet is bending first towards the pressure anti-node and then towards the node further downstream, the same behavior as was seen from the velocity and RMS fields. This is similar to what Lespinasse *et al.* (2013) observed, although they did not see the initial bending away from the pressure node. At $y/\frac{\lambda}{4} = 1$, the time averaged centerline is again close to $r = 0$, while

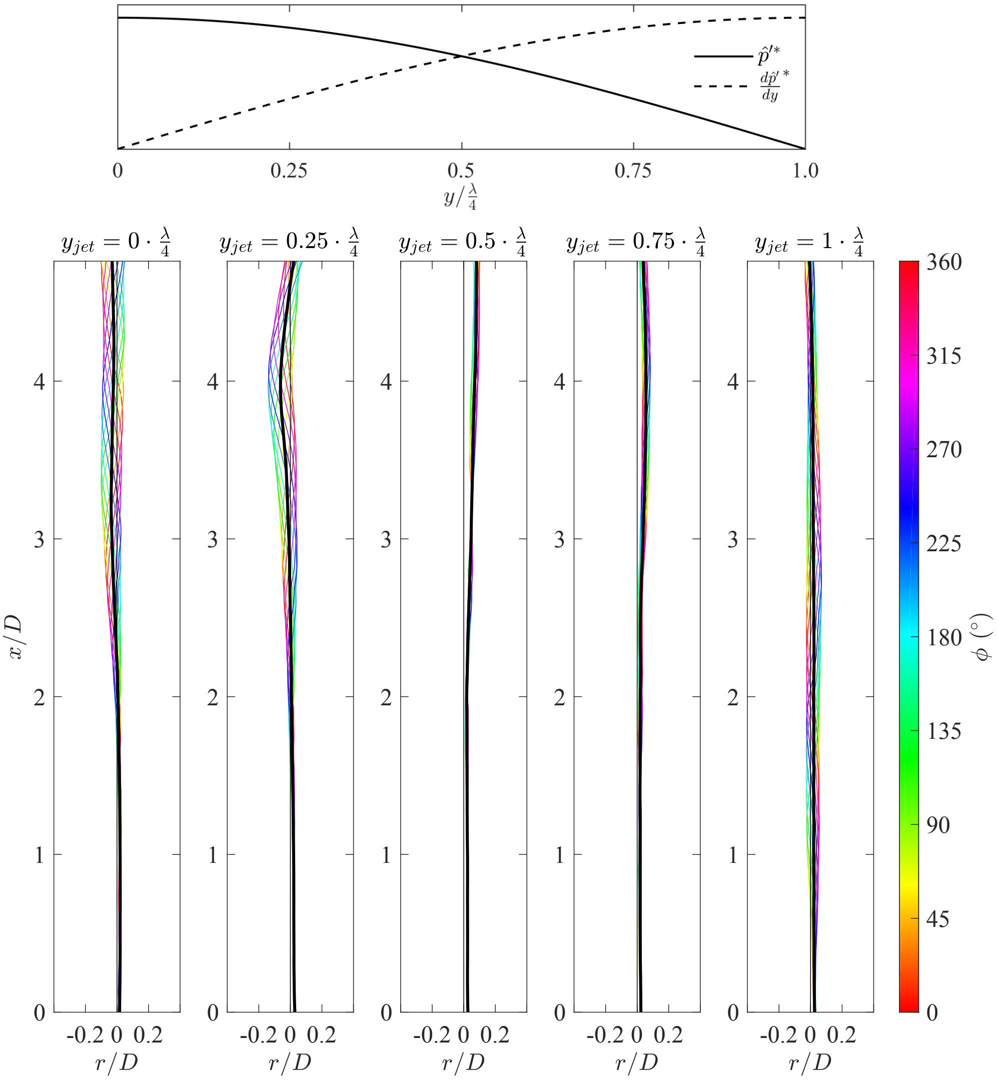

Figure 3.21: Radial position of the jet centerline for $f = 250$ Hz and $U_e = 6.8$ m/s. Phase averaged centerlines are colored by phase in the forcing cycle, and the thick, black lines show the time averaged position of the centerline. Above the centerlines, the theoretical pressure wave in the enclosure is sketched.

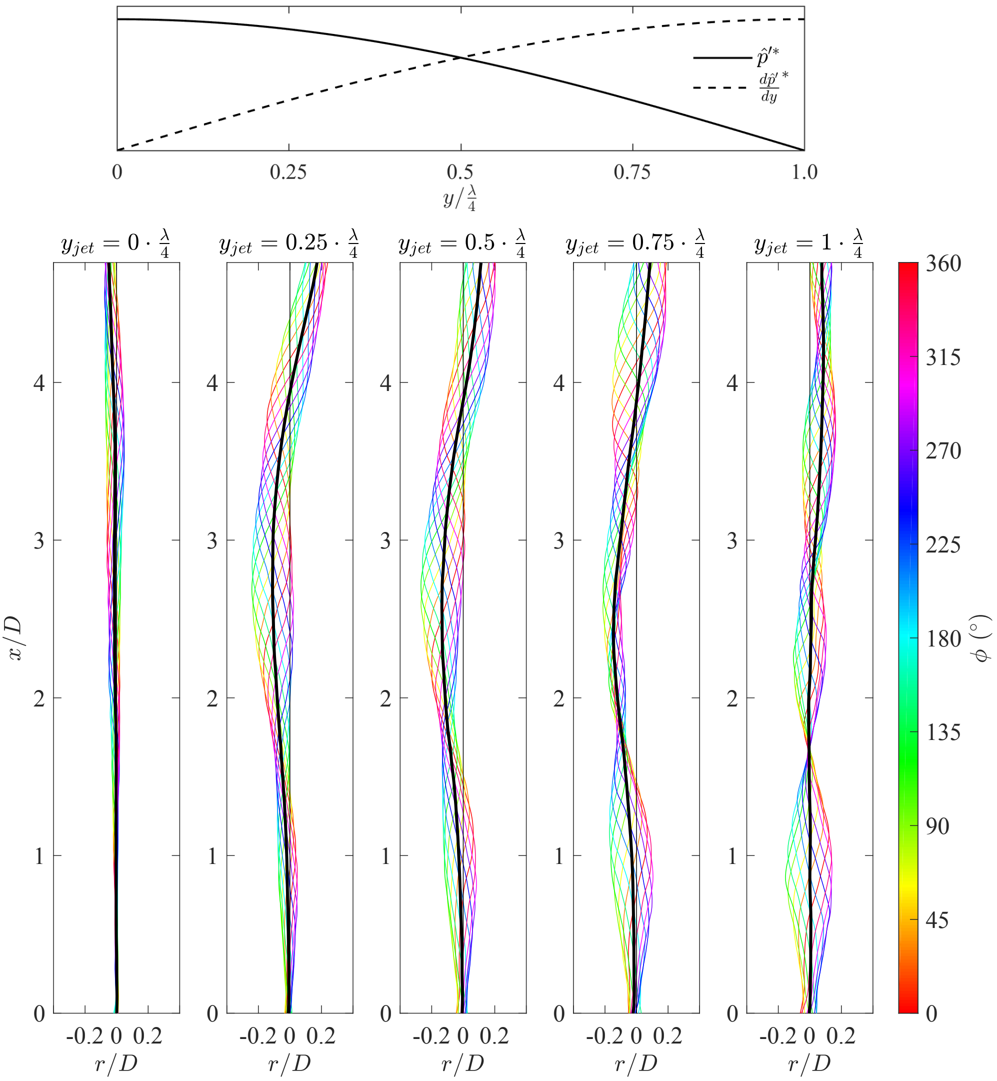

Figure 3.22: Radial position of the jet centerline for $f = 450$ Hz and $U_e = 13.1$ m/s. Phase averaged centerlines are colored by phase in the forcing cycle, and the thick, black lines show the time averaged position of the centerline. Above the centerlines, the theoretical pressure wave in the enclosure is sketched.

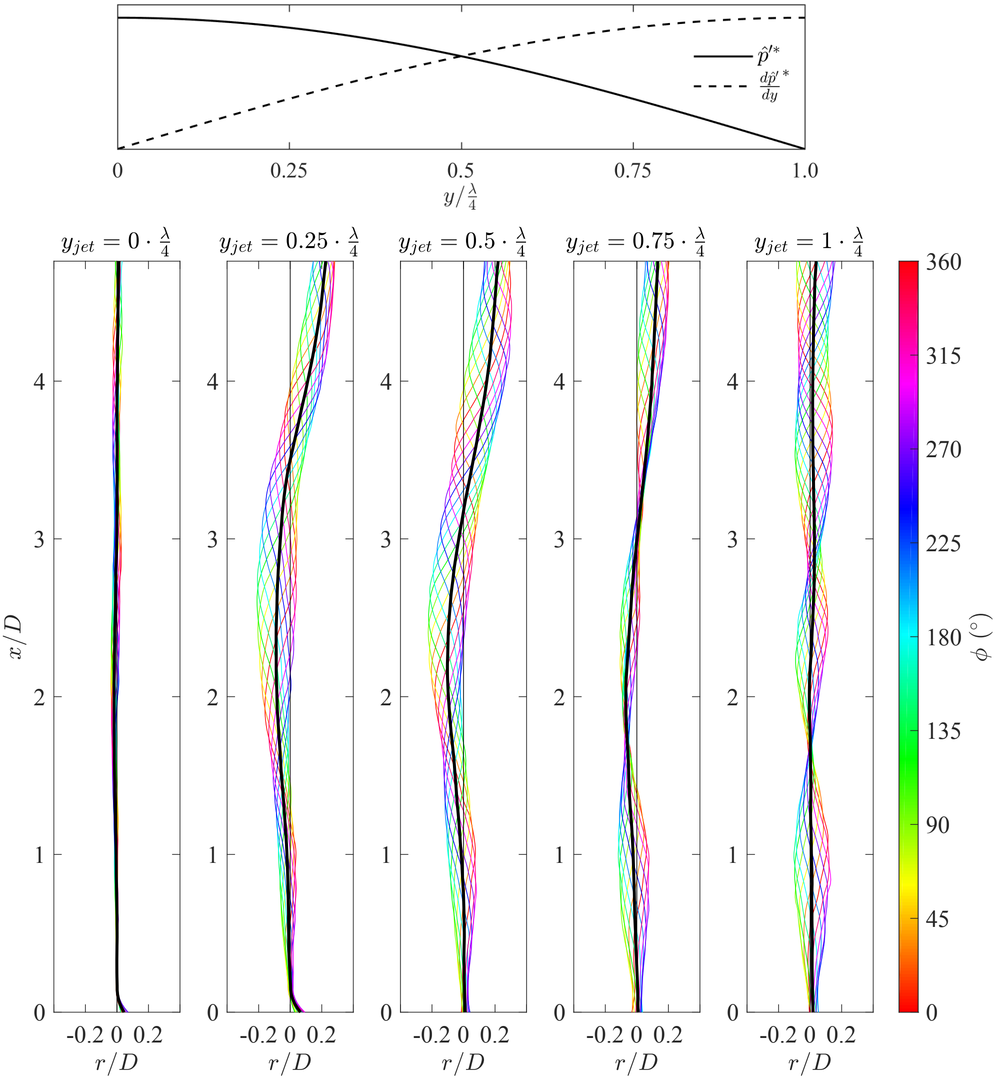

Figure 3.23: Radial position of the jet centerline for $f = 655$ Hz and $U_e = 18.9$ m/s. Phase averaged centerlines are colored by phase in the forcing cycle, and the thick, black lines show the time averaged position of the centerline. Above the centerlines, the theoretical pressure wave in the enclosure is sketched.

the centerlines for the different phases in the forcing period are fluctuating about this line. An interesting observation at this jet position is that there is a point downstream, $x/D \approx 1.7$ for both $f = 450$ Hz and $f = 655$ Hz, where all the phase centerlines are intersecting and the amplitude of the transverse movement tend to zero. This intersection point corresponds quite well to the distance the vortex structures travel in one forcing cycle; by approximating the vortices to follow the velocity estimated by the slug model in equation (1.26), i.e. the axial convection velocity of the vortex structures is half of the jet velocity, $u_{v,c} = 0.5 \cdot U_e$, we get $x/D = 0.5 \cdot \frac{U_e}{fD} = \frac{0.5}{St} = 1.46$ for $U_e = 13.1$ m/s, $f = 450$ Hz, and $x/D = \frac{0.5}{St} = 1.44$ for $U_e = 18.9$ m/s, $f = 655$ Hz. A simple model of the transverse movement of the vortex structures can be obtained by looking at a fluid element with a constant axial velocity $u_{v,c}$ moving in the transverse direction due to the pressure gradient force alone. From Newton's second law of motion we obtain:

$$dv = \frac{\nabla p}{\rho} dt. \tag{3.2}$$

By assuming that the pressure gradient force is acting on a fluid element from the moment it leaves the nozzle exit, we get the transverse velocity of this element at (x, t) by integrating from $\tau = t - \frac{x}{u_{v,c}}$ to $\tau = t$:

$$\begin{aligned} v(t) &= \int_{t-\frac{x}{u_{v,c}}}^{t} \frac{\nabla p}{\rho} d\tau = \int_{t-\frac{x}{u_{v,c}}}^{t} \frac{2Ak}{\rho} \sin(ky) \cos(\omega\tau)\, d\tau \\ &= \frac{2A}{\rho c} \sin(ky) \left(\sin(\omega t) - \sin\left(\omega t - \frac{\omega}{u_{v,c}} x \right) \right). \end{aligned} \tag{3.3}$$

Here we obtain ∇p by differentiating the expression for p given in equation (1.47), but with x substituted by y since the pressure waves are acting in the transverse direction. By again integrating with respect to time, we get the transverse position of the fluid element:

$$\begin{aligned} r/D &= \int_{t-\frac{x}{u_{v,c}}}^{t} \frac{2A}{\rho c}\sin(ky)\left(\sin(\omega\tau) - \sin\left(\omega\tau - \frac{\omega}{u_{v,c}}x\right)\right) d\tau \\ &= \frac{2A}{\omega\rho c}\sin(ky)\left(2\cos\left(\omega t - \frac{\omega}{u_{v,c}}x\right) - \cos(\omega t) - \cos\left(\omega t - \frac{2\omega}{u_{v,c}}x\right)\right). \end{aligned} \tag{3.4}$$

This equation satisfies the condition $r = 0$ at

$$x/D = n\frac{u_{v,c}}{fD}, \tag{3.5}$$

where n is an integer. The result of the transverse position of this fluid element is plotted in figure 3.24 for the case $u_{v,c} = 0.5 \cdot U_e$, $U_e = 18.9$ m/s, $f = 655$ Hz in the same way as for the experimental results. For the jet position $y/\frac{\lambda}{4} = 1$, there is good agreement between the shape of the theoretical and experimental results one forcing period downstream, with the largest transverse displacements at one half of the forcing period downstream and all the centerlines intersecting at $r/D = 0$ one period downstream. The amplitude of the transverse movements, however, differs significantly between the theoretical and experimental data. Also for the second period downstream, traces of the same shape is visible for the experimental data. At $y/\frac{\lambda}{4} = 0.75$ the phase centerlines are also intersecting after one forcing period downstream for the experimental data (and even two periods for $f = 655$ Hz), but here the time averaged line does not follow the $r/D = 0$ line. For the two jet positions $y/\frac{\lambda}{4} = 0.25$ and $y/\frac{\lambda}{4} = 0.5$ there is no point downstream where all the centerlines intersect, and both the mean and phase averaged centerlines are different from the theoretical solution. It is also worth mentioning that the amplitude of the oscillations at half the forcing cycle downstream seem to increase from $y/\frac{\lambda}{4} = 0$ to $y/\frac{\lambda}{4} = 1$ for the experimental cases. This is in agreement with the theoretical case, where the amplitude is proportional to $\sin(ky) = \sin(y/\lambda)$ and is therefore zero at $y/\frac{\lambda}{4} = 0$ and largest at $y/\frac{\lambda}{4} = 1$.

According to equation (3.5), the axial position where the phase averaged centerlines cross is proportional to the jet velocity. The measured centerline

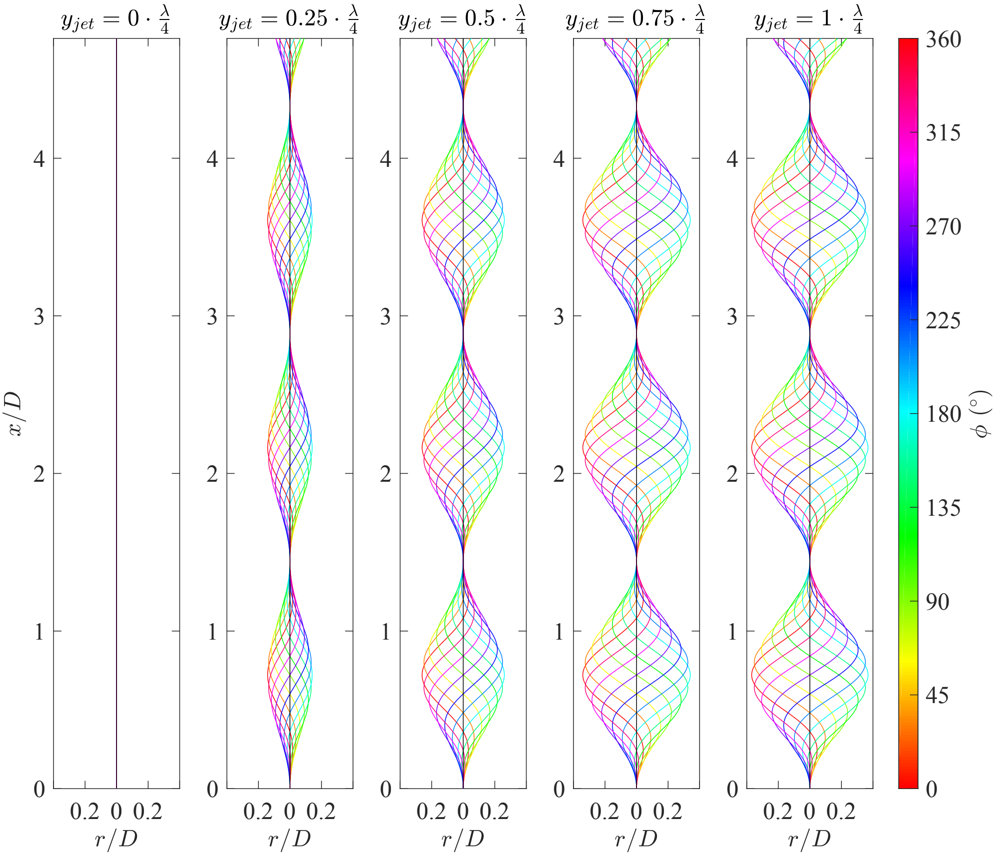

Figure 3.24: Theoretical radial position of the jet centerline for $f = 655$ Hz and $U_e = 18.9$ m/s. Phase averaged centerlines are colored by phase in the forcing cycle.

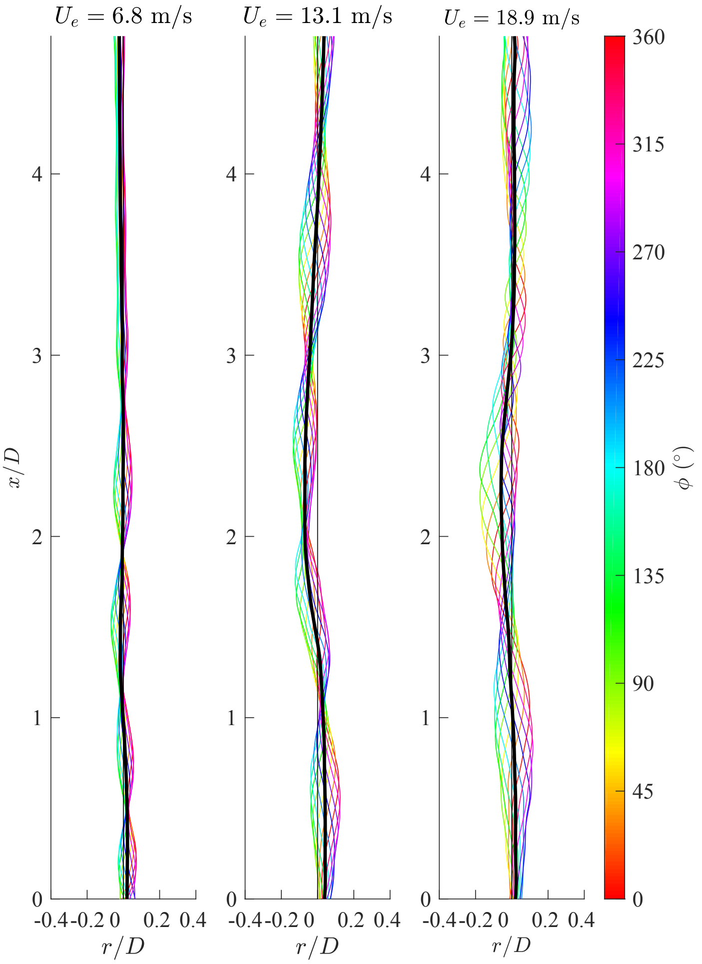

Figure 3.25: Theoretical radial position of the jet centerline for $f = 655$ Hz and $y/\frac{\lambda}{4} = 1$ for different exit velocities. Phase averaged centerlines are colored by phase in the forcing cycle, and the thick, black lines show the time averaged position of the centerline.

Table 3.2: Axial intersection points of the phase averaged jet centerlines at $y/\frac{\lambda}{4} = 1$

Period	$f = 250$ Hz, $U_e = 6.8$ m/s		$f = 450$ Hz, $U_e = 13.1$ m/s		$f = 655$ Hz, $U_e = 18.9$ m/s	
	Measured	Theoretical	Measured	Theoretical	Measured	Theoretical
1	0.48	0.52	1.1	1.0	1.6	1.4
2	1.1	1.0	2.1	2.0	-	2.9
3	1.9	1.6	3.0	3.0	-	4.3
4	2.7	2.1	-	4.0	-	5.8

for forcing frequency $f = 655$ Hz and jet position $y/\frac{\lambda}{4} = 1$ match reasonably well in shape with the theoretical solution. Figure 3.25 shows the experimental results of this case for varying jet exit velocities. The highest velocity has the same conditions as the $y/\frac{\lambda}{4} = 1$ case in figure 3.23, and the shape and centerline crossings are also similar ($x/D \approx 1.6$ in figure 3.25 compared to $x/D \approx 1.7$ in figure 3.23). For the lower velocities the shape is preserved for a longer time, 3-4 forcing periods. A comparison of the measured and theoretical downstream position of the centerline intersection for the different velocities are listed in table 3.2. In general, the measured and theoretical values agrees well, but for $U_e = 6.8$ m/s the values deviate more the further downstream.

3.3 Summary of the characterization

To finalize this chapter, a summary of the findings follows:

- Standing waves were produced in the jet enclosure at $f = 250$ Hz, $f = 450$ Hz and $f = 655$ Hz, corresponding to the 2nd, 4th and 6th transverse mode, respectively.
- The nozzle setup responds as a Helmholtz resonator with mean flow described in section 1.4.1 with resonance frequency $\omega_0 = 2\pi \cdot 260$ Hz. The phase of the velocity response relative to the ambient enclosure pressure

vary with frequency. This means that the phase between the axial and transverse velocity fluctuations at the nozzle exit depends on the forcing frequency.

- The nozzle responds linearly in terms of axial velocity fluctuations when exposed to ambient pressure fluctuations coming from the pressure anti-node of a standing wave in the jet enclosure, and the behavior is sinusoidal in time.
- The unforced jet is near top-hat and symmetric for the velocities investigated.
- It was decided to scale the Strouhal numbers for the varying jet position cases to $St_D \approx 0.35$ for all the forcing frequencies. By doing so, the vortex structures are expected to have the same axial separation distance, independent of forcing frequency.
- The mean and RMS velocity fields showed significantly different behavior at varying positions in the standing wave. This difference is more pronounced for $f = 450$ Hz and $f = 655$ Hz than for $f = 250$ Hz.
- The mean and RMS velocity fields are symmetric for the jet placed in the pressure anti-node and node.
- At the other positions for$f = 450$ Hz and $f = 655$ Hz, the jet potential core bends towards the anti-node, while the jet bends back towards the node further downstream.
- The potential core is shorter for the forced jet compared to the unforced jet, and the core length also seems to be dependent on the jet position, being longer at the pressure node compared to the anti-node.
- For $f = 450$ Hz and $f = 655$ Hz the transverse velocity fluctuations at $r/D = 0$ are zero at the pressure anti-node and increase towards the node. The axial component has the opposite behavior, being zero at the pressure node, and increasing towards the pressure anti-node. The product of the axial and transverse velocity fluctuations seem to be a good measure of the asymmetry in the jet, as suggested by Lespinasse *et al.* (2013).

- For the $f = 250$ Hz case, the centerline of the jet does not meander significantly. For the two higher frequencies, the centerline meanders for all jet positions, except at $y/\frac{\lambda}{4} = 0$, where no pressure gradient is present. At $y/\frac{\lambda}{4} = 1$, the behavior of the centerline is symmetric and for some diameters downstream similar in shape as the analytical solution of a passive tracer in equation (3.4), while at $y/\frac{\lambda}{4} = 0.25$, $y/\frac{\lambda}{4} = 0.5$ and $y/\frac{\lambda}{4} = 0.75$ the centerline position during the forcing cycle is asymmetric.

Chapter 4

Vortex structures

In this chapter, the vortex structures in the near-field of the forced jet are studied. The vorticity field is introduced, and all the results presented in this chapter are phase averaged to give an insight in how the jet responds to the acoustic forcing throughout the forcing cycle. In section 4.1, results of the jet when positioned in the pressure anti-node are shown. At this position, only axial velocity fluctuations are present. Then section 4.2 investigate the effect of varying the position from the anti-node to the node. Section 4.3 shows results from the pressure node position, where the transverse fluctuations are dominating. Finally, the role of the axial and transverse velocity fluctuations in the vortex formation is discussed in section 4.4.

4.1 The pressure anti-node

Figure 4.1 shows contours of normalized phase averaged vorticity (see section 2.5.2) for different forcing frequencies, jet exit velocities and forcing amplitudes for the jet positioned in the pressure anti-node ($y/\frac{\lambda}{4} = 0$). For all forcing configurations, the vorticity fields are taken from the start of the forcing cycle, $t/T = 0$, defined by the enclosure pressure as shown in figure 3.3. The vorticity fields show axisymmetric vortex structures, similar to what has been found for

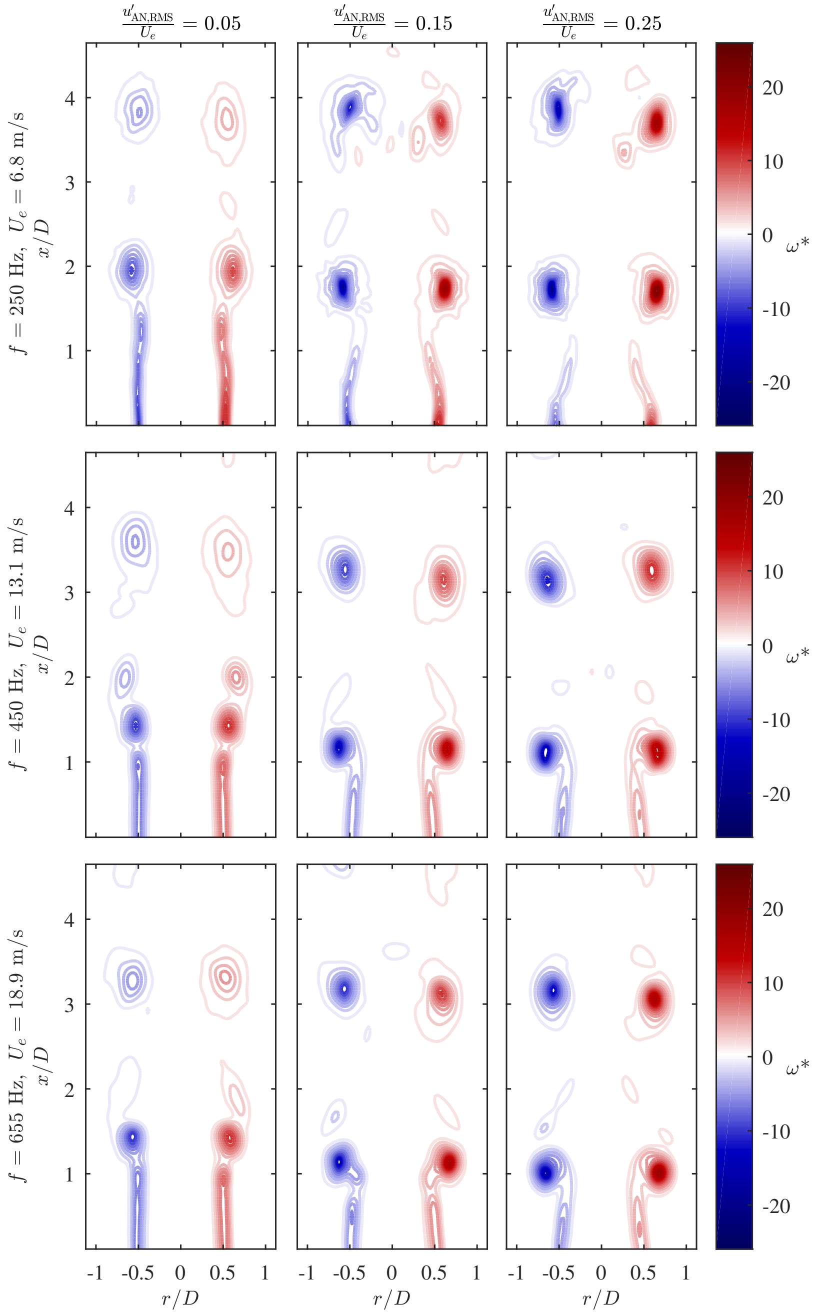

Figure 4.1: Phase averaged vorticity contours for varying forcing frequencies, exit velocities and forcing amplitudes, $y/\frac{\lambda}{4} = 0$, $t/T = 0$.

longitudinal forcing (Aydemir *et al.*, 2012; Zaman & Hussain, 1980) and previous anti-node experiments (Baillot & Lespinasse, 2014; O'Connor & Lieuwen, 2011; Saurabh & Paschereit, 2013). These structures are well known to be vortex rings. The forcing amplitude increase from left to right in the figure, causing the strength of the vortices to increase in terms of vorticity. The vortex rings are also rolling up closer to the nozzle exit, as seen in figure 4.2, that shows time-series of the $f = 450$ Hz cases. Since these time-series are phase averaged, they are periodic. This means that the vortex structures formed somewhere in the cycle can be followed until the end of the cycle, continuing at $t = 0$ and through several cycles until they disappear out of the field of view. For the lowest forcing amplitude, $u'_{\mathrm{AN,RMS}}/U_e = 0.05$, the separation of the vortices from the shear-layer happens later and more gradually. Some smaller vortex structures are formed both upstream and downstream of the largest vortex for this forcing amplitude, and these vortices eventually merge into one structure. The separation distance between the vortex rings in figure 4.1 is approximately constant and independent of forcing frequency, as is expected since St_D is matched. According to the slug model, however, the ring velocity increases with forcing amplitude. This implies that the separation distance between the vortices also should increase with forcing amplitude. This is not seen clearly from the vorticity fields.

To be able to investigate the velocity and other properties of the vortex structures more in detail, an algorithm for tracking the individual vortices was developed (see section 2.5.2). Figure 4.3 shows the axial position of the individual vortex structures on the left and right hand side of the jet as a function of time for the same cases as in figure 4.1. The black, solid line has a slope equal to the velocity obtained by combining the axial convection velocity of a vortex ring predicted by the slug model given in equation (1.26), and the piston velocity for a sinusoidally pulsed jet given in equation (1.32) using $A = (\sqrt{2}/2)u'_{\mathrm{RMS}}/U_e$. The black, dashed line has its slope from equation (1.33) with $T_s = T/2$. Asadi *et al.* (2018) obtained this empirical formula from numerical simulations on a pulsed jet with constant flow of duration T_s of the forcing period T, and no flow between the pulses. This velocity program differs from the sinusoidally pulsed jet which does not have a parameter similar to T_s defined. $T_s = T/2$ corresponds to the part of the cycle the fluctuating axial velocity is positive,

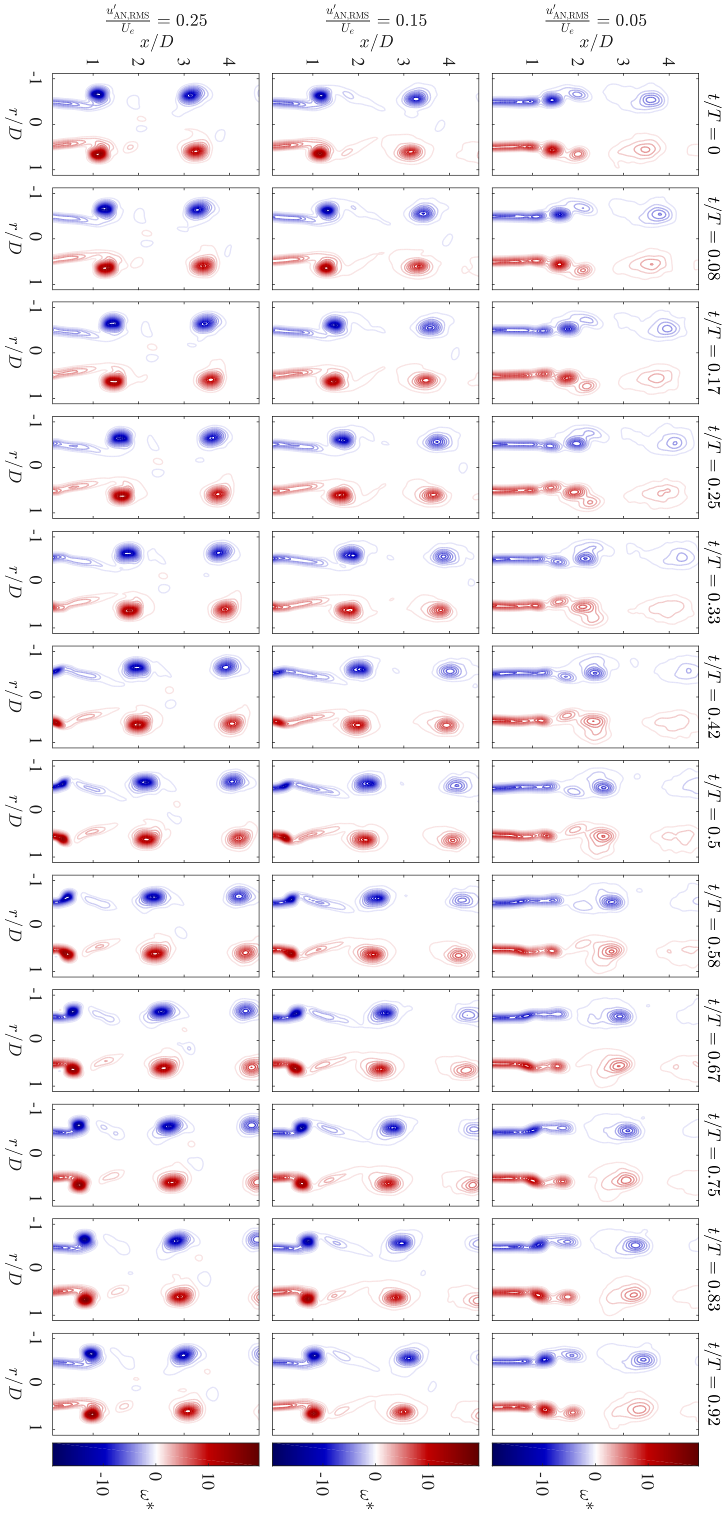

Figure 4.2: Time-series of phase averaged vorticity contours for varying forcing amplitudes, for $y/\frac{\lambda}{4} = 0$, $f = 450$ Hz, $U_e = 13.1$ m/s.

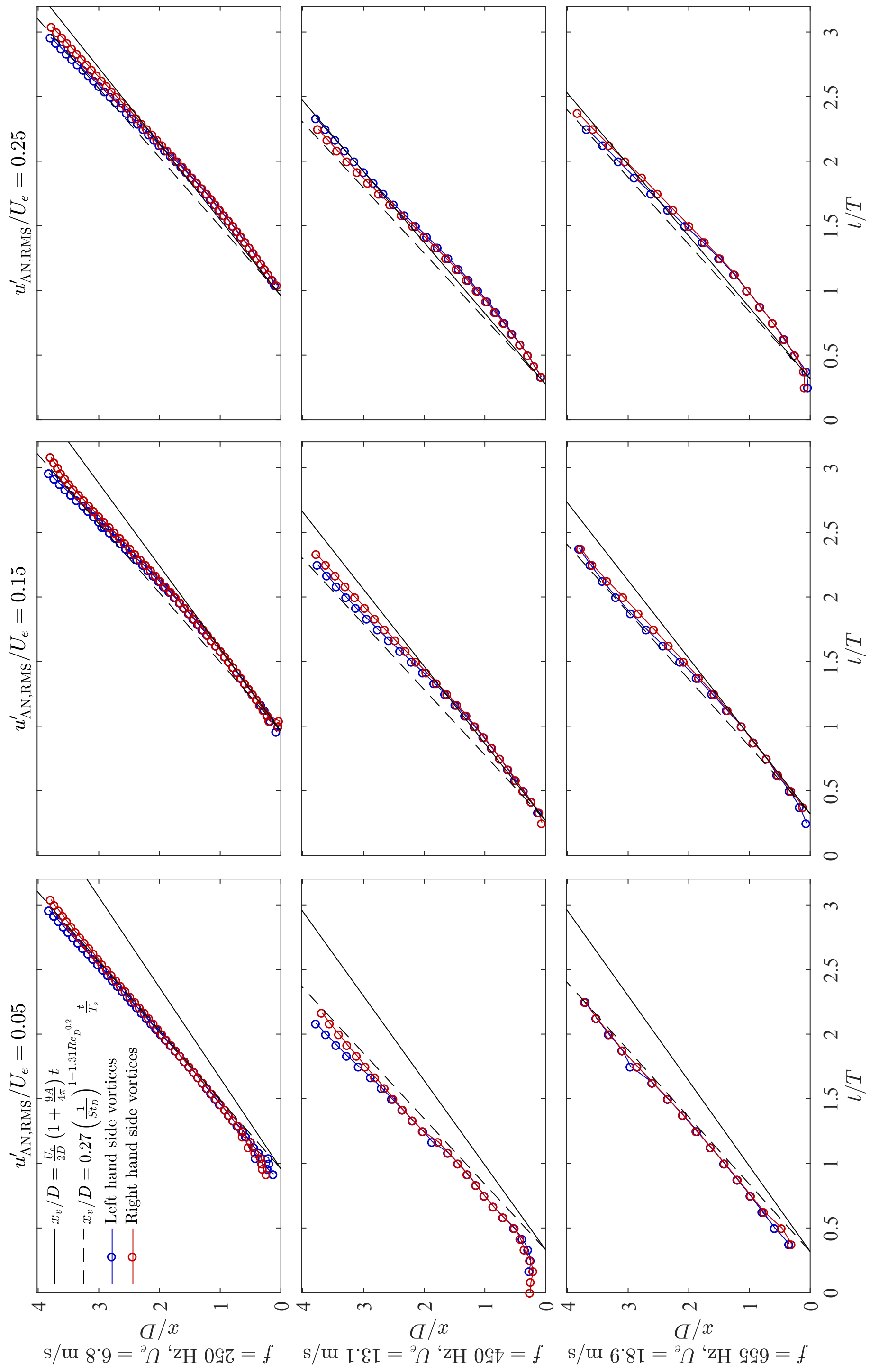

Figure 4.3: Axial position of the individual vortex structures on the left (blue) and right hand side (red) of the jet for varying exit velocities and forcing amplitudes at $y/\frac{\lambda}{4} = 0$.

and was chosen since it gave a good match to the experimental data. One can argue that $T_s = T/3$ should be used since Aydemir *et al.* (2012) found that this is the effective forcing period of a sinusoidally pulsed jet, as described in section 1.2.4. By using $T_s = T/3$, however, the velocity was considerably higher than the experimental data for all forcing conditions. Both the solid and the dashed line starts at the nozzle exit, $x/D = 0$, at time $t_{\tilde{u}'_0}$, defined in figure 3.8 to be when the fluctuating part of the phase averaged axial velocity at the jet exit is changing sign from negative to positive.

The left and right hand side vortices have approximately the same axial position for all cases, and therefore also the same speed. For $u'_{\mathrm{AN,RMS}}/U_e = 0.05$ this speed is considerably higher than the slug model speed and the vortices start slightly downstream of the black line. The vortex paths match quite well with the empirical path predicted by Asadi *et al.* (2018). For $u'_{\mathrm{AN,RMS}}/U_e = 0.15$, the vortex positions match well with the slug model path and better than the path by Asadi *et al.* (2018), for almost one forcing period. Then the vortices accelerate away from the slug model path and end up in agreement with Asadi *et al.* (2018). The vortices at $u'_{\mathrm{AN,RMS}}/U_e = 0.05$ accelerate as well, but to a lesser extent. For $u'_{\mathrm{AN,RMS}}/U_e = 0.25$ the vortex paths are starting at the same point as the two model paths, but with a lower velocity. Also here the vortices accelerate with the result that they end up in good agreement with both models. Both Didden (1979) and Asadi *et al.* (2018) reported that the vortex rings increased their convection velocity during the formation process, which is seen for all the forcing conditions in figure 4.3. The phase angle between the enclosure pressure and the axial velocity, that in figure 3.5 were found to vary with forcing frequency, are also seen here; while the phase of the axial velocity fluctuations and therefore the vortex formation is approximately the same for $f = 450$ Hz and $f = 655$ Hz, it is shifted more than 90° for $f = 250$ Hz.

In figure 4.4, the mean convection velocities averaged over the time interval from $t_{\tilde{u}'_0}$ to when the vortices cannot longer be tracked, are marked as circles for the different anti-node cases. According to the slug model, the ring velocity increase with forcing amplitude. There is no clear trend for this in figure 4.4, and this is also the case when excluding the formation period of the rings when calculating the mean convection velocity. For all forcing conditions, the

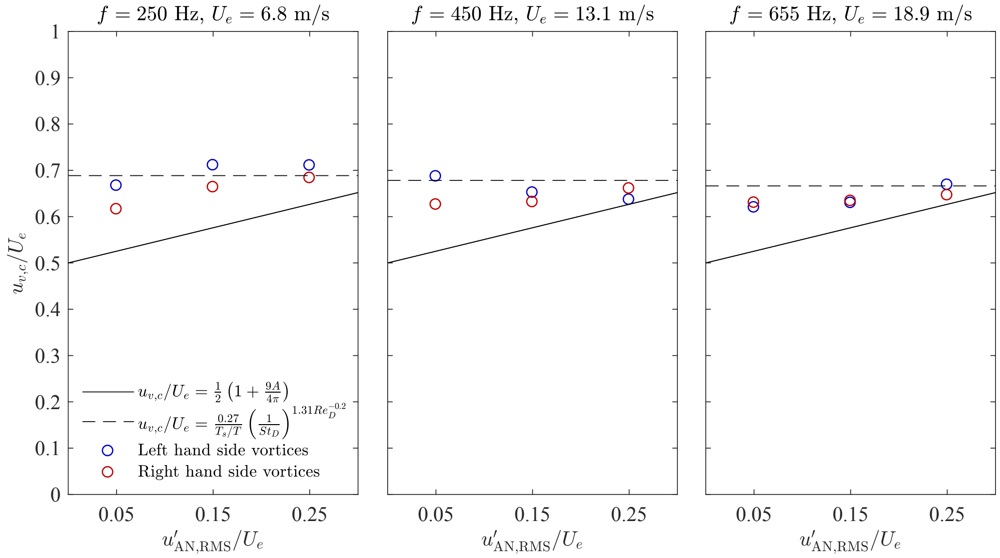

Figure 4.4: Axial velocity of the individual vortex structures on the left (blue) and right hand side (red) of the jet for varying exit velocities and forcing amplitudes at $y/\frac{\lambda}{4} = 0$.

measured convection velocity of the vortex rings is higher than the predicted velocity from the slug model. This is in agreement with Mohseni & Gharib (1998) who reported that the vortex ring velocity in practice is higher than half of the piston velocity (equation (1.26)). Asadi *et al.* (2018) developed equation (1.33) to match the mean ring speed when including the formation period, and the model is in good agreement with the experimental data for all forcing conditions. Asadi et al. found the convection velocity of the vortex rings to be more sensitive to St_D than Re_D, but unfortunately equation (1.33) was not tested against data of varying St_D.

4.2 Varying jet position

Figure 4.5 shows contours of normalized phase averaged vorticity for different forcing frequencies, jet exit velocities and jet positions at time $t/T = 0$. Above the vorticity fields the theoretical pressure wave in the enclosure is sketched.

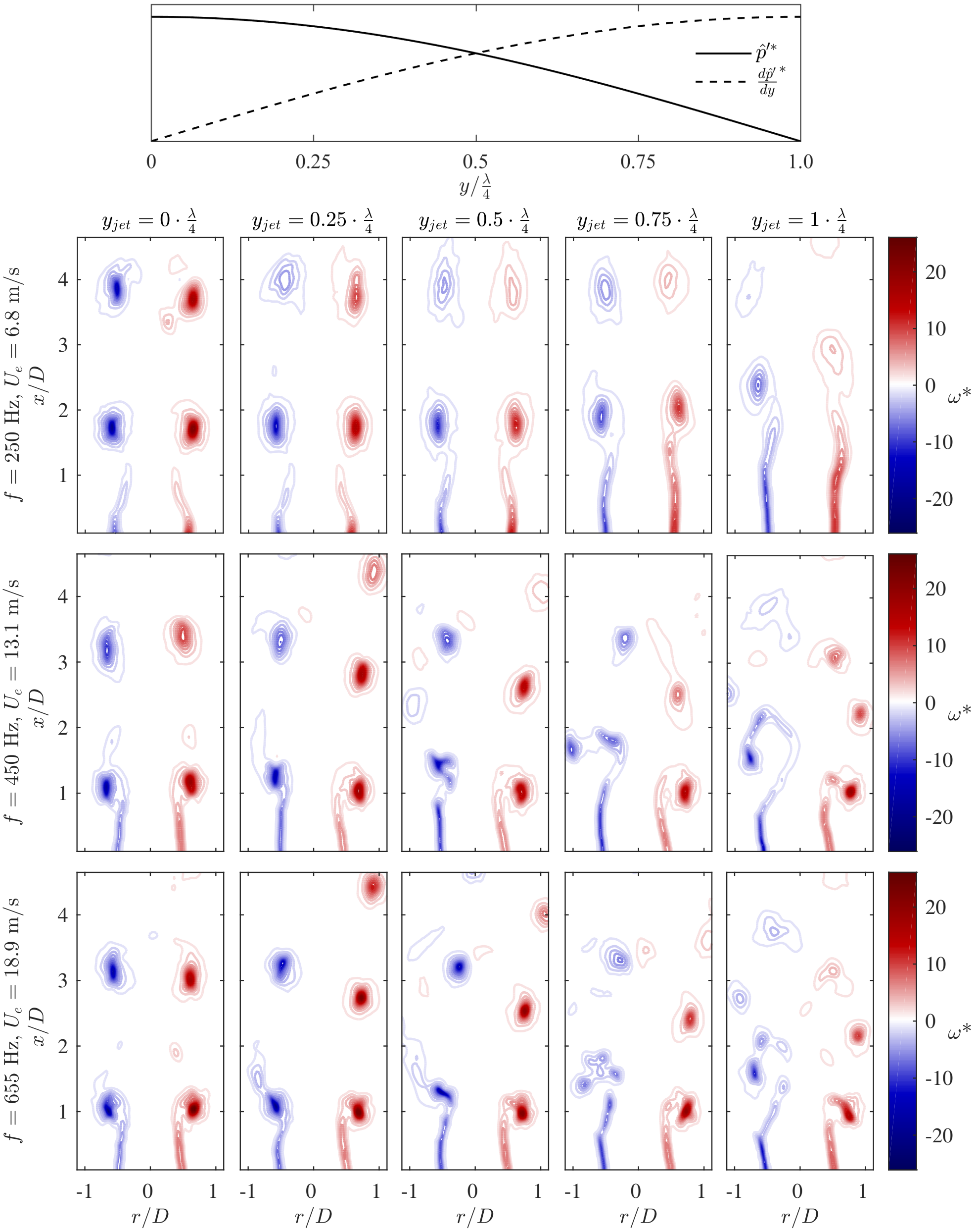

Figure 4.5: Phase averaged vorticity contours for different forcing frequencies, jet exit velocities and jet positions, for $u'_{\mathrm{AN,RMS}}/U_e = 0.25$ at $t/T = 0$. Above the vorticity fields the theoretical pressure wave in the enclosure is sketched.

Similar to what was seen in the previous chapter, the response of the jet does not have nearly the same development for $f = 250$ Hz as for the higher forcing frequencies when the jet position is changed. For $f = 250$ Hz, there is no noticeable difference in the vorticity field from $y/\frac{\lambda}{4} = 0$ to $y/\frac{\lambda}{4} = 0.5$. At $y/\frac{\lambda}{4} = 0.75$, the roll-up of the shear-layer happens slightly further away from the nozzle exit, and the symmetry breaks as the vortex on the right side of the jet, facing towards the pressure node is slightly downstream of the vortex on the left side, towards the anti-node. $y/\frac{\lambda}{4} = 1$ is the only jet position where the asymmetry is clear, and the right vortex is significantly further downstream of the left. An effect of changing the jet position towards the pressure node is that the vortex structures are getting weaker in terms of lower maximum vorticity value, and the right hand side vortex is also getting weaker relative to the vortex on the left side. Lespinasse *et al.* (2013) also reported that the vortices on the side towards the anti-node were visually larger than the vortices on the side towards the node, but while this difference was not present at the pressure node in their experiments, the difference between the vortices is largest at this position for $f = 250$ Hz in this study.

For the rest of this section the jet forced at 450 Hz is investigated. The vorticity fields for $f = 450$ Hz and $f = 655$ Hz has similar developments when the jet position is changed from $y/\frac{\lambda}{4} = 0$ to $y/\frac{\lambda}{4} = 1$. The main difference between these two frequencies is the vorticity structures at $y/\frac{\lambda}{4} = 1$, and this will be discussed in the next section. For all the three middle positions for $f = 450$ Hz, the vortices are not convecting downstream in a straight line but move slightly towards the pressure node. This is similar to the behavior of the mean centerline positions in figures 3.22 and 3.23. In contrast to $f = 250$ Hz, the symmetry is broken already at $y/\frac{\lambda}{4} = 0.25$. On the right hand side the vortices roll up at approximately the same x/D and t/T for all jet positions, but the shape of the shear-layer forming a tail behind the vortex changes with jet position. This is clearly seen by investigating the time-series of the vorticity fields in figure 4.6[a]. Also here the time-series are periodic, and the vortex structures formed somewhere in the cycle can be followed until the end of the cycle, continuing at $t = 0$ and through several cycles until they disappear out of the field of view. From $t/T = 0.5$ to $t/T = 0.92$ at jet position $y/\frac{\lambda}{4} = 0$, the shear-layer

---

[a] The time-series for $y/\frac{\lambda}{4} = 0.25$ can be found in figure B.1 in appendix B

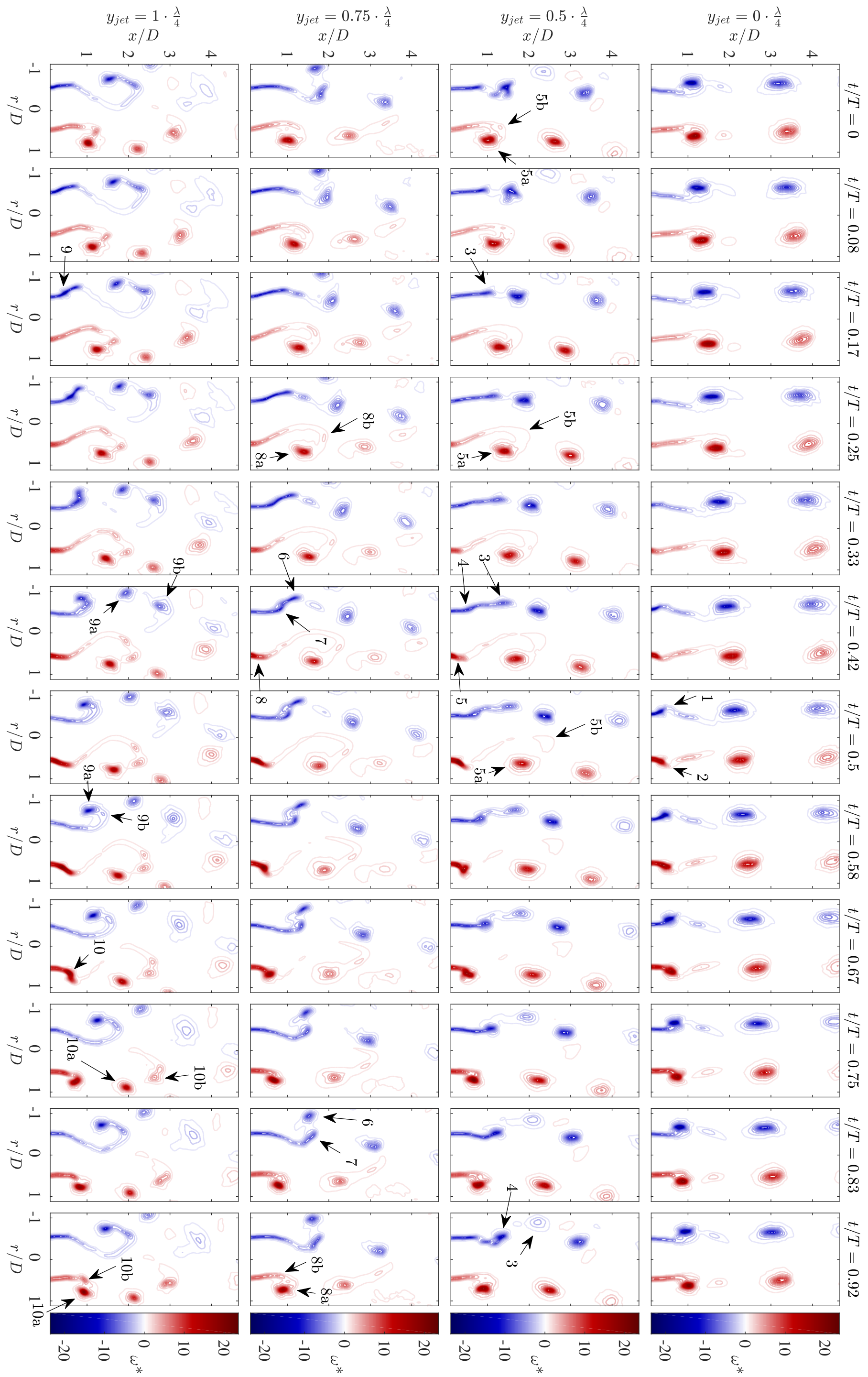

Figure 4.6: Time-series of phase averaged vorticity contours for different jet positions, for $f = 450$ Hz, $U_e = 13.1$ m/s, $u'_{\mathrm{AN,RMS}}/U_e = 0.25$.

behind the vortices marked as 1 and 2 develop into an almost straight, vertical line from the nozzle exit, and connecting to the lower left side of the vortex. Then the shear-layer starts to gradually tilt to the left from $t/T = 0$ until the iso-contour of lowest vorticity is not longer connected to the vortex at $t/T = 0.5$. For the other jet positions, the vortex and its trailing shear-layer on the right hand side has a similar development from the time the vortex is formed, until around $t/T = 0$. After this, the lower part of the shear-layer tilts to the left simultaneously as the shear-layer closer to the vortex is bending to the right. The part of the vortex connected to the shear-layer gradually moves clockwise in time, starting at the lower, left side, and ends up on top of the vortex. As the jet is moved towards $y/\frac{\lambda}{4} = 1$, the vorticity contours break down later in the forcing cycle and the bending of the shear-layer gets more pronounced. At $y/\frac{\lambda}{4} = 1$, $t/T = 0.58$, the vortex, its tail and the upstream vortex that starts to roll up, are all connected and form an S shaped structure before the tail breaks down. At $y/\frac{\lambda}{4} = 0.5$, a small vortex, marked as 5b, breaks off from the tail of the larger vortex and slowly disappears. At $y/\frac{\lambda}{4} = 0.75$ and $y/\frac{\lambda}{4} = 1$, similar vortices are marked as 8b and 10b, respectively. 8b is slightly larger than 5b, while 10b is of comparable size as vortex 10a and is visible through the whole field of view.

The vortex on the left hand side has another development as the jet is moved from the pressure anti-node to the node. At $y/\frac{\lambda}{4} = 0.25$, the position of the left vortex is slightly downstream of the right one. The same is observed at $y/\frac{\lambda}{4} = 0.5$, but here another slightly smaller vortex, marked as vortex 3 in figure 4.6, forms out of phase of the vortex marked as 4. Vortex 3 has a negative transverse velocity transporting it outside the field of view of the PIV measurements at $x/D \approx 3$. A similar vortex is found at $y/\frac{\lambda}{4} = 0.75$, marked as 6 in figure 4.6. Vortex 6 has an even stronger transverse velocity and exits the field of view at $x/D \approx 2$. It is comparable in size as vortex 7, the other vortex on the left side at $y/\frac{\lambda}{4} = 0.75$. At this jet position, the meandering that was seen in figure 3.22 gets pronounced. The meandering is at its strongest at $y/\frac{\lambda}{4} = 1$, where the vortex structures on the left hand side have developed to be similar to the right hand side in size and shape, but forming in anti-phase. Vortex 9a has approximately the same size and shape as vortex 10a, and the same is true for vortex 9b and 10b. The meandering and the vortices forming in anti-phase at $y/\frac{\lambda}{4} = 1$ is in agreement with the flapping motion Matta *et al.* (1996) observed in their experiments on a round jet at the pressure node.

While the vortices on the side towards the anti-node were visually larger than the vortices on the side towards the node in the experiments by Lespinasse *et al.* (2013), this is not seen for the positions between the pressure anti-node and node for $f = 450$ Hz and $f = 655$ Hz in this study. The vortex structures on the right side of the jet, towards the pressure node, are in general slightly larger than the vortex structures on the left side, but for the cases where several structures appear on both sides this is difficult to compare.

The shape in the near-field of the jet at the pressure node, and also on the right hand side of the jet at $y/\frac{\lambda}{4} = 0.5$ and 0.75, where the shear-layer curves around the front of the vortex, has similarities to the plane along the minor axis of jets from oval and elliptic shaped nozzles as described in section 1.3 and seen in figure 1.14b. In these cases the explanation for the characteristic shape is the lower convection velocity of the vortex relative to the shear-layer in this plane. This again is due to the vortex convection velocity being inversely proportional to the local curvature radius of the nozzle. By increasing the stroke ratio, it has been reported that the curved shear-layer downstream of the vortex can separate and form an isolated structure (Adhikari, 2009; O'Farrell & Dabiri, 2014). This is similar to the vortices 9b and 10b forming at $y/\frac{\lambda}{4} = 1$. Low convection velocity of the vortices at the pressure node and the right hand side of the jet at $y/\frac{\lambda}{4} = 0.5$ and 0.75 in the current experiments can be due to meandering causing these vortices to move away from the jet centerline and into an area of lower velocity.

To again investigate the paths of the individual vortex structures more thoroughly, their axial position is plotted against time in figure 4.7 for forcing frequency $f = 450$ Hz and amplitude $u'_{\mathrm{AN,RMS}}/U_e = 0.25$. In addition to the black line showing the slug model path for $u'_{\mathrm{AN,RMS}}/U_e$, a dashed line is plotted showing the slug model velocity for $u'_{\mathrm{RMS}}/U_e \to 0$, which is the case at the pressure node position. The black, dashed line starts at $t_{\tilde{u}'_0}$, while there are also blue and red, dashed lines with the same slope starting at $t_{\tilde{v}_{0-}}$ and $t_{\tilde{v}_{0+}}$ These time constants specify when in the forcing cycle the transverse velocity

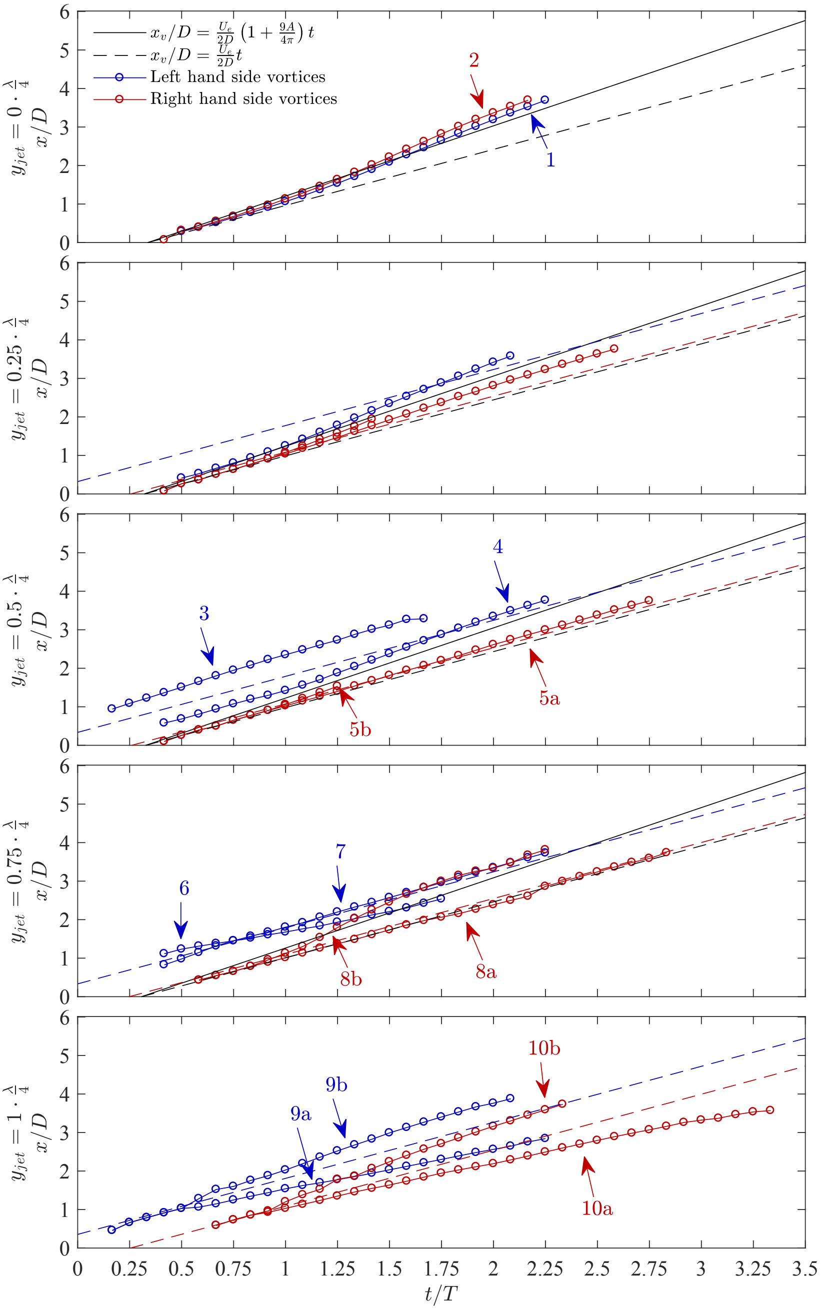

Figure 4.7: Axial position of the individual vortex structures on the left (blue) and right hand side (red) of the jet as a function of time at different jet positions, for $f = 450$ Hz, $u'_{\mathrm{AN,RMS}}/U_e = 0.25$.

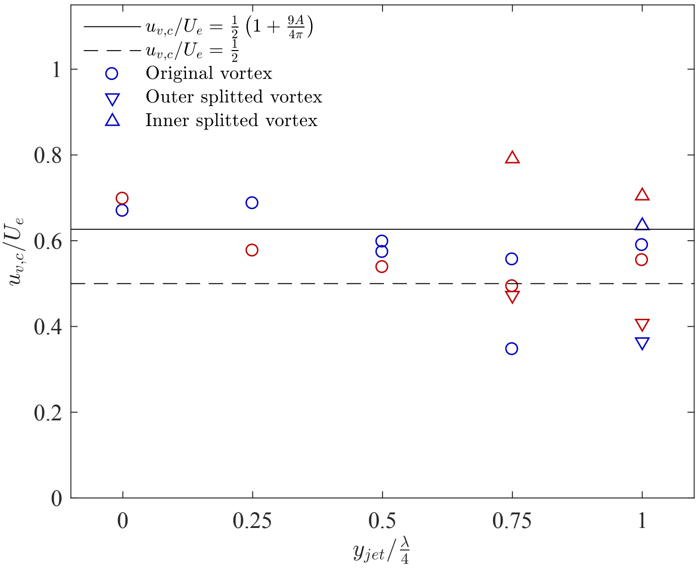

Figure 4.8: Axial velocity of the individual vortex structures on the left (blue) and right hand side (red) of the jet at different jet positions, for $f = 450$ Hz, $u'_{\mathrm{AN,RMS}}/U_e = 0.25$.

at $x = 0, r = 0$ changes direction to the left and right, respectively, as shown in figure 3.3. Figure 4.8 shows the velocity of the vortices averaged over the period they are tracked, alternatively before and after the vortex splits if this occur. Already at position $y/\frac{\lambda}{4} = 0.25$ the vortices on the two sides of the jet clearly have different paths. The vortex on the left side facing towards the anti-node has a similar development as the vortices in the anti-node position. It starts out by following the solid, black line before it accelerates. The vortex on the right side, towards the node, starts out closer to the dashed, black line, and also this vortex accelerates and ends up between the solid and dashed, black lines. At $y/\frac{\lambda}{4} = 0.5$, vortex 5 on the right hand side follows both the black and the red, dashed lines closely, while vortex 4 on the left side is positioned further downstream for the whole path. Vortex 4 also accelerates, while the right hand side vortex does not change its speed significantly. Vortex 4 is approximately in anti-phase with the other vortex on the same side, vortex 3, and these two vortices have about the same speed. At $y/\frac{\lambda}{4} = 0.75$, the vortex on the right hand side starts out by following the black and the red, dashed lines, but are shortly after splitting up. The smaller of the two resulting vortices, 8b, are closer to the jet centerline and gains higher speed, while vortex 8a continues to follow the dashed lines. On the left side, vortex 7 has approximately the same path as the blue, dashed line, but it has a slightly higher speed, as seen in figure 4.8. Vortex 6 has a transverse velocity moving it away from the area of high axial velocity into the slower surrounding area. Therefore, it has a significantly lower speed than vortex 7, and even though it starts out most downstream of the two, it is passed by vortex 7 before it leaves the field of view. At $y/\frac{\lambda}{4} = 1$, the left and right hand side vortices start out by following the blue and red, dashed lines, respectively, implying they are in anti-phase. Then both vortices split up into an outer part with lower axial velocity and an inner part with higher axial velocity. Except for vortex 6, all the vortices start out with approximately the same axial velocity bounded by the two slug model speeds. Later however, most of the vortices are either accelerating or splitting up, with the resulting velocities outside this velocity region.

4.3 The pressure node

We now investigate in detail the response of the jet positioned at $y/\frac{\lambda}{4} = 1$. Figure 4.5 showed that the vortex structures for $f = 250$ Hz did not have the same transition as the higher frequencies, when moving the jet from the pressure anti-node to the pressure node. In section 3.2, figure 3.18 showed that the amplitude of the transverse velocity fluctuations for $f = 250$ Hz was approximately constant for all jet positions, and significantly lower than for the other frequencies at $y/\frac{\lambda}{4} = 1$. As seen from equation (1.47), the acoustic velocity scales with pressure amplitude. Therefore, it is interesting to investigate the jet behavior for $f = 250$ Hz for higher forcing amplitudes at $y/\frac{\lambda}{4} = 1$ to see if this gives a change in the response. Figure 4.9 shows the vorticity field for forcing amplitudes up to $u'_{\mathrm{AN,RMS}}/U_e = 1.0$. As the forcing increases, the response is more similar to the pressure node response of the other frequencies that was shown in figure 4.5. The shear-layer rolls up closer to the nozzle exit, and the vortex structures grows in strength and are more distinct. However, the vortex structures on the left and right hand side are not completely in anti-phase even for $u'_{\mathrm{AN,RMS}}/U_e = 1$. The vortices move radially towards the

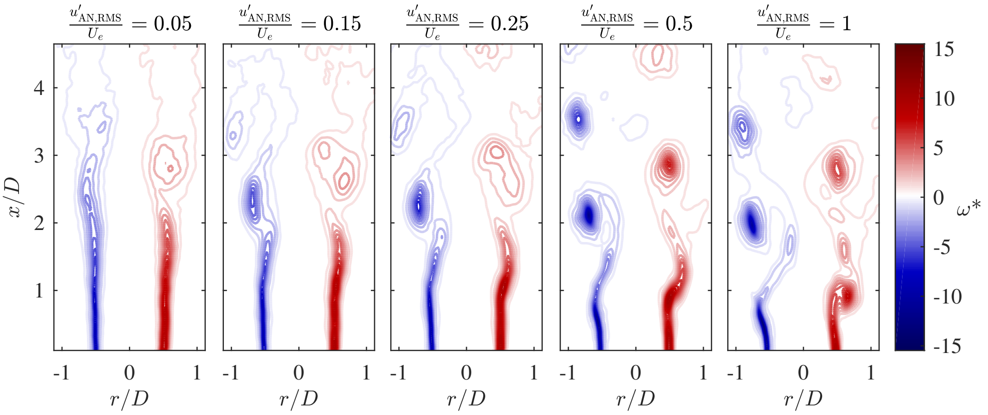

Figure 4.9: Phase averaged vorticity contours for different forcing amplitudes, for $f = 250$ Hz, $y/\frac{\lambda}{4} = 1$, $t/T = 0$.

left as they convect downstream, which is the opposite direction of what was observed for the middle positions for $f = 450$ Hz and $f = 655$ Hz. Figure 4.10 shows the axial position of the tracked vortex structures as a function of time. For $u'_{\mathrm{AN,RMS}}/U_e = 0.05$ and on the right hand side for $u'_{\mathrm{AN,RMS}}/U_e = 0.15$, the tracking algorithm could not find any distinct vortices disconnected from the shear-layer. The paths that are tracked show that the left hand side vortex is slowly approaching the blue dashed line as the forcing is increased, and that this vortex moves with a fairly constant velocity. For all forcing amplitudes, the right hand side vortex follows the red dashed line to begin with, before it accelerates and moves off the dashed line.

The jet positioned at $y/\frac{\lambda}{4} = 1$ is also investigated in detail for $f = 450$ Hz and $f = 655$ Hz. Figure 4.11 shows phase averaged vorticity contours for varying jet velocities and forcing amplitudes for $f = 450$ Hz at time $t/T = 0$. Time-series of these vorticity fields can be found in figure B.2-B.4 in appendix B. The vortex separation distance increases with higher jet velocity, since the vortices then move a longer distance in one forcing period. For the case $U_e = 6.8$ m/s, $u'_{\mathrm{AN,RMS}}/U_e = 0.05$, 5 vortices from 5 consecutive forcing cycles are visible on each side of the jet in the field of view. For the velocities $U_e = 13.1$ m/s and $U_e = 18.9$ m/s, only vortices from two and one forcing cycle, respectively, are visible. This large difference is also due to the fact that the vortices roll up

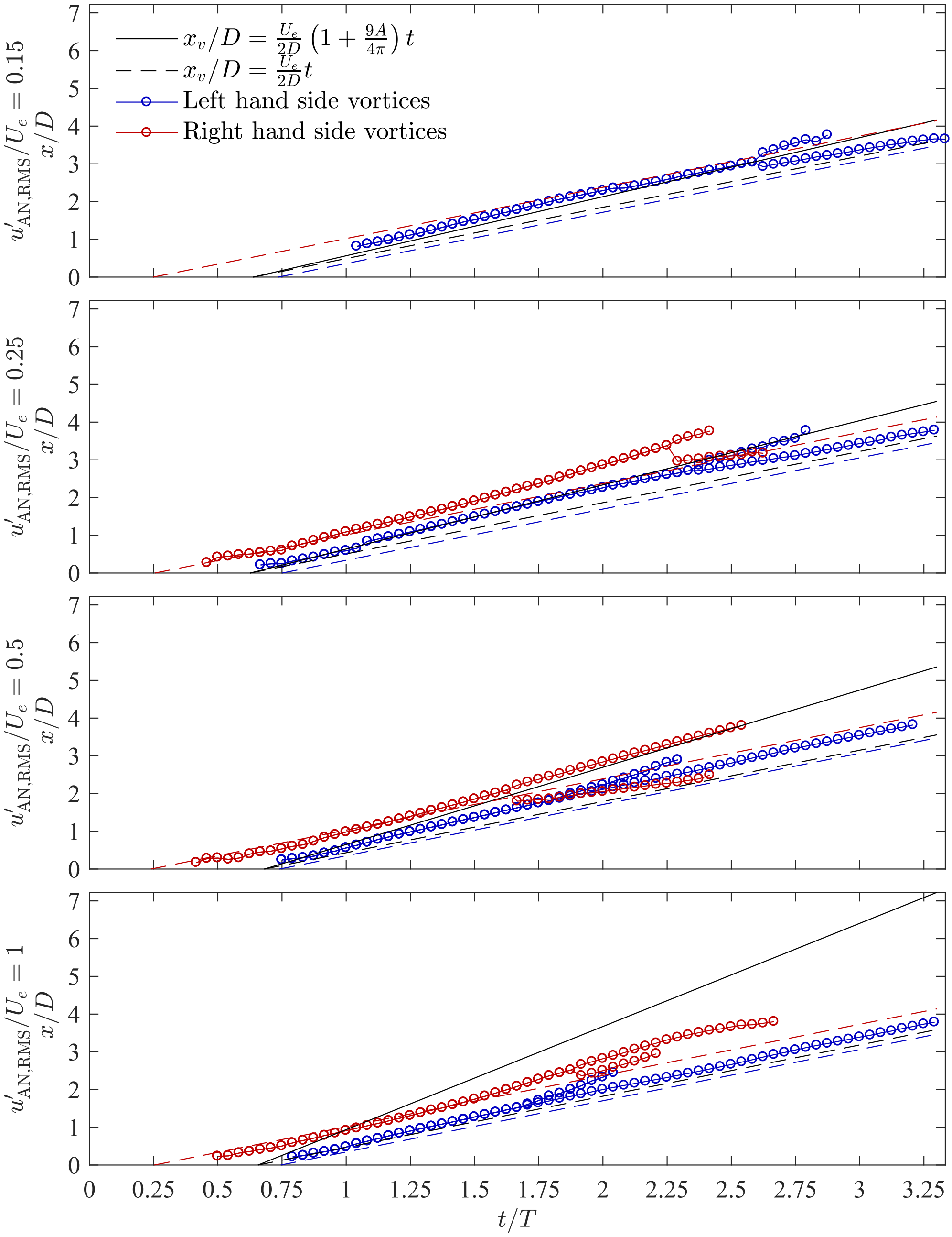

Figure 4.10: Axial position of the individual vortex structures on the left (blue) and right hand side (red) of the jet as a function of time for different forcing amplitudes, at $y/\frac{\lambda}{4} = 1$, $f = 250$ Hz.

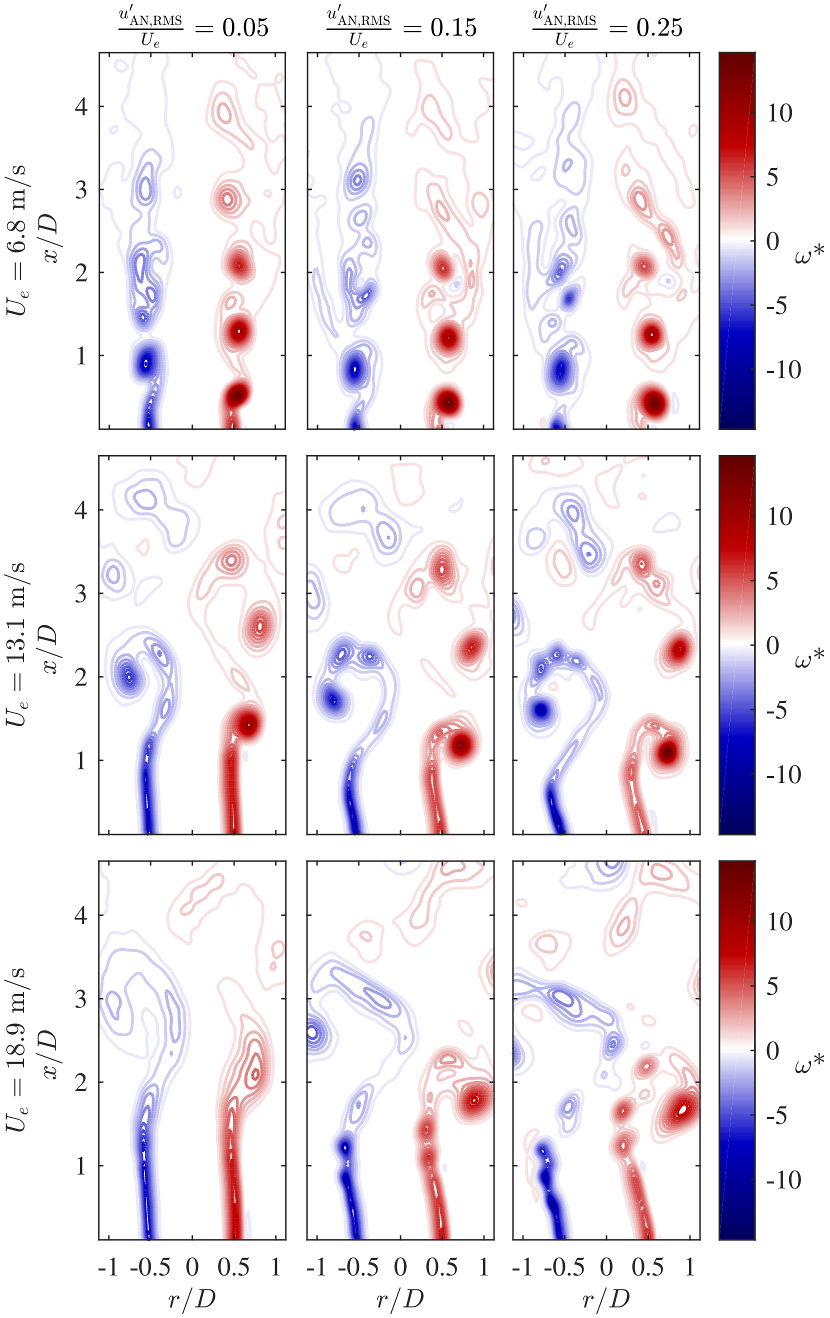

Figure 4.11: Phase averaged vorticity contours for different jet velocities and forcing amplitudes, for $f = 450$ Hz, $y/\frac{\lambda}{4} = 1$, $t/T = 0$.

closer to the nozzle exit for lower U_e. For $U_e = 18.9$ m/s, $u'_{\mathrm{AN,RMS}}/U_e = 0.05$, the shear-layer, seen as lines of high vorticity, start to roll up approximately 2 diameters downstream, but no clear and distinct vortices appear within the field of view. The axial roll-up position also depends on the forcing amplitude. Higher forcing amplitude makes roll-up happen closer to the exit, similar to what was seen for the jet in the pressure anti-node in figure 4.1. For jet velocity $U_e = 6.8$ m/s, the shear-layer does not have the same S shape as for the other jet velocities. Here the distance between the vortices are shorter and the roll-up happens closer to the nozzle exit compared to the higher velocities. Therefore, there is no trailing shear-layer following the vortex that are able to form such an S shape. For most of the cases, the vortices on both sides split in two in the same way as the node cases for $f = 450$ Hz and $f = 655$ Hz in section 4.2. The exceptions are $u'_{\mathrm{AN,RMS}}/U_e = 0.05$ and $u'_{\mathrm{AN,RMS}}/U_e = 0.15$ for $U_e = 6.8$ m/s, and $u'_{\mathrm{AN,RMS}}/U_e = 0.05$ for $U_e = 18.9$ m/s. This is clearly seen in figure 4.12, where the axial positions of the tracked vortices are plotted as a function of time. For most of the cases the vortex paths start by following the dashed lines; the left hand side vortex follows the blue lines starting at $t_{\tilde{v}_{0-}}$, and the right hand side vortex follows the red line starting at $t_{\tilde{v}_{0+}}$. For jet velocity $U_e = 6.8$ m/s, the vortices move upstream of the dashed line as the forcing amplitude increases, and the roll-up happens closer to the nozzle exit. The mean vortex convection velocities are shown in figure 4.13, averaged over the time period the vortices are tracked, alternatively before and after the vortices split if this occur. For the vortices that split up, the result is a vortex outside $r = \pm 0.5$ with lower velocity than the original vortex, and a faster moving vortex closer to the jet centerline. The exception is for $U_e = 6.8$ m/s. For the cases where the vortices split up at this jet velocity, the vortex closest to the centerline is much smaller than the outer vortex, and the outer vortex also stays inside $r = \pm 0.5$ and has a small increase in velocity. For the outer vortex, the increase in velocity relative to U_e, decreases with jet velocity.

Figure 4.14 shows the phase averaged vorticity contours for different jet velocities and forcing amplitudes for $f = 655$ Hz, $y/\frac{\lambda}{4} = 1$, at time $t/T = 0$. The main trends are similar to $f = 450$ Hz in figure 4.11; the separation distance between the vortices increases for higher jet velocity, and the distance from the nozzle exit to where the vortices roll up increase with jet velocity and decrease with

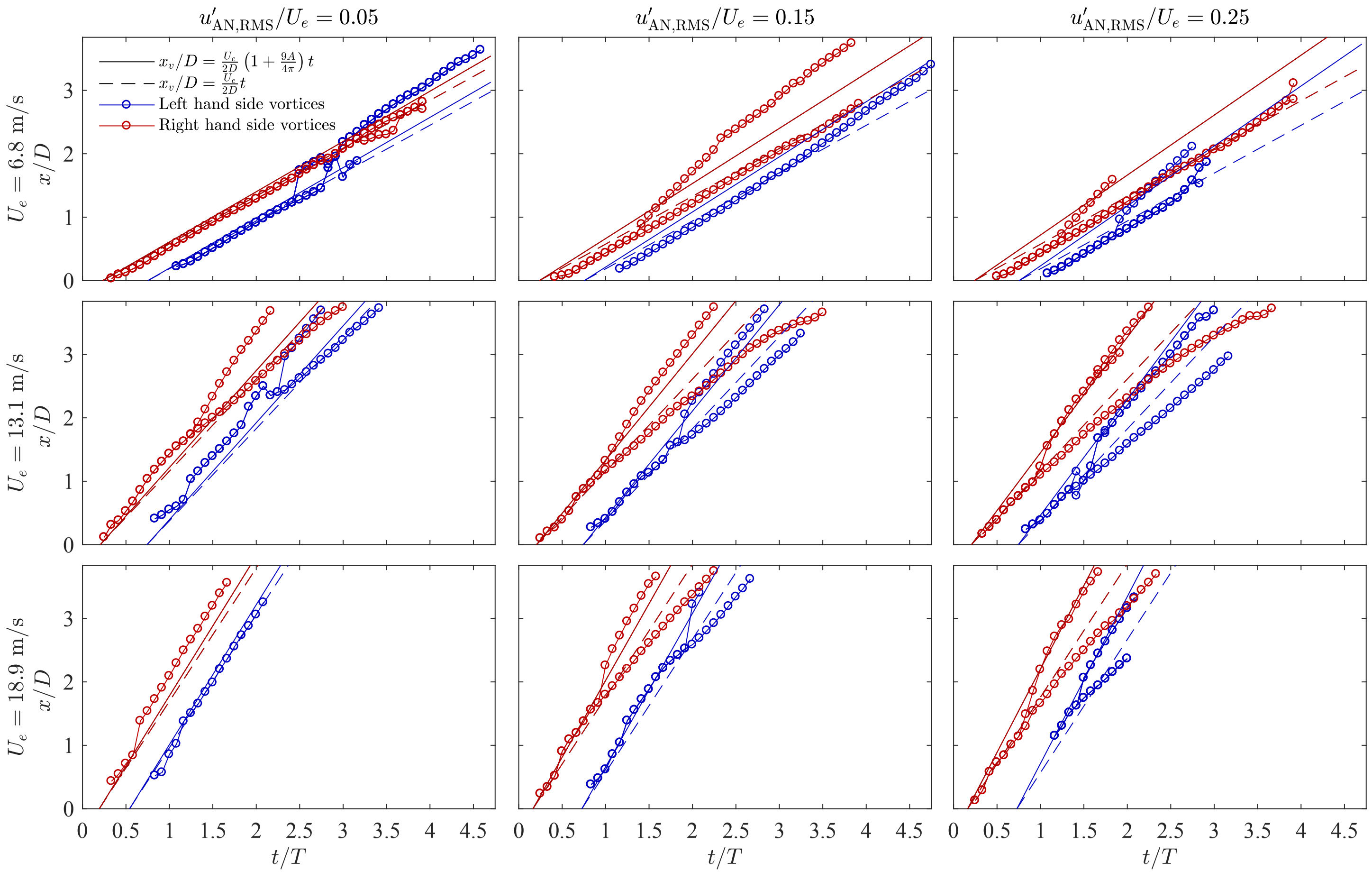

Figure 4.12: Axial position of the individual vortex structures on the left (blue) and right hand side (red) of the jet as a function of time for different exit velocities and forcing amplitudes, at $y/\frac{\lambda}{4} = 1$, $f = 450$ Hz.

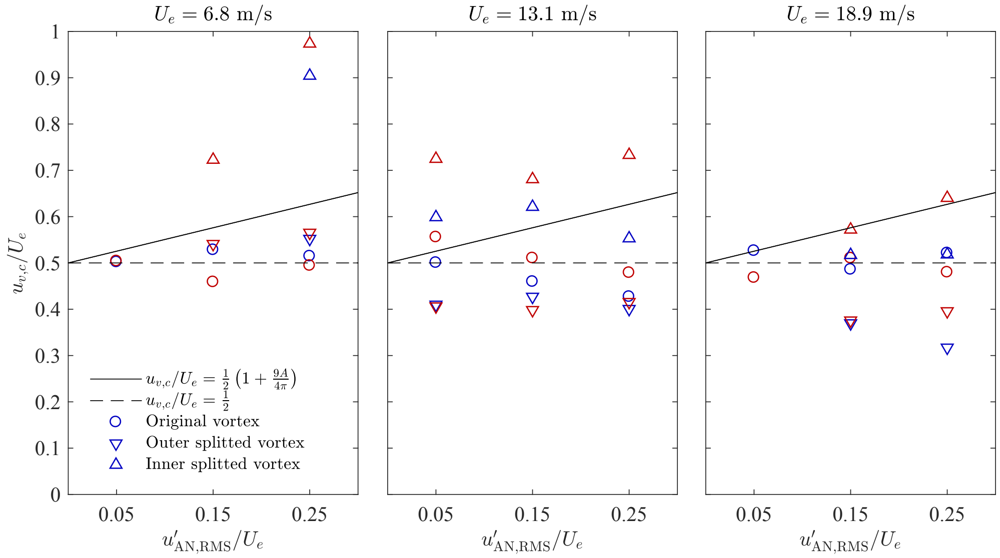

Figure 4.13: Axial velocity of the individual vortex structures on the left (blue) and right hand side (red) of the jet for different exit velocities and forcing amplitudes, at $y/\frac{\lambda}{4} = 1$, $f = 450$ Hz.

forcing amplitude. Row 2 in figure 4.11 has same St_D as row 3 in figure 4.14. By comparing these two cases we can find some differences. For the lowest amplitude, $u'_{\mathrm{AN,RMS}}/U_e = 0.05$, the vortex that rolls up is more pronounced and has higher vorticity for $f = 450$ Hz, compared to $f = 655$ Hz that never develops to a distinct vortex. For the same forcing amplitude the shear-layers in the $f = 655$ Hz case do not form the S shape that is seen for $f = 450$ Hz. For the two highest forcing amplitudes for $f = 655$ Hz, $U_e = 18.9$ m/s, the shear-layers roll up into an additional vortex, seen on the left hand side of the jet at $x/D \approx 1.1$, instead of forming the S shape. By investigating the time-series of the vorticity field and the path of the tracked vortices for the case $U_e = 18.9$ m/s, $f = 655$ m/s, $u'_{\mathrm{AN,RMS}}/U_e = 0.25$ in figure 4.15-4.16, it is clear that there are now three vortices formed on either side of the jet during each forcing cycle, two that are splitting up from the same vortex, and a third forming in anti-phase. This means that vortices are forming simultaneously on both sides of the jet twice per forcing period.

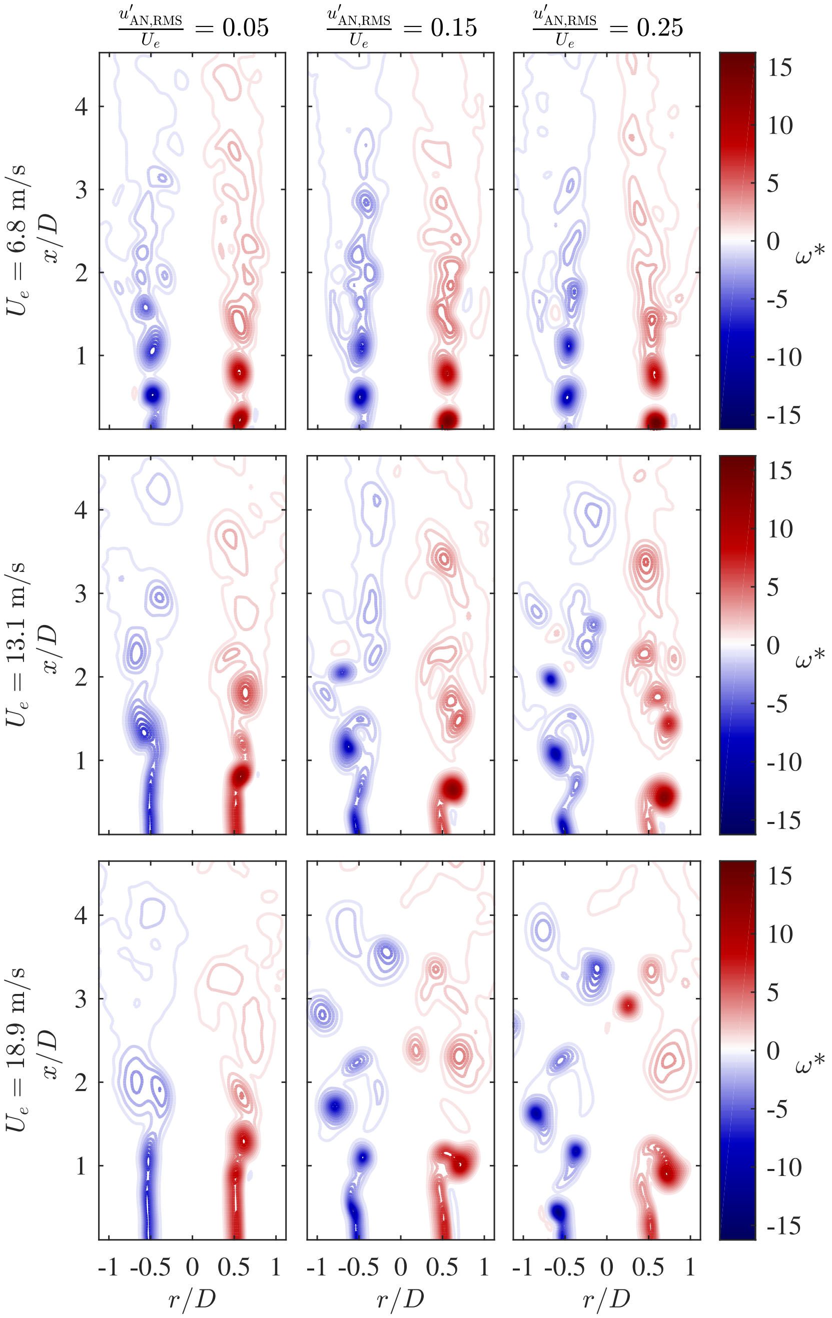

Figure 4.14: Phase averaged vorticity contours for different jet velocities and forcing amplitudes, for $f = 655$ Hz, $y/\frac{\lambda}{4} = 1$, $t/T = 0$.

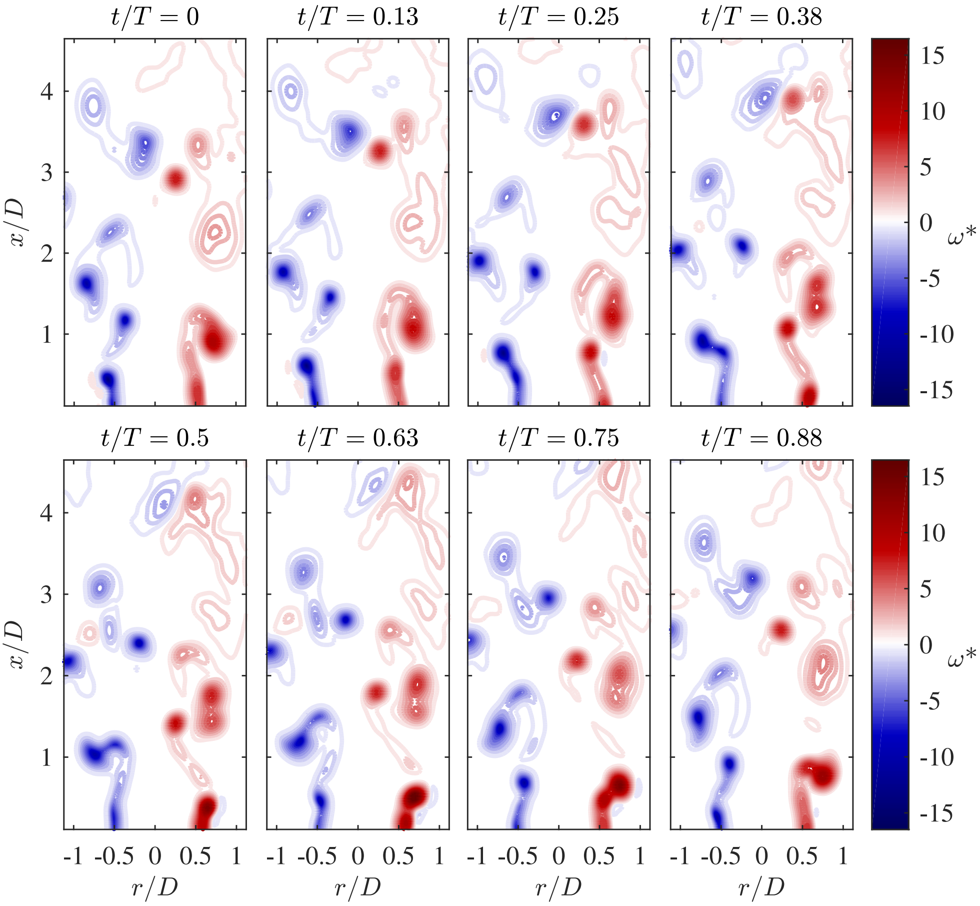

Figure 4.15: Time-series of phase averaged vorticity contours for $y/\frac{\lambda}{4} = 1$, $f = 655$ Hz, $U_e = 18.9$ m/s, $u'_{\mathrm{AN,RMS}}/U_e = 0.25$.

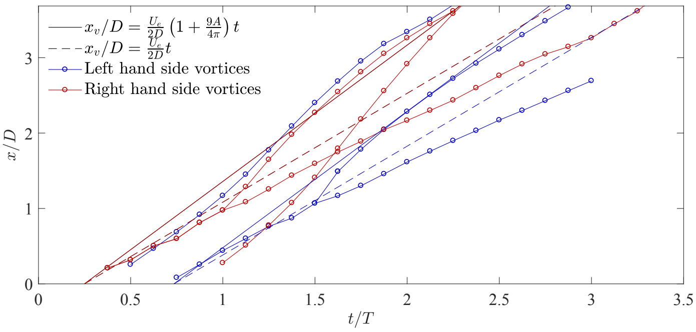

Figure 4.16: Axial positions of the individual vortex structures on the left (blue) and right hand side (red) of the jet as a function of time for $y/\frac{\lambda}{4} = 1$, $f = 655$ Hz, $U_e = 18.9$ m/s, $u'_{\mathrm{AN,RMS}}/U_e = 0.25$.

4.4 The role of the fluctuating velocity components in vortex formation

In this chapter the large-scale vortex structures in the near-field of the jet has been investigated. As the jet is moved from the pressure anti-node to the pressure node, the vortex structures change from the well-known axisymmetric vortex rings to more complex structures. Except for $f = 250$ Hz, these structures are seen as vortices in anti-phase in the $z = 0$ plane. At the pressure anti-node position, where only axial velocity fluctuations are present, the formation of the vortex rings start at t_{u0}. At the pressure node, where the transverse velocity fluctuations are at their maximum and the axial fluctuations are negligible, the results indicate that the vortex formation starts at t_{v0-} on the left hand side and t_{v0+} on the right hand side. The pressure anti-node and node positions show the pure response of the jet exposed to velocity fluctuations in the axial and transverse direction, respectively. For the other positions, both fluctuations are present simultaneously.

When comparing the vortex structures for varying jet positions in figure 4.6, similar structures can be found in neighboring plots suggesting that they change gradually as the jet position in the standing wave is changed. We can therefore divide vortex structures that are similar across the jet positions into groups. On the left hand side of the jet, vortex 1 at $y/\frac{\lambda}{4} = 0$ (and the left side vortex at

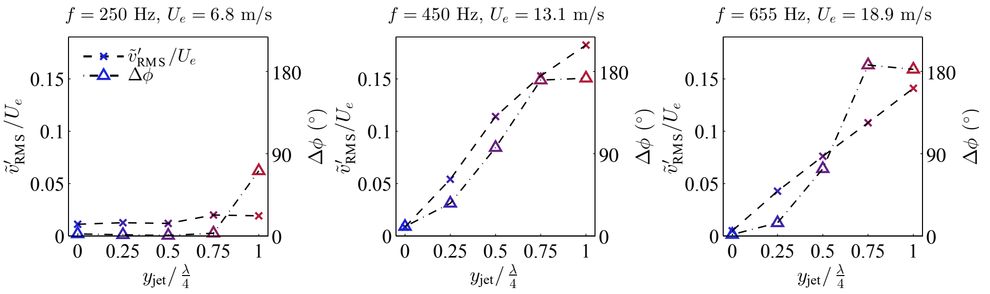

Figure 4.17: Transverse velocity RMS at the jet centerline, and phase difference, plotted against jet position for $u'_{\mathrm{AN,RMS}}/U_e = 0.25$.

$y/\frac{\lambda}{4} = 0.25$ that is not shown), vortex 4 at $y/\frac{\lambda}{4} = 0.5$, vortex 7 at $y/\frac{\lambda}{4} = 0.75$ and vortex 9b that splits off from vortex 9 at $y/\frac{\lambda}{4} = 1$ is one such group. Likewise, vortex 3 at $y/\frac{\lambda}{4} = 0.5$, vortex 6 at $y/\frac{\lambda}{4} = 0.75$ and vortex 9/9a at $y/\frac{\lambda}{4} = 1$ is another group of vortices with similar properties. On the right hand side of the jet the vortex structures have a less prominent development, and vortex 2, 5/5a, 8/8a and 10/10a changes only slightly between the jet positions. Vortex 5b, 8b and 9b, that all split up from the shear-layer of their original vortices, can be defined as a fourth group. An explanation for the similarities of the vortices within each group can be that the underlying mechanism that triggers and drives their formation is the same, and that their differences are due to a change in magnitude of the driving velocity fluctuation. This, however, cannot be the case for all the groups. The formation of vortex 2 for example, that is formed when the jet is placed in the pressure anti-node with only axial velocity fluctuations present, cannot be due to the same mechanisms as vortex 10/10a from the jet placed in the pressure node with only transverse velocity fluctuations present. Somewhere between these jet positions there might be a transition point where the transverse velocity fluctuations take over for the axial fluctuations as the driving mechanism. The same may also be the case for the group of vortices on the left side of the jet including vortex 1, 4, 7 and 9b. The two other groups of vortices, vortex 3, 6 and 9/9a, and vortex 5b, 8b and 9b, does not have any vortices at $y/\frac{\lambda}{4} = 0$ and $y/\frac{\lambda}{4} = 0.25$ where the axial fluctuations are dominating, and can possibly be a result of the transverse fluctuations alone.

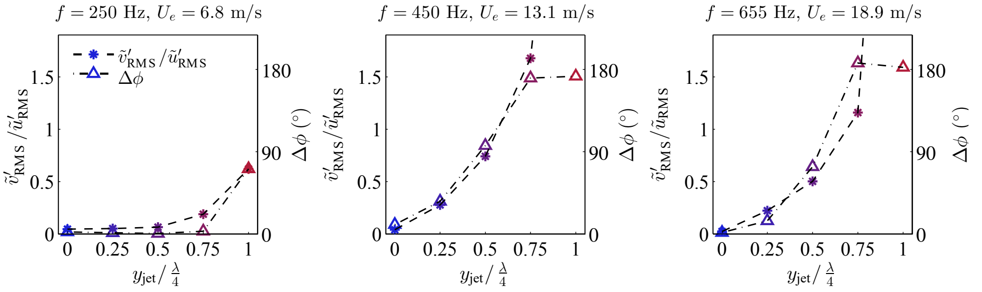

Figure 4.18: Velocity RMS ratio at the jet centerline, and phase difference, plotted against jet position for $u'_{\mathrm{AN,RMS}}/U_e = 0.25$.

The two groups that include vortices 1 and 2 at the pressure anti-node, are in phase at this jet position. As soon as the jet is moved away from the pressure anti-node to where the transverse velocity fluctuations are present, the symmetry breaks as the vortex on the left side of the jet moves downstream relative to the vortex on the right side. This suggests that there might be a relationship between this asymmetry and the presence of transverse velocity fluctuations. As a measure of the asymmetry we define the phase shift between the vortices on either side of the jet, $\Delta\phi$, as the time difference relative to one forcing period T between when the vortices have the same axial position. A time shift of T then corresponds to 360°. The phase is calculated as an average over an axial distance $D/2$ from $x/D = 0.6$ to $x/D = 1.1$. In figure 4.17, $\Delta\phi$ together with $\tilde{v}'_{\mathrm{RMS}}$ at $x/D = 0.6$, $r/D = 0$ is plotted against jet position for forcing frequencies $f = 250$ Hz, $f = 450$ Hz and $f = 655$ Hz. It is clear that these two variables do not consistently follow the same trend. For example, for $f = 250$ Hz the phase angle increases even though $\tilde{v}'_{\mathrm{RMS}}$ is approximately constant from $y/\frac{\lambda}{4} = 0$ to $y/\frac{\lambda}{4} = 1$. An alternative parameter that could determine the vortex phase shift is the ratio between the transverse and axial velocity fluctuations, $\tilde{v}'_{\mathrm{RMS}}/\tilde{u}'_{\mathrm{RMS}}$. Figure 4.18 shows $\tilde{v}'_{\mathrm{RMS}}/\tilde{u}'_{\mathrm{RMS}}$ on the left vertical axis and $\Delta\phi$ on the right, versus jet position. These two values follow a similar development for $f = 250$ Hz, and also for $f = 450$ Hz and $f = 655$ Hz from $y/\frac{\lambda}{4} = 0$ to $y/\frac{\lambda}{4} = 0.5$. As the jet position gets closer to $y/\frac{\lambda}{4} = 1$, however, $\Delta\phi$ locks to 180°, while $\tilde{v}'_{\mathrm{RMS}}/\tilde{u}'_{\mathrm{RMS}}$ continue to increase as $\tilde{u}'_{\mathrm{RMS}}$ goes to zero.

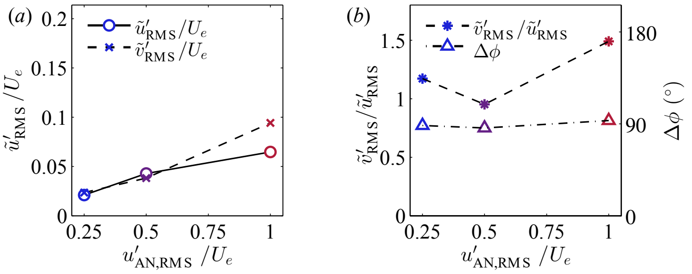

Figure 4.19: (a) Velocity RMS at the jet centerline and (b) velocity RMS ratio at the jet centerline and phase difference, as a function of forcing amplitude for $f = 250$ Hz.

In section 4.3, $f = 250$ Hz with forcing amplitudes up to $u'_{\mathrm{AN,RMS}}/U_e = 1.0$ was applied while the jet was positioned at the pressure node. As the forcing amplitude was increased, the vorticity fields became more similar to the pressure node response for the higher frequencies. Figure 4.19 (a) shows $\tilde{u}'_{\mathrm{RMS}}$ and $\tilde{v}'_{\mathrm{RMS}}$ at the jet centerline for these cases. Even for $u'_{\mathrm{AN,RMS}}/U_e = 1$, $\tilde{v}'_{\mathrm{RMS}}/U_e$ is lower than it was for the pressure node cases for $f = 450$ Hz and $f = 655$ Hz presented in section 4.2, and closer to the values at $y/\frac{\lambda}{4} = 0.5$ (see figure 4.17). Figure 4.19 (a) also shows that $\tilde{u}'_{\mathrm{RMS}}$ increases with almost the same rate as $\tilde{v}'_{\mathrm{RMS}}$ for increasing $u'_{\mathrm{AN,RMS}}/U_e$, implying that $y/\frac{\lambda}{4} = 1$ is not strictly a pressure node for $f = 250$ Hz. Figure 4.19 (b) compares the ratio of the two components of velocity fluctuations with the phase difference between the vortex structures on the left and the right side, similar to figure 4.18. Even though the ratio of the velocity fluctuations varies between 1 and 1.5, the phase difference is stable at $\Delta\phi \approx 90°$.

It seems not sufficient to describe the asymmetry in the jet only by the $\tilde{u}'_{\mathrm{RMS}}$ and $\tilde{v}'_{\mathrm{RMS}}$ values at the jet centerline, since this cannot explain why the development of the vortex structures are different on the left and right side of the jet from $y/\frac{\lambda}{4} = 0$ to $y/\frac{\lambda}{4} = 1$. An explanation for this difference can be that the jet experiences different pressure fluctuations in the shear-layer on the left and right hand side. The jet is then said to be *not* acoustically compact, and for this to apply the jet diameter relative to the acoustic wave needs to be sufficiently large. By assuming 1-dimensional pressure distribution in the jet enclosure, $p \sim \cos(2\pi(y + r)/\lambda)$, where y is the jet centerline position and r is the radial position in the jet, the forcing condition with the largest pressure difference between the left and the right jet shear-layer is $f = 655$ Hz, $y/\frac{\lambda}{4} = 0.75$. Then the pressure fluctuations are as much as 33 % larger at $r/D = -0.5$ (left side) compared to $r/D = 0.5$ (right side) (see appendix C). If this is the reason for the differences between the left and right side of the jet, it is expected that the left shear-layer, experiencing the highest pressure fluctuations, also would be where the highest axial velocity fluctuations occur. Figure 3.16, however, shows the opposite. For $f = 450$ Hz and $f = 655$ Hz, $\tilde{u}'_{\mathrm{RMS}}$ is largest on the right half of the jet, where the pressure fluctuations are smallest. This can be explained by the fact that the pressure fluctuations do not directly cause the axial velocity fluctuations. Instead, the pressure fluctuations in the jet enclosure propagate into the nozzle setup and the pipe upstream of the nozzle exit. These pressure waves then cause the air to oscillate at the nozzle exit. It is unlikely that the pressure differences sustain into the nozzle setup, which in reality would require an acoustic mode in the radial direction of the pipe upstream of the nozzle. Neither the asymmetry in the RMS profiles of *transverse* velocity in figure 3.16 is likely to be due to the pressure difference between the left and right shear-layer. Since the acoustic velocity in a standing wave is proportional to the pressure gradient, and the relative difference in this gradient over the nozzle is largest at $y/\frac{\lambda}{4} = 0.25$ for a 1-dimensional pressure wave, this jet position is also where $\tilde{v}'_{\mathrm{RMS}}$ would be expected to have the largest difference between the left and right shear-layer. In addition, for both velocity components the differences should increase with frequency since the wavelength then becomes smaller. None of these trends are found in the RMS profiles in figure 3.16.

Another more likely explanation for the differences in vortex structures on the left and right side of the jet for the positions between the pressure anti-node and node, is the phase between the axial and transverse velocity fluctuations experienced by the jet. This can also explain some of the differences in behavior seen for $f = 250$ Hz compared to the other frequencies. While the transverse velocity fluctuations are always 90° behind the pressure fluctuations, the phase between the axial velocity and pressure fluctuations was seen in figure 3.5 to depend on the forcing frequency. This means that also the phase between the axial and transverse velocity fluctuations is dependent on this frequency. As we have seen, transverse velocity fluctuations can drive vortex formation, and

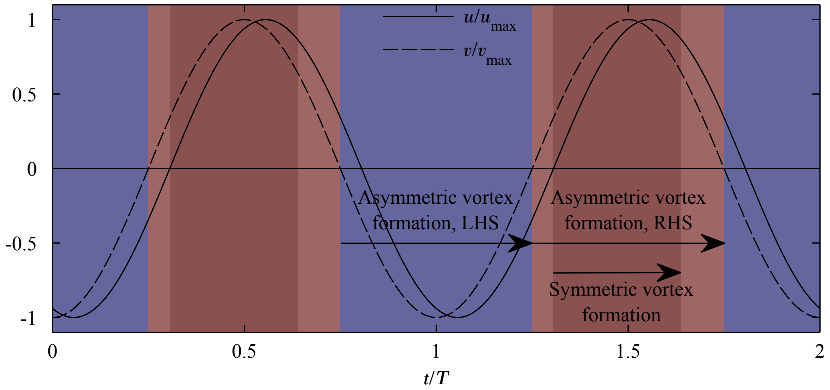

Figure 4.20: Illustration of periods of symmetric and asymmetric vortex formation, for $f = 450$ and $f = 655$ Hz.

vortex structures begin to form on the side of the jet where this velocity starts pointing away from the centerline. We can define the *radial* velocity similar to the transverse velocity, but with positive direction away from the jet centerline:

$$u_r(x,r) = \begin{cases} -v(x,r), & r \leq 0, \\ v(x,r), & r > 0. \end{cases} \tag{4.1}$$

This is the velocity that together with the axial velocity is of importance in vortex formation. The phase differences between the axial and radial velocity fluctuations are small on the right hand side for $f = 450$ Hz and $f = 655$ Hz, varying between 15° and 25°. On the left hand side, however, they are almost in anti-phase. This means that for the positions where both the axial and transverse velocity fluctuations of a certain amplitude is present, the two vortex formation mechanisms are working simultaneously on the right hand side while they are working against each other on the left hand side. This explains why the vortex structures are changing less on the right hand side compared to the left. Furthermore, it can explain the creation of two independent vortices on the left hand side for certain positions, *one* is created by the axial fluctuations (vortex 4 and 7 in figure 4.6), while the other is created by the transverse fluctuations (vortex 3 and 6).

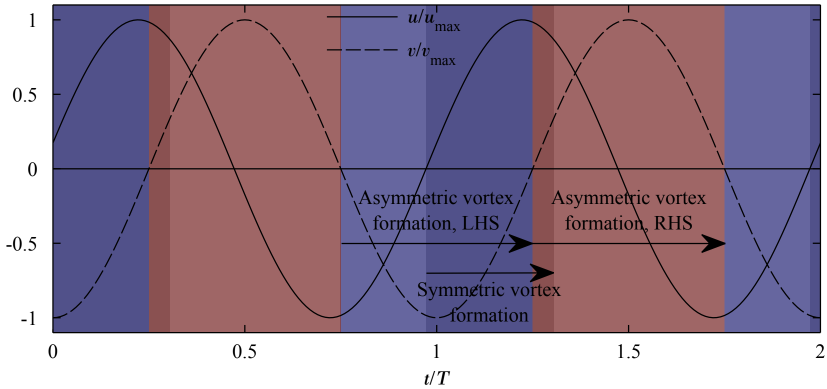

Figure 4.21: Illustration of periods of symmetric and asymmetric vortex formation, for $f = 250$ Hz.

By studying the vortex structures at $y/\frac{\lambda}{4} = 0$ and $y/\frac{\lambda}{4} = 1$, we have been able to state when in the forcing cycle the vortex formation happens for the cases with only axial and with only transverse fluctuations, respectively. By assuming that this can be superimposed to the jet positions where both axial and transverse velocity fluctuations are present, the different regimes of vortex formation when the transverse velocity fluctuation is 20° before the axial, which is approximately the case for $f = 450$ Hz and $f = 655$ Hz, is shown in figure 4.20. The duration of the two formation processes are determined by the pinch-off time, which is considered in chapter 5. Figure 4.20 shows that the whole period of symmetric vortex formation falls within the period of asymmetric formation on the right hand side, and not at all during the left hand side asymmetric formation. Figure 4.21, where the phase difference between $\tilde{u}'_{\mathrm{RMS}}$ and $\tilde{v}'_{\mathrm{RMS}}$ is similar to the $f = 250$ Hz case, shows another picture. Here the symmetric formation starts approximately halfway into the asymmetric formation on the left hand side, and finishes just after the right hand side asymmetric formation has started. This might explain some of the differences between the vortex structures for $f = 250$ Hz and the other frequencies. For $f = 450$ Hz and $f = 655$ Hz, the axial position of the left hand side vortex for constant t/T increases as the jet is moved away from the pressure anti-node, while the right hand side vortex has approximately constant axial position. This is in contrast to the $f = 250$ Hz case, where vortices on both sides move downstream, with the right hand side vortex slightly downstream of the left. If the vortices for the jet positions away from the pressure anti-node are still connected structures forming vortex rings, the reason for this asymmetry can be that the transverse velocity causes the rings to tilt in the direction this velocity has during the formation of the ring. This is in agreement with the direction of the tilting for the different forcing frequencies seen in figure 4.5. A velocity pointing into the jet center may also force the shear-layer to roll up further downstream. This can also explain why the jet bends to the right for the three middle jet positions for $f = 450$ Hz and $f = 655$.

Chapter 5

Symmetric and asymmetric pinch-off

An important phenomenon related to the formation of the vortex structures is the pinch-off. As described in section 1.2.3 this is the process where the vorticity from the jet stops entraining the ring. While the pinch-off of symmetric vortex rings are studied in detail (Aydemir *et al.*, 2012; Gharib *et al.*, 1998; Lawson & Dawson, 2013; Schlueter-Kuck & Dabiri, 2016), little is known about the pinch-off process of the asymmetric vortex structures formed in the near-field of transversely forced jets. This chapter will address this by applying three methods for pinch-off estimation, all which have shown to successfully predict pinch-off for axisymmetric vortex rings.

5.1 Vortex circulation and estimation of pinch-off

When discussing vortex ring pinch-off, the stroke ratio, $L_P/D = \bar{u}_p(t)t/D$, is an important parameter. Aydemir *et al.* (2012) showed that for a pulsed jet with velocity program $u_p \approx U_e(1 + A\sin(2\pi ft))$, the formation number is the same as for an impulsively starting jet, $(L_P/D)_{\mathrm{lim}} \approx 4$, as long as $t = T/3 = 1/(3f)$ is used for calculating the stroke ratio over one forcing cycle. In this study

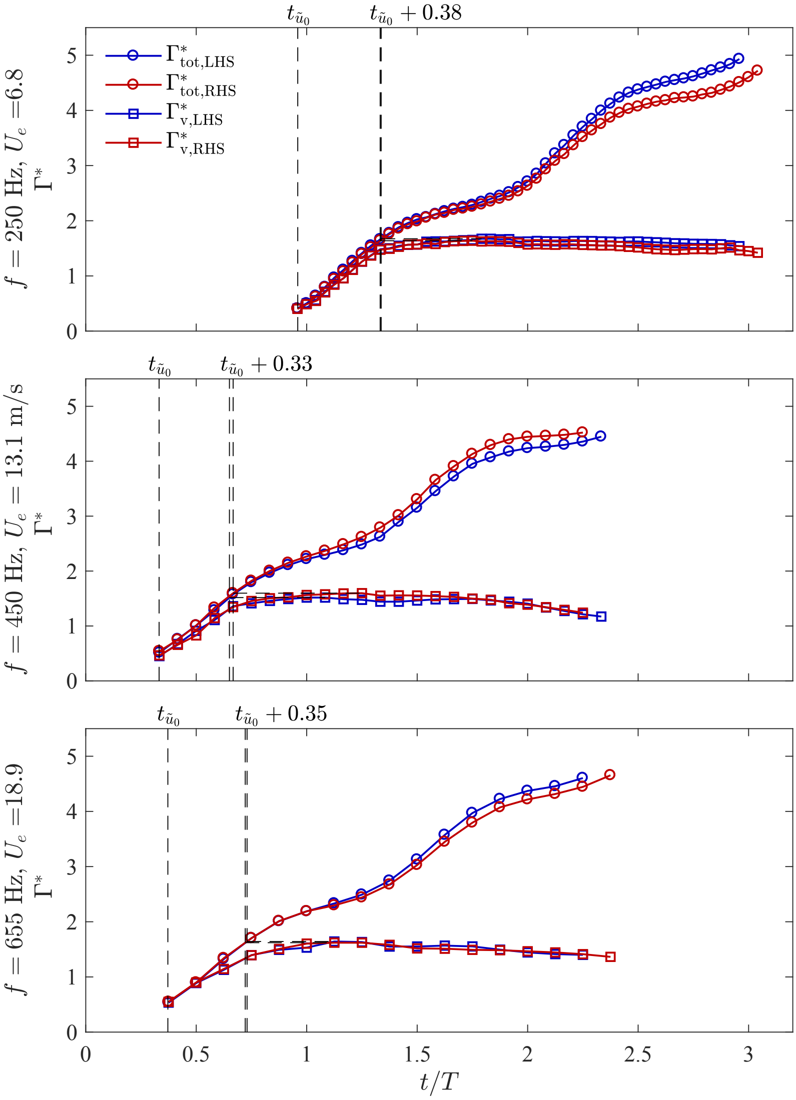

Figure 5.1: Total circulation (circles) and vortex circulation (squares) on the left and right hand side of the jet as a function of time at the pressure anti-node for $u'_{\mathrm{AN,RMS}}/U_e = 0.25$. The calculation of circulation is started at $t_{\tilde{u}_0}$.

the same sinusoidal velocity program in the axial direction is obtained in the pressure anti-node, and the effective forcing period can therefore be expected to be $T/3$ also in this case. The stroke ratio of a sinusoidal forcing cycle is obtained by combining equation (1.31) and (1.32)

$$L_P/D = \frac{U_e T}{3D}\left(1 + \frac{9A}{4\pi}\right) = \frac{1}{3St_D}\left(1 + \frac{9A}{4\pi}\right). \tag{5.1}$$

As seen, this stroke ratio is a function of Strouhal number and forcing amplitude. The largest stroke ratio obtained in this study is for the case $St_D \approx 0.35$ and $A \approx (\sqrt{2}/2) \cdot 0.25$. This gives $L_P/D \approx 1.07$, which is considerably smaller than the formation number $(L_P/D)_{\mathrm{lim}} \approx 4$. We can therefore expect that the pinch-off time for the symmetric vortex rings formed in the jet when positioned at the pressure anti-node, is limited by the stroke ratio and not the formation number, and that the rings should pinch off at $t/T \approx 0.33$.

As described in section 1.2.3, Gharib *et al.* (1998) introduced a method to find the pinch-off time of a vortex ring where the total circulation downstream of the nozzle exit was calculated and plotted against time. When the vortex ring was clearly separated from the shear-layer, also the circulation of the ring was calculated. The pinch-off time was then set to be when the total circulation had reached the value of steady circulation of the separated vortex ring. As explained in section 2.5.3, the method of Gharib *et al.* was adjusted to be able to calculate the circulation of the vortex structures obtained in this study. Figure 5.1 shows the total circulation and vortex circulation versus time for the jet placed in the pressure anti-node for different forcing frequencies using this method. The calculation was started at the same phase in the forcing cycle as Aydemir *et al.* (2012) did, at $t_{\tilde{u}_0}$. This is the time when the axial velocity fluctuations change from negative to positive as defined in figure 3.8, and is also the time in the forcing cycle when the axisymmetric vortex rings start to form. The circulation on the left and right hand side in figure 5.1 is similar for all frequencies, which is expected as the jet is symmetric at this position. The pinch-off time is found to lay between $t/T = 0.32$ and $t/T = 0.38$. This is in good agreement with the results by Aydemir *et al.* (2012), and the results deviate less than $0.03T$ from the pinch-off times achieved when using the original method by Gharib *et al.* on the same data (see figure B.5 in appendix

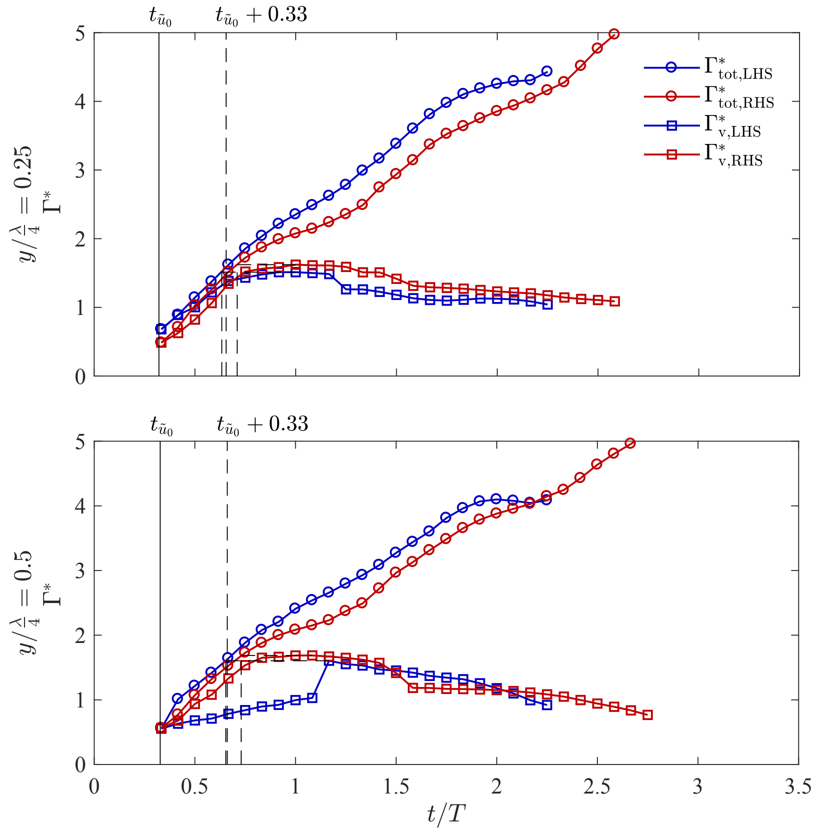

Figure 5.2: Total circulation (circles) and vortex circulation (squares) on the left and right side of the jet as a function of time, for $f = 450$ Hz, $U_e = 13.1$ m/s, $u'_{\text{AN,RMS}}/U_e = 0.25$. The calculation of circulation is started at $t_{\tilde{u}_0}$.

B). In addition, the shape of the total circulation plots is similar to the slug model circulation shown in figure 1.6, with a linearly growing term plus a term fluctuating with the forcing frequency.

For the jet placed at $y/\frac{\lambda}{4} = 0.25$, shown in the upper part of figure 5.2, both the total circulation and the vortex circulation have similar development as for the anti-node, even though there is a small asymmetry as the total circulation is slightly lower and the pinch-off happens slightly later on the right hand side compared to the left. At $y/\frac{\lambda}{4} = 0.5$, shown in the lower part of figure 5.2, the total circulation is very similar to $y/\frac{\lambda}{4} = 0.25$. On the right hand side the vortex circulation has an almost identical development as the right hand

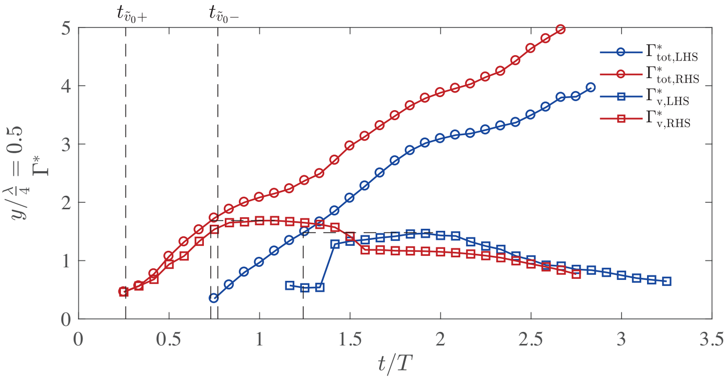

Figure 5.3: Total circulation (circles) and vortex circulation (squares) on the left and right side of the jet as a function of time, for $y/\frac{\lambda}{4} = 0.5$, $f = 450$ Hz, $U_e = 13.1$ m/s, $u'_{\text{AN,RMS}}/U_e = 0.25$. The calculation of circulation is started at $t_{\tilde{v}_0-}$ and $t_{\tilde{v}_0+}$ on the left and right hand side, respectively.

side at $y/\frac{\lambda}{4} = 0.25$ until its maximum value at $t/T \approx 1$. At this time, the vortex circulation on the right hand side at $y/\frac{\lambda}{4} = 0.5$ includes both the vortex marked as 5a and 5b in figure 4.6. Shortly after this the circulation start to decrease, before it stabilizes at a lower circulation value at $t/T \approx 1.58$. The reason for this decrease in vortex circulation is that vortex 5b becomes weaker and eventually the tracking algorithm is no longer able to track the vortex. From $t/T \approx 1.58$, $\Gamma^*_{\text{v,RHS}}$ includes only the circulation of vortex 5a. The vortex circulation on the left side at $y/\frac{\lambda}{4} = 0.5$ grows considerably slower than the other vortex circulations for the first three quarters of the cycle. During this period, $\Gamma^*_{\text{v,LHS}}$ includes only the circulation of the vortex marked as 4 in figure 4.6. Then there is a jump in the vortex circulation at $t/T \approx 1.17$ at the same time as vortex 3 (see figure 4.6) is tracked by the vortex tracking algorithm. After this point, $\Gamma^*_{\text{v,LHS}}$ is the sum of circulation of both vortex 3 and 4, and is at about the same level as $\Gamma^*_{\text{v,RHS}}$. Despite a different development of the left hand side vortex circulation, the estimated pinch-off time on both sides are similar as for the jet positioned at $y/\frac{\lambda}{4} = 0.25$, with the vortex on the right side pinching off slightly later than the left vortex.

Until now the circulation is calculated from $t_{\tilde{u}_0}$, which is when the vortex structures start to form in the axisymmetric case. However, in section 4.2 we saw that *when* in the forcing cycle the vortex structures form is highly affected by the jet position. At the pressure node, the vortex structures start to form at $t_{\tilde{v}0-}$ and $t_{\tilde{v}0+}$ on the left and right hand side, respectively, while for the positions in between the picture is more complicated. As shown in figure 3.3, $t_{\tilde{v}0-}$ marks the time in the forcing cycle when the transverse velocity fluctuations change direction from right to left, while $t_{\tilde{v}0+}$ marks when the transverse velocity fluctuations changes from left to right. In figure 5.3, circulation versus time is shown again for $y/\frac{\lambda}{4} = 0.5$, but now the circulation on the left side of the jet is calculated starting at $t_{\tilde{v}0-}$, while the circulation on the right hand side is calculated starting at $t_{\tilde{v}0+}$. Both the total and vortex circulation for the right side of the jet is almost identical as the lower plot of figure 5.2, which is expected since $t_{\tilde{v}0+} \approx t_{\tilde{u}0}$ for $f = 450$ Hz. For the left hand side, the total circulation is shifted towards $t_{\tilde{v}0-}$, but the shape is not changing much compared to when the circulation was calculated from $t_{\tilde{u}0}$. The vortex circulation, however, has a different shape. It starts when vortex 3 (see figure 4.6) is tracked by the vortex tracking algorithm, which is also the time when the vortex circulation calculated from $t_{\tilde{u}0}$, lower plot in figure 5.2, had a jump. Then, the vortex circulation calculated from $t_{\tilde{v}0-}$ has a jump when vortex 4 are tracked by the vortex tracking algorithm at approximately $t/T = 1.42$. The pinch-off time is estimated to $t \approx t_{\tilde{v}0-} + 0.5T \approx t_{\tilde{v}0+}$. This is when the transverse velocity is zero and the jet starts to move to the right, away from the vortices formed on the left hand side. Around $t/T = 2$, the vortex circulation starts to decrease, and again stabilizes around $t/T = 2.58$. From figure 4.6 this can be identified as when vortex 3 moves outside the field of view. Therefore, the vortex circulation at $t/T = 2.58$ represents the circulation of vortex 4 alone. By adding this to the circulation of vortex 3 at $t/T = 1.33$, it matches quite well with the vortex circulation at $t/T = 1.92$ where the circulation from both vortex 3 and 4 is included: $\Gamma_3^* + \Gamma_4^* = 0.54 + 0.92 \approx 1.48 = \Gamma_{3+4}^*$.

These results show that the circulation plots and the estimated pinch-off time can be highly dependent on when in the forcing cycle the calculation is started. By defining the start of the forcing cycle at $t_{\tilde{u}0}$, vortex 3 forms later and is positioned upstream compared to vortex 4. Therefore, the pinch-off time at $t/T \approx 0.74$ from the lower plot in figure 5.2 can be seen as an estimate of the pinch-off time of vortex 3 since this is attached to the shear-layer later in the cycle. With the same reasoning, figure 5.3 gives the estimate of the pinch-off time of vortex 4.

Figure 5.4 and 5.5 show some examples of the circulation against time for the jet placed in the pressure node. For $y/\frac{\lambda}{4} = 0.75$, and for the rest of the forcing conditions at the pressure node, the circulation plots did not give any reasonable results, and are therefore left out. The circulation was calculated from when the vortex structures started to form at this jet position, which was shown in section 4.3 to be at $t_{\tilde{v}0-}$ for the vortices on the left hand side and at $t_{\tilde{v}0+}$ for the vortices on the right hand side. The pinch-off, seen on the figures as the time when the horizontal, dashed line crosses the line of total circulation, happens in anti-phase on either side of the jet. For most of the cases the pinch-off time coincides with $t_{\tilde{v}0-} \approx t_{\tilde{v}0+} + 0.5T$ on the right hand side and with $t_{\tilde{v}0+} \approx t_{\tilde{v}0-} + 0.5T$ on the left hand side, both marked with vertical, dashed lines. This is the time when the jet starts to move away from the side where the vortices are rolling up, and this change in direction of the jet seems to initiate the pinch-off.

According to the slug model, the total circulation should increase linearly for the node position since the axial velocity is nearly constant here ($u'_{\mathrm{RMS}}/U_e < 0.04$ for all cases with $f = 450$ Hz and $f = 655$ Hz), which according to equation (1.24) gives a nearly constant vorticity flux. For the low forcing cases, $u'_{\mathrm{AN,RMS}}/U_e = 0.05$, in figure 5.4, and both cases in figure 5.5, the total circulation grows approximately linearly in time. For the higher forcing cases in figure 5.4, however, the growth in total circulation is, similar to the pressure anti-node cases, fluctuating with the forcing frequency. But unlike for the anti-node, the increase in circulation for these cases stops suddenly, suggesting that the oscillating term of the circulation is on the form $\sim -\sqrt{1 - \cos(2\pi t^*)}$ instead of $\sim 1 - \cos(2\pi t^*)$ as in equation (1.30). This might be due to nonlinear effects, that gets stronger as the forcing amplitude is increased and the vortex structures grow. The time when the total circulation suddenly stops to increase, coincides quite well with the pinch-off time. The vortex circulation and the average growth of the total circulation does not change significantly with forcing amplitude, but are, in accordance with the slug model, growing with decreasing Strouhal number. One possibility is therefore that the average vorticity flux is

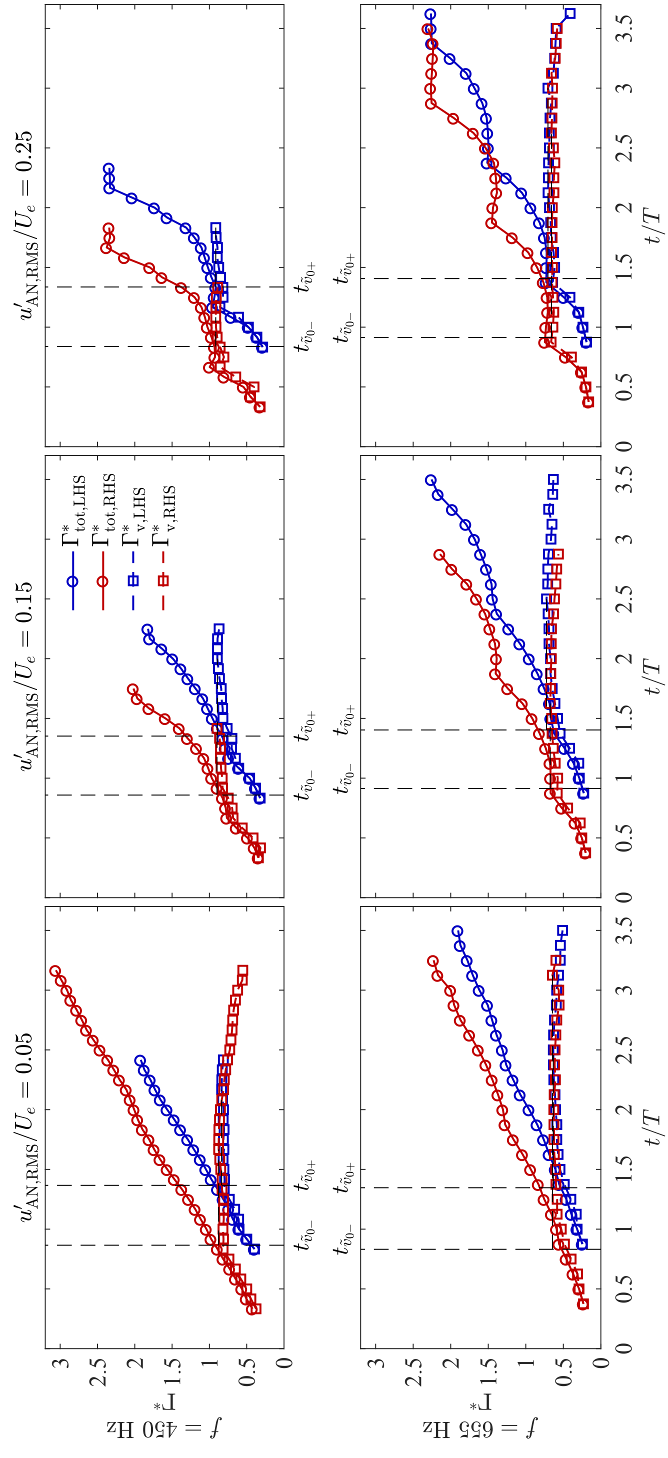

Figure 5.4: Total circulation (circles) and vortex circulation (squares) on the left and right side of the jet as a function of time for varying forcing frequencies and amplitudes at the pressure node for $U_e = 6.8$ m/s.

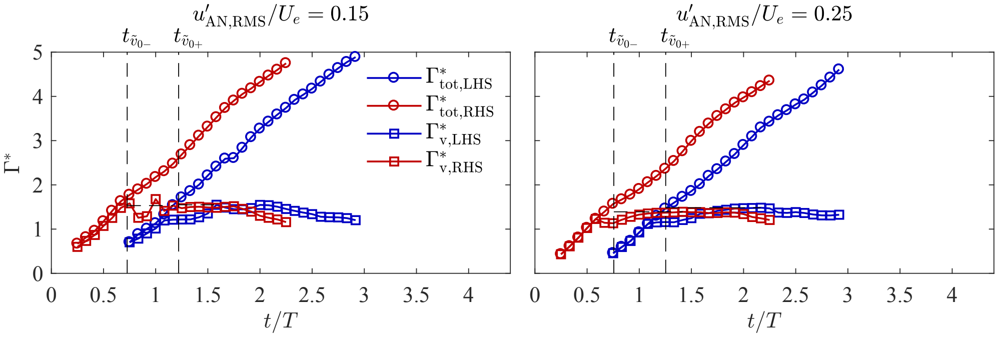

Figure 5.5: Total circulation (circles) and vortex circulation (squares) on the left and right side of the jet as a function of time for varying forcing amplitudes at the pressure node for $f = 450$ Hz, $U_e = 13.1$ m/s.

determined by the axial velocity and follows the slug model, while the effect of the transverse velocity fluctuation is that it redistributes the vorticity flux within the forcing cycle.

5.2 Investigation of pressure maxima and their role in the pinch-off process

As described in section 1.2.3, Lawson & Dawson (2013) showed that the formation of a trailing pressure maximum can be used as an estimate for the pinch-off time of vortex rings formed in a starting jet. The adverse pressure gradient upstream of the pressure maximum stops the vorticity flux from the jet to enter the ring structure, and therefore divides the ring from the rest of the shear-layer. Lawson & Dawson found that the formation of the trailing pressure maximum coincided with the pinch-off time estimated using the circulation method by Gharib *et al.* (1998), when tested on a longitudinally forced, synthetic jet. This section will investigate if the same holds for the vortex structures formed in a transversely forced jet, and specifically the method will be tested on some of the same forcing conditions as investigated in the previous section; forcing frequency of $f = 450$ Hz, and jet positions $y/\frac{\lambda}{4} = 0$, $y/\frac{\lambda}{4} = 0.25$, $y/\frac{\lambda}{4} = 0.5$ and $y/\frac{\lambda}{4} = 1$.

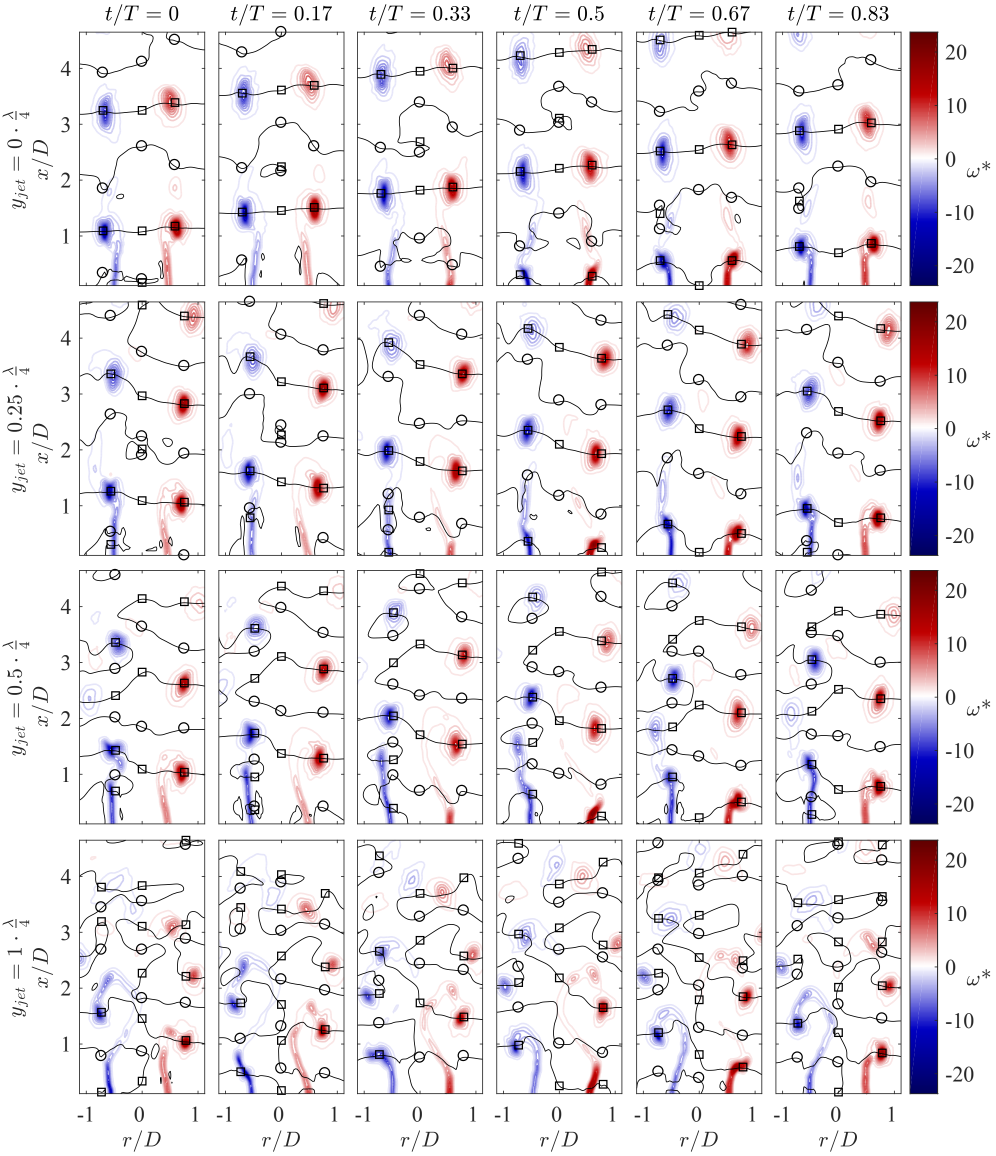

Figure 5.6: Time-series of phase averaged vorticity contours for $f = 450$ Hz, $U_e = 13.1$ m/s, $u'_{\mathrm{AN,RMS}}/U_e = 0.25$. Also, contours of the x component of material acceleration, $Du/Dt = 0$, are shown in black. On $r = 0$ and in the shear-layers, ◯ represents a pressure maximum and ☐ a pressure minimum.

Figure 5.6 shows time series of phase averaged vorticity for these forcing conditions together with contours of $Du/Dt = 0$, which is calculated as described in section 2.5.4. According to equation (2.22), $Du/Dt = 0$ is equivalent to $\partial p/\partial x = 0$ since viscous forces are assumed to be negligible. As previously described, the vortex structures formed somewhere in these phase averaged time-series can be followed until the end of the cycle, continuing at $t = 0$ and through several cycles until they disappear out of the field of view. The upper row shows the jet positioned at the pressure anti-node. At $t/T \approx 0.5$, a $Du/Dt = 0$ contour appears close to the nozzle exit. This contour represents a local pressure minimum in x direction, and is marked with □ on $r = 0$ and in the shear-layers. Here the shear-layer is defined as the radial position on each side of $r = 0$ having the lowest pressure when averaging in time and x direction. The contour crosses the field of view horizontally, through the vortex cores that has started to form in each shear-layer, and follows the vortex ring as it moves downstream. At $t/T \approx 0$, when the vortex ring has moved around one diameter away from the nozzle exit, an additional $Du/Dt = 0$ contour starts to form upstream of the ring, and after some time steps this has developed to a contour crossing the field of view horizontally. This contour represents a local pressure maximum in x direction, and is marked with ○ on $r = 0$ and in the shear-layers. The contour keeps an almost constant distance behind the ring as it convects downstream. This is the only pressure maximum appearing before a new vortex ring forms during the next forcing cycle. For all other forcing conditions tested with the jet positioned at the anti-node, only one pressure maximum appears between two consecutive vortex rings. This is in contrast to the experiments by Lawson & Dawson (2013), which showed two pressure maxima between the rings, one trailing maximum belonging to the downstream ring and one leading maximum belonging to the upstream ring. In addition, a pressure minimum was found between these maxima. The difference between the pressure fields in the two studies is probably related to the fact that the separation distance between the vortex rings are considerably smaller in the current experiment. One explanation can therefore be that the short ring spacing has caused the trailing pressure maximum of the downstream ring to merge with the leading pressure maximum of the upstream ring. If so, the maximum is expected to split in two for sufficient ring distance, i.e. low enough Strouhal number. Alternatively, the same pressure extrema that was seen in the measurements by Lawson & Dawson may exist in the flow, but they are not shown in the result, e.g. because of the resolution of the data or the processing method. The current measurements have a significantly lower temporal resolution than the measurements by Lawson & Dawson (2013)[a], which may affect the accuracy of the temporal derivatives calculated. Also, an averaging filter has been applied to the data to remove noise, and the position and shape of the $Du/Dt = 0$ contours have shown to be sensitive to the filter size.

The phenomena can be investigated analytically by combining two Hill's vortices given in equation (1.22), with centers at $x = \pm x_0$, $r = 0$, and with uniform axial flow equal to the mean jet exit velocity U_e:

$$\psi = \begin{cases} -\frac{3}{4}\frac{U_e r^2}{a^2}\left(a^2 - (x - x_0)^2 - r^2\right), & (x - x_0)^2 + r^2 \leq a^2. \\ -\frac{3}{4}\frac{U_e r^2}{a^2}\left(a^2 - (x + x_0)^2 - r^2\right), & (x + x_0)^2 + r^2 \leq a^2. \\ \frac{1}{2}U_e r^2\left(1 - \frac{a^3}{((x-x_0)^2+r^2)^{3/2}} - \frac{a^3}{((x+x_0)^2+r^2)^{3/2}}\right), & (x \pm x_0)^2 + r^2 > a^2. \end{cases} \tag{5.2}$$

The vorticity of a Hill's vortex ring is bounded by a sphere of radius a. The material acceleration, $D\mathbf{u}/Dt$, of this flow field is shown in figure 5.7 with varying separation distance between the two vortex rings. As for figure 5.6, contours of $Du/Dt = 0$ are shown in black, and on $r = 0$, ○ represents a local pressure maximum in x direction and □ a pressure minimum. As the separation distance between the vortex rings decreases, the two pressure maxima between the rings come closer together. Then for $x_0 = 1.25a$, the pressure minimum disappears and only one pressure maximum exists. By closer investigation it is found that the limiting value of x_0 when the maxima merge is $x_0 \approx 1.26a$.

The vortex centers for a Hill's vortex are located at $r = \pm\frac{\sqrt{2}}{2}a \approx \pm 0.71a$, while the axial separation distance between two ring centers are $2x_0$. For $x_0 = 1.26a$, the separation distance between the ring centers are approximately 1.78 times the separation distance between the vortex centers. In figure 5.6 the corresponding

---

[a] 8-24 measurements per forcing cycle (depending on forcing frequency) in the current study, compared to 41 measurements per forcing cycle in Lawson & Dawson (2013)

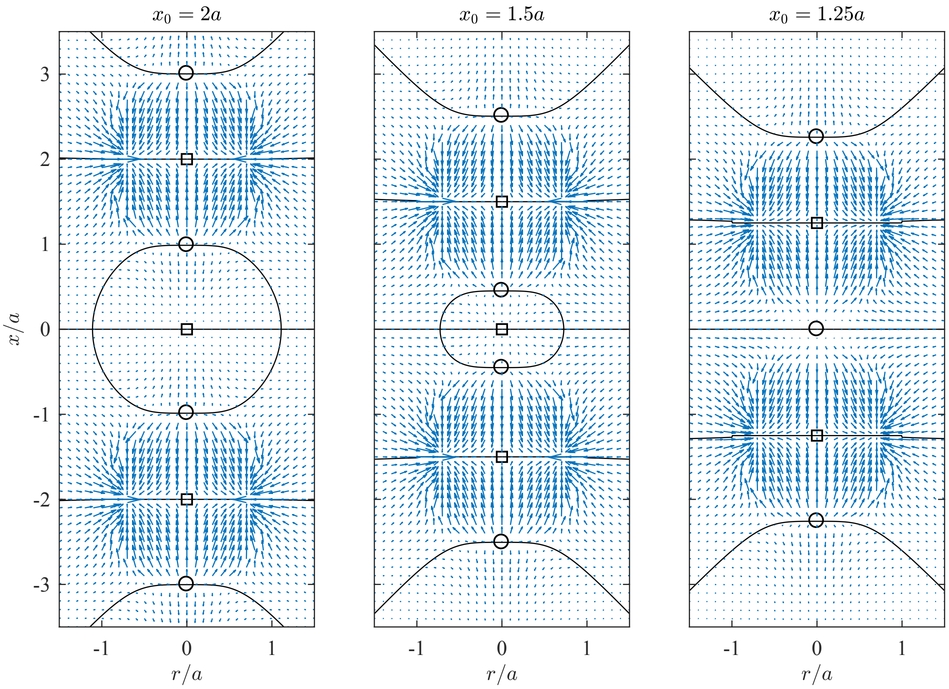

Figure 5.7: Material acceleration, $D\mathbf{u}/Dt$, of two Hill's vortex rings with common symmetry axes and separation distance $4a$ (left), $3a$ (middle) and $2.5a$ (right) between the ring centers. Contours of $Du/Dt = 0$ are shown in black, and on $r = 0$, ○ represents a pressure maximum and □ a pressure minimum.

ratio is approximately 1.5, and the vortices in the experiments are therefore more closely spaced than the limiting distance where the pressure maxima between two Hill's vortices merge. Even though the vorticity distribution of the vortex rings in the experiments are clearly different from a Hill's vortex ring, this supports that there might be only one pressure maximum between the vortex rings in the experiments. However, while the contour between the vortex rings in the plot to the right in figure 5.7 is a completely straight, horizontal line, this is not the case for the contour in the upper line of figure 5.6. At $t/T = 0.33$, both the contour upstream and downstream of the vortex ring form almost enclosed rings around the jet centerline, similar to the middle plot in figure 5.7. This may indicate that for the vortex separation in the experiments, the trailing contour of the downstream ring and the leading contour of the upstream ring are about to merge into one.

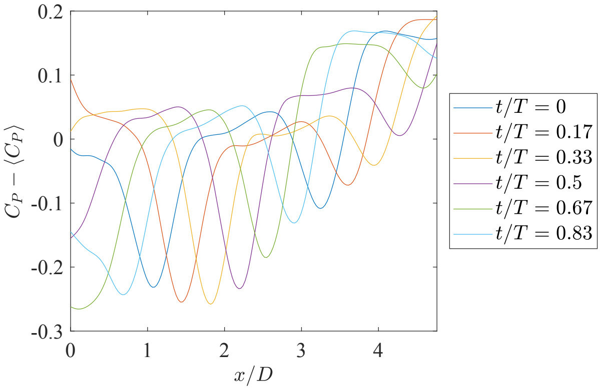

Figure 5.8: Pressure along the centerline for different times in the forcing cycle for $y/\frac{\lambda}{4} = 0$, $f = 450$ Hz, $U_e = 13.1$ m/s, $u'_{\mathrm{AN,RMS}}/U_e = 0.25$.

This is investigated further by plotting the pressure along the centerline for different times in the forcing cycle, as shown in figure 5.8. The pressure coefficient C_P is calculated from phase averaged velocity fields as explained in chapter 2.5.4. $\langle C_P \rangle$, the pressure coefficient averaged in x direction, is subtracted from the pressure coefficient, and the reason for this will be explained in section 5.3. This plot supports that the two pressure maxima between the vortex rings are about to merge. Between $t/T = 0.33$ and $t/T = 0.66$, where the vortex formation happens according to the middle circulation plot in figure 5.1, a pressure minimum develops at the nozzle exit, $x/D = 0$. Later, while the pressure minimum moves downstream, a saddle point with a maximum at $x/D = 0$ forms, instead of the local pressure maximum that would be expected behind a vortex ring. This is probably due to the decreasing velocity program of the jet in this period, which causes the pressure at the nozzle exit to rise until the jet velocity reaches a minimum at $t/T \approx 0.08$. At $t/T = 0.33$, the pressure at $x/D = 0$ has dropped and a wide peak has formed. This is most likely the result of the trailing pressure maximum that is partly merged with the leading pressure maximum of the upstream vortex ring. In the following time steps a region of negative second derivative appears in the middle of the peak, which can be traces of the pressure minimum between the rings.

The separation distance between vortex rings formed by periodic forcing are decreasing with increasing St_D. In the experiments by Lawson & Dawson

(2013), St_D is considerably smaller than in the current study, which can explain why the same effect of merging of the pressure maxima between the vortex rings is not observed. In the studies by Gharib *et al.* (1998) and Schlueter-Kuck & Dabiri (2016), only one vortex ring was generated by the starting jet for each experimental run, and naturally no interaction between vortex rings was seen. In other studies, like the experiments by Aydemir *et al.* (2012) and the simulations by Asadi *et al.* (2018), periodic vortex rings was generated with larger St_D than in the current study, but here the pressure fields were not investigated.

Figure 5.7 shows that the merging of the pressure maxima affects the position of the trailing and leading pressure maximum relative to the center of the Hill's vortex rings. When the vortices are far away from each other, the pressure maxima are a distance a from the ring center. For this case the trailing and leading pressure maxima of the ring marks the extent of its vorticity along the symmetry axis. Lawson & Dawson (2013) used this as an argument for the pressure maxima as a good estimate of the extent of the vortex ring bubble, both upstream and downstream. In the limiting case when the pressure maxima merges, for $x_0 \approx 1.26a$, the maximum is positioned at $x = 0$, which is $1.26a$ from the ring centers. Then the trailing and leading pressure maxima is not longer an accurate estimate of the vortex ring boundaries. The position of the pressure maxima in the experiments might also be affected by the other vortex rings in a similar way as is seen to happen for the Hill's vortex. This will however not likely be an issue when using the pressure maximum to estimate vortex pinch-off and time of formation, since the formation process of one ring is expected to finish before the next ring starts to form. If so, the position of the trailing pressure maximum is not affected during the formation process.

Figure 5.9 plots the axial position of the trailing pressure maxima from the upper row of figure 5.6 together with the vortex core centers, as a function of time. The position of the trailing pressure maxima is taken from the shear-layer, and not at the centerline as was done by Lawson & Dawson (2013). For the jet positioned in the pressure anti-node, the pressure maxima at the centerline is in general found to be downstream of the pressure maxima at the shear-layer, as seen in figure 5.6. This is in agreement with the findings of Schlueter-Kuck

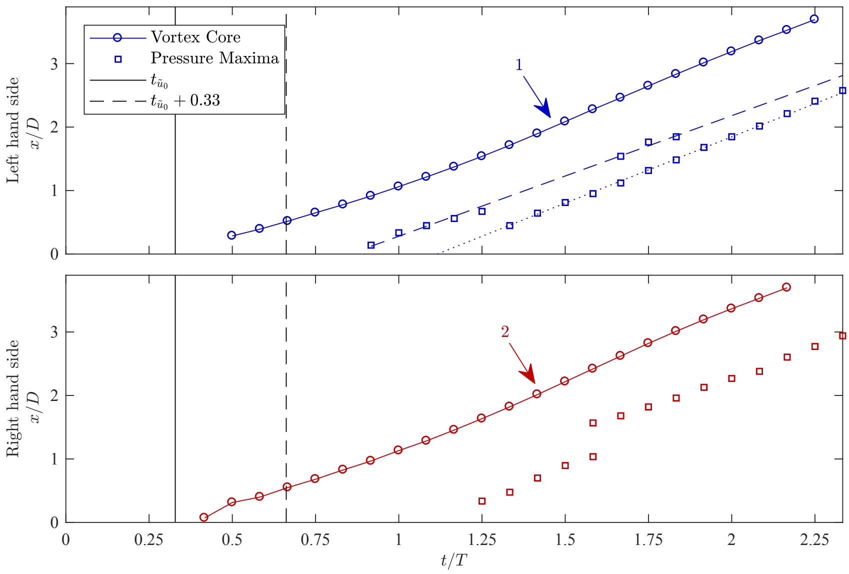

Figure 5.9: Axial position of the individual vortex structures together with the pressure maxima on the left and right hand side of the jet as a function of time, for $y/\frac{\lambda}{4} = 0$, $f = 450$ Hz, $U_e = 13.1$ m/s, $u'_{\mathrm{AN,RMS}}/U_e = 0.25$.

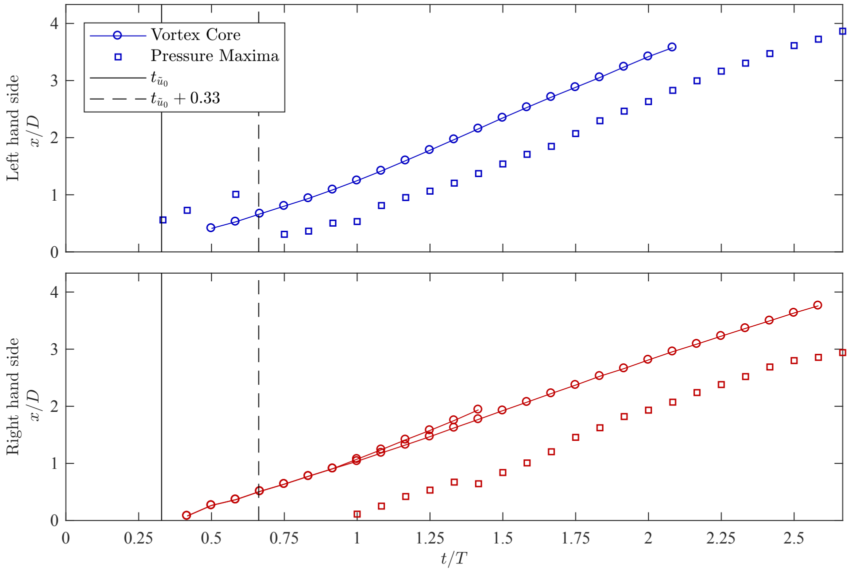

Figure 5.10: Axial position of the individual vortex structures together with the pressure maxima on the left and right hand side of the jet as a function of time, for $y/\frac{\lambda}{4} = 0.25$, $f = 450$ Hz, $U_e = 13.1$ m/s, $u'_{\mathrm{AN,RMS}}/U_e = 0.25$.

& Dabiri (2016), who reported a difference in pinch-off time of approximately $0.1T$ between using the pressure at the centerline compared to in the shear-layer. Using the pressure maxima at the shear-layer is also necessary for the jet positions with asymmetric flow fields, where the pressure maximum at the centerline does not give information about the individual vortex structures on each side of the jet. On both sides of the jet the pressure maximum in the shear-layer is positioned upstream of the vortex ring, but instead of forming a straight line of constant velocity, the pressure maxima seem to follow two different paths. This supports the hypothesis that the trailing and leading pressure maxima of the consecutive vortex rings are about to merge, and the pressure maxima shown are most likely the one with the highest pressure at each time instant on the broad peaks in figure 5.8. This is indicated on the left hand side by two regression lines, one dashed, blue line representing the paths of the trailing pressure maxima of the downstream vortex ring, and one dotted, blue line representing the leading pressure maxima of the upstream vortex ring. The vertical, dashed line in black color shows $t_{\tilde{u}_0} + 0.33T$, which is where the circulation plots in section 5.1 estimated pinch-off for this jet position. In the shear-layer on both sides of the jet the pressure maxima appear after the dashed line, also when extrapolating the path of the pressure maxima down to the $x = 0$ line. Also for $f = 250$ Hz and $f = 655$ Hz at this jet position, the trailing pressure maxima give estimations of pinch-off later than the circulation plots.

The two middle rows in figure 5.6 show vorticity and $Du/Dt = 0$ contours for the jet positioned at $y/\frac{\lambda}{4} = 0.25$ and $y/\frac{\lambda}{4} = 0.5$. As discussed in section 4.2, the jet symmetry is broken for these jet positions as the vortex on the left hand side is downstream of the right hand side vortex. The $Du/Dt = 0$ contours also change in a similar way, as each contour crosses the left shear-layer downstream of the right shear-layer. The right hand side looks for both jet positions very similar to the pressure anti-node case, with only one pressure maximum between two vortices from consecutive forcing cycles. On the left side, an additional pressure maximum appears. For $y/\frac{\lambda}{4} = 0.25$ this is present only for a short period of time. First, a pressure minimum appears close to the nozzle exit at $t/T = 0.83$. Then at $t/T = 0.33$ a pressure maximum appears, while shortly after both the minimum and maximum disappears. The axial position of this

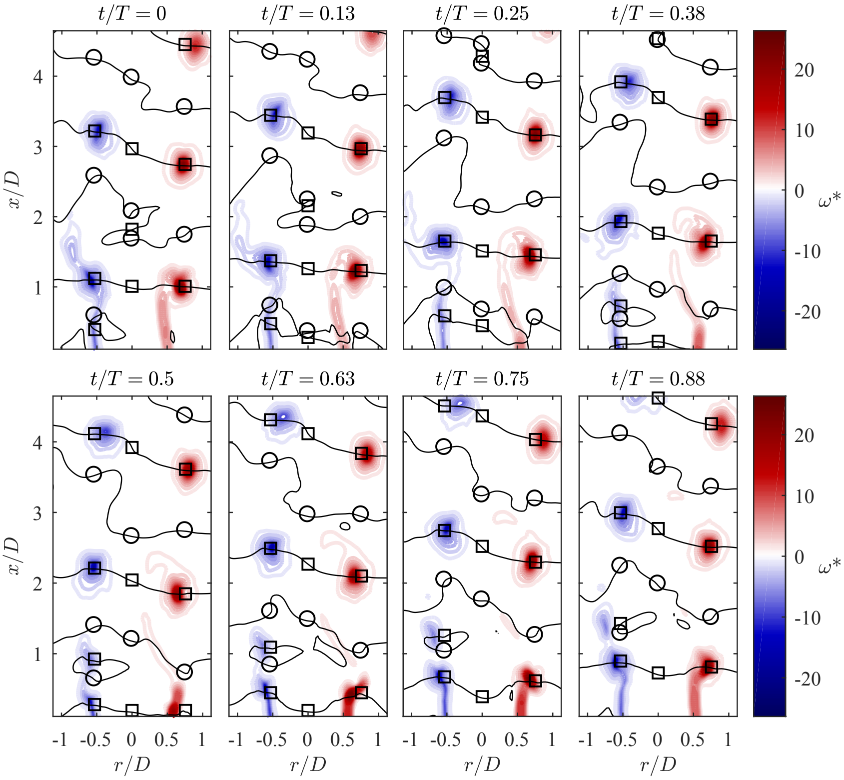

Figure 5.11: Time-series of phase averaged vorticity contours, for $f = 655$ Hz, $U_e = 13.1$ m/s, $y/\frac{\lambda}{4} = 0.25$, $u'_{\mathrm{AN,RMS}}/U_e = 0.25$. Also, contours of the x component of material acceleration, $Du/Dt = 0$ are shown in black. On $r = 0$ and in the shear-layers, ◯ represents a pressure maximum and □ a pressure minimum.

pressure maximum is plotted as a function of time in the upper part of figure 5.10 where it is found downstream of the main vortex center and its trailing pressure maximum. There is no vortex center corresponding to the second pressure minimum seen in figure 5.6. For the same jet position with forcing frequency $f = 655$ Hz, a secondary vortex corresponding to the additional pressure minimum is however identified, as shown in figure 5.11 and 5.12. It is situated downstream of the temporary pressure maximum before it merges with the main vortex at the same time as the second pressure maximum disappears. Also at $y/\frac{\lambda}{4} = 0.5$, two vortices are found on the left hand side. At this jet position the vortices do not merge, but are separated by the pressure maximum between them throughout the field of view. For $y/\frac{\lambda}{4} = 0.25$, the pinch-off is

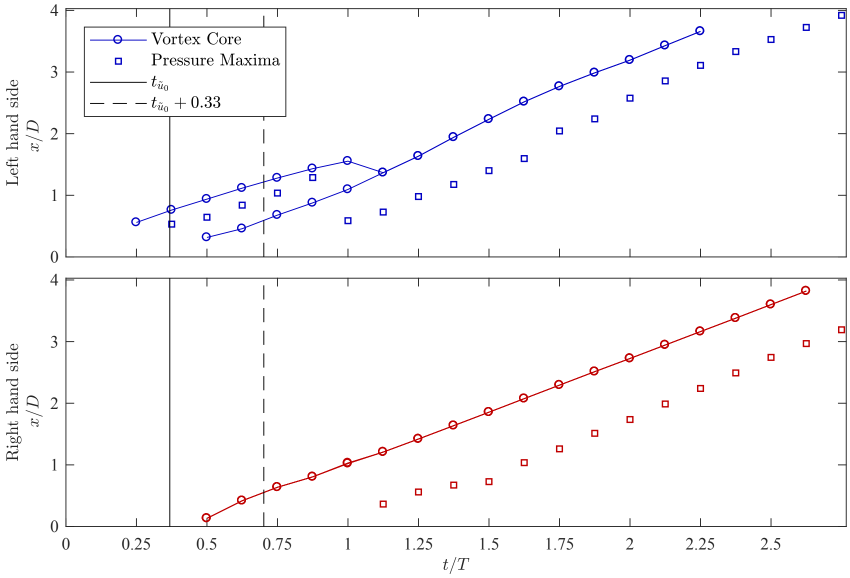

Figure 5.12: Axial position of the individual vortex structures together with the pressure maxima on the left and right hand side of the jet as a function of time, for $y/\frac{\lambda}{4} = 0.25$, $f = 655$ Hz, $U_e = 18.9$ m/s, $u'_{\mathrm{AN,RMS}}/U_e = 0.25$.

estimated to occur at $t/T \approx 1$ on the right hand side by extrapolating the path of the pressure maxima down to the $x = 0$ line. This is about $0.25T$ later than the pinch-off time estimated by the corresponding circulation plot. By the same method, the pinch-off time on the left hand side is estimated at $t/T \approx 0.66$, which is the same as estimated by the circulation plot. For $y/\frac{\lambda}{4} = 0.5$, the path of the trailing pressure maxima in figure 5.13 estimates pinch-off to occur later for both the right hand side ($t/T \approx 1$) and for both vortices on the left hand side ($t/T \approx 0.5$ and $t/T \approx 0.75$) compared to the findings from the circulation plots.

The lower row in figure 5.6 shows vorticity and $Du/Dt = 0$ contours for the jet positioned at the pressure node, while figure 5.14 shows axial position of pressure maxima and vortex cores in the shear-layer as a function of time. Even though the vortex structures for this jet position are in anti-phase and clearly different from the axisymmetric vortex ring, also they are followed by a trailing pressure maximum. Some time after the vortices split in two, a second pressure maximum appears behind the vortices 9b and 10b, and follow just upstream

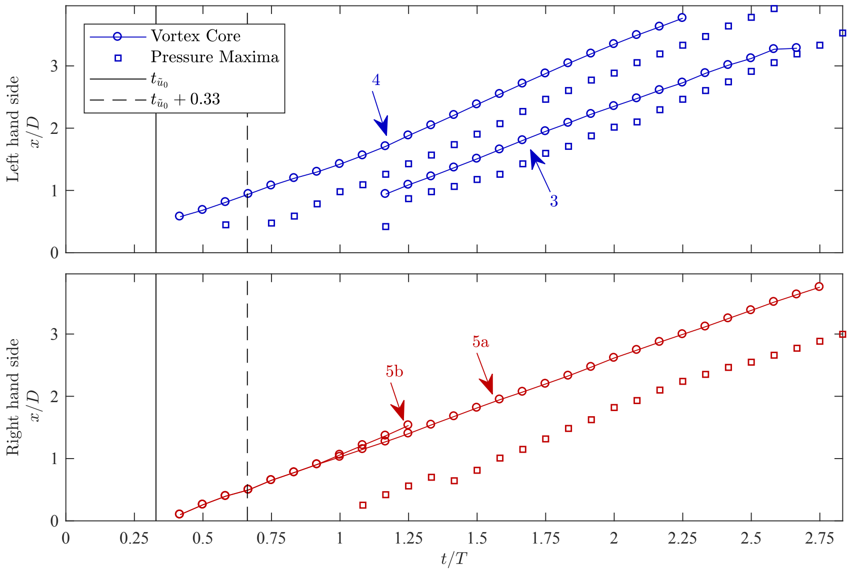

Figure 5.13: Axial position of the individual vortex structures together with the pressure maxima on the left and right hand side of the jet as a function of time, for $y/\frac{\lambda}{4} = 0.5$, $f = 450$ Hz, $U_e = 13.1$ m/s, $u'_{\mathrm{AN,RMS}}/U_e = 0.25$.

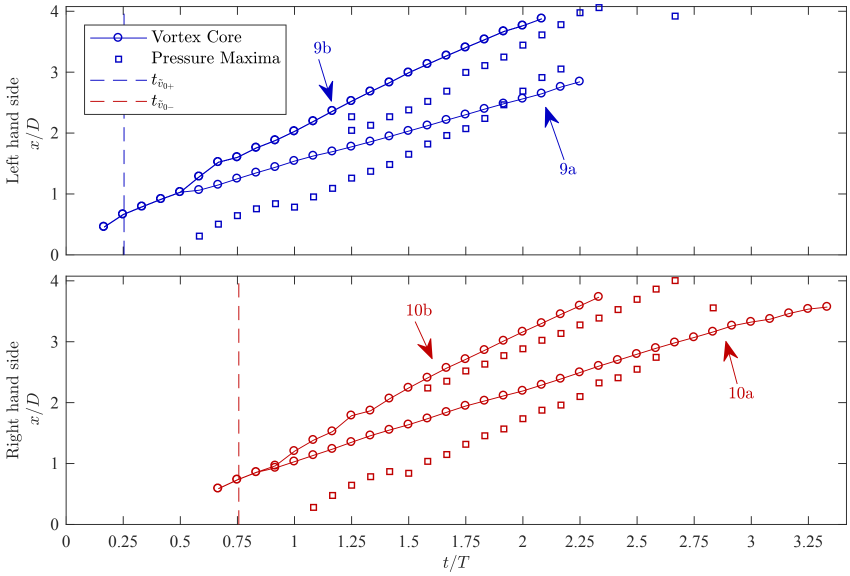

Figure 5.14: Axial position of the individual vortex structures together with the pressure maxima on the left and right hand side of the jet as a function of time, for $y/\frac{\lambda}{4} = 1$, $f = 450$ Hz, $U_e = 13.1$ m/s, $u'_{\mathrm{AN,RMS}}/U_e = 0.25$.

of these vortices as they move out of the field of view. The vertical, dashed lines in figure 5.14 shows $t_{\tilde{v}_{0+}}$ and $t_{\tilde{v}_{0-}}$, which is where the circulation plots estimated pinch-off for the left and right hand side vortex, respectively. Also for this jet position the trailing pressure maxima appear later than the pinch-off times estimated by the circulation plots, and for both sides the deviation is around $0.25T$.

In general, the pinch-off times estimated by extrapolating the paths of the trailing pressure maxima to the nozzle exit do not coincide with the pinch-off times estimated py the circulation plots in section 5.1. Both methods gave similar results when Lawson & Dawson (2013) used them to predict the pinch-off of vortex rings formed by a synthetic jet. Even though there seem to be consistently a trailing pressure maximum behind each individual vortex structure forming in the jet, these maxima might not give a good estimate of the pinch-off time of the vortices in this study, even not the axisymmetric vortex rings. The reason for this can be due to the velocity program of the forced jet, as noted by Lawson & Dawson (2013). For a sinusoidally forced jet, Aydemir *et al.* (2012) found that it is the decreasing of the shear-layer velocity below the ring's propagation velocity that stops the ring from growing. Therefore the formation of the trailing pressure maximum might not have an important role in the pinch-off in this case.

5.3 The pressure in the jet shear-layer as an estimation of pinch-off

This section treats a third method used to estimate pinch-off, adapted from Schlueter-Kuck & Dabiri (2016) and described in section 1.2.3 and figure 1.8. This method builds on the idea of Lawson & Dawson (2013) that a trailing pressure maximum divides the ring from the rest of the shear-layer, and therefore initiate pinch-off. Instead of contours of $Du/Dt = 0$, Schlueter-Kuck & Dabiri plotted the pressure in the shear-layer of a starting jet in a $x - t$ diagram, and by tracing the origin of the high-pressure region behind the fully formed vortex ring back to the nozzle exit plane ($x = 0$), they found a pinch-off time

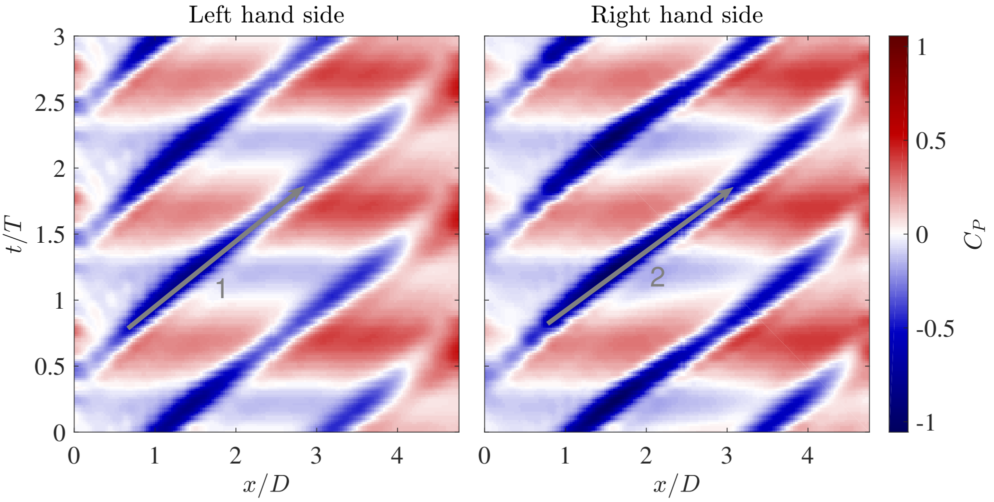

Figure 5.15: Pressure evolution in the shear-layer on the left and right hand side of the jet, for $f = 450$ Hz, $U_e = 13.1$ m/s, $y/\frac{\lambda}{4} = 0$, $u'_{\mathrm{AN,RMS}}/U_e = 0.25$. Pressure coefficient $C_P = P/\rho U_e^2$.

coinciding with that found when using the circulation method by Gharib *et al.* (1998). Figure 5.15 shows the pressure evolution in the shear-layer of the jet positioned at $y/\frac{\lambda}{4} = 0$. The pressure coefficient $C_P = P/\rho U_e^2$ is calculated from phase averaged velocity fields as explained in section 2.5.4, and plotted in a $x - t$ diagram. Horizontal lines in the plot represent the pressure in the shear-layer for different downstream positions at a time instant, while vertical lines show how the pressure develops in time for a given axial position. The pressure is taken from the radial position in the shear-layer having the lowest pressure when averaging in time and axial direction. The core of a vortex is a local pressure minimum, and in the plot the vortex cores are identified as diagonal lines of low pressure and marked according to the numbering in figure 4.6. In addition, horizontal lines of positive and negative pressure are seen. These lines come from the standing waves from the loudspeakers, making the pressure in the whole jet enclosure to oscillate in time. Similar pressure lines were not found in the results by Schlueter-Kuck & Dabiri (2016), because in their study they used a piston upstream of the nozzle exit that did not directly affect the pressure downstream of the nozzle exit. We are interested in investigating the vortex formation, and therefore it is the pressure caused by the vortex structures that are of interest. Since this is present together with the horizontal lines from the transverse forcing, the diagonal lines from the vortex structures are not as pronounced as in the results by Schlueter-Kuck & Dabiri. To remove the pressure waves caused directly by the speakers and obtain an estimate for the pressure coming from the vortex structures alone, the pressure was averaged in the axial direction for each point in time and subtracted from the pressure:

$$C_{P,\mathrm{v}}(x,t) \approx C_P(x,t) - \frac{1}{x_{\mathrm{end}}} \int_0^{x_{\mathrm{end}}} C_P(x,t)dx = C_P(x,t) - \langle C_P \rangle(t). \tag{5.3}$$

Here x_{end} is the axial position at the end of the field of view. The result is shown in the upper row of figure 5.16, where the lines of low pressure representing the vortex structures are more distinct. At the nozzle exit, $x = 0$, the pressure is positive, and at $t/T \approx 0.3$ it turns negative on both sides, which coincide approximately with $t_{\tilde{u}_0}$. Then the pressure stays negative while the vortices 1 and 2 form at the nozzle exit, and the pressure again changes sign and stays positive from $t/T \approx 0.7$ to $t/T \approx 1.3$. Schlueter-Kuck & Dabiri found the pinch-off time by fitting a line to the local maximum of the high-pressure region that followed the low-pressure region representing the vortex, and extrapolated it backward in time to the nozzle exit at $x/D = 0$. The high-pressure region in this case does not have a distinct local maximum, but stays at a fairly constant, positive pressure for more than half of the forcing cycle. This is probably due to the merging of the pressure maxima between the vortex rings as discussed in section 5.2, and it makes it difficult to accurately predict the pinch-off time by using this method. Taking the middle point in the region of positive pressure gives an estimated pinch-off time at $t/T \approx 1$, while taking the beginning of the region of positive pressure gives an estimated pinch-off time at $t/T \approx 0.7$. The latter is close to the prediction from the circulation plots.

The pressure in the jet shear-layer for $y/\frac{\lambda}{4} = 0.25$ is shown in the middle row in figure 5.16. Also for this position it is difficult to give an estimate of the pinch-off time. The small vortex that breaks off the main vortex on the right hand side is seen here as a thin, white line starting at $t/T \approx 1.5$, $x/D \approx 2.2$, and quickly disappearing. A similar but more pronounced line is seen on the right hand side of the jet when positioned at $y/\frac{\lambda}{4} = 0.5$, as shown in the lower

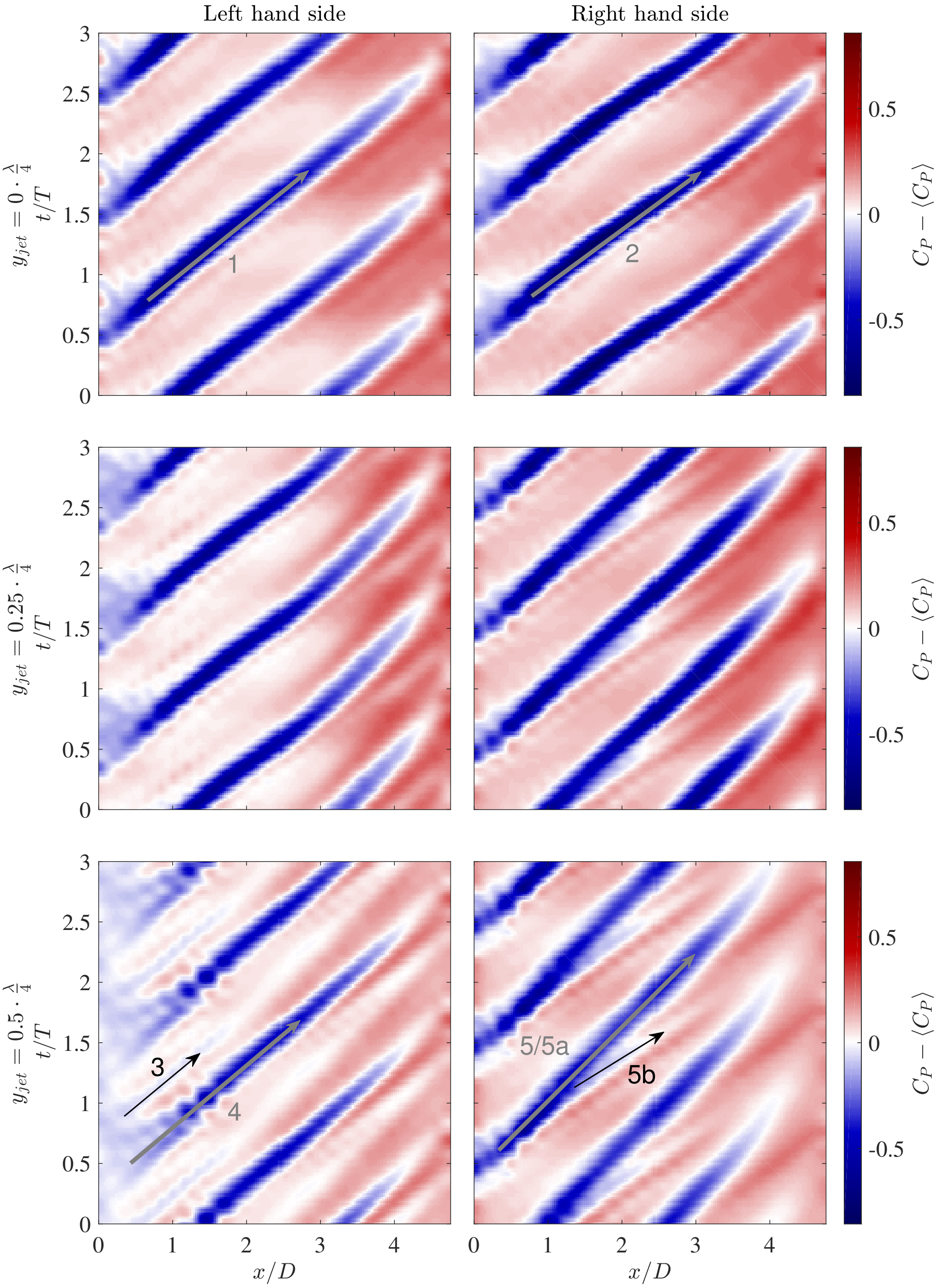

Figure 5.16: Pressure evolution in the shear-layer on the left and right hand side of the jet, for $f = 450$ Hz, $U_e = 13.1$ m/s, $u'_{\mathrm{AN,RMS}}/U_e = 0.25$ for jet positions $y/\frac{\lambda}{4} = 0$, $y/\frac{\lambda}{4} = 0.25$ and $y/\frac{\lambda}{4} = 0.5$. Pressure coefficient $C_P = P/\rho U_e^2$, and $\langle C_P \rangle$ is given in equation (5.3).

row in figure 5.16. The line starts at $t/T \approx 1.2$, $x/D \approx 1.2$, which coincides with when vortex 5b breaks off the main vortex 5/5a. On the left hand side, the pressure is positive at the nozzle exit through the whole forcing cycle. Here there are two diagonal lines of positive pressure per forcing cycle, one wide line of dark blue representing the larger vortex 4, and one thin line of lighter blue representing the smaller vortex 3.

In general, the pressure in the shear-layer of the jet positioned from $y/\frac{\lambda}{4} = 0$ to $y/\frac{\lambda}{4} = 0.5$ have some fundamental similarities, with a distinct, diagonal line of low pressure from the vortex structures, and with a wide area of positive pressure in between. By moving the jet away from $y/\frac{\lambda}{4} = 0$, the symmetry gradually breaks as the main vortex structures on the left and right hand side goes out of phase, and additional, asymmetric vortex structures appear. This is in agreement with what the vorticity fields in section 4.2 showed.

For the jet positions $y/\frac{\lambda}{4} = 0.75$ and $y/\frac{\lambda}{4} = 1$ shown in figure 5.17[b], the shear-layer pressure has developed to become considerably different from the symmetric case in the pressure anti-node, but also here the different vortex structures seen in section 4.2 can be identified. In the shear-layer on the left side of the jet positioned at $y/\frac{\lambda}{4} = 0.75$, the lines of low pressure from vortex 6 and 7 are crossing, while the splitting of vortex 8 into 8a and 8b on the right side of the jet is seen as an additional, thin line of low pressure coming off the ticker, main line at $t/T \approx 1$, $x/D \approx 1$. One can even identify that vortex 8a splits up again later in the cycle as another, thin line of low pressure comes off the main line at $t/T \approx 1.7$, $x/D \approx 2$. For the jet placed in the pressure node we have seen that the vortices form in anti-phase, and this is also shown here on the pressure lines appearing due to the vortices. The lines of low pressure on the left and right side have similar shape but are shifted $0.5T$ relative to each other. On both sides the lines of low pressure split up, at $t/T \approx 0.5$, $x/D \approx 1$ on the left and $t/T \approx 1$, $x/D \approx 1$ on the right hand side. Since the larger,

---

[b] The "dotted" behavior of the negative pressure, especially on the right hand side for jet position $y/\frac{\lambda}{4} = 1$, is most probably an artifact, and might be due to an insufficient resolution of the measurements or the way the pressure is calculated. A known issue with integrating the pressure gradient field is that it can cause the error originating from the PIV measurements to accumulate. Dabiri *et al.* (2014) suggests integrating the pressure gradient along several different paths, and select the pressure at each point from median polling to remove noise, but this did not improve the results.

upstream vortex is moving radially, the line of low pressure from this vortex quickly disappears from the plot. All this is in agreement with the vorticity fields in figure 4.6. In the left shear-layer at $x/D = 0$, the pressure turns negative at $t/T \approx 0.2$, while it does at $t/T \approx 0.77$ on the right hand side. Then it again turns positive at $t/T \approx 0.8$ on the left side, and $t/T \approx 1.33$ on the right side of the jet. The circulation plots in section 5.1 suggested that the vortices pinch off approximately when the jet starts to move away from the shear-layer where the vortex is forming, i.e. at $t = t_{v_0+}$ and $t = t_{v_0-}$ for the left and right hand side, respectively. For this specific case this happens at $t/T \approx 0.25$ and $t/T \approx 0.75$. As for the other jet positions, the high-pressure region between the vortices does not have a distinct local maximum, which makes it difficult to predict the pinch-off time accurately. Taking the time at the middle point in the region of positive pressure gives an estimated pinch-off at $t/T \approx 0.5$ and $t/T \approx 1.0$ for the left and the right hand side, respectively, which is the same as the trailing pressure maxima predicted but around $t/T = 0.25$ later than the predictions from the circulation plots.

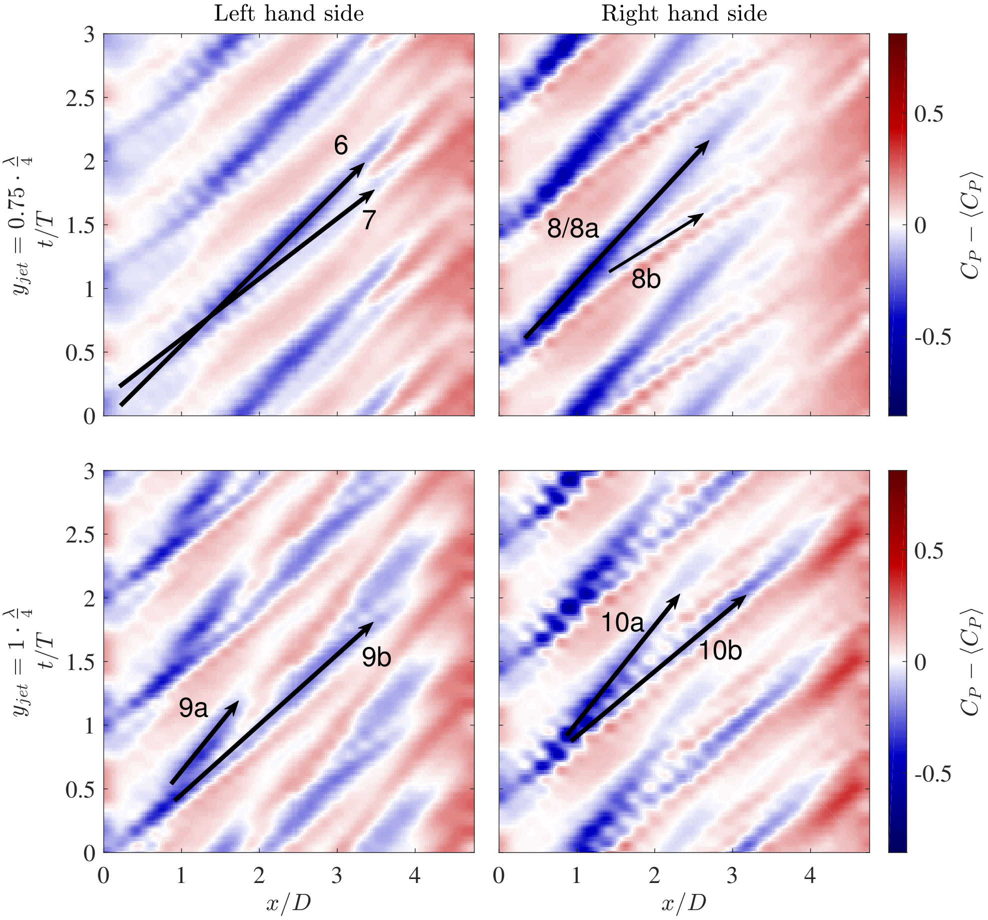

Figure 5.17: Pressure evolution in the left and right hand side shear-layer for $f = 450$ Hz, $U_e = 13.1$ m/s, $u'_{\mathrm{AN,RMS}}/U_e = 0.25$ for jet positions $y/\frac{\lambda}{4} = 0.75$ and 1. Pressure coefficient $C_P = P/\rho U_e^2$, and $\langle C_P \rangle$ is given in equation (5.3).

Chapter 6

Conclusions and future work

6.1 Conclusions

In this thesis the response of a round air-jet subjected to transverse acoustic forcing has been investigated. The effect of changing the forcing frequency and amplitude, the jet speed and the position of the jet in the standing-wave pressure field has been quantified by conducting microphone measurements, hot-wire anemometry and particle image velocimetry.

This work has shown that the nozzle setup can be modeled as a Helmholtz resonator with mean flow, and with resonance frequency $\omega_0 \approx 2\pi \cdot 260$ Hz. As for a Helmholtz resonator, the jet induced axial velocity fluctuations when subjected to pressure fluctuations at the nozzle exit, and these velocity fluctuations varied in phase and amplitude for different forcing frequencies. For that reason, the phase between these axial velocity fluctuations and the transverse velocity fluctuations present in the acoustic standing wave was changing with frequency. For $f = 250$ Hz, the axial velocity fluctuations are more than $90°$ behind the transverse, while for the other frequencies investigated, $f = 450$ Hz and $f = 655$ Hz, the axial velocity fluctuations are slightly before the transverse, with $15° - 25°$.

The response of the jet when positioned in the pressure anti-node has been investigated for different forcing frequencies and amplitudes, and jet exit velocities. For all forcing configurations, the vorticity fields show axisymmetric vortex structures similar to what has been found for longitudinal forcing (Aydemir *et al.*, 2012; Zaman & Hussain, 1980) and previous anti-node experiments (Baillot & Lespinasse, 2014; O'Connor & Lieuwen, 2011; Saurabh & Paschereit, 2013). These structures are well known to be vortex rings. The increase in vortex convection velocity with forcing amplitude, as estimated by the slug model is not seen. The vortex paths, and therefore the convection velocity, matched however well with the empirical path predicted by Asadi *et al.* (2018) for all available forcing conditions, but the measurements conducted in this study did not enable testing the validity for different Strouhal numbers, St_D.

The response of the jet at different positions in the acoustic wave has been investigated thoroughly. For all the frequencies the jet spreads more in the near-field, and the shear-layer breaks down more rapidly downstream as the jet is moved from $y/\frac{\lambda}{4} = 0$ to $y/\frac{\lambda}{4} = 1$. The response of the jet when forced at $f = 250$ Hz, was fundamentally different from the other forcing frequencies investigated. At this frequency the jet stayed close to unchanged for all positions except for the pressure node, where the symmetry was clearly broken as the right hand side vortex was positioned downstream of the left.

For the higher frequencies, however, the symmetry was broken immediately when moving the jet away from the pressure anti-node. For the positions between the pressure anti-node and node, the jet was found to first bend towards the left, before bending back towards the right longer downstream. The centerline of the jet was meandering in the radial direction for all jet positions, except at $y/\frac{\lambda}{4} = 0$, where no pressure gradient is present. At $y/\frac{\lambda}{4} = 0.25$, $y/\frac{\lambda}{4} = 0.5$ and $y/\frac{\lambda}{4} = 0.75$, the phase averaged centerline showed an asymmetric pattern over the forcing cycle. At $y/\frac{\lambda}{4} = 1$, the centerline showed a symmetric pattern, and for some diameters downstream similar in shape as the analytical solution of a passive tracer moving in a constant, axial flow with transverse, sinusoidal fluctuations. As the jet was moved away from the pressure anti-node, the left hand side vortex moved downstream relative to the right hand side vortex, and at the pressure node the formation of the left and right hand side vortices were in anti-phase. For the positions $y/\frac{\lambda}{4} = 0.5$ and $y/\frac{\lambda}{4} = 0.75$, the jet showed complex vortex structures that were fundamentally different on either side. On the left hand side vortices formed twice during a forcing cycle, while on the right hand side the vortex divided into two. In general, both the axial velocity fluctuations induced by pressure fluctuations, and the transverse velocity fluctuations induced by pressure gradient fluctuations, seemed to be the mechanism behind the vortex formation. The vortex formation in the shear-layer was found to start when the velocity at the nozzle exit turned positive in the cycle; either out of the nozzle in axial direction, or away from the jet centerline for the transverse direction. For the positions with both fluctuations present at a sufficient amplitude, they either formed *one* vortex in the jet shear-layer if the fluctuations were approximately in phase, or they formed separate structures at different times in the cycle if the phase difference between the velocity fluctuations was sufficiently large.

Even though the jet response is highly dependent on the local pressure gradient present at the jet position in the enclosure, the results do not support that the difference in shear-layer pressure on the left and right side of the jet play a role. It is however the transverse velocity fluctuations caused by the pressure gradient, and its phase relative to the axial velocity fluctuations present in the jet, that causes the jet response to vary with jet position and also being responsible for the vortex structures forming in the shear-layers on the left and right side of the jet to be different.

There seems to be two reasons for the different behavior of the jet when subjected to a forcing frequency of $f = 250$ Hz compared to $f = 450$ Hz and $f = 655$ Hz, and both are related to the acoustic property of the nozzle. Since the forcing frequency of $f = 250$ Hz is close to the resonance frequency of the nozzle, the axial velocity fluctuations in the jet for $y/\frac{\lambda}{4} = 0$ are orders of magnitude larger relative to the pressure fluctuations in the enclosure, compared to the other forcing frequencies. This together with the imperfection of the standing wave causes the axial velocity fluctuations to be non-negligible even at $y/\frac{\lambda}{4} = 1$. The other reason is the frequency dependent phase difference between the axial and transverse velocity fluctuations, resulting in a different interaction between the vortex formations driven by the axial fluctuations and those driven by the transverse fluctuations, for $f = 250$ Hz compared to the other forcing frequencies investigated.

The jet positioned at $y/\frac{\lambda}{4} = 1$ was also investigated in detail in this study. For $f = 450$ Hz and $f = 655$ Hz, the vortex structures on the left and right side of the jet were similar in shape but formed in anti-phase. For most cases the vortices on both sides were shown to split in two, but prior to this the shear-layer curved around the front of the vortex, forming an S shaped structure, similar to the shape found in the plane along the minor axis of jets from oval and elliptic shaped nozzles (Adhikari, 2009; O'Farrell & Dabiri, 2014). Because of the transverse velocity at the pressure node, the original vortex moved radially away from the high-velocity region in the jet, causing the jet shear-layer to curve around the front of the vortex and separate into an independent vortex of higher velocity. For some cases when forcing at $f = 655$ Hz, three vortices were seen to form on either side of the jet during each forcing cycle, two that were splitting up from the same vortex, and a third forming in anti-phase. This means that twice per forcing period, vortices formed in phase on either side of the jet.

An important phenomenon related to the formation process of the vortex structures, is the pinch-off. This study has compared three methods for estimating the pinch-off time. The method by Gharib *et al.* (1998) estimates pinch-off as the time when the total circulation in the jet shear-layer reaches the value of the vortex ring circulation, implying that pinch-off appears when the shear-layer stops delivering vorticity to the ring. In the pressure anti-node, the vortex rings were found to pinch off about $0.33T$ after the vortex ring started to form. This is in agreement with the findings of Aydemir *et al.* (2012). As the jet was moved away from the pressure anti-node for the cases $f = 450$ Hz and $f = 655$ Hz, the vortex on the right side of the jet pinched off slightly later in the forcing cycle, and at the pressure node position the vortex structure was found to pinch off when the transverse velocity changed direction to the left and moved the jet away from the side the vortex was formed. On the left side of the jet, the estimated pinch-off time stayed unchanged from the anti-node position to the position closest to the pressure anti-node, $y/\frac{\lambda}{4} = 0.25$. At $y/\frac{\lambda}{4} = 0.5$, however, where two distinct vortex structures formed, which of the two vortex structure the method estimates the pinch-off time for, seemed to be dependent on when the formation process is defined to start. By carefully defining the start of the different formation processes, the method was able to estimate the pinch-off time for both vortex structures, one being in accordance with the pinch-off time for the vortex rings at the pressure anti-node, and the other in accordance with the vortex structures at the pressure node. At the pressure node position also the left side vortex was found to pinch off when the transverse velocity changed direction away from the shear-layer in which the vortex was formed, which means towards the right for this case.

The methods by Lawson & Dawson (2013) and Schlueter-Kuck & Dabiri (2016) are both built on the idea that a trailing pressure maximum divides the vortex ring in a jet from the shear-layer, and therefore initiates pinch-off. Neither of these methods gave reliable estimates of the pinch-off time of the vortex structures in the jet in the current study. There may be several reasons for this. First of all, because of a relatively high Strouhal number, the vortex rings formed at the pressure anti-node seem to be too closely spaced for the pressure field around the vortex rings to be completely unaffected by each other. Secondly, it is questionable whether the measurement data have high enough resolution for the pressure and pressure gradient field to be calculated accurately. At last, it is questionable whether the trailing pressure maxima has an important role in the pinch-off process for the forcing configuration in this study, since for a sinusoidally forced jet it may be the decrease of the shear-layer velocity below the ring's propagation velocity that stops the ring from growing, and therefore initiate pinch-off (Aydemir *et al.*, 2012). Nevertheless, both methods give additional and useful insight about the jet's flow field. The $x - t$ diagrams of pressure in the shear-layer give good visualization of the development of the vortex structures. The contours of $Du/Dt = 0$ on the other hand revealed that, even though the vortex rings at the pressure anti-node seemed to be isolated from each other when only inspecting the vorticity fields, the pressure field around them might interact and cause the vortex rings to affect each other to an unknown degree.

The 2-dimensional measurements presented in this study are not sufficient to explain the 3-dimensional flow structures of the different positions in the standing wave. At the pressure anti-node it is known from the literature that the left and right hand side vortices are connected and form vortex rings. For the other jet positions, the vortices might still be connected structures, forming tilted vortex rings, but it is also possible that the vortices are independent structures and that the connection between the left and right hand side is broken. The ratio $\tilde{v}'_{\mathrm{RMS}}/\tilde{u}'_{\mathrm{RMS}}$ was shown to have some correlation to the phase between the two main vortex structures on either side of the jet, at least for moderate values of $\tilde{v}'_{\mathrm{RMS}}/\tilde{u}'_{\mathrm{RMS}}$. If the vortices are still connected, this ratio may be of importance for the tilting angle of the ring. The mechanism behind the tilting can simply be that the transverse velocity moves the ring sideways. This causes the left and right side of the ring to have different axial convection velocities since one side moves closer to the jet centerline with higher velocity, and the other side moves into the ambient region. The phase between the axial and transverse velocity fluctuations then decides the direction of the tilting; if the transverse velocity is pointing to the right while the ring is formed, the ring tilts clockwise, while if the transverse velocity is pointing to the left, the ring tilts counterclockwise. At the pressure node, previous studies suggest that the vortex structures on the left and the right hand side are not connected. Matta *et al.* (1996) did not observe vortices in the shear-layers perpendicular to the wave direction, while simulations by Urbin & Métais (1997) and Danaila & Boersma (2000) suggest that the structures are hairpin like vortices appearing in anti-phase on either side of the jet and forming twice per forcing period in total. These hairpin vortices are tilted with the legs pointing downstream and partly connecting to the next downstream vortex. These studies do not show the additional vortex structures observed at the pressure node position in this study, and their 3-dimensional shape remains unknown.

6.2 Future work

The measurements presented in this thesis gave new insight to the near-field response of a transversely forced jet, but they also revealed many new questions.

First of all, the 3-dimensional shape of the vortex structures for all positions in the standing wave except the pressure anti-node is still unknown to a certain degree. This can be investigated further by e.g. conducting tomographic PIV measurements for these cases, which gives all three velocity component in a volume.

Investigating the pressure field of the jet positioned at the pressure anti-node, revealed that the vortex rings might interact even though the vorticity field suggests they are completely separated. This led to the questions related to the development of the pressure field between the vortex rings as the axial separation distance change. It would be interesting to investigate this further in terms of the formation process of the rings and the role of the trailing and leading pressure maxima. In that case it is important to conduct measurements with sufficient resolution for the calculated pressure fields to be reliable.

An important question which arose during this work was how the phase difference between the axial and transversal velocity fluctuations affects the jet response of the jet, and also their role in the formation of vortex structures for the positions where both these velocity fluctuations are present. This can be done in practice by having a nozzle setup that act as a Helmholtz resonator, as the one in the current study. Then there is a phase shift around the resonance frequency of about 180°, and the phase difference between velocity fluctuations can be adjusted by changing the length of the jet enclosure together with the forcing frequency. It is possible to make the phase change of the nozzle setup less abrupt, and therefore easier to control, by increasing the jet velocity. It is then important to not get too close to the resonance frequency of the nozzle setup as it will give the same problem as was seen in this study, that it is difficult to achieve high enough velocity fluctuation ratios ($v_{\mathrm{RMS}}/u_{\mathrm{RMS}}$). Alternatively, it is possible to keep the forcing frequency constant, but have a nozzle setup with an adjustable pipe length. This will make it possible to change the resonance frequency of the nozzle setup and with that also the phase difference between the velocity fluctuations. A third option is to use a setup that combines longitudinal and transverse forcing, similar to what has been studied with combustion (Hauser *et al.*, 2010, 2012; Saurabh & Paschereit, 2013). By doing this type of setup it is simple to adjust the phase amplitude ratio between the axial and transverse velocity fluctuations that the jet experiences.

Traveling waves have not been investigated in this study, but are of importance in gas turbine dynamics. A jet subjected to a traveling wave experiences both pressure gradient fluctuations resulting in transverse velocity fluctuations, and pressure fluctuations resulting in axial velocity fluctuations. This is also the case for a jet subjected to any position in a standing wave except for at the pressure anti-node and node. The difference, however, is that for a traveling wave the maximum pressure occurs when the pressure gradient is zero (and vice versa), while for a standing wave the maximum pressure comes simultaneously as the maximum pressure gradient. The phase between the pressure fluctuations and the pressure gradient fluctuations are therefore different. But as we have seen, the phase between the axial and transverse velocity fluctuations that are induced by the pressure are not only dependent on the forcing, but also the nozzle setup. Therefore, it would be interesting to see if it is possible to obtain the same response by forcing the jet with a traveling wave, as if the jet is positioned in a standing wave between the pressure anti-node and node. In that case the phase angle and ratio between the axial and transverse fluctuations need to be the same for the two cases. The phase angle between the axial and transverse velocity fluctuations can be adjusted as suggested in the previous paragraph, while the ratio of the amplitudes can be adjusted by changing the jet position in the standing wave case.

References

Adhikari, Deepak. *Some experimental studies on vortex ring formation and interaction.* PhD Thesis, 2009.

Adrian, Ronald J. and Westerweel, Jerry. *Particle image velocimetry.* Number 30. Cambridge University Press, 2011.

Anthoine, Jérôme. *Measurement Techniques in Fluid Dynamics: An Introduction.* Von Karman Institute for Fluid Dynamics, 2009.

Arms, R. J. and Hama, Francis R. 1965. Localized-induction concept on a curved vortex and motion of an elliptic vortex ring. *The Physics of fluids*, **8**, 553–559.

Asadi, H., Asgharzadeh, H. and Borazjani, I. 2018. On the scaling of propagation of periodically generated vortex rings. *Journal of Fluid Mechanics*, **853**, 150–170.

Aydemir, E., Worth, N. A. and Dawson, J. R. 2012. The formation of vortex rings in a strongly forced round jet. *Experiments in fluids*, **52**, 729–742.

Baillot, Françoise and Lespinasse, Florian. 2014. Response of a laminar premixed V-flame to a high-frequency transverse acoustic field. *Combustion and Flame*, **161**, 1247–1267.

Balachandran, R., Ayoola, B. O., Kaminski, C. F., Dowling, A. P. and Mastorakos, E. 2005. Experimental investigation of the nonlinear response of turbulent premixed flames to imposed inlet velocity oscillations. *Combustion and Flame*, **143**, 37–55.

Batchelor, G. K. and Gill, A. Eo. 1962. Analysis of the stability of axisymmetric jets. *Journal of Fluid Mechanics*, **14**, 529–551.

Bechert, D. and Pfizenmaier, E. 1975. On the amplification of broad band jet noise by a pure tone excitation. *Journal of Sound and Vibration*, **43**, 581–587.

Bethke, Sven, Wever, Utz and Krebs, Werner. Stability analysis of gas-turbine combustion chamber. In *11th AIAA/CEAS Aeroacoustics Conference*, page 2831, 2005.

Blimbaum, J., Zanchetta, M., Akin, T., Acharya, V., O'Connor, J., Noble, D. and Lieuwen, T. 2012. Transverse to longitudinal acoustic coupling processes in annular combustion chambers. *International journal of spray and combustion dynamics*, **4**, 275–298.

Bradbury, L. J. S. and Khadem, A. H. 1975. The distortion of a jet by tabs. *Journal of Fluid Mechanics*, **70**, 801–813.

Brown, Garry L. and Roshko, Anatol. 1974. On density effects and large structure in turbulent mixing layers. *Journal of Fluid Mechanics*, **64**, 775–816.

Corke, T. C. and Kusek, S. M. 1993. Resonance in axisymmetric jets with controlled helical-mode input. *Journal of Fluid Mechanics*, **249**, 307–336.

Crow, S. Cj and Champagne, F. H. 1971. Orderly structure in jet turbulence. *Journal of Fluid Mechanics*, **48**, 547–591.

da Silva, Carlos B. and Métais, Olivier. 2002. Vortex control of bifurcating jets: a numerical study. *Physics of Fluids*, **14**, 3798–3819.

Dabiri, John O., Bose, Sanjeeb, Gemmell, Brad J., Colin, Sean P. and Costello, John H. 2014. An algorithm to estimate unsteady and quasi-steady pressure fields from velocity field measurements. *Journal of Experimental Biology*, pages jeb–092767.

Danaila, Ionut and Boersma, Bendiks Jan. 2000. Direct numerical simulation of bifurcating jets. *Physics of fluids*, **12**, 1255–1257.

Davis, Dustin and Chehroudi, Bruce. The effects of pressure and acoustic field on a cryogenic coaxial jet. Technical report, Engineering research and consulting inc (ERC inc) Edwards AFB CA, 2003.

De Kat, R. and Van Oudheusden, B. W. 2012. Instantaneous planar pressure determination from PIV in turbulent flow. *Experiments in fluids*, **52**, 1089–1106.

Didden, Norbert. 1979. On the formation of vortex rings: rolling-up and production of circulation. *Zeitschrift für angewandte Mathematik und Physik ZAMP*, **30**, 101–116.

Domenichini, F. 2011. Three-dimensional impulsive vortex formation from slender orifices. *Journal of Fluid Mechanics*, **666**, 506–520.

Elias, Isidor. 1959. Acoustical Resonances Produced by Combustion of a Fuel-Air Mixture in a Rectangular Duct. *The Journal of the Acoustical Society of America*, **31**, 296–304.

Emerson, Benjamin, Mondragon, Ulises, Acharya, Vishal, Shin, Dong-Hyuk, Brown, Christopher, McDonell, Vincent and Lieuwen, Timothy. 2013. Velocity and flame wrinkling characteristics of a transversely forced, bluff-body stabilized flame, part I: experiments and data analysis. *Combustion Science and Technology*, **185**, 1056–1076.

Evesque, Stephanie, Polifke, Wolfgang and Pankiewitz, Christian. Spinning and azimuthally standing acoustic modes in annular combustors. In *9th AIAA/CEAS Aeroacoustics Conference and Exhibit*, page 3182, 2003.

Fraenkel, Lo E. 1972. Examples of steady vortex rings of small cross-section in an ideal fluid. *Journal of Fluid Mechanics*, **51**, 119–135.

Freund, Jonathan B. and Moin, Parviz. 2000. Jet mixing enhancement by high-amplitude fluidic actuation. *AIAA journal*, **38**, 1863–1870.

Gharib, Morteza, Rambod, Edmond and Shariff, Karim. 1998. A universal time scale for vortex ring formation. *Journal of Fluid Mechanics*, **360**, 121–140.

Gutmark, Ephraim and Ho, Chih-Ming. 1983. Preferred modes and the spreading rates of jets. *The Physics of fluids*, **26**, 2932–2938.

Hauser, Martin, Lorenz, Manuel and Sattelmayer, Thomas. November 2010. Influence of Transversal Acoustic Excitation of the Burner Approach Flow on the Flame Structure. *Journal of Engineering for Gas Turbines and Power*, **133**, 041501–041501.

Hauser, Martin, Wagner, Michael and Sattelmayer, Thomas. Transformation of transverse acoustic velocity of the burner approach flow into flame dynamics. In *ASME Turbo Expo 2012: Turbine Technical Conference and Exposition*, pages 803–814. American Society of Mechanical Engineers, 2012.

Hill, Micaiah John Muller. 1894. VI. On a spherical vortex. *Philosophical Transactions of the Royal Society of London.(A.)*, pages 213–245.

Huang, Ying, Wang, Shanwu and Yang, Vigor. 2006. Systematic analysis of lean-premixed swirl-stabilized combustion. *AIAA journal*, **44**, 724–740.

Huang, Ying and Yang, Vigor. 2005. Effect of swirl on combustion dynamics in a lean-premixed swirl-stabilized combustor. *Proceedings of the Combustion Institute*, **30**, 1775–1782.

Hussain, Abul Khair Muhammad Fazle and Reynolds, William C. 1970. The mechanics of an organized wave in turbulent shear flow. *Journal of Fluid Mechanics*, **41**, 241–258.

Hussain, Fazle and Husain, Hyder S. 1989. Elliptic jets. Part 1. Characteristics of unexcited and excited jets. *Journal of Fluid Mechanics*, **208**, 257–320.

Hutt, John J. and Rocker, Marvin. 1995. High-frequency injection-coupled combustion instability. *Liquid rocket engine combustion instability*, **169**, 345–376.

Jeong, Jinhee and Hussain, Fazle. 1995. On the identification of a vortex. *Journal of fluid mechanics*, **285**, 69–94.

Jørgensen, Finn E. How to measure turbulence with hot-wire anemometers - a practical guide, August 2005.

Kibens, V. and Wlezien, R. Active control of jets from indeterminate-origin nozzles. In *Shear Flow Control Conference*, page 542, 1985.

Kibens, Valdis. 1980. Discrete noise spectrum generated by acoustically excited jet. *AIAA Journal*, **18**, 434–441.

Külsheimer, C. and Büchner, H. 2002. Combustion dynamics of turbulent swirling flames. *Combustion and flame*, **131**, 70–84.

Kozlov, G. V., Grek, G. R., Sorokin, A. M. and Litvinenko, Yu A. 2008. Influence of initial conditions at the nozzle exit on the structure of a plane jet. *The bulletin of Novosibirsk State University. Series: Physics*, **3**, 25–37.

Kozlov, V. V., Grek, G. R., Kozlov, G. V. and Litvinenko, Yu A. Physical aspects of the subsonic jet flows evolution. In *Successes of the Continuum Mechanics, Proc. All-Russia Conf. Dated for the 70th Anniversary of Academician VA Levin*, page 331, 2009.

Kozlov, V. V., Grek, G. R., Litvinenko, Yu A., Kozlov, G. V. and Litvinenko, M. V. 2011. Round and plane jets in a transverse acoustic field. *Journal of Engineering Thermophysics*, **20**, 272.

Kusek, S. M., Corke, T. C. and Reisenthel, P. 1990. Seeding of helical modes in the initial region of an axisymmetric jet. *Experiments in Fluids*, **10**, 116–124.

Kuttruff, Heinrich. *Acoustics: an introduction.* CRC Press, 2007.

LaVision, . FlowMaster, Product-Manual for DaVis 8.4, January 2017.

Lawson, J. M. and Dawson, J. R. 2013. The formation of turbulent vortex rings by synthetic jets. *Physics of Fluids*, **25**, 105113.

Lespinasse, Florian, Baillot, Françoise and Boushaki, Toufik. 2013. Responses of V-flames placed in an HF transverse acoustic field from a velocity to pressure antinode. *Comptes Rendus Mécanique*, **341**, 110–120.

Lim, T. T. and Nickels, T. B. Vortex rings. In *Fluid vortices*, pages 95–153. Springer, 1995.

Linden, P. F. and Turner, J. S. 2001. The formation of ‘optimal’vortex rings, and the efficiency of propulsion devices. *Journal of Fluid Mechanics*, **427**, 61–72.

Longmire, E. K. and Duong, L. H. 1996. Bifurcating jets generated with stepped and sawtooth nozzles. *Physics of Fluids*, **8**, 978–992.

Mankbadi, R. and Liu, J. T. C. 1981. A study of the interactions between large-scale coherent structures and fine-grained turbulence in a round jet. *Philosophical Transactions of the Royal Society of London. Series A, Mathematical and Physical Sciences*, **298**, 541–602.

Matta, L., Wuersig, H., Choung, A., Jagoda, J. and Zinn, B. Excitation of a round jet by transverse standing acoustic oscillations. In *34th aerospace sciences meeting and exhibit*, page 642, 1996.

Michalke, Alfons. Instabilitaet eines kompressiblen runden Freistrahis unter Beruecksichtigung des Einflusses der Strahigrenzschichtdicke (instability of a compressible circular jet considering the influence of the thickness of the jet boundary layer). Technical report, Deutsche forschungs- und versuchsanstalt fuer luft- und raumfahrt e v Berlin, 1971.

Michalke, Alfons and Hermann, Gunter. 1982. On the inviscid instability of a circular jet with external flow. *Journal of Fluid Mechanics*, **114**, 343–359.

Mohseni, Kamran and Gharib, Morteza. 1998. A model for universal time scale of vortex ring formation. *Physics of Fluids*, **10**, 2436–2438.

Mohseni, Kamran, Ran, Hongyu and Colonius, Tim. 2001. Numerical experiments on vortex ring formation. *Journal of Fluid Mechanics*, **430**, 267–282.

Noiray, Nicolas and Schuermans, Bruno. 2013. On the dynamic nature of azimuthal thermoacoustic modes in annular gas turbine combustion chambers. *Proc. R. Soc. A*, **469**, 20120535.

Norbury, J. A steady vortex ring close to Hill’s spherical vortex. In *Mathematical Proceedings of the Cambridge Philosophical Society*, volume 72, pages 253–284. Cambridge University Press, 1972.

O’Connor, Jacqueline, Acharya, Vishal and Lieuwen, Timothy. 2015. Transverse combustion instabilities: Acoustic, fluid mechanic, and flame processes. *Progress in Energy and Combustion Science*, **49**, 1–39.

O’Connor, Jacqueline and Lieuwen, Tim. February 2011. Disturbance Field Characteristics of a Transversely Excited Burner. *Combustion Science and Technology*, **183**, 427–443.

O’Connor, Jacqueline and Lieuwen, Tim. 2012a. Further characterization of the disturbance field in a transversely excited swirl-stabilized flame. *Journal of Engineering for Gas Turbines and Power*, **134**, 011501.

O'Connor, Jacqueline and Lieuwen, Tim. July 2012b. Recirculation zone dynamics of a transversely excited swirl flow and flame. *Physics of Fluids*, **24**, 075107.

O'Connor, Jacqueline, Worth, Nicholas A. and Dawson, James R. Flame and flow dynamics of a self-excited, standing wave circumferential instability in a model annular gas turbine combustor. In *ASME Turbo Expo 2013: Turbine Technical Conference and Exposition*. American Society of Mechanical Engineers, 2013.

O'Farrell, Clara and Dabiri, John O. 2014. Pinch-off of non-axisymmetric vortex rings. *Journal of Fluid Mechanics*, **740**, 61–96.

Pankiewitz, Christian and Sattelmayer, Thomas. Time domain simulation of combustion instabilities in annular combustors. In *ASME Turbo Expo 2002: Power for Land, Sea, and Air*, pages 309–320. American Society of Mechanical Engineers, 2002.

Parekh, D., Reynolds, W. and Mungal, M. Bifurcation of round air jets by dual-mode acoustic excitation. In *25th AIAA Aerospace Sciences Meeting*, page 164, 1987.

Parekh, David Espineli, Leonard, A. and Reynolds, W. C. Bifurcating jets at high Reynolds numbers. Technical report, Stanford University, Department of Mechanical Engineering, 1988.

Perumal, A. K. and Zhou, Y. 2018. Parametric study and scaling of jet manipulation using an unsteady minijet. *Journal of Fluid Mechanics*, **848**, 592–630.

Pope, Stephen B. *Turbulent flows*. IOP Publishing, 2001.

Raffel, Markus, Willert, Christian E., Kompenhans, Jürgen and others, . *Particle image velocimetry: a practical guide*. Springer Science & Business Media, 2007.

Raman, G., Rice, E. J. and Reshotko, E. 1994. Mode spectra of natural disturbances in a circular jet and the effect of acoustic forcing. *Experiments in fluids*, **17**, 415–426.

Reeder, M. F. and Samimy, M. 1996. The evolution of a jet with vortex-generating tabs: real-time visualization and quantitative measurements. *Journal of Fluid Mechanics*, **311**, 73–118.

Reynolds, W. C., Parekh, D. E., Juvet, P. J. D. and Lee, M. J. D. 2003. Bifurcating and blooming jets. *Annual review of fluid mechanics*, **35**, 295–315.

Rienstra, Sjoerd W. and Hirschberg, Avraham. An Introduction to Acoustics, 2017.

Rogers, Don E. 1956. A mechanism for high-frequency oscillation in ramjet combustors and afterburners. *Journal of Jet Propulsion*, **26**, 456–462.

Ruith, M. R., Chen, P., Meiburg, E. and Maxworthy, T. 2003. Three-dimensional vortex breakdown in swirling jets and wakes: direct numerical simulation. *Journal of Fluid Mechanics*, **486**, 331–378.

Saffman, Philip G. *Vortex dynamics.* Cambridge university press, 1992.

Saurabh, Aditya and Paschereit, Christian Oliver. Combustion instability in a swirl flow combustor with transverse extensions. In *ASME Turbo Expo 2013: Turbine Technical Conference and Exposition.* American Society of Mechanical Engineers, 2013.

Saurabh, Aditya, Steinert, Richard, Moeck, Jonas P. and Paschereit, Christian O. Swirl flame response to traveling acoustic waves. In *ASME Turbo Expo 2014: Turbine Technical Conference and Exposition.* American Society of Mechanical Engineers, 2014.

Schlueter-Kuck, Kristy and Dabiri, John O. 2016. Pressure evolution in the shear layer of forming vortex rings. *Physical Review Fluids*, **1**, 012501.

Schmid, Peter J. and Henningson, Dan S. *Stability and transition in shear flows*, volume 142. Springer Science & Business Media, 2012.

Schwing, Joachim, Grimm, Felix and Sattelmayer, Thomas. A model for the thermo-acoustic feedback of transverse acoustic modes and periodic oscillations in flame position in cylindrical flame tubes. In *ASME Turbo Expo 2012: Turbine Technical Conference and Exposition*, pages 553–566. American Society of Mechanical Engineers, 2012.

Schwing, Joachim and Sattelmayer, Thomas. High-frequency instabilities in cylindrical flame tubes: Feedback mechanism and damping. In *ASME Turbo Expo 2013: Turbine Technical Conference and Exposition.* American Society of Mechanical Engineers, 2013.

Schwing, Joachim, Sattelmayer, Thomas and Noiray, Nicolas. Interaction of vortex shedding and transverse high-frequency pressure oscillations in a tubular combustion chamber. In *ASME 2011 Turbo Expo: Turbine Technical Conference and Exposition*, pages 259–268. American Society of Mechanical Engineers, 2011.

Seybert, A. Fl and Ross, D. Fl. 1977. Experimental determination of acoustic properties using a two-microphone random-excitation technique. *the Journal of the Acoustical Society of America*, **61**, 1362–1370.

Shariff, Karim and Leonard, Anthony. 1992. Vortex rings. *Annual Review of Fluid Mechanics*, **24**, 235–279.

Shusser, Michael and Gharib, Morteza. 2000. Energy and velocity of a forming vortex ring. *Physics of Fluids*, **12**, 618–621.

Staffelbach, Gicquel, Gicquel, L. Y. M., Boudier, G. and Poinsot, Thierry. 2009. Large Eddy Simulation of self excited azimuthal modes in annular combustors. *Proceedings of the Combustion Institute*, **32**, 2909–2916.

Suzuki, H., Kasagi, N. and Suzuki, Y. 2004. Active control of an axisymmetric jet with distributed electromagnetic flap actuators. *Experiments in fluids*, **36**, 498–509.

Suzuki, Masataro, Atarashi, Takao and Masuda, Wataru. 2007. Behavior and structure of internal fuel-Jet in diffusion flame under transverse acoustic excitation. *Combustion Science and Technology*, **179**, 2581–2597.

Thomson, William. 1871. XLVI. Hydrokinetic solutions and observations. *The London, Edinburgh, and Dublin Philosophical Magazine and Journal of Science*, **42**, 362–377.

Urbin, Gérald and Métais, Olivier. Large-eddy simulations of three-dimensional spatially-developing round jets. In *Direct and Large-Eddy Simulation II*, pages 35–46. Springer, 1997.

von Helmholtz, Hermann. *über discontinuirliche Flüssigkeits-Bewegungen.* Akademie der Wissenschaften zu Berlin, 1868.

White, Frank. *Viscous fluid flow.* McGraw-Hill International Edition, third edition, 2006.

Wlezien, R. W. and Kibens, V. 1986. Passive control of jets with indeterminate origins. *AIAA journal*, **24**, 1263–1270.

Wolf, Pierre, Balakrishnan, Ramesh, Staffelbach, Gabriel, Gicquel, Laurent YM and Poinsot, Thierry. 2012a. Using LES to study reacting flows and instabilities in annular combustion chambers. *Flow, turbulence and combustion*, **88**, 191–206.

Wolf, Pierre, Staffelbach, Gabriel, Gicquel, Laurent and Poinsot, Thierry. Massively parallel LES of azimuthal thermo-acoustic instabilities in annular gas turbines. In *Journal of Physics: Conference Series*, volume 180, page 012035. IOP Publishing, 2009.

Wolf, Pierre, Staffelbach, Gabriel, Gicquel, Laurent YM, Müller, Jens-Dominik and Poinsot, Thierry. 2012b. Acoustic and large eddy simulation studies of azimuthal modes in annular combustion chambers. *Combustion and Flame*, **159**, 3398–3413.

Worth, Nicholas A. and Dawson, James R. November 2013a. Modal dynamics of self-excited azimuthal instabilities in an annular combustion chamber. *Combustion and Flame*, **160**, 2476–2489.

Worth, Nicholas A. and Dawson, James R. 2013b. Self-excited circumferential instabilities in a model annular gas turbine combustor: Global flame dynamics. *Proceedings of the Combustion Institute*, **34**, 3127–3134.

Yang, H., Zhou, Y., So, R. M. C. and Liu, Y. 2016. Turbulent jet manipulation using two unsteady azimuthally separated radial minijets. *Proceedings of the Royal Society A*, **472**, 20160417.

Zaman, KBMQ and Hussain, AKMF. 1980. Vortex pairing in a circular jet under controlled excitation. Part 1. General jet response. *Journal of fluid mechanics*, **101**, 449–491.

Zaman, KBMQ, Reeder, M. F. and Samimy, M. 1994. Control of an axisymmetric jet using vortex generators. *Physics of fluids*, **6**, 778–793.

Appendix A

Instability analysis of a round jet

In a vertical jet of constant density, there is an interface on each side of the jet between the jetflow and its surroundings. We can assume both regions are incompressible, irrotational and inviscid. At the left interface, or shear-layer, which divides the two flows with different velocity, both flows have a velocity potential and a static pressure distribution (White (2006)):

$$r < 0: \qquad \Phi_1 = 0, \qquad p_1 = p_0 - \rho g x \tag{A.1}$$

$$r > 0: \qquad \Phi_2 = Ux, \qquad p_2 = p_0 - \rho g x \tag{A.2}$$

Since the flow is inviscid there is tangential slip at the interface. We can introduce a disturbance, denoted by a prime:

$$\Phi_1 = \Phi_1'(x, r, t) \tag{A.3}$$

$$\Phi_2 = Ux + \Phi_2'(x, r, t) \tag{A.4}$$

At the interface we have $r = \eta(x, t)$, as seen in figure A.1. Since the flow is irrotational it must satisfy the unsteady Bernoulli equation:

$$p_i = C_i - \rho \frac{\partial \Phi_i}{\partial t} - \frac{\rho_i}{2} |\nabla \Phi_i|^2 - \rho_i g x \tag{A.5}$$

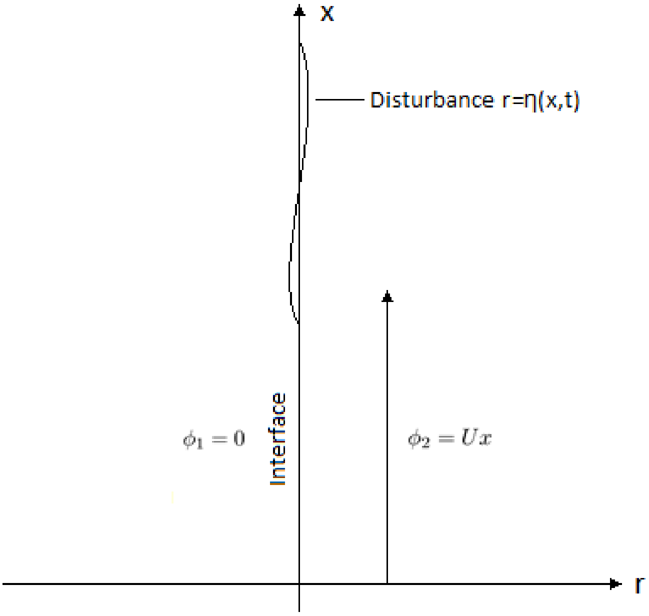

Figure A.1: Kelvin-Helmholtz instability

The relation between C_1 and C_2 can be found by looking at the flow without disturbance at $r = 0$:

$$C_1 - \rho g x = C_2 - \frac{\rho}{2}U^2 - \rho g x \tag{A.6}$$

or

$$C_1 = C_2 - \frac{\rho}{2}U^2 \tag{A.7}$$

One boundary condition that must be satisfied is that there cannot be a discontinuity in the pressure over the interface. At $r = \eta$ we then have

$$C_1 - \rho\frac{\partial \Phi_1}{\partial t} - \frac{\rho}{2}|\nabla\Phi_1|^2 - \rho g x = C_2 - \rho\frac{\partial \Phi_2}{\partial t} - \frac{\rho}{2}|\nabla\Phi_2|^2 - \rho g x \tag{A.8}$$

which can be reduced to

$$C_1 - \rho\frac{\partial \Phi_1}{\partial t} - \frac{\rho}{2}|\nabla\Phi_1|^2 = C_2 - \rho\frac{\partial \Phi_2}{\partial t} - \frac{\rho}{2}|\nabla\Phi_2|^2 \tag{A.9}$$

A second boundary condition is that the horizontal velocity of the flow at each side of the interface at $r = \eta$ must equal the motion of the interface:

$$v_1 = \frac{\partial \Phi_1}{\partial r} = \frac{d\eta}{dt} = \frac{\partial \eta}{\partial t} + \frac{\partial \Phi_1}{\partial x}\frac{\partial \eta}{\partial x} \tag{A.10}$$

$$v_2 = \frac{\partial \Phi_2}{\partial r} = \frac{d\eta}{dt} = \frac{\partial \eta}{\partial t} + \frac{\partial \Phi_2}{\partial x}\frac{\partial \eta}{\partial x} \tag{A.11}$$

The last boundary condition is that the disturbance does not affect the flow far away from the interface:

$$\lim_{x\to-\infty} \nabla \Phi_1' = \lim_{x\to\infty} \nabla \Phi_2' = 0 \tag{A.12}$$

Since the flow is assumed to be incompressible, the continuity equation expressed with the velocity potential reduces to Laplace's equation:

$$\nabla^2 \Phi_1 = 0 \qquad\qquad \nabla^2 \Phi_2 = 0 \tag{A.13}$$

By subtracting the mean flow, we get

$$\nabla^2 \Phi_1' = 0 \qquad\qquad \nabla^2 \Phi_2' = 0 \tag{A.14}$$

By inserting equation (A.7) into (A.9) and assuming that the disturbance is small compared to the original flow, we get the linearized pressure condition:

$$\frac{\partial \Phi_1'}{\partial t} \approx U\frac{\partial \Phi_2'}{\partial x} + \frac{\partial \Phi_2'}{\partial t} \tag{A.15}$$

In the same way we can obtain the linearized kinematic conditions:

$$\frac{\partial \Phi_1'}{\partial r} \approx \frac{\partial \eta}{\partial t} \tag{A.16}$$

$$\frac{\partial \Phi_2'}{\partial r} \approx \frac{\partial \eta}{\partial t} + U\frac{\partial \eta}{\partial x} \tag{A.17}$$

If we assume that the disturbance is a two-dimensional traveling wave

$$\eta = \eta_0 e^{i(\alpha x - \sigma t)} \tag{A.18}$$

we get

$$\Phi_1' = \hat{\Phi}_1'(r)e^{i(\alpha x-\sigma t)} \tag{A.19}$$

$$\Phi_2' = \hat{\Phi}_2'(r)e^{i(\alpha x-\sigma t)} \tag{A.20}$$

For equation (A.14) to be satisfied we need:

$$\hat{\Phi}_1' = A_1 e^{\alpha r} + B_1 e^{-\alpha r} \tag{A.21}$$

$$\hat{\Phi}_2' = A_2 e^{-\alpha r} + B_2 e^{\alpha r} \tag{A.22}$$

The condition in equation (A.12) demands $B_1 = B_2 = 0$:

$$\hat{\Phi}_1' = A_1 e^{\alpha r} \tag{A.23}$$

$$\hat{\Phi}_2' = A_2 e^{-\alpha r} \tag{A.24}$$

Combining this with equation (A.18)-(A.20) and inserting it into (A.16) and (A.17) give us:

$$A_1 = -i\eta_0 \frac{\sigma}{\alpha} \quad \text{and} \quad A_2 = i\eta_0 \left(\frac{\sigma}{\alpha} - U\right) \tag{A.25}$$

We have then found the form of the velocity potentials:

$$\Phi_1' = -i\eta_0 \frac{\sigma}{\alpha} e^{\alpha r} e^{i(\alpha x-\sigma t)} \tag{A.26}$$

$$\Phi_2' = i\eta_0 \left(\frac{\sigma}{\alpha} - U\right) e^{-\alpha r} e^{i(\alpha x-\sigma t)} \tag{A.27}$$

We can now use the velocity potential to say something about the stability of the flow. If σ is imaginary or complex, the exponent containing time, $-i\sigma t$, will contain a real part, and the disturbance η together with the velocity potential will diverge as $t \to \infty$. The flow is then unstable. If σ on the other hand is purely real, $-i\sigma t$ will be purely imaginary and the flow is stable. Inserting (A.26) and (A.27) into equation (A.15) gives us σ at $r = 0$:

$$\sigma = \frac{U\alpha}{2}(1 \pm i) \tag{A.28}$$

Therefore, the flow is unconditionally unstable and oscillations in the shear-layer of the jet will grow in amplitude.

Appendix B

Supplementary results

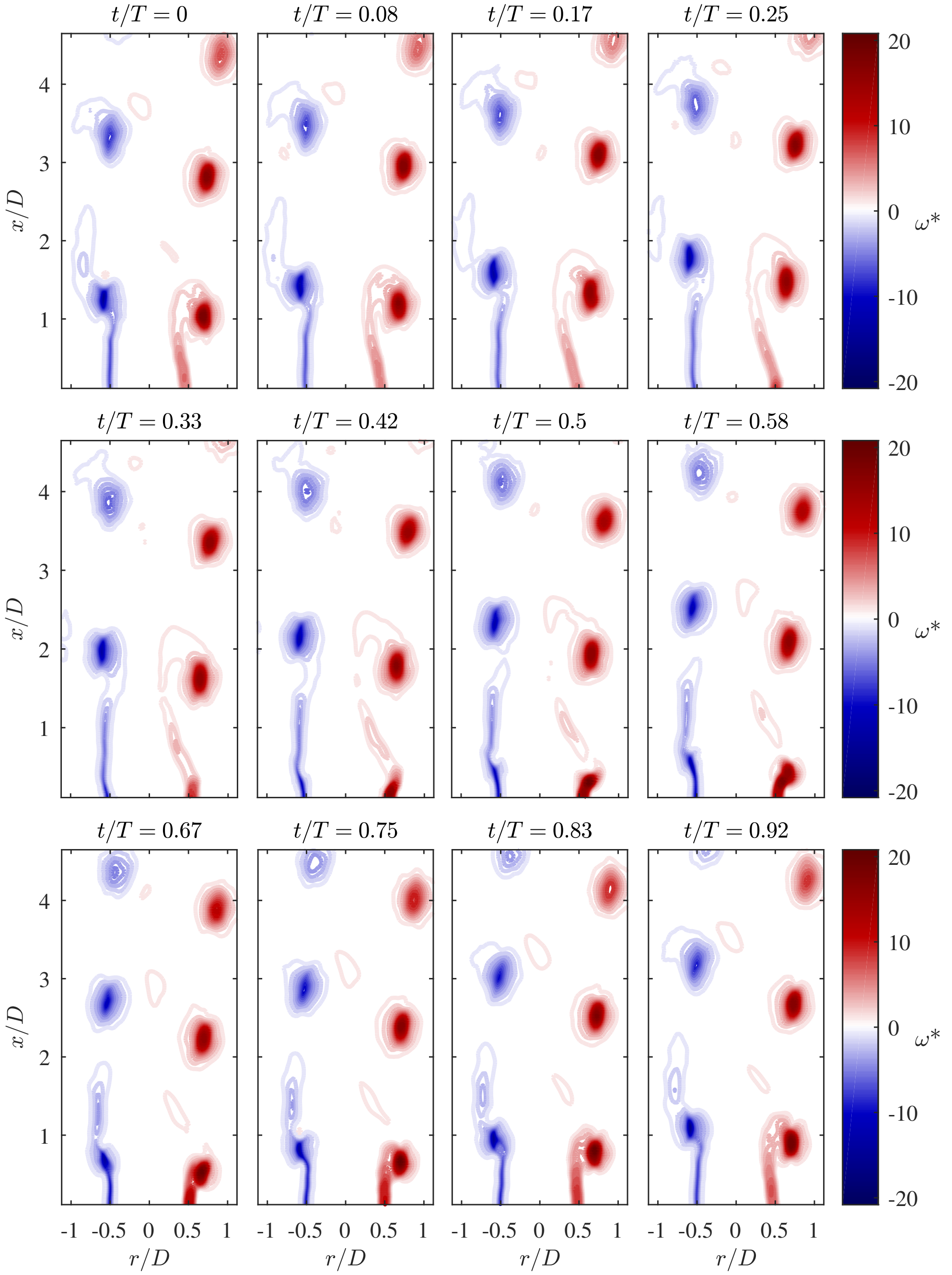

Figure B.1: Time-series of phase averaged vorticity contours for $y/\frac{\lambda}{4} = 0.25$, $f = 450$ Hz, $U_e = 13.1$ m/s, $u'_{\mathrm{AN,RMS}}/U_e = 0.25$.

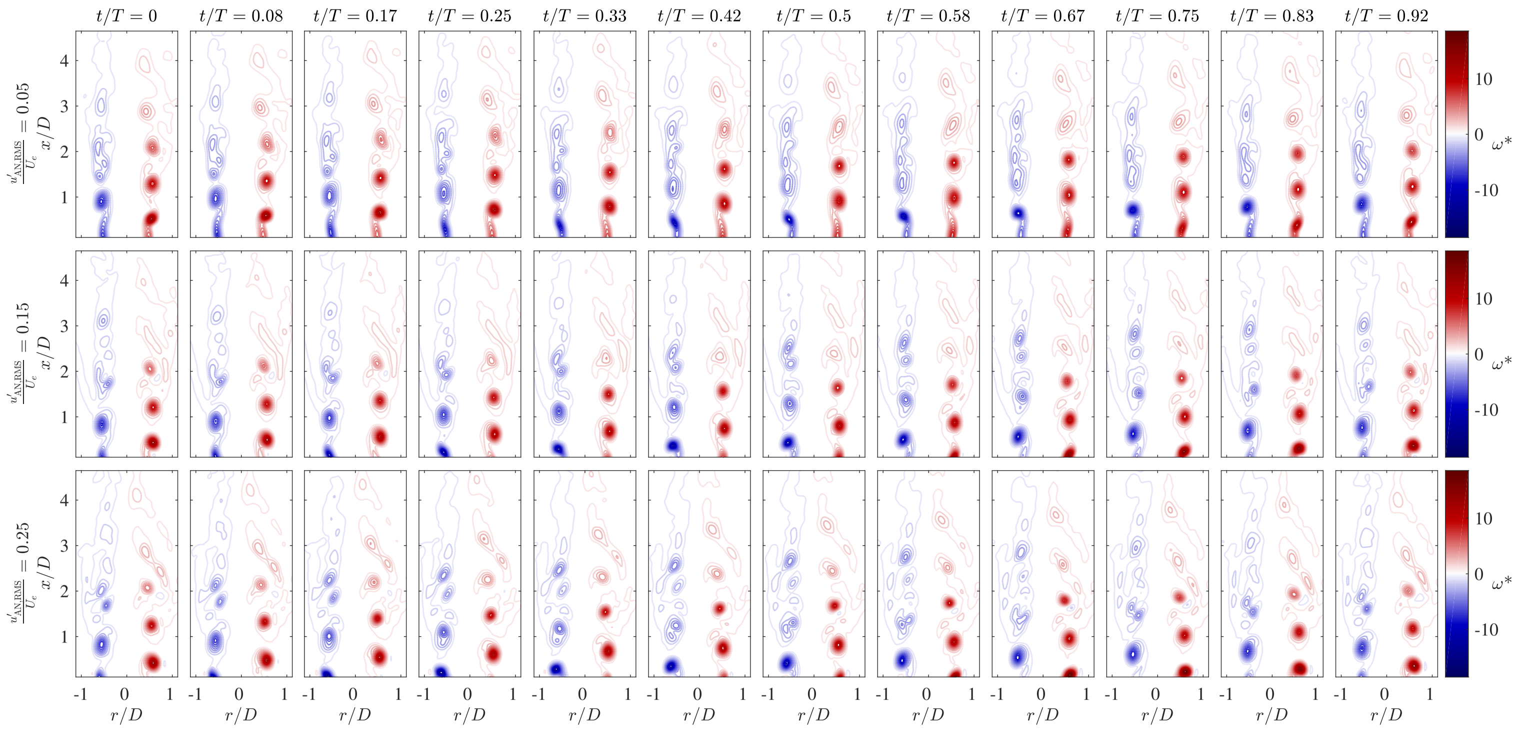

Figure B.2: Time-series of phase averaged vorticity contours for $y/\frac{\lambda}{4} = 1$, $f = 450$ Hz, $U_e = 6.8$ m/s.

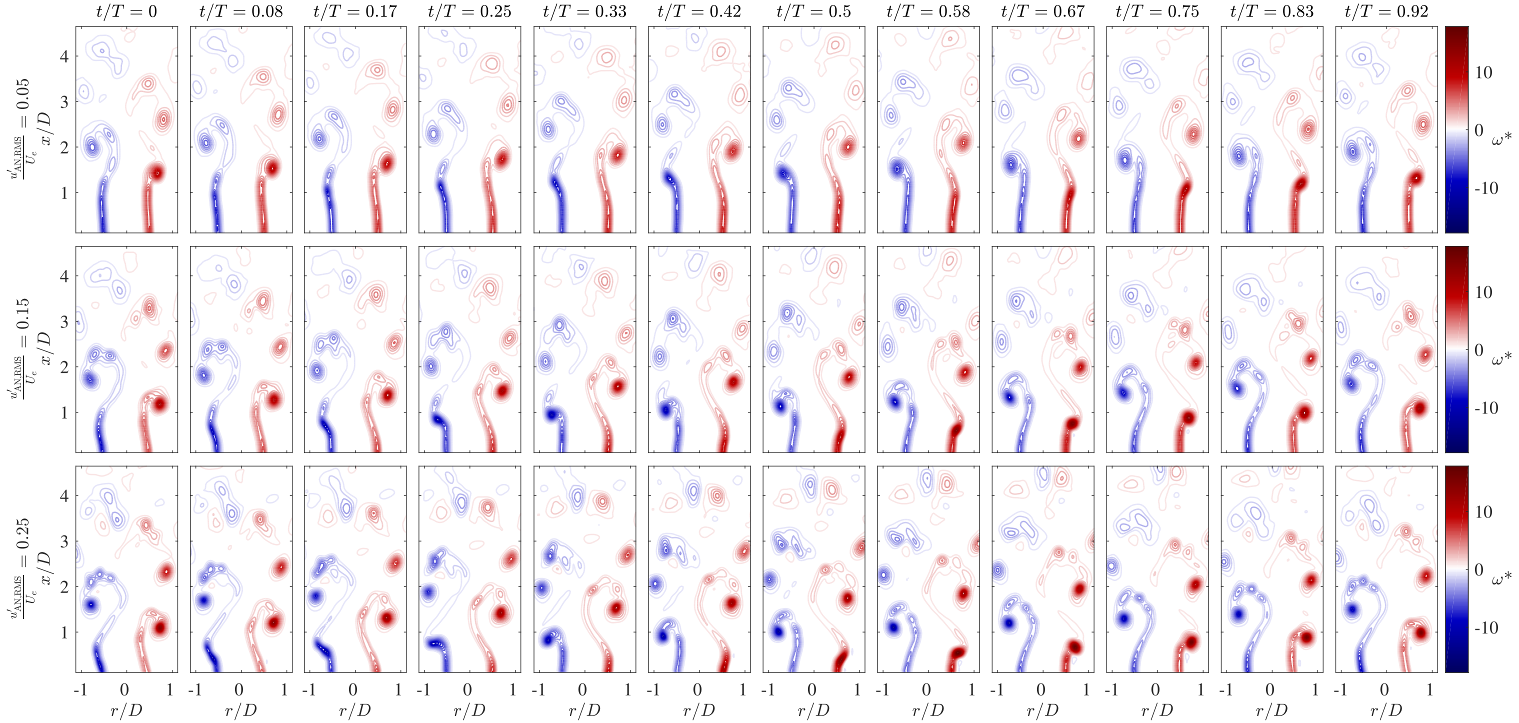

Figure B.3: Time-series of phase averaged vorticity contours for $y/\frac{\lambda}{4} = 1$, $f = 450$ Hz, $U_e = 13.1$ m/s.

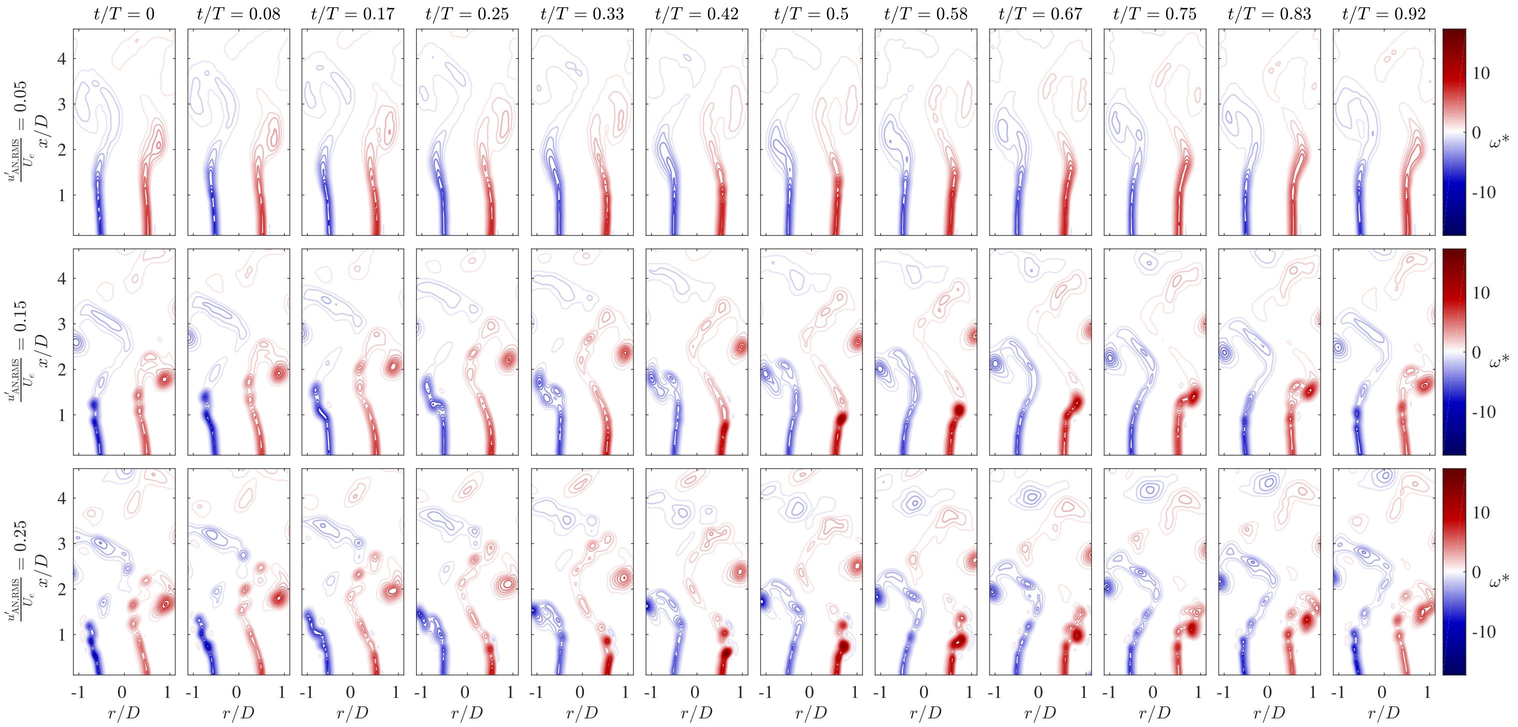

Figure B.4: Time-series of phase averaged vorticity contours for $y/\frac{\lambda}{4} = 1$, $f = 450$ Hz, $U_e = 18.9$ m/s.

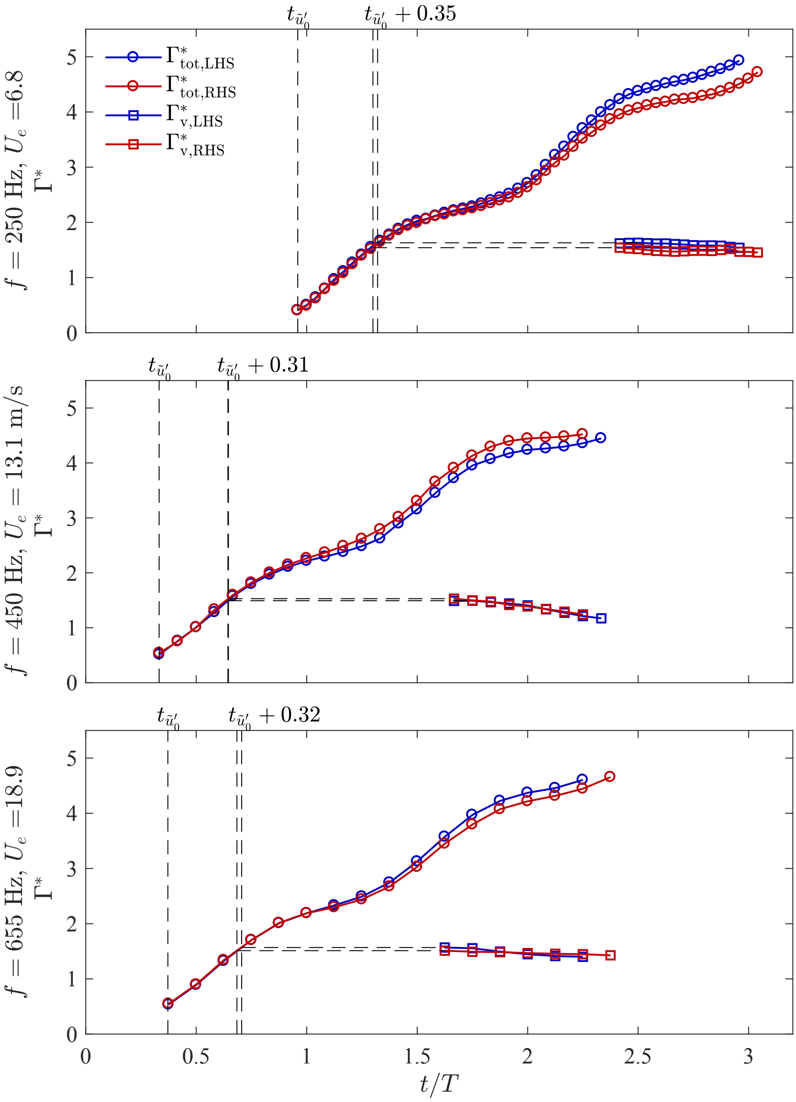

Figure B.5: Total circulation (circles) and vortex circulation (squares) on the left and right hand side of the jet as a function of time at the pressure anti-node for $u'_{\text{AN,RMS}}/U_e = 0.25$, using the original method by Gharib *et al.* (1998). The calculation of circulation is started at $t_{\tilde{u}_0}$.

Appendix C

Acoustically compact nozzle

The nozzle diameter is said to be acoustically compact if it is much smaller than the acoustic wavelength, so that the nozzle experiences the same pressure over the whole diameter:

$$D \ll \lambda. \tag{C.1}$$

In this study the nozzle diameter is constant, while the wavelength varies with forcing frequency. The shortest wavelength appears at the highest frequency and mode number, which for this study is $f = 655$ Hz and 6, respectively. This gives the following ratio between the nozzle diameter and the length of the transverse acoustic wave in the jet enclosure:

$$\frac{D}{\lambda} = \frac{D}{L_y/\frac{m}{2}} = \frac{1\ \mathrm{cm}}{(160/3)\ \mathrm{cm}} = 0.019. \tag{C.2}$$

For the nozzle positioned at the pressure node, the shear-layer of the nozzle, at $r/D = \pm 0.5$, experiences the following pressure:

$$\begin{aligned}\frac{|\hat{p}'(r/D = \pm 0.5)|}{|\hat{p}'_{\mathrm{AN}}|} &= \cos\left(\frac{2\pi}{\lambda}(\lambda/4 \pm D/2)\right)\\ &= \cos\left(2\pi\left(1/4 \pm \frac{0.5\ \mathrm{cm}}{(160/3)\ \mathrm{cm}}\right)\right)\\ &= \pm 0.059.\end{aligned} \tag{C.3}$$

At $y/\frac{\lambda}{4} = 0.75$, the pressure fluctuations are as much as 33% larger at $r/D = -0.5$ compared to $r/D = 0.5$:

$$\begin{aligned}\frac{|\hat{p}'(r/D = -0.5)|}{|\hat{p}'(r/D = 0.5)|} &= \frac{\cos\left(\frac{2\pi}{\lambda}(0.75 \cdot \lambda/4 - D/2)\right)}{\cos\left(\frac{2\pi}{\lambda}(0.75 \cdot \lambda/4 + D/2)\right)}\\ &= \frac{\cos\left(2\pi\left(0.75/4 - \frac{0.5\ \mathrm{cm}}{(160/3)\ \mathrm{cm}}\right)\right)}{\cos\left(2\pi\left(0.75/4 + \frac{0.5\ \mathrm{cm}}{(160/3)\ \mathrm{cm}}\right)\right)}\\ &= 1.33.\end{aligned} \tag{C.4}$$

ISBN 978-82-326-4632-6 (printed version)
ISBN 978-82-326-4631-9 (electronic version)
ISSN 1503-8181

NTNU
Norwegian University of
Science and Technology

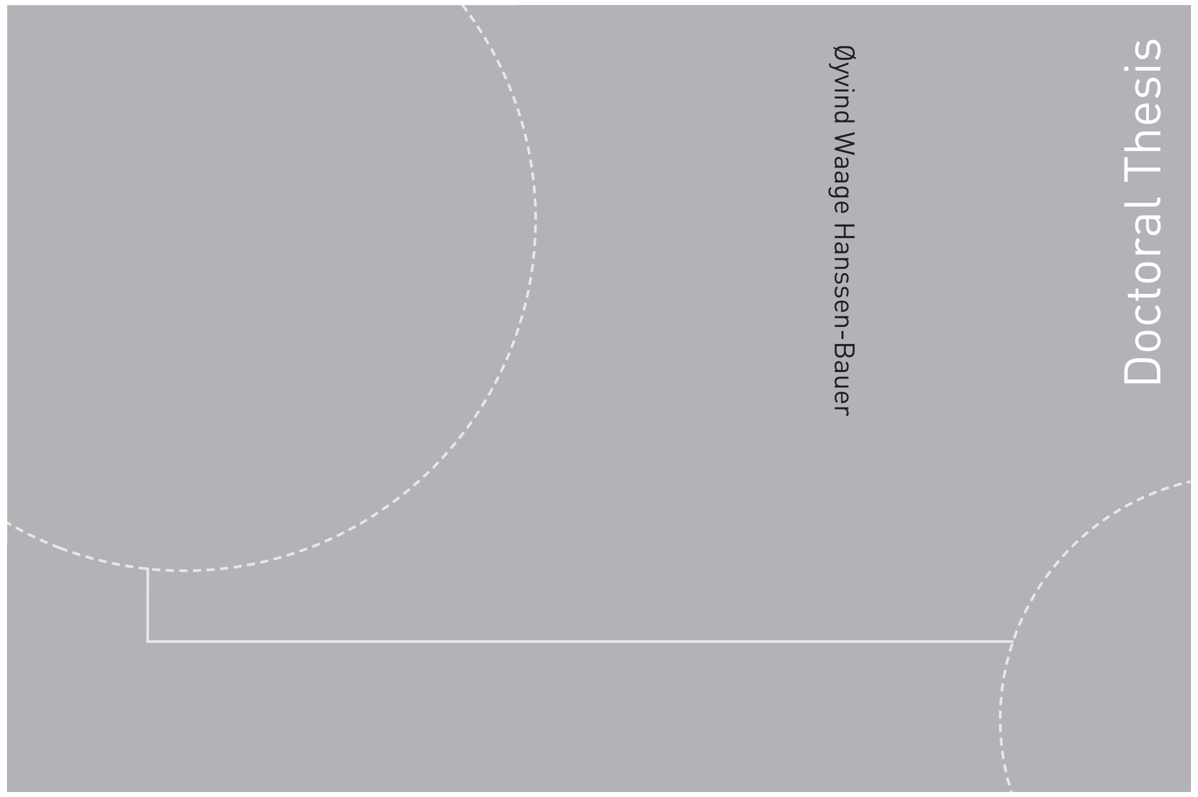

Øyvind Waage Hanssen-Bauer

Doctoral theses at NTNU, 2020:142

NTNU

Doctoral Thesis

NTNU
Norwegian University of
Science and Technology
Faculty of Engineering
Department of Energy and Process Engineering

Doctoral theses at NTNU, 2020:142

Øyvind Waage Hanssen-Bauer

Near-field response of an axisymmetric jet to transverse acoustic forcing

NTNU
Norwegian University of
Science and Technology